Manufacturing method, microstructure and mechanical property relationships for a metal matrix composite

Chapman, A. R.

Award date:
1991

Awarding institution:
University of Bath

MANUFACTURING METHOD, MICROSTRUCTURE AND MECHANICAL PROPERTY RELATIONSHIPS FOR A METAL MATRIX COMPOSITE.

Submitted by A.R. Chapman

for the degree of PhD

of the University of Bath

1991

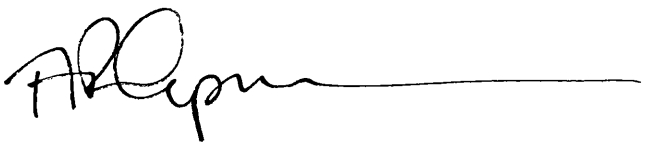

ProQuest LLC
789 East Eisenhower Parkway
P.O. Box 1346
Ann Arbor, MI 48106-1346

ABSTRACT.

Aluminium and aluminium alloy metal matrix composites fabricated by liquid metal infiltration are investigated. Reinforcements used are mainly Nicalon continuous fibre but studies on an alumina and Borsic fibre hybrid have also been carried out. The microstructure is characterized using scanning and transmission electron microscopy as well as electron-probe microanalysis (EPMA).

In the composite based on an aluminium-7% silicon-0.4% magnesium alloy, the silicon morphology relating to the cast eutectic microstructure is modified by the manufacturing method. Contamination, during fabrication, with iron is also found as evidenced in the formation of $FeSiAl_5$ intermetallics. Other composite defects include porosity which is particularly noticeable in regions of closely packed fibre, especially where a glass weft has been used in preform fabrication.

Detailed studies of the x-ray emission peaks from the Nicalon fibre show that it is not simply silicon carbide but contains substantial amounts of a silicon-carbon-oxygen phase and free carbon. The aluminium in the matrix reacts with components in the Nicalon to form Al_4C_3, but when silicon is present the SiC/Al reaction does not occur. Alumina is found at the fibre/matrix interface and segregation of magnesium to the outer surface of the fibre was noted.

Measured fracture strength of the composite is typically ~130 MPa, well below the ~1 GPa predicted using a simple rule of mixtures. This is explained by formation of interphases which lower the fibre strength. Use of the Al-Si-Mg precipitation-hardening alloy as the matrix did not result in any increase in transverse properties; indeed, the thickness of the interphase was increased and the fibre strength further reduced. The initiation of fibre fracture and subsequent composite failure is attributed to the presence of Al_4C_3 but matrix phases also contributed to the poor properties by acting as flaws.

CONTENTS.

CHAPTER.1. INTRODUCTION

1.1. Metal Matrix Composites.

Combining two or more materials to produce a desired set of properties is by no means a new concept and has been performed for numerous reasons, but essentially the choice of components is aimed at optimisation of properties, whether mechanical, physical or chemical. The term composite embraces a multitude of materials which will by nature have a diverse character, the majority of research and development haws been concerned with polymeric matrix composites, which in itself is a highly variable field. One of the main driving forces for the development of composite materials has been the desire to produce materials having high specific properties under severe environmental conditions. The use of metal matrix composites (MMC) produces a material with lower anisotropy than the polymer matrix composite and for a service temperature above 200°C, MMCs become more attractive materials than polymer-based composites and indeed conventional alloys. Early development of MMCs was limited by the availability of suitable non-reactive reinforcements and was confined to large monofilaments of boron and silicon carbide. However, with the commercial production of more chemically inert reinforcements the interest in MMCs has enjoyed a revival.

The choice of components is application dependent and each will have a specific role. The reinforcement is a material with a higher theoretical strength, which means that these have predominantly covalent bonding and are generally ceramic materials. In the bulk form such reinforcement materials show poor strength due to a dependence on the population of flaws and in general greater mechanical strength

is achieved only when small diameter filaments are used. The best strengths are associated with whisker materials but these have problems of handling, which limits their application. However, any reinforcement material is near useless for engineering applications without the matrix constituent. The matrix has several roles. These include the transfer of stress to the reinforcement, so that the composite has the ability to withstand compression and shear as well as tensile loads. Also, since the fibres are the principal load bearing component, the matrix must be able to protect them from physical or chemical induced damage. Isolation of the fibres from one another is an important role, as they are generally brittle and the resistance of the crack progression is imparted by the matrix. Therefore a ductile matrix will clearly provide a means of slowing down any cracks which may have originated at the failed fibres.

In recent years an interest in metal matrix composites (MMCs) has been renewed[1-3]. In addition to the basic strength and stiffness of metal matrix composites it is desirable that these room temperature properties should be retained at elevated temperatures.

Since the reinforcements are usually low density the component weight is not increased and so the specific properties (property/density) are increased. This is particularly important with applications where fuel costs are paramount, as in civil aviation and the automotive industries. A second phase may also be added to confer greater wear resistance and dimensional stability.

The metal also contributes to the mechanical properties of the MMC particularly those in the transverse orientation. High strength alloys may be used such as alloys which can be strengthened by the formation of a thermodynamically metastable

precipitate phase. However, for applications at elevated temperatures the second phase may coarsen and loss of strength or embrittlement result.

Early MMC research[4-8] was restricted by the available reinforcements. Difficulties in the incorporation of whiskers[6] and the reactions between matrix metal and fibre[4,5] resulted in the lack of production of useful components. With the advent of more inert fibres of alumina[9,13-15], boron[15,65,66] and silicon carbides[14-36] a resurgence of interest has occurred. Much work has recently been carried out on these materials and in many cases there has been a marked improvement in the properties of the MMC.

The need for a fairly inert reinforcement concerns the strength of the interfacial bond. As mentioned above, the bond is should allow load transfer to the fibres and a reasonable bond strength is needed to achieve this. However, if an extensive reaction occurs between the fibre and matrix then another phase may form which might be a brittle material and act as an initiation site for failure. Furthermore, the ability of the composite to withstand crack propagation also depends on the degree of bonding. For example, too strong a bond may restrict the pull out during stressing the composite and limit the fracture toughness of the composite.

Much work has been carried out on methods of reducing deleterious interface reactions. The application of coatings to the fibre with an inert material is one such approach and layers of silicon carbide are usually applied to reactive fibres such as boron[65,66]. The converse is applied also[172], where the reinforcement surface is treated to enhance an interfacial reaction, with the intention of increasing the interfacial bond.

The choice of matrix material depends partly on the final application and manufacturing route but generally light alloys such as aluminium, magnesium and titanium are used. Other metals include lead, copper and iron, where the final composites have usually non-strength/stiffness critical applications. For example, the addition of conducting carbon fibres to lead in batteries gives a reduced weight[38].

MMC materials, because of their hard reinforcement constituent, are very difficult and expensive to machine and secondary processing is avoided if possible. There are two main fabrication routes for MMCs, solid state and liquid state. The latter tends to encompass more techniques as it potentially a cheaper method of producing the component, having fewer fabrication steps. This is especially true when the technique is able to yield near-net-shape. The liquid metal forming techniques are varied and include squeeze casting and vacuum infiltration. Casting alloys with a high fluidity are used as they should provide good penetration into the fibre mass.

Clearly, the behaviour of the composite will depend not only on the nature of the fibre and the matrix but on the way in which the composite is fabricated.

1.2. Matrix Alloys

The matrix metal used depends on the intended application and these are usually alloys. A prime requirement for the matrix material, is low density and the alloys utilized are consequentially those which have been applied historically in the aerospace industry such as titanium, magnesium and aluminium. Titanium alloys have typically been used in critical load bearing applications in the aerospace

industry and although their basic cost is greater than aluminium alloys this may be more than offset by the possibility of utilizing fabrication techniques such as superplastic forming and diffusion bonding. The alloys of titanium generally have a better resistance to environment and potential high strengths and fracture resistance than the aluminium alloys. Magnesium alloys can have very desirable specific properties, although their corrosion resistance and chemical compatibility are relatively poor compared with the aluminium due to the lack of passivation in aqueous and acidic environments.

Aluminium alloys have been more widely used as matrix material because of a combination of good specific properties and low cost. With fabrication routes based upon liquid metal processing, casting alloys such as the aluminium-silicon type have been used[40-44,52-55]. The mechanical strength of a composite with unidirectionally aligned fibres will be dependent largely on the properties of the fibre component but in the transverse orientation properties will be controlled essentially by the matrix.

In order to improve the matrix strength alloying additions are made to the aluminium alloy in order to develop age hardening precipitates. Alloys such as Al-Cu[47,119], Al-Zn-Mg[48], Al-Li[68] and Al-Mg-Si[40-43,167] have been investigated for this purpose. The addition of elements such as magnesium and lithium reduce the surface tension of the melt and so aid the wetting of the reinforcement[179]. The wetting is important when the infiltration of the preform is considered. In several studies alloying elements have been added to enhance the interfacial bond, these often involve some chemical reaction between matrix and reinforcement. In the study by Choh and Oki[136] the alloy additions found to improve the wetting of silicon carbide were those which readily form carbides.

The aluminium-silicon alloy matrix, which is particularly relevant to the composites investigated in the present work, forms a simple eutectic system[59] in which are included a range of useful foundry compositions. Silicon is one of the alloying additions which can be combined with aluminium without increasing the specific gravity. The microstructure is that of a typical eutectic system[59,60], the silicon growing in a faceted anisotropic manner and the aluminium is typically non-faceted. Figure 1.1 shows the Al-Si phase diagram[58,60], indicating the limited solid solubility of aluminium in silicon, up to 1.65 wt % silicon at the eutectic temperature (577°C). The silicon-rich constituent contains 0.5% aluminium[59,60]

The silicon imparts a high degree of fluidity and a low amount of shrinkage. This in turn results in a good castability which is desirable in MMCs for good infiltration. The microstructure shows primary α-dendrites in an eutectic mixture. It is the shape and distribution of the silicon that has the largest influence on the mechanical properties of the alloy[59]. The exact structure depends more on its thermal history[61], especially close to the eutectic point, than on its silicon content. Fast cooling results in the formation of primary silicon[59,61], while slow cooling rates yield high proportions of eutectic material.

Whilst the formation of small, rounded and evenly distributed particles of silicon will result in high ductility, faceted acicular crystals may reduce the ductility and the resistance to impact damage and fatigue resistance. Heating also tends to spherodize the silicon.

The more desirable microstructure of finely dispersed silicon particles with a more fibrous morphology may be induced by small additions of sodium[59,61,63] (or larger

additions of strontium). Sodium levels of little over 0.01% are known to modify the microstructure.

Magnesium is sometimes added to aluminium silicon alloys in small percentages to encourage the formation of a second phase, Mg_2Si, and to promote an hardening response[60,61]. The relevant corner of the Al-Mg-Si phase diagram is shown in figure 1.2, a quasibinary line Al-Mg_2Si occurring at the ratio Mg:Si of 1:7.3

In the Al-Mg-Si system, growth of the second phase starts with the formation of Guinier-Preston (GP) zones. These are transient particles which assume a needle shape and are elongated in the [100] matrix direction. The precipitate which then forms is termed β" and is monoclinic, with a=b=0.616 nm, c=0.71 nm, $\alpha=\beta=90^\circ, \gamma=82^\circ$. The orientation relationship with the aluminium matrix may be written:

$$(111)_{\beta''} \parallel (110)_{Al} ; [110]_{\beta''} \parallel [001]_{Al}$$

The next intermediate phase which develops, β', is semicoherent with the aluminium lattice and it has been proposed to have either a cubic lattice with a=0.642 nm or hexagonal with a=0.705nm, c=0.405nm and the orientation relationships:

$$(001)_{\beta'} \parallel (100)_{Al} : [100]_{\beta'} \parallel [01\bar{1}]_{Al} \text{ or } [011]_{Al}$$

The final phase β, (Mg_2Si), which has a cubic structure with a = 0.64 nm, forms with the orientation relationship;

$(100)_\beta \parallel (100)_{Al}$

It is believed to nucleate at the β'-matrix interface and grow at the expense of β'.

Summarising, the route for the formation of Mg_2Si precipitates in Al-Si-Mg alloys is as follows;

$GP_{zones} \rightarrow \beta''_{needles} \rightarrow \beta'_{rods} \rightarrow \beta_{(Mg2Si)}$

Whilst, however, additions of magnesium can increase substantially the strength, a corresponding reduction in ductility has been reported. In non-equilibrium conditions Mg_2Si can coexist with $CuAl_2$ and Si, although the phase $Cu_2Mg_8Si_6Al_5$ may also form when copper is present.

1.3. FIBRE MATERIALS.

Reinforcements may be divided into continuous and discontinuous, the latter group including particulate, plate, whisker and short fibre. The development of new reinforcement materials has expanded with the resurgence of interest in metal matrix composites and the requirement for structural materials suitable for high temperature applications has resulted in several different types. The choice of ceramic material as reinforcement involves consideration of their high specific strength and high elastic modulus, high melting temperature, and the retention of mechanical properties to temperatures of around 1000°C. Continuous fibre and high aspect ratio discontinuous fibres offer the highest potential mechanical

strengths. A selection of typical fibre properties is given in table 1.1.

In addition to the performance of the reinforcement, its compatibility with the matrix materials must be considered. For example, carbon fibres have a high strength at a relatively low cost but are known to be reactive with aluminium alloys (see section 1.6.). The fabrication route for producing the reinforcement may also result in retained flaws which will affect the final components properties.

There are two main routes to produce a ceramic fibre, pyrolysis of a polymeric precursor and deposition of a material by, for example, chemical vapour deposition, upon a substrate wire. In the following examples the manufacture of those reinforcements used in the present study is described, although many of the stages are similar to those used to produce other types of fibre.

1.3.1. Nicalon fibre.

This type of fibre was developed by Yajima and co workers[14,17,32] and is claimed to consist of predominantly β-silicon carbide (~70%). The fibres are produced commercially by the Nippon Carbon company and marketed under the trade name Nicalon. A large amount of work has been published on these and similar fibres, particularly their structure[14-36].

The first stage in Nicalon fibre production involves forming a dimethylpolysilane by dechlorination of dichlorodimethylsilane using molten sodium (or lithium). Then by heating in an autoclave at about 450°C in an argon atmosphere for around 8 hours, polysilapropylene is produced.

The polysilapropylene is melt spun at about 350°C under nitrogen gas to yield fibres with a strength around 10MPa. The fibres are cured to prevent melting in subsequent stages of manufacture by heating in air at temperatures up to 200°C or by oxidation with ozone at room temperature. The fibres are now rendered infusible due to cross-linking of the molecular chains by oxygen, the silicon combining with the oxygen to give Si-O-Si and some Si-O-C bonding.

The cured polycarbosilane fibre is finally fired in vacuum or nitrogen atmosphere at a temperature which is slowly increased up to 1300°C. The fabrication route is summarized in figure 1.3.

Although Nicalon fibre is usually referred to as being a β-silicon carbide it has been demonstrated that significant amounts of oxygen and carbon are present[14,15,21]. Furthermore, chemical analysis using Auger spectrometry[29] and electron-probe microanalysis[14] showed that the amount of silicon, carbon and oxygen varied considerably between individual fibres, the average composition being given in table 1.2. Bunsell, Simon, Abe and Akiyama[14] reported that the distribution of elements was uniform across the fibre but that there was the possibility of a silica layer on the surface that the microprobe could not resolve.

It has been suggested that the fibre consists of microcrystallites of β-silicon carbide which range in size from 2nm to 7nm but certain grades of Nicalon contain amorphous material[14-18]. In all cases the crystalline component of SiC is found to comprise of the beta polymorph, the size of the microcrystallites being dependent upon the final heat treatment[17,20].

The form in which the oxygen is present in the Nicalon fibre is more complicated.

Early work[14-22] assumed all the oxygen existed as silica throughout the fibre, to give compositions such as those shown in table 1.3. However, further investigation[35,36] showed the probable presence of a ternary phase such as a silicon oxycarbide, SiO_xC_y. Laffon, Flank, Lagrarde, Laridjani, Hagege, Olry, Cotteret, Dixmier, Miguel, Hommel and Legrand[36] proposed that the fibre consisted of a "continuum" of tetrahedra of two structure types: SiC_4 and SiC_xO_y (with x+y=4). Furthermore, they located a thin layer of silica on the fibre surface of a thickness no more than a few angstroms but none within the fibre bulk. The proposed structure of Laffen et al is shown in figure 1.4. The free carbon is considered to be in the form of aromatic rings of about 1nm in size which are stacked in groups of two or three and distributed throughout the fibre.

A range of diameters for the Nicalon fibre is commonly found, figure 1.5, with a mean value of around 15μm. Mechanical strength of the Nicalon fibre has been shown to be dependent on the defect population and on the gauge length of the fibre tested[19,21,67]. Measured strengths are typically about 1.3GPa, see figure 1.6, although the manufacturers (Nippon Carbon Co.) quote a value of 2.8GPa[34] with no gauge length given. The fibre exhibits brittle failure characteristics due to the presence of defects. Anderson and Warren[21] have categorized the defects as: (i) large defects which arise when spinning the precursor fibre, (ii) moderate surface defects which are formed during heat treatment and handling and (iii) defects which are intrinsic to the fibre's structure although they do not elucidate any further.

1.3.2. Alumina

The main limitation to the use of this reinforcement has been the difficulty in producing fibres of adequate quality. The mechanical properties are strongly affected by the presence of pores and defects as well as crystallite size and these, in turn, are very dependent on the manufacturing process. Several types of alumina fibre are available commercially.

A fibre referred to as FP-alumina (Du Pont) was used in this study[9,14,15,64]. It was manufactured utilizing a textile fibre spinning process in three main stages. Firstly, an aqueous slurry is prepared consisting of aluminium chlorohydroxide ($Al(OH)_5Cl.nH_2O$) containing a small amount of $MgCl_2.6H_2O$ and alumina particles of a size <0.5nm. A suitable spin-mix is made by careful control of the viscosity of the solution and this is then drawn through a spinneret to form fibres of diameter 20 to 30μm. Finally, the precursor is fired in air to temperatures of 1300°C to convert it to α-alumina. Further treatment in a propane-air flame for a few seconds allows the fibre to sinter.

The product is polycrystalline alumina (99.5%) diameter 20μm, with the α (hexagonal) structure and a grain size of approximately 0.5μm. It is claimed[9,64] that the fibres are stable in air up to 1100°C and they are electrically insulating. They have a Youngs modulus typically 355-379GPa, a density of 3.9 g cm^{-3} and a tensile strength of 1.38GPa.

Similar melt spinning techniques have been developed for producing precursors used in the manufacture of γ-alumina fibres[14]. Here an organoaluminium compound is employed. In the starting material aluminium and silicon atoms are

homogeneously mixed. This results in a very fine crystallite size (0.01μm) with a homogeneous distribution of silica and alumina in proportions of about 15% and 85% respectively.

Alumina fibres have also been made by growing single crystals in a molybdenum capillary tube from the melt[14,15]; this produces continuous filaments. Extrusion blowing of a viscous liquid form followed by firing in air above 1100°C is another method developed for producing fibres[14,15], (ICI Saffil fibres).

1.3.3. Borsic.

The technique[15,65,66] uses a chemical vapour deposition (CVD) process, involving the reduction by hydrogen of a boron halide gas on a heated substrate according to a reaction of the form:

$$2BX_3(g) + 3H_2(g) \rightarrow \text{heat} \rightarrow 2B(s) + 6HX(g).$$

where X may be Cl, Br or I.

The solid boron is deposited onto the precursor fibre which is drawn through a vertical glass tube with mercury seals at the ends, figure 1.7. The substrate wire is heated as it is drawn through the chamber, the temperature being kept below 1350°C in order to minimize the crystallite size of the deposit and achieve optimum strength. Such a high temperature requires the use of a refractory substrate, usually a tungsten wire of diameter 12μm which has the advantage of being electrically conductive. Other core materials investigated include molybdenum, tantalum and carbon. The first two are very brittle, producing residual stresses in the fibre and

poor mechanical performance, whilst the third carbon, may fracture and lead to catastrophic degradation of fibre properties. The carbon does not, however, react with the boron deposit whereas the tungsten does, producing a series of tungsten borides which provide a strong bond with the boron deposit.

Typically the boron fibre has a nodular or "corn-on-the-cob" microstructure which is attributed to enhanced growth of boron at scratches and asperities on the drawn tungsten wire. Use of boron fibres in metal matrix composites is, however, limited because of the reactivity of the surface when in contact with metals at elevated temperatures[3,37,66]. This also limits the temperature at which the composite may be used.

Protective coatings may be applied to boron fibres, such as silicon carbide, to give the product which is known by the trade name Borsic. The silicon carbide coating is applied by CVD and is approximately 2.5μm thick. It allows retention of fibre properties at elevated temperatures but any break up of the coating results in the possibility of reactions occurring.

The CVD process is also used to fabricate silicon carbide fibres[12], a carbon substrate being usually employed.

1.4. Fabrication Techniques for Metal Matrix Composites

This section will review the major techniques used to fabricate MMCs but will concentrate on liquid metal infiltration since this technique was used to produce the composites studied in the present programme. The schematic diagram, figure 1.8, separates the fabrication of metal matrix composites into a. solid state techniques

and b. liquid state techniques.

Early attempts to use standard casting techniques for MMC production involved mixing together the alloy melt and reinforcement and then casting the mixture. However, the reinforcement had a tendency to flocculate and segregate which limited the amount of reinforcement which could be incorporated, typically as little as 10%[68]. Improvements have been made by use of stir casting[69] but this limits the fabrication method to low aspect ratio reinforcements. For discontinuous fibre and particulate reinforcements further improvements were made by using a modified rheocasting method, known as compocasting[70]. In this technique a semi-solid is vigorously agitated so that the primary phase is non-dendritic, giving a slurry with a thixotropic nature, see figure 1.9. An additional stage for densification is needed which involves pressure and this can cause further mechanical damage to the reinforcement.

Powder metallurgy techniques, figure 1.10, involve a combination of high unaxial or isostatic pressure and elevated temperatures[68,69,71] This also results in reinforcement degradation which is why this technique is limited to particulates, whiskers and low aspect ratio fibres.

Sheets of preformed composite may be joined to form the required component by diffusing bonding[62,65,69], figure 1.11, the preformed sheets being produced by techniques such as plasma spraying, chemical and physical vapour deposition (CVD and PVD) as well as casting methods. In plasma spraying the matrix metal is fed into a hot gas zone and vaporized to be deposited in a controlled manner onto the fibres. The deposit is built up at a very high freezing rate which results in pore formation and the generation of thermal stresses, which may give rise to crack

formation and/or adhesive failure. The preforms which are essentially composite plies, are laid down in the required form with metal foils, to achieve the desired volume fraction of the fibre and thickness. Bonding then takes place at a temperature below the melting point of the metal matrix in conjunction with applied pressure. With metals which form tenacious oxide films, such as aluminium, cleaning is necessary and to retain the clean surfaces diffusion bonding would have to be performed in an inert atmosphere or under vacuum. In practice there will be an oxide film on the surface which would require disrupting, usually by application of pressure, although this may cause mechanical damage to the reinforcement, especially fibres.

Other production techniques use similar processes to those mentioned above for the preform fabrication. Particulate reinforcements may be introduced into a stream of molten metal and the composite built up[73,77]; composites fabricated in this manner cut out the blending and consolidation stages that are incurred in other techniques.

Infiltration techniques utilize a reinforcement preform which is permeated by a molten metal. The simplest technique is atmospheric pressure infiltration[69] and is used most commonly when dealing with continuous fibres. Either the fibres are held stationary and the metal formed about them or the fibres are drawn through a molten metal bath. Composites formed in this way usually contain many pores and are therefore suitable only for low volume fraction composites.

By applying a vacuum to one side of the preform, fibres or whiskers which exhibit poor oxidation resistance when exposed to the molten metal in the presence of air, can be infiltrated[87]. The atmospheric pressure acts on the melt pushing it through the reinforcement.

With all the infiltration techniques the first stage is the formation of the desired fibre preform[15]. This may be achieved by using a binder or binding or both to hold the reinforcement in place prior to infiltration. A binder is usually either polymeric or silica based; prior to infiltration the binder will be removed by thermal or chemical means. Bindings are used for continuous fibres and are in the form of wefts of fibres or metal strips. The quantity and mode of stacking of reinforcement within the preform can be controlled as required. Continuous fibre preforms can be made by filament winding. This positions the fibres from a bobbin onto a mandrel where they are then sprayed with a binder and cut to required dimensions for the component. Short fibre preforms are made in a similar way to the manufacture of paper, in that they are first suspended in a solvent with the binder. The mass is then placed on a porous material and a low pressure and/or temperature applied to remove the solvent. The retained fibre mat has a random in the plane orientation distribution of fibres.

Squeeze casting[69,74,75,78-85] uses applied pressure to force the molten metal into a preform whilst it is held at elevated temperature. Figure 1.12 summarizes the squeeze casting process. The preform is placed within a mould and molten metal is poured in. Pressure is applied mechanically via a piston. After cooling, the solidified composite is extracted from the mould and excess metal removed by machining, the piston usually being shaped to aid extraction of the component[74].

Increased pressure elevates the freezing temperature of the metal, 100-200MPa resulting in about 10-25K[74]. Pressure also helps the melt to expel air gaps at the mould wall and so increases the cooling rate. The two factors result in a fine-grained microstructure, thereby enhancing mechanical properties when compared with gravity die-cast products. Excess alloy is used to prevent any squashing of the preform, and this necessitates subsequent machining to provide the finished component.

Liquid metal infiltration (LMI)[86] combines the use of pressure and evacuation of the preform and is the fabrication method used for the MMC studied in this investigation. The steps in LMI are shown in figure 1.13. The reinforcement preform is placed within the cavity of the split metal die. The shape of the die and placement and choice of reinforcement will be dependent on the desired finished product. The die is preheated to the processing temperature and connected to the melt reservoir by means of a transfer tube. Both the die cavity and the melt chamber are evacuated in order to degas the metal melt and remove air from the die cavity, both of which will reduce the likelihood of porosity in the final component. In addition there is less back pressure on the melt and more intimate contact with the die walls. Lower back pressure means that the applied pressure for infiltration will be lower and more intimate contact of melt and die wall will result in more rapid solidification and a finer grain structure. Inert gas pressure is applied to the melt chamber and the melt passes through the transfer tube into the die cavity. The melt is kept under pressure until full infiltration has occurred. Die design may require selective heating or cooling to produce an even solidification rate. This is mainly to reduce or eliminate local shrinkage problems.

Once solidification has taken place and the applied pressure is removed, the die is

opened and the melt in the transfer tube falls back into the reservoir. The component is then ejected from the die and little or no further processing is required apart from removal of any runners and gates of unreinforced metal.

Particular combinations of reinforcement, matrix and component specification require differing processing variables. The operating temperature of the die may be too low and premature solidification may occur prior to full infiltration. This would result in a highly porous composite. If the die temperature is excessive the cooling time is too long with the metal being in its most reactive state, molten. Normally the die temperature would be kept well below the solidus.

The need for intimate contact between fibre and matrix in order to promote load transfer is fundamental to the principle of a composite material. The ability of the melt to wet and therefore spread over the reinforcement surface is thus important when considering both infiltration and adhesion in composites. Pressure requirements depend on the viscosity of the melt and the packing density of the fibres, i.e. the smaller the size of the space to be infiltrated or the higher the viscosity, then the higher the required pressure. For most aluminium alloys the melt temperature is approximately 100°C above the liquidus. Increasing the melt temperature decreases the viscosity but not appreciably and has the disadvantage of increasing the solidification time. The pressures adopted, typically less than 10MPa, are generally lower than those used in other pressure-assisted techniques.

1.5. Mechanical Properties of Composite Materials.

This section provides a very brief view of the basic concepts of composite materials and for a more in depth study the reader should refer to publications such as those by Harris[88], Hull[89], Agarwal and Broutman[90].

For a unidirectional composite with good bonding between fibre and matrix, the load in the longitudinal orientation is shared between the fibres and the matrix in the proportions given by the equation:

$\sigma_c = \sigma_f.V_f + \sigma_m.(1-V_f)$ ..... *equation 1.1.*

where σ_c is the stress on the composite, σ_f the stress on the fibres and σ_m that on the matrix and V_f the volume fraction of fibres. Equation 1.1 is known as the rule of mixtures (ROM) and this is the bases for the Voigt estimate for the modulus of the composite:

$E_c = E_m.V_m + E_f.V_f$ ..... *equation 1.2.*

this can be represented by the straight line in figure 1.14.

The stresses are considered to be $E_f.\varepsilon$ and $E_m.\varepsilon$ where ε is the strain on the composite.

The equation 1.1 is valid if the longitudinal failure strains of the matrix and the fibre is the same. This is an unlikely situation and the actual case is normally that the fibre strain is less than the matrix failure strain. The matrix stress at the fibre

failure strain is given as σ_m' to give:

$\sigma_c^* = \sigma_f^*.V_f + \sigma_m'.(1-V_f)$ ..... *equation 1.3.*

These terms are defined in figure 1.15.

For discontinuous fibres the length and orientation of the fibres must be considered. Since the stress is transferred by shear forces at the fibre/matrix interface, the load carried by the fibre builds up from each end, the way in which this build-up occurs depending on the interfacial bond. The mean load on each fibre will be lower than the comparable continuous fibre composite strained to the same level and there is an ineffective length, δ, at each end of the fibre as shown in figure 1.16, The critical length for reinforcement (l_c) is thus twice the ineffective length.

Any variations in the length of the fibres can be accounted for by applying correction factors to the rule of mixtures but when the fibre length is ~$100.l_c$ it is approximately the same as the equations above.

The fibre being a brittle material is known to have a strength which varies with the population of flaws and is characterised by a Wiebull probability distribution. The probability of failure of a sample in any batch of fibres is given by:

$P_f = 1-exp[-V.\sigma^m/\sigma_o^m]$ ..... *equation 1.4.*

where m is Weibull modulus or Weibull shape factor (a measure of the scatter in the population) and σ_0 is a normalizing factor. The mean strength of the fibre, at constant volume, is therefore given when $P_f = 0.5$ and by the following relationship:

$\bar{\sigma}_f = [\sigma_0^m . ln(2)/V]^{1/m}$ ..... *equation 1.6.*

The composite strength will be affected by the variability of the fibres which means that predicting composite strength is complicated, depending not only on the constituents but also on their interaction with each other. Upon the first fibre failure the composite may behave in a number of ways. Ideally the matrix will redistribute the load to the broken fibre segments and the failed fibre is thus able to retain some load bearing ability. The larger the scatter in the population of flaws in the fibre the less likely the fibres are to fail in the same area, so the composite should sustain a load after a number of fibre failures. If the scatter in the fibre strengths is small it is more likely that the failure of the first fibre will cause a stress overload in a close neighbour. The minimum strength of the composite would be equivalent to that of the failure of the first fibre which implies that the strength of the composite would depended upon the bundle strength of dry fibres.

Much research is being undertaken to produce a data base for the MMC materials. This includes measurement of the static, fatigue, creep and impact strengths, and of the stiffness for particulate and discontinuous and continuous fibre reinforcements[12,13,39,53,54,73,78,91-118]. For continuous fibre composites the transverse properties are rarely reported, however, the majority of the studies concentrating on the longitudinal behaviour.

Whilst the stiffness of fibre reinforced materials is typically close to the rule of mixtures value, the strength (or fracture stress) varies considerably depending on the system in question. Reported strengths[12,87] for CVD monofilament silicon carbide reinforced aluminium-silicon alloy are typically ~1.7GPa with a stiffness of ~210GPa, approximately 75% of that predicted by the rule of mixtures. Lee and Kim[39] investigated Nicalon-based aluminium composites and reported a tensile strength of ~440MPa for a pure aluminium/Nicalon produced by squeeze casting; no volume fraction of fibres was quoted but the micrographs would suggest 40-50%. They have also reported that a Nicalon/aluminium-silicon alloy had a much lower strength, although they do not produce the evidence for this. Skinner[113] has studied Nicalon/aluminium and Nicalon/aluminium-silicon alloy composites fabricated by LMI and found the flexural strength to be much higher in the former, 916MPa compared with 302MPa and close to the rule of mixtures value of 1100MPa.

1.6. Structure of Fibre Composites Based on Aluminium Alloys

Most published data on aluminium alloy composites fabricated by pressure assisted techniques report that the fibre array was well infiltrated with little or no porosity[74-85,117-120]. The structure in fibre-free regions of the composite was similar to that expected in the parent alloy, with slight modifications; such as a reduction in dendrite arm spacing when fibres are present[119]. In the case of aluminium-silicon and other eutectic matrix alloys, the reinforcements, whether fibres or particulates, tend to occur within the eutectic regions.

Thus the incorporation of the fibres into the metal may induce a change in the matrix structure and properties. Although these structural modifications are often noted very little work is published concerning the repercussion on the mechanical properties.

As mentioned above the mechanical behaviour of the composite material is dependent on the transfer of applied loads to the reinforcement and hence the bond and the interface zone between fibre and matrix is of paramount importance. The bond depends upon the microstructure of the interfacial region between fibre and matrix and can be considered as being a, entirely mechanical, b, the result of chemical interaction or, c, a combination of the two. In general, a composite which has only mechanical bonding will show a very poor transverse strength, whereas at the other extreme excessive chemical interaction may result in the formation of phases with poor properties and loss in the effectiveness of the reinforcement. Most of the published reports, which are concerned with the consequence of modification of microstructure on mechanical properties, have considered the interfacial reactions and particularly the reaction product formed, if any.

Table 1.4 summarizes some of the relevant matrix/fibre interactions which have been found by different authors. Generally the exact nature of the interface depends not only on the constituents but also on the fabrication technique, especially the amount of time spent at elevated temperature. Research on silicon carbide-aluminium systems reports no reaction in some cases but in others aluminium carbide may form at the interface. The presence, however, of a small amount (~4-7%) silicon to the aluminium inhibits the reaction. Aluminium carbide is always found in carbon fibre reinforced aluminium alloys. In some SiC-Al

investigations based on casting fabrication, no conspicuous reaction product was observed on the fibre surface, but the presence of aluminium and/or magnesium within the outer layer of the reinforcement was noted. Tafto, Kristiansen, Westengan, Nygard, Borradaile and Karlsen[135] suggest that this was due to an exchange of cations on the surface for more electropositive cations from the matrix.

Choh and Oki[136] have studied the effect of adding carbide-forming elements to aluminium in order to enhance the reaction at the silicon carbide interface. These elements include vanadium, niobium, tantalum, titanium, zirconium and hafnium, the formation of the carbides being associated with an increase in the distance the melt travels, due to the wetting, along a capillary.

There are several reports of second phases at the fibre/matrix interface which are not considered to result from an interface reaction but to be due to deposition of contaminants during melt solidification. Particles of Mg_2Si were found by Saggese, Scott and Trumper[48] and Neite, Dudek, Kleine and Borath[130] report a variety of contaminant elements. Sometimes the deposited phase is an oxide of one or more of the matrix constituents, possibly the result of melt front oxidation, an effect which is especially noticeable in magnesium-based composites.

A thin layer of silica is often found on many short fibre reinforcement types, usually a remnant of the technique used in the manufacture of the fibre or preform, which may influence the interfacial reaction product in light alloy matrices. Hughes, Hedges and Sexton[134] have investigated the effect of a silica layer on bulk silicon carbide reactions with aluminium and found that a layer ~5nm can result in alumina formation and the suppression of aluminium carbide When no silica was present the carbide formed above 800°C and if the layer of silica was patchy a

combination of aluminium oxide and carbide was observed.

The aluminium carbide does not grow as a continuous layer; Peteves, Tambuyser, Helbach, Audier, Laurent and Chatain[126], working with bulk silicon carbide and aluminium, have shown that nucleation of the carbide is non-specific although they report a SiC-Al_4C_3 orientation relationship of the form:

$[0001]SiC \parallel [0001]Al_4C_3$

$[210]SiC \parallel [210]Al_4C_3$

Yang and Scott[53] have shown that aluminium carbide forms as needles in a carbon fibre-Al-Si system. The needles are aligned with the basal planes of Al_4C_3 along their length. Peteves et al[136] report a hexagonal morphology for the aluminium carbides in the presence of silicon carbide particulates.

In alumina reinforcement systems an interphase is less commonly observed, especially in aluminium based composites. Some reduction of the alumina is reported when magnesium is present in the matrix. The reaction product formed is often a spinel of the type $MgAl_2O_4$ and is present as fine crystals on the fibre surface. MgO is also reported, either in the form of discrete crystals or within the fibre surface as microcrystals. Normally the alumina did not react with aluminium and its alloys, Yang and Scott[54] and Fox, Flower and West[129] have shown the segregation of magnesium to alumina fibres, the latter authors finding a depth of penetration 100-500nm depending on the melt temperature. For the more porous low density fibre the penetration of the magnesium was greater than the high density form.

1.7. Aims of the Present Investigation.

The alloy system investigated is based upon an aluminium-7% silicon alloy with a small percentage of magnesium added. This is selected as it has a good casting fluidity and reasonable mechanical properties whilst the magnesium addition is known to produce a precipitation reaction in the unreinforced alloy which may be beneficial to the transverse strength of the MMC. An additional benefit of this alloy composition is that the melting temperature is reasonably low which should minimize any chemical reaction between fibre and matrix. The composites are made by liquid metal infiltration of a fibre preform. Most of the composite material used incorporates Nicalon fibres, although some work is reported on an alumina-Borsic hybrid composite. Parallel studies are performed on Nicalon-reinforced commercially pure aluminium.

The matrix microstructure and interactions between fibre and matrix in these composites are characterized using a variety of ultrastructural techniques, including analytical scanning and transmission electron microscopy. Wavelength-dispersive electron-probe microanalysis is applied to studies of the composition of the Nicalon fibre, utilizing detailed analysis of the shape of the soft x-ray emission spectra from the relevant elements. The microstructural information is related to the parameters of the fabrication process, in particular the temperature and cooling time.

Complementary studies are conducted on the mechanical properties of the different composites, although tests are limited to tensile and flexural measurements because of lack of material. The fibre/matrix bond strength is studied utilizing a fibre indentation test and the strength of single fibres measured from fibres extracted from the composite. Correlations are then sought between microstructure and the

fabrication route, and also between microstructure and mechanical properties of these systems.

CHAPTER 2. EXPERIMENTAL

2.1. Materials Used.

The MMC used in this study was based on aluminium alloy matrix systems reinforced with continuous fibres; with nominally 40% by volume fibres. They were produced by liquid metal infiltration (LMI) and supplied as flat sheets by Advanced Materials Systems, formerly Cray Advanced Materials, Yeovil. The applied pressure used was below 7MPa with a melt temperature of ~750°C. The as-received sheets were assigned a number, and this together with the dimensions and a description of each sheet are given in table 2.1.

2.1.1. Fibre

The major part of the investigation involved composites incorporating Nicalon fibres, a commercial product supplied by Nippon Carbon, Japan, as tows of approximately 500 fibres; the grade of fibre used was NLM 202. In the as-received state they have a covering of polymeric "size". The tows were woven into plies with a weft of glass or as a plain weave with other Nicalon fibre tows. The plies were stacked into the desired configuration to make the preform. A third type of preform was used which consisted of a filament-wound fibres about a square section mandrel with a single woven layer used as a restraint. Each type of preform is shown schematically in figure 2.1. An alumina/Borsic hybrid was used in one composite which consisted of three plies of FP-alumina fibre and a monolayer of Borsic fibre held together by a weft strip of titanium, figure 2.1.. Prior to infiltration the preforms, while in the die cavity, were desized by a thermal

treatment in air.

2.1.2. Matrix Alloys

Two matrix metals were studied, commercially pure aluminium and an aluminium-7%silicon-0.4%magnesium casting alloy; these were designated 1000 and 357 respectively and their nominal compositions are given in table 2.2. The corresponding Nicalon-reinforced composite materials are referred to by the acronyms N100 and N357. The N357 composite incorporated the preform with the glass weft, whereas the N100 utilized the woven and filament wound fibre and these were designated N100w and N100f respectively. The FP alumina/Borsic hybrid was provided as a single sheet and was used to reinforce the alloy matrix; this is referred to as F357. Table 2.1. summarizes the composites used in this study.

2.2. Heat treatment.

To investigate the precipitation reaction in the unreinforced 357 alloy and in the N357 and F357 composites, the following thermal treatment[62], referred to as T6, was applied:

1. The specimen was solution treated at 540°C for 16 hours in air.
2. It was then removed from the furnace and quenched into boiling water (100°C).
3. This was followed by artificial ageing at 160°C for ten hours.

Ageing curves were produced by carrying out experiments for times ranging from 1 to 180 hours at 160°C.

2.3. MECHANICAL TESTS.

The choice of test configuration and specimen size was determined by the limited dimensions and availability of the composite plates. Both tensile and four-point bend geometries were utilized, the majority of the work on the Nicalon composites being concerned with the tensile configuration. Only a small number of alumina-Borsic composites were tested and then only in flexure.

2.3.1. Tensile Tests

The tensile test technique ASTM D3552[142] sets out several different specimen geometries which may be considered for the testing of MMCs and particularly FRMs. A parallel-sided test sample was chosen based on the test geometry designated F in ASTM 3552. This is similar to that used in the investigation by Roebuck, Gorley and McCartney[143]. Although the standard suggests this geometry should be used primarily for transverse property measurement, it was shown that the strength was no different when a tapered section test bar was utilized. A set of three specimens was tested with a tapered section machined in the gauge length.

Figure 2.2 shows where longitudinal and transverse orientation specimens were cut from as-received sheets. Cutting was performed using a diamond impregnated wheel on a Acutom machine. The cut faces were ground parallel on a diamond wheel, an operation which also produced an uniform surface finish. These grinding stages utilized slurries containing , in turn, abrasives of particle size 45μm, 15μm and 9μm. Early experiments used silicon carbide papers to grind the faces of the test bars, but this was changed to diamond slurries when they became

available since they produced less damage to fibre and composite.

A pair of shot-peened aluminium end tabs were affixed using an epoxy adhesive. The use of end tabs allowed stress transfer to the composite to occur while minimizing any grip damage incurred during testing. In addition to information on the failure stress, data concerning failure strain and the elastic modulus were required. Strain gauges were employed since the use of extensometers was impractical due to the very small strains involved. The strain gauge was a FLA-2AS-23 type with a 6mm gauge length, which was bonded to the central portion of the specimen with cyanoacrylate adhesive. A length of wire was soldered to each terminal of the gauge via a terminal pad which was also bonded to the specimen. Figure 2.3 shows the position of the strain gauges and also the acoustic emission transducer. Acoustic emission is a non-destructive testing technique which monitors the response of a material or structure to applied stress. The transducer detects the stress wave generated by some event in the material under investigation. The transducer uses the piezoelectric effect to detect the stress wave pulse from an event. The a.e. transducer was attached to the test bar surface after a coupling agent had been applied to the face of the disc, to link accoustically the two components. The voltage output of the transducer was amplified and the signal fed to a Marandy unit via a preamplifier and the data recorded on a dedicated microprocessor.

Preliminary experiments were carried out using a pair of strain gauges, one on either side of the test specimen in order to take account of any misalignment and bending during testing. Very little difference was found in their output so in subsequent strength tests a single strain gauge was used. For the measurement of strain and calculation of modulus, however, a pair of strain gauges were still required. Testing was carried out on an Instron 1195 machine at a cross-head

displacement rate of 0.05mm min^{-1}, the strain gauge output being recorded using the data storage system. The Marandy MR10004 system was used primarily for recording acoustic emission data but it also had a facility for measuring voltages such as the outputs from the Instron and the strain gauges. The sampling time interval was set at 500 or 1000 mS and the raw data converted into stress and strain values by use of dedicated microprocessor facilities. After failure the specimen halves were set aside for fractographic studies.

2.3.2. Flexural Tests.

Test bars were cut using a diamond wheel, the exact dimensions of the bars depending upon the size of the available sheet. Each cut face was polished using a selection of diamond slurries as above.

The test geometry for use in four-point-bend flexural tests required[144] that the inner to outer span ratio of the loading rig was set at 1:3, the span-to-depth ratio 16:1 and the depth-to-width ratio 1:4. Unfortunately, with the bars available it was not possible to produce these dimensions and still be able to produce tensile specimens from the same sheet. Therefore, non-standard dimension bars were tested with the geometries shown in figure 2.4 and designated A, B or C, in each case the inner to outer span ratio was as above. The main errors would be expected to occur in geometry A. as the shear forces would be expected to contribute to the final failure.

Strain gauges, when used, were affixed to the tensile surface, midway between the inner load points. Acoustic emission recordings were not made with this test geometry due to the limited dimensions of the specimen. Testing to failure was

carried out on an Instron 1195 machine at a cross-head displacement rate of 0.05mm min^{-1}.

2.3.3. Shear Tests

The specimen geometry used is shown in figure 2.5. It is a block of material with a notch cut using a diamond impregnated wheel to a depth which passed through the central plane of the composite test specimen. Test specimens were cut from the 4mm N357 sheet (800) and the 6mm N100 filament wound sheet (1100). The end faces were then polished parallel on silicon carbide or diamond grinding wheel and the specimen loaded in compression. Testing to failure was carried out on an Instron 1195 machine at a cross head rate of 1mm min^{-1}. The technique was based on the tests used to measure the shear properties of MMC by Diwanji and Hall[85]. The technique was based on ASTM D3846-79[145] as used for the shear testing of polymeric matrix composites. Testing the composite revealed that the failure did not usually occur in the plane of the fibres but by bending at the notch position. Diwanji and Hall did not mention using a constraining jig in their tests but the original standard does. A jig was constructed that would enable the reduction of the bending load; this is also shown in figure 2.5.

2.3.4. Single Fibre Tests.

The testing technique was based on ASTM D3379-75[146] and used the arrangement shown schematically in figure 2.6. Single filaments of Nicalon were randomly selected and affixed to a card former with a hard wax adhesive, sufficient wax being applied to minimize any pull out of the fibre.

The fibre, mounted on the card former, was clamped in the jaws of an Instron 1122 testing machine, . The card former was cut so that the filament was unsupported and the force applied until failure occurred. Cross-head displacement was set at 1 mm min^{-1}

To examine the effect on the mechanical properties of the fibres at the different stages in the production of the final composite plate, single fibres were tested in the following conditions:

1. Fibres as-received from the manufacturer on a bobbin.
2. Fibre tows woven with a glass weft in the form of a preform.
3. Extracted from (see below) the composite (N357), the preform infiltrated with 357 alloy.
4. Extracted from the composite (N357), the preform infiltrated with 357 and heat treated (T6).
5. Extracted from the composite (N100), a preform infiltrated with commercially pure aluminium.
6. Fibres as-received on the bobbin exposed to a heat treatment of 540°C for 16 hours.

However, this is only applicable where the fibres have been extracted from their surrounding environment. Removal from the bobbin or preform was relatively easy requiring only manipulation with tweezers. In the case of fibre extraction from the composite a selective etch was employed as follows. Firstly the composite was immersed in an acid bath containing hydrochloric, hydrofluoric and nitric acids to remove all matrix constituents. The Nicalon fibres were then washed in water and air dried. To create a valid comparison between fibres from different environments

each set of fibres was given the same acid bath immersion prior to mechanical testing. Additional fibres were tested from the bobbin in the non acid immersed state.

To investigate the fracture surface of the fibres and attempt to find the flaws responsible for the failure, the following procedure was performed. The fibres were mounted on the card formers as described above and then coated in a silicone material. After loading to failure the silicone was removed using a solvent to allow the fracture surface to be examined in a scanning electron microscope. Only a small number of these tests were performed and most of the failures could not be found.

2.3.5. Microhardness Measurements

The microhardness was measured using a Leco M400 microhardness testing machine.

Most of the microhardness measurement was performed within the α-aluminium dendrites in order to follow the effect of heat treatment. This was carried out on both the unreinforced 357 and on the N357 and F357 composites. An indenter force of 50 g was found to be necessary with a dwell time of 20 seconds. The sample was in the polished condition and a transverse section chosen so that sub-surface features, such as silicon particles or fibres, did not influence the indent size.

2.3.6. Fibre/Matrix Interfacial Shear Tests.

This technique was developed by Marshal[147-149] to establish the fibre/matrix interfacial shear strength (τ) in brittle matrix composite materials. It measures the movement of the fibre under an applied force and applies a simple geometrical relationship, such as that illustrated in figure 2.7. This gives the fibre displacement in terms of the indent size in the matrix and fibre. These dimensions are then used to calculate the interfacial shear strength (τ), by applying the relationship:

$$\tau = \frac{F^2}{4\pi^2.u.R^3.E_f}$$

where F is the force in Newtons exerted on the fibre, u is the fibres downward movement, R the fibre's radius and E_f the fibre's stiffness (for Nicalon, values of 200 GPa are quoted for the fibre stiffness).

The force on the fibre, F, is related to the hardness of the fibre, H, and the half length of the indent in the fibre, a, by the equation:

$$F = 2.a^2.H$$

By simple geometry, see figure 2.7, the downward displacement may be calculated and shown to be:

$$u=(b-a).cot\ \omega$$

For a Vickers indenter of the type used ω is 37°; b is the half length of the indent in the matrix.

Using a transverse polished section a circular fibre was chosen as this is the most likely to lie parallel to the loading direction. The pyramidal diamond of the microhardness machine (Leco M400) was positioned using the eyepiece cross wires. The choice of load was made by observing the result of differing loads on the indent size. If the load was excessive there would be only a single indent produced. This usually resulting in fragmentation of the fibre. Insufficient load resulted in no movement of the fibre. The fibre diameter also had an effect on the indent sizes. If the load preferred for a fibre of diameter 12μm was applied to a fibre of diameter less than ~8μm the fibre would often fail. Conversely if the chosen load was applied to a fibre of approximately 18μm there was no discernible fibre movement.

A number of indents were produced in fibres, generally selected from areas where the fibres were surrounded by aluminium matrix as opposed to silicon or other fibres. Some fibres within tows were also tested, but these required careful selection in order that a suitable matrix indent could be produced (see figure 2.8).

Once the pair of indents had been produced in fibre and in the matrix, see figure 2.7, calculation of the hardness of the Nicalon fibre was necessary. To provide this value the load was reduced to a level which allowed indentation of the fibre without any resulting movement of the fibre relative to the matrix. A large diameter fibre was chosen as its larger bond area would require a higher force to cause relative displacement. The fibre hardness found was 17GPa.

It was necessary to undertake a large number of indents because it was difficult to position the diamond indenter accurately on the fibre; the bond strength was variable, a large amount of experimental scatter occurred, and the quality of the

indent produced was often poor with matrix yielding or fibre splitting.

This technique was utilized for N357 and N100 composites in the as-received condition and the N357 composite in heat-treated condition.

2.4. Optical microscopy

The standard method of preparing specimens for optical microscopy is by "polishing" sections, i.e. mechanically removing material with a hard abrasive material. In a composite the various phases present complicate the process, since the different constituents usually have a different hardness and respond differently to the polishing process. Furthermore, it was important to have a process which did not damage the fibres and the matrix phases. Early experiments carried out using standard silicon carbide or alumina abrasives gave unsatisfactory results and when a choice of diamond slurries became available this was the technique selected. It required less preparation time with fewer stages, generally produced an improved finish and is described below.

From the bulk composite a section was cut; either to provide a transverse or a longitudinal fibre section. Figure 2.8 shows the two sections diagrammatically. The cutting was performed using a Accutom diamond wheel consisting of diamond impregnated in an ablative epoxy resin. This was preferred to diamond bonded to a metal since the latter became clogged with the soft aluminium phase during use whereas the ablative epoxy exposed clean diamond during cutting. The result was less surface damage and a reduction in preparation time. The speed with which the composite was fed to the wheel also affected the quality of the cut, the faster the feed rate the more extensive the damage, which was seen to extend up to ~300μm

from the cut surface.

After sectioning, the specimen was mounted in resin which contained a filler to confer some wear resistance and minimize the development of surface relief. The filler was either a short fibre glass or carbon powder, the latter being preferred when an electrically conductive mount was required, as for subsequent examination of the specimen in the scanning electron microscope (see section 2.5).

To produce a planar surface the mounted specimen was ground on a fixed diamond wheel with water lubrication. The diamond size at this stage was 50μm (alternatively the use of a 45μm slurry on a #10 Beuler wheel could be selected). Subsequent grinding and polishing stages are detailed in the plan set out in figure 2.10.

For microscopy it was desirable that the specimen was dry and free from deposits from the preparation technique. The use of detergent followed by solvent wash often left a deposit on the surface and so flushing with distilled water followed by drying on a clean Metlap wheel was preferred . This was critical when analysis in the scanning electron microscope was subsequently required.

The prepared sections were studied in a Zeiss ICM 405 reflection microscope fitted with a 35mm roll film camera.

2.5. Scanning Electron Microscopy.

The scanning electron microscope (SEM) gives a resolution which is dependent on the size of the focused beam, approximately 5nm. Compared with the optical microscope it has a larger depth of field and, when fitted with an x-ray analyzer (see section 2.6) compositional information may be provided. The principle of the SEM technique may be described briefly as follows. An electron beam incident on a surface undergoes certain interactions as summarized in figure 2.10, and which yield information about the structure of the specimen. In the SEM a beam of focused electrons is produced and scanned across an area of the specimen. By detection of either secondary or backscattered electrons emitted from the specimen, an image may be built up. These pass to a scintillator producing light photons which in turn pass to a photomultiplier. This signal is used to control the brightness of the electron beam in a cathode ray tube (CRT) which scans in synchronism with the electron beam incident on the specimen. Thus the brightness of the CRT image corresponds to the variation in the density of electrons emitted over the scanned area of the specimen.

The mount material should be electrically conductive in order to reduce the specimen charging problem when irradiated by the electron beam. The mount materials available were either a copper-filled or carbon-filled thermo-setting resin. Both provided adequate conductivity but the copper filled mount showed preferential material removal such that the specimen became bevelled at the edges. Carbon-filled mount material provided adequate edge coupled retention with the desired conductivity and was therefore preferred. An alternative was to use a hard filled facing material with a backing of a conductive mount material.

Cleaning of the polished surface was especially important when any analysis was to be undertaken. For example, it was found that the use of organic solvents results in the deposition of carbon on the specimens surface, which introduced false results when carbon was being analysed. For phases which were non-conductive, the use of a sputtered coating of gold was applied and in some cases copper was evaporated on to the specimen.

Examination of the prepared specimens was carried out in either a JEOL 35C SEM or a JEOL JXA 8600M electron probe microanalyser (EPMA), see section 2.7.

In addition to the examination of polished sections, the SEM was used to study fracture surfaces. This required cutting of the fractured test bar away from the fracture surface so that it could be accommodated in the SEM chamber. The fracture surface was coated with gold to reduce any charging. The chemical composition of phases could be identified in the JEOL 35C using the EDS (energy dispersive spectrometer; see section 2.7). Analysis could be made from a selected area or from a "spot". Spot analysis was generally used as this minimized the zone of x-ray generation and excitation from material surrounding the phase in question.

SEM was used also to investigate "deep etched" specimens where certain constituents are selectively removed. A standard aluminium alloy etchant containing nitric hydrochloric and hydrofluoric acids was used.

The SEM can also be used to produce three-dimension images. This technique is known as stereomicroscopy; essentially this uses two different views of the same area taken under identical conditions, except for a specimen tilt angle difference of a few degrees (typically about 5°-7° tilt). Each image is set so a given feature is in

the identical position in both images. These images then represent the view that the left and right eye see. With the use of a viewing aid the pair of images can be interpreted as a single three dimensional image. This technique was used for both fracture and deep etched specimens but was not used extensively as the requirement for a special viewer made reporting the results difficult.

Using either optical or scanning electron micrographs the volume fraction of fibres was measured by either fibre counting or image analysis. This was carried out using a Magiscan 2A image analyzer and by direct measurement from fibre diameter and number distributions in a transverse section. Although each of these provides an area fraction the volume fraction is assumed to be the same as the fibres are continuous.

2.6. Transmission Electron Microscopy (TEM).

The contrast from a crystalline specimen is dependent on the intensity of the transmitted electron beam. There are three main contrast mechanisms; mass-thickness, diffraction and phase contrast. For a specimen which is sufficiently thin for useful TEM it can be assumed that all bar a few backscattered electrons pass through the foil. The energy and angular spread of these transmitted electrons will vary due to elastic and inelastic scattering within the specimen. By addition of an aperture, centred about the optical axis, electrons scattered beyond a given angle will not be observed. Regions of greater thickness or higher density scatter more and so will appear darker, less electron intensity. This is known as mass-thickness contrast. For a crystalline material an additional contrast mechanism can occur. This is diffraction contrast and principally due to the increased intensity of the scattered electron beam at certain angles. Differences in the lattice parameter,

plane orientation relative to the incident beam and thickness can cause interference to produce regions of increased or diminished transmitted intensity, which form the contrast. The final contrast mechanism utilizes interference of electron beams which are out of phase. Since it is usual for a phase change to occur when scattering takes place, this type of contrast mechanism is usually present but not always noticeable at lower magnifications. The contrast, being due to interference is thus in the form of a series of fringes of light and dark.

The resolving power of the TEM is a function of the electron wavelength (λ) according to:

$$\delta = 0.61.\lambda/N.A.$$

where *N.A.* is the numerical aperture and is ~0.01 radians and the wavelength is ~0.003nm. This gives the separation of closest resolved points, δ, as approximately 0.2 nm.

For examination in the TEM the specimen must be prepared in the form of a thin section. This requirement is a result of the image forming mechanisms. Additionally the specimen will, ideally, have parallel faces, to reduce thickness contrast, be stable in the microscope and during handling, be representative of the bulk specimen and not be changed by the preparation technique.

The preparation technique used is outlined in the following paragraphs. First a disc of diameter 3mm, with a thickness of 300-500μm was cut from the bulk material. This required the use of a diamond wheel, an Accutom machine fitted with an automatic sample feed was applied. The bulk specimen was clamped in the feeder

and initial squaring or roughing cut made. This provides a surface from which a parallel sided slice was cut. Subsequent cuts were made by setting the built-in micrometer to the required thickness, 200-500 μm. Consideration was made of the width of the cut; to a first approximation this was the thickness of the diamond wheel.

A number of 3mm discs of material were punched out of each slice; this however was found to be too aggressive for some of the thinner slices. Hence either thicker slices were used or the alternative of using a hollow drill was applied. The hollow drill technique followed the slice production as above; the slice would be mounted on a glass slide with either a wax or double sided tape and the disc drilled out. There were two types of drill bit available; these were either a steel bit used with a diamond containing gel or a diamond impregnated bit. The former tended to wear preferentially when used with the composite materials, and both types of bit were found to melt the wax if excessive load or speed were applied.

The thinning stage was important; the use of electrochemical thinning was considered inappropriate as it results in differential thinned regions. The preparation route used was thus as follows: further mechanical thinning was undertaken to reduce the thickness of the disc to approximately 200μm. The abrasive medium used was silicon carbide; although this was shown to produce damage to fibres when used for metallographic preparation this was not generally the case here. This was thought to be due to reduced area and pressure factors. Once the disc thickness was reduced to ~200μm a "dimple" was machined into both faces, figure 2.12. A VCR group dimpler was used, this technique utilizes a diamond slurry, either 3μm or 1μm, with a hardened steel grinding wheel to abrade a dimple in the centre of the two opposing faces of the disc. The dimensions

of the steel wheel used allowed an approximation of the depth of the dimple to be made. Dimples of approximately equal depth were put in each face so the retained thickness in the centre of the disc was ~30-40μm. A final polish of the dimpled surface provides an improved surface finish; this was performed using a colloidal silica suspension on a soft polishing wheel.

Once the desired central thickness was achieved the dimpled disc was transferred to an ion-mill for final thinning. Ion beam thinning (milling) uses energetic ions to thin specimens. The specimen was rotated and thinned from both sides by application of two guns simultaneously, figure 2.12. Argon gas was used with an accelerating potential of a few keV (typically below 5keV).

The ion beam thinning was carried out on a Gatan Dual Ion Mill, although some thinning was performed on a Ion Tech machine. The thinning angle was kept at 12° until perforation and then reduced to 8° to provide an extended thinned area. The point of initial perforation was measured using a "terminator"; in the Gatan mill this was a laser beam orientated perpendicular to the disc being thinned. The amount of thinning at the lower angle was set initially for ~3 hours; further thinning could be performed if necessary after initial inspection in the TEM.

It was found that some of the more frail specimens, such as those from the heat treated N357, fractured during an early stage of handling and were thus rendered useless for TEM examination. To provide an adequate thinned section the disc was ground to approximately 60 μm and then transferred to the ion-mill until perforation. The final foil often required placing on a fine grid of copper for examination in the TEM as although thinned sufficiently it would normally fail during mounting in the microscope. The main problem with this approach of

thinning, was the prolonged time exposed to the elevated temperatures within the ion-mill. A cold stage has now been fitted to the Gatan machine and may show if the results are an artifact of the production or not.

Inspection of the thinned specimen was carried out in a JEOL 2000FX microscope at an accelerating voltage of 200kV. This TEM was also fitted with a high angle EDS detector. Using the EDS in the TEM has an improved spatial resolution compared with that in the SEM. The volume of material from which the elemental information emanates is much reduced due to the sample being thin. Also the beam may be focused down to a very small area in which to concentrate the elemental analysis.

Insertion of a small aperture allowed the production of diffraction patterns, these are known as selected area diffraction patterns (SADP). These are formed from the interference of the diffracted electron beam, constructive interference resulting in bright spots, the spatial and angular distribution of which relate to the crystallography of the examined crystal. The diffracted beams are reinforced when the Bragg's Law is met, i.e:

$$2d.sin\,\theta = n.\lambda$$

where d is the lattice plane spacing, θ the diffraction angle and λ. In the TEM some of the electrons pass through the specimen unaffected; the diffracted electrons hit the screen at a distance r from this non-deviated position. The screen

is a distance, the camera length, L away from the specimen and so the image on the screen can be related to the crystal structure by:

$$r.d = L.\lambda$$

SADP may be analysed to provide detail of the crystal structure of the phase under investigation.

The type of holder used depended on the facility required; for general observation a simple single tilt stage was applied. However, when EDS was carried out the elements from the holder itself could cause confusing results, so a beryllium holder was used. Beryllium is too low in the x-ray energy scale to be measured by EDS. For diffraction it is not usually the case to have the planes aligned such that they can produce a regular diffraction pattern, it was therefore necessary to utilize a double tilt holder so the specimen could be positioned with the different tilt angles.

2.7. Electron Probe Microanalysis (EPMA).

As shown in figure 2.11 when an electron beam strikes a sample various electron-electron interactions result. Of particular interest for the identification of elements is the emission of X-rays. The energy and wavelength of the x-rays emitted are characteristic of given electron transitions within the element(s) present and the intensity of the "characteristic" x-rays is a measure of the quantity of that element present. Thus we have a means of providing data on both elements present within a specimen and on their concentration.

The detection systems used in EPMA may either measure the energy or the

wavelength of the x-rays emitted. They are referred to as energy dispersive spectrometry (EDS) or wavelength dispersive spectrometry (WDS). The first type of detection system (EDS) uses a silicon semiconductor; the incoming x-rays which fall upon the detector excite a number of electrons into the conduction band of the silicon thus creating an equivalent number of positively charged holes in the outer electron shells. The individual energy of each excitation is very small and therefore the number of electron-hole pairs is proportional to the energy of the incident x-ray photon. With a voltage applied across the silicon a current can flow as each x-ray is absorbed and the magnitude of the current is proportional to the x-ray energy. The signal is normally enhanced by reducing the conductivity of the silicon by doping with lithium and cooling to liquid nitrogen temperature. A 'window' is utilized to stop contaminants from the specimen chamber condensing on the detector. The windows are made of beryllium and the thickness kept to a minimum to reduce the absorption of x-rays, unfortunately this means that low energy x-rays are prevented from falling on the detector and light elements, below sodium, can not be detected. With systems which can achieve a high vacuum the window can be removed and light element analysis carried out, the JEOL 35C used in the present study, has a windowless capability. The EDS fitted to the JEOL 35C and JEOL 2000FX were connected to Link AN10000 analysis systems.

WDS measures the wavelength of the x-rays. This technique uses crystals of known lattice spacing, d, to "select" the x-ray wavelength , λ, which is

characteristic for a given element. The relationship between the two quantities is given by the Bragg law:

$n\lambda = 2dsin\ \theta$

where θ is the angle between the incident x-rays and the crystal lattice planes.

The WDS detector on the JEOL JXA 8600M was fitted with four double-crystal spectrometers which could be used to analyse the x-ray spectrum from an element. The crystals used are summarized in table 2.3. The JXA 8600M could be used in the manual mode or it could be computer controlled. Several analysis options were available. These included qualitative investigation, where each crystal scans through a preset wavelength range and peaks are detected at given characteristic wavelength values, dependent on the elements present. A quantitative analysis routine was available which required the use of standard samples containing the element in question in an exactly known form (often this will be the pure element). Standards were required because the intensity of the x-ray is rarely a direct measure of the concentration. By comparing the intensity of an unknown with a standard a correction may be made. The relationship between standard concentration c_{std} and specimen concentration c_{spc}, is given by $c_{spc}=k.c_{std}$ where k, is the ratio of the intensity of x-rays from the specimen and the standard. Corrections are usually required, referred to as the ZAF method, to account for the atomic number factor (Z), the absorption of x-rays (A), and a fluorescence factor (F). Ideally the value of the ZAF correction would be 1, and the intensity would give a direct measure of the concentration. However, in reality one or more of the factors will deviate from unity.

The atomic number effect depends on the efficiency with which the electron beam generates x-rays in the element concerned. This in turn depends on (i) the electron penetration before loss of energy allows no further x-ray excitation and (ii) the number of electrons which are backscattered without x-ray generation. Generally Z>1 for analysis of a heavy element in a light element matrix and Z<1 for a light element in a heavy element matrix.

The x-ray absorption factor is dependent on the mass absorption coefficients of the combination of elements in the specimen relating to the energy of the x-ray line being measured. The fluorescence factor results from indirect x-ray production by other x-rays. However, it is a very inefficient process and is usually only a problem in compounds with similar atomic number elements causing a disproportionately high intensity of the lower atomic number element.

The JEOL JXA 8600M was fitted with a computerized package which calculated the ZAF correction and provided a concentration output. However, in the investigation of the Nicalon fibres the ZAF correction parameters of Scott and Love[150] was used since this was believed to be more accurate for the analysis of light elements such as carbon and oxygen. Specimen requirements for WDS demanded a planar surface as the measurement technique depended sensitively on the 'height' of the specimen to be set.

The EDS system fitted to the JEOL 35C was capable of detecting elements down to Z=5 (boron) in the periodic table. This instrument was used more as a general purpose SEM and had the capability for backscattered electron imaging (BSI) as well as secondary electron imaging (SEI).

2.8. Differential Scanning Calorimetry.

This technique was applied to investigate the changes in state which occur within the systems concerned. By comparison of the energy input needed to maintain the temperature or heating rate of a specimen and of a standard (usually a pure aluminium pan), chemical reactions, melting points and phase transformations may be investigated. The technique is summarized schematically in figure 2.14. The equipment used was a Du Pont system fitted with a 9900 DSC cell.

In this case the DSC was principally used to follow the precipitation reaction within the matrix alloy and observe whether this also occurred in the N357 composite. This was performed by using a series of solution treated samples and studying the DSC energy-temperature curve produced. Each series of measurements was preceded by an experiment with an indium standard in order to provides a set point from which the thermocouples output may be characterized. Once the DSC was calibrated using the standard a specimen of either 357 alloy or N357 composite was introduced. The mass of the specimen required lay in the range 4-12 mg so that reasonable energy changes can be noted while the whole of the specimen can respond to the heating rate. It was found that a typical 3mm disc as produced for TEM, prior to thinning, was of a suitable mass and easy to handle.

The specimen was weighed to within 0.001 mg and "cramped" within an aluminium pan. The specimen and reference pan were subjected to a simple ramp heating at 10°C min^{-1} from 23°C to 610°C and any heat flow required to produce physical changes was automatically recorded.

RESULTS.

3.1. Microstructure

3.1.1. Aluminium-7%Silicon-0.4%Magnesium Alloy.

Chemical analysis data are given in table 3.1.

A polished section of unreinforced as-cast alloy 357 is shown at low magnification in figure 3.1. The microstructure consists of dendrites of α-aluminium (A) surrounded by an eutectic mixture of aluminium and silicon (B). In addition to the eutectic silicon, particles of primary silicon are found (C) which have a blue grey colour in the optical microscope. The lighter grey phases (D) were found to contain aluminium, iron and silicon by use of electron probe microanalysis (EPMA), an EDS trace being shown in figure 3.2. Table 3.2 gives quantitative data for the acicular intermetallic phases corresponding to 15.0 ± 0.5 wt% silicon and 25.4 ± 0.4 wt% iron. These compositions are in accord with the phase $FeSiAl_5$[59]. Analysis of smaller particles of intermetallic gave a higher aluminium concentration. Since, however, the iron and silicon atom ratio was still 1:1 these were also believed to be $FeSiAl_5$, the extra aluminium x-ray emanating from the surrounding aluminium matrix.

A second intermetallic phase was observed which took the form of a 'script' phase marked E in figure 3.3. EDS analysis shows it to contain iron, silicon and aluminium but that the percentage of silicon was higher than in the $FeSiAl_5$, figure 3.2.b. The weight percentages are 23.6 ± 0.5 wt% silicon and 24.2 ± 0.3 wt% iron, table 3.3, from which the intermetallic phase was deduced to be $FeSi_2Al_4$.

A third phase within the aluminium dendrite arms was observed, marked F, figure 3.4.a. The EDS trace, figure 3.4.b, revealed the presence of magnesium and silicon only, with a small aluminium content coming from the matrix. These were considered to be Mg_2Si. An x-ray map of the magnesium distribution, figure 3.5.a, showed that the majority of the magnesium in the alloy was confined to these interdendritic phases, with only a small amount being present in solution in the aluminium. A second magnesium-containing phase was observed, figure 3.5.b, with iron, silicon and aluminium being present, in addition to the magnesium.

Figure 3.6. shows that the most noticeable effect of heat treatment on the microstructure was modification of the silicon morphology. The eutectic silicon, which initially was in the form of fine needles, had become spherodized after heat treatment. The iron-rich intermetallics were present in the same form as in the as-cast specimens.

No large magnesium-containing phases were detected in the heat treated alloy. EPMA analysis of the composite, such as figure 3.7, showed that the magnesium was evenly distributed throughout the aluminium dendrites.

A typical DSC thermograph for the 357 alloy is given in figure 3.8. The curve shows an endotherm at approximately 580°C which could be resolved into two peaks, at 576°C and 589°C. The first peak corresponds with the eutectic temperature and the second with the $FeSiAl_5$ phase. An exothermic peak was found at 240°C, figure 3.9, with an area of $12.3 \pm 2.7 Jg^{-1}$ and is related to the formation of magnesium silicide, Mg_2Si.

3.1.2. 1000 Series Alloy.

The microstructure of the commercially pure aluminium (1000), in the as-cast condition, Figure 3.10, consists of dendrites of aluminium. A second phase was observed, (H), which EDS, figure 3.10.b, shows contains aluminium and iron. Quantitative analysis gave 32.3 ± 0.2wt% iron and 67.5 ± 0.5wt% aluminium, confirming it to be the $FeAl_3$ intermetallic.

3.1.3. Nicalon-357 Alloy Composites, N357.

Chemical analysis data for each sheet are given in table 3.1, showed a noticeable variation in the magnesium content of the matrix, ranging from 0.03 to 0.58 weight percent. The weight percentage of iron ranged from 0.60 to 1.00%.

Figure 3.11.a and b show a transverse section of an as-received composite (N357) and figure 3.11.c and d are micrographs of a longitudinal section. In addition to the reinforcing fibres the following features were observed; weft fibres, G, porosity, P, silicon phase particles, S, various intermetallics, D, and interfaces. Each of these features are dealt with below.

The Nicalon fibres show little variation in section shape but the diameter was found to vary, figure 3.12. The mean value of ~14.8μm was determined, in good agreement with published data[14]. In these measurements care was taken to account for fibres cutting the sectioned plane at some angle deviating from 90°. The tows were closely packed, typically containing 500 fibres.

The fibre volume fraction was measured as 0.43 overall and 0.59 within a fibre tow. In many of the composite sheets the fibres had a higher proportion of large diameter fibres. Hence, in calculating the fibre volume fraction the use of the mean diameter over-estimates the value. A more accurate technique accounts for the actual fibre diameter and this was used to calculate the figure above. The same result was also found when image analysis was utilized to find the volume fraction. Also with image analysis it was easy to over-estimate the volume fraction because the equipment could consider the fibre tows as a single item. The composite manufacturer gave a volume fraction of 0.40 based on the amount of fibre placed in the die.

Qualitative data, such as the EDS trace in figure 3.13, show that there were only three elements in the Nicalon fibre, silicon, carbon and oxygen. Quantitative EPMA was carried out using the JEOL JXA 8600M instrument to establish the composition of Nicalon fibres. The fibres studied were in a prepared transverse section of the composite and had a thin (~20nm thick) coating of gold or an evaporated coat of copper, ~100Å thick. The analysis was carried out, at an accelerating voltage of 10 keV and the ZAF correction provided in the JXA 8600M was used. The standards used were silicon carbide for the silicon and the carbon, and silica for the oxygen. The corrected data are given in table 3.4. There were two distinct sets of fibre compositions and these either contained ~14wt% or ~9wt% oxygen. The corresponding carbon percentage changed from ~31wt% to 33wt% but the silicon content was constant at ~53wt%. The total weight percentages found were rarely 100% and it was not obvious what was causing the errors; it was therefore decided to investigate the individual x-ray emission lines and the ZAF correction applied.

Firstly the silicon content of the Nicalon fibre was investigated, the standards utilized being pure silicon, silicon carbide and silica. Figure 3.14 shows the silicon Kα x-ray emission peak from the four substances obtained using the PET analysing crystal. The x-ray intensity (k) ratio relating to each standard is given in table 3.5. These figures were used to calculate the weight percentage of the silicon present using the ZAF correction of Scott and Love, the mass absorption coefficients of Bastin[161] were applied. The values obtained are given in table 3.6. Use of the silica standard indicated that ~57 wt% silicon was present, whilst the other values were ~52 wt%. It was considered that the first value is likely to be an overestimate. The carbon analysis utilized the STE crystal and a silicon carbide standard. This gave a k ratio of 0.986 and a ZAF corrected value of 26.8 wt%. These values were based on measurement of x-ray peak intensities but as figure 3.15 shows, there was a difference in the peak shapes for the standard and the specimen. The Nicalon produced a slightly broader peak than the silicon carbide, whether in α- or β- form. This would imply that the use of peak height underestimated the carbon content of Nicalon. A shape factor was therefore calculated from the ratio of the area of the curve to its intensity or peak height, in order to transform peak height into a peak area. The revised values for the Nicalon and silicon carbide are given in table 3.6, and the new weight percentage of carbon was calculated to be 27.9 ± 0.5 wt%.

The oxygen K_α x-ray line for the Nicalon was studied, this was measured on the LDE1 crystal and compared with that from a silica standard. The wavelength resolution of this crystal was poor and so the intensity of the peak was considered to be a sufficiently accurate measure of the concentration of oxygen. The k ratio of the intensities was 0.17 and the weight percentage was calculated, after ZAF correction, as 11.8 ± 0.5 wt%. Thus the total weight percentage of the three

elements in the Nicalon fibre was ~92 wt% but it was not clear what was causing this discrepancy. No other elements were present and no large amounts of porosity observed, but the validity of the silica standard has already been questioned and may account for some of the inaccuracies. The work is being continued in order to produce a more accurate measure of the composition. In the meantime, however, it was assumed that the proportions of each element were correct, and if it is valid to normalize the weight percentages to 100 wt%. This gives the weight percentages for each element as 56.5% silicon , 30.4% carbon and 13.1% oxygen, figure 3.16.

To establish the way in which these elements combine in the fibre, i.e. the compounds which are formed, the shape of the x-ray emission peaks was studied. Figure 3.17 shows the silicon K_β lines for the silicon carbide, silica and the Nicalon. This emission is produced by the transition of a M-level electron and is thus dependent upon the valance bond. These peaks have been normalized to the same height and there is clearly a difference between that obtained for the silicon carbide and the silica respectively. This reflects differences associated with the silicon-carbon bonding and the silicon-oxygen bonding. Examination of the silicon K_β peak from Nicalon appears to indicate that this material has some characteristics of both the other substances but that it is somewhat closer to the silicon carbide in position and shape. In addition, the satellite peak at ~6.82Å in the silica trace, which was not found in the silicon carbide example, was observed for the Nicalon, albeit much less intense. An indication of the area of the peak may be obtained from the full width at half maximum (FWHM). Table 3.7 shows that the FWHM is greater for the Nicalon, ~0.028Å, than either silicon carbide, 0.021 Å, or silica, 0.017 Å.

Figure 3.18 shows the carbon K_α x-ray emission peaks from Nicalon, silicon carbide, glassy carbon and graphitic carbon. The shape of the Nicalon peak can be seen to be closest to that of the silicon carbide although it is somewhat broader. The peak shape factor described earlier, was measured for each carbon-containing compound and the results are given in table 3.8. The value calculated for the Nicalon lay between that for silicon carbide and those for the other forms of carbon. The graphite gave a peak shape which depended on the sampling position, and in some areas it was broader on the shorter wavelength side. The narrow carbon K_α peak for graphite was closely similar to that recorded from glassy carbon.

The differences in the peak shape for the carbon K_α x-ray emissions were more clearly evident when the second order lines were investigated. Figure 3.19 shows the spectra for silicon carbide, graphite, glassy carbon and the Nicalon.

The oxygen x-ray peak, as measured on the LDE crystal, figure 3.20.a, showed no shape difference between Nicalon and silica. However, as figure 3.20.b shows, the utilization of the TAP crystal with its better wavelength resolution, reveals that the peak is broader for the Nicalon. These curves, again height normalized, were produced using a count time of 20 seconds to compensate for the low count efficiency of the TAP crystal.

The above measurements and observations indicate that the Nicalon is predominantly silicon carbide but that it contains some carbon which is not associated with silicon or oxygen. Furthermore, the shape of the silicon K_β peaks reveals that silicon-oxygen bonding and silicon-carbon bonding existed but that the oxygen was not in the form of silica. This leads to the conclusion that some ternary silicon-carbon-oxygen phase must be present, i.e. silicon oxycarbide.

Next, an estimate was made of the amounts present of these different phases in the Nicalon fibre. First it was assumed that the oxycarbide could be considered as an average of the stable carbide, SiC and the oxide, SiO_2, ie. Si_2CO_4. Using the measured weight percentage of oxygen (~13.1%) and assuming all of this element was present in the ternary phase (48.5 wt% oxygen), the amount of Si_2CO_4 was deduced to be ~27 wt%. The remaining silicon (45 wt%) must therefore be in the form of silicon carbide. This contains 70 wt% silicon which indicates that this phase constitutes 64 wt% of the Nicalon. These calculations show that ~10 wt% of free carbon is present. The results are summarized in table 3.9 and figure 3.21. Values for the batches of Nicalon, measured using the JXA 8600M ZAF correction, gave 30 wt% oxycarbide, 59 wt % silicon carbide, and 11 wt% free carbon for the first batch and 20 wt%, 68 wt% and 13 wt%, respectively, for the second. Figure 3.21 shows also these values converted to a volume percentage of compound.

Figure 3.22 shows the normalized carbon x-ray peaks for Nicalon and also a predicted peak produced by combining 9% of graphite and 91% of silicon carbide. The two curves are near identical with the calculated peak being slightly broader on the long wavelength side; peak shape factors were 8.7 eV for the Nicalon and 9.2 eV for the calculated peak.

Surface analysis data from the Nicalon fibre, obtained using the JEOL 8600M EPMA with the electron probe at normal incidence are shown in figure 3.23.a. The idea was to compare the surface of a Nicalon fibre with the central region at differing accelerating voltages so that any oxygen enhancement at the surface, if present, might be detected. The fibre was aligned such that its length was in the

direction of the required detector in order to reduce any effect of surface topography of the fibre on the x-ray intensity. A similar experiment comparing the surface of the Nicalon and a silica standard is illustrated in figure 3.23.b. The plots of x-ray intensity ratio against accelerating voltage show an increase with decrease in keV in both cases, for the oxygen, which indicates a surface enhancement in oxygen but not necessarily in the form of a layer of silica since then the curve in figure 3.23.b would have tended toward unity as the accelerating voltage was reduced. Such an increase in oxygen was not uniform on the fibre surface nor was it found on all fibres. For flame desized fibres an enrichment was always recorded whereas acid desized fibres showed some areas without oxygen enrichment. Figure 3.23.c shows the data from quantitative EPMA for oxygen, silicon and carbon. A series of analysis points were taken across a fibre, in a composite; the section gave a high aspect ratio ellipse and showed a higher level of oxygen at the surface.

A TEM micrograph of a Nicalon fibre is shown in figure 3.24. The approximate size of the silicon carbide microcrystallites was ~5nm. The diffraction pattern, figure 3.24.b, corresponds to polycrystalline β-silicon carbide, a cubic phase with a_0=4.358Å. The SAD pattern showed also that there was an amount of amorphous material within the fibre. EDS analysis of the fibre confirmed the presence of silicon, carbon and oxygen, whether the beam was positioned on the central area of a fibre or the surface region. Figure 3.24.d shows an EDS trace from a surface region taken from the uninfiltrated fibre region so as to minimize any effect from the matrix. It was observed that there was an increase in the concentration of the oxygen peak when compared with EDS analysis of the centre of the fibre, figure 3.24.c.

Figure 3.25.a shows the glass weft fibres, ~5μm diameter, which were woven

about the Nicalon tows. The spacing of the weft was ~4 mm and the total volume fraction of the weft was 0.02. Figure 3.25.b, EDS data of the weft fibres, showed that they contained aluminium, silicon, calcium, oxygen and magnesium, confirming them to be a glass. Figure 3.25.c, a diffraction pattern from the weft, shows it to be amorphous.

Two types of porosity were found in the composite. The first type was observed where fibres were in close contact, figure 3.26, and may be classified into three- and four-fibre pores. The number of each of these pores was counted from a polished section. Based upon a fibre diameter of 15μm, the cross-sectional area of an individual pore of each type was calculated as $9\mu m^2$ and $48\mu m^2$ respectively. A porosity of 0.12% was then deduced, although this is an over estimate since it assumes that the pores are continuous along the length of the composite sheet. Attempts to determine an average pore length were not possible due to the difficulty of producing a longitudinal section prepared which bisected the pores at their mid point. In addition there was not always infiltration between pairs of fibres which were in contact.

The second type of porosity was observed only in the thicker sheets and occurred in inter-tow regions in the centre of the sheet. Figure 3.27 shows an area where there was no infiltration, the large rounded features were matrix material which had squeezed through the fibres and solidified prior to infiltration.

The darker constituent in figure 3.11, marked (S) was identified with EDS as pure silicon. After selective removal of the aluminium matrix by chemical etching, it was seen, figure 3.28, that the silicon was in the form of interlocking branches and not the eutectic morphology characteristic of un-reinforced alloy. Where the silicon

contacted the fibres its morphology was spheroidized, whilst the remainder of the particle away from the fibre was coarse. Bridging between fibres and fibre tows was common, forming three-dimensional networks in contact with the Nicalon and weft fibres. The exact morphology of the silicon varied from sheet to sheet, sheet 500 showing much coarser silicon than the majority of the composite materials.

Figure 3.29 is a TEM of a thin section containing a second phase which EDS confirmed was pure silicon. Selected area diffraction of this phase showed that the silicon was extensively twinned. Frequently a silicon particle formed a bridge between two fibres. Figure 3.30 shows a common feature, the fracture of a silicon phase, probably produced during TEM sample preparation. EDS analysis of the point where the crack meets the aluminium matrix reveals the presence of a phase containing iron, silicon and aluminium. The crack extended into the aluminium but was soon arrested. Dislocation networks were often observed in the aluminium surrounding the fractured silicon particle, figure 3.31. The micrograph shows a silicon particle which has separated from the fibre, the adjacent aluminium remaining bonded to the fibre.

Earlier it was shown that iron-containing intermetallics were present in the unreinforced matrix alloy, despite the small concentration of iron impurity, ~0.13%. Chemical analysis of plates of N357 composite showed an even higher iron content of 0.5% overall corresponding to a matrix content of 1.16%. This produced an increase in the number of intermetallic particles, marked (D) in figure 3.11. They were similar in composition to those found in the unreinforced alloy; quantitative analysis results for these phases are given in table 3.10, with 14.7 ± 1.3 wt% silicon

and 24.4 ± 2.4 wt% iron. The $FeSi_2Al_4$ intermetallic was not, however, observed in the composite.

In sheets of N357 produced in early production runs, chromium and nickel were found in some intermetallic particles. The chromium-containing intermetallics were not acicular, see figure 3.32.a, and the relevant EDS trace is given in figure 3.32.b. There was between 3.3 and 5.4 wt% chromium and the iron and silicon contents were ~20 wt% and ~10 wt% respectively. Wet chemical analysis gave the total percentage of chromium in the matrix as 0.02%, table 3.1. Figure 3.33, a WDS x-ray map of an area which includes a chromium-containing intermetallic, shows the presence of x-rays from different elements above a given set level. The chromium-containing intermetallic is close to several $FeSiAl_5$ intermetallics but this was not always the case; figure 3.34 shows an example where a chromium-containing intermetallic is separate from the $FeSiAl_5$ type. The nickel-containing intermetallics, such as that marked N in figure 3.35, were invariably observed in contact with a $FeSiAl_5$ intermetallic. This latter figure shows also a large intermetallic of the $FeSiAl_5$ type sectioned at low angle to reveal its plate-like morphology.

The quantity of intermetallic phase varied from sheet to sheet for the N357 composite but phases containing chromium or nickel were found only in a few sheets. Figure 3.36 shows micrographs for different sheets produced at different times throughout the period of study. Composites from more recent production runs contained fewer and smaller intermetallic particles and none contained chromium.

Examination by optical and scanning electron microscopy, such as figure 3.11,

revealed no interfacial chemical interaction between fibre and matrix, merely the segregation of silicon and the presence of some intermetallic particles. However, a more detailed study using WDS in the JXA 8600M showed a detectable segregation of magnesium to the Nicalon fibres, figure 3.34 and figure 3.35. This was not revealed by EDS analysis in the SEM because of the close proximity of magnesium to the aluminium x-ray peak. The magnesium could not be precisely located using the WDS because of the size of the x-ray generation zone ($1\mu m^3$) and the pixel size of the x-ray map ($1\mu m^2$). Thus the magnesium may have been present as a diffused layer on or at the fibre surface or as discrete particles. Figure 3.37 shows (a) line analysis and (b) stepped quantitative analysis, where the concentration of magnesium was about 0.2wt% but not all sheets showed such segregation. Generally the segregation was detectable in those sheets which were known to have a higher magnesium content, see table 3.1. Further information was therefore sought utilizing the improved spatial resolution available in the analytical TEM.

EDS in the TEM revealed an interface layer of magnesium at all fibres in sheets where segregation occurred. A SAD pattern from a region containing the magnesium, showed a ring pattern typical of the β-SiC, indicating that the magnesium had actually entered the fibre. Where the fibre was in contact with a silicon particle, figure 3.38, or an intermetallic, figure 3.39, the penetration of the magnesium was difficult to detect. The depth of magnesium penetration in the Nicalon fibre ranged from ~200nm where the aluminium was in contact to <40nm where silicon or an intermetallic contacted the fibre. A small amount of aluminium was also found in these fibre surface regions, which was considered a genuine effect since the bulk fibre showed no aluminium x-rays. Figure 3.40, shows an area where limited or no reaction has occurred and although a magnesium peak could be observed, the depth of penetration could not be measured. No apparent

reaction was observed between the silicon and the intermetallic.

It was not possible to make generalisations about the interface between the Nicalon and the aluminium since in the same composite sheet the interface was found to differ considerably. Sometimes a reaction product was detected at the interface; in other cases an interface with little or no reaction was present, and on a number of occasions discrete particles were located at the fibre surface with no obvious sign of chemical reaction.

Figure 3.41.a shows an interface where a reaction product was formed. This first phase varied in size and shape and figure 3.41.b shows a second example where this interphase was of a more bulky form. EDS analysis, figure 3.41.c, showed x-ray peaks for aluminium and oxygen. A SAD pattern of a region containing the interphase is shown in figure 3.41.d, giving a discontinuous ring pattern indicative of a polycrystalline cubic phase with a_0=0.79nm. Together with the EDS data this confirms the presence of alumina.

Figure 3.42.a shows an interface structure which contains needle-like crystals which extend into the aluminium matrix for a distance up to about 250nm. Analysis of the microdiffraction pattern, figure 3.42.c, shows that these phases are aluminium carbide, Al_4C_3, a rhombohedral structure with a_0=0.334nm and c/a=7.49. At higher magnification the lattice planes of the carbide may be imaged, figure 3.42.d, the basal planes of the carbide being aligned along the crystal length. The carbide needles were associated at various angles to the fibre but they occurred on fewer fibres than the alumina phases and rarely in combination with one another, see figure 3.43. A dark field image produced from the [0001] plane of the aluminium carbide crystal, figure 3.42.b, shows some carbide formation within the

outer 100-200nm of the fibre.

The type of phase which appeared to show no reaction with the fibre is illustrated in figure 3.44. They varied in shape and size and the bulky phase, marked A, contains, aluminium, magnesium, oxygen and a small amount of silicon; the silicon content varied from negligible, figure 3.44.c, to significant, figure 3.44.d. SAD of these phases, figure 3.44.b, would suggest that they are spinels of the type $MgAl_2O_4$, a cubic lattice with $a_0 = 0.808$nm. With the higher silicon levels, the crystal structure tended to depart from that of the spinel. Sometimes the phases existed close to but not on the fibre surface, figure 3.45; the large needle-like phase in this figure is aluminium oxide.

A second type of discrete phase is illustrated in figure 3.46.a. The diffraction pattern, figure 3.46.b, shows an amorphous structure and EDS, figure 3.46.c, reveals that the phase contains aluminium, silicon, calcium, oxygen and magnesium. Some particles were found in the matrix close to the Nicalon which had a fibrous appearance, figure 3.47.a. These also contain aluminium, silicon, calcium, magnesium and oxygen, figure 3.47.b. Both phases appeared to be associated with fracture at the matrix/Nicalon interface although they had no observed interaction with the Nicalon. Their distribution was random, although in some cases as shown in figure 3.48 they were trapped in the space between two fibres, inhibiting the infiltration of fibres.

A phase with a similar composition to that in figure 3.46 occurred at the fibre surface as a very fine layer, typically 10-50 nm thick. Figure 3.49 gives an example of such a phase at the interface between a silicon particle and the fibre. EDS of the region showed x-ray emission from the fibre and the matrix constituent together

with calcium and magnesium. Again these phases are often found to be partially fractured.

Figure 3.50 shows the interface in a heat-treated N357 composite. The interface product was more extensive, its thickness being typically ~300nm and generally surrounding the whole fibre. It was mainly aluminium carbide with small amounts of alumina. The magnesium penetration was still observed but was no more extensive than in the as-cast composite. The silicon in the heat-treated composite showed a similar spatial distribution to that observed in the as-cast specimens with segregation and bridging of fibres but there was less twinning. In addition in the heat treated composite the reaction product was sometimes observed between the fibre and the silicon phase suggesting a regrowth process, figure 3.51.

Figure 3.52 shows a DSC thermogram for the composite in the solution-treated state. Endothermic peaks at 570°C and 590°C, as seen in the unreinforced alloy, were again present but no peak at 230°C was observed. In some specimens a double exothermic peak at 360°C was found, figure 3.53. Similar tests carried out on Nicalon fibres from the bobbin gave a thermogram, figure 3.54, with a similar double peak.

3.1.4. Nicalon-1000 Composite.

Figure 3.55 is an SEM micrograph of the N100w composite and shows that in addition to the Nicalon fibres a number of carbon fibres were present. These were in the 01 orientation and they were randomly positioned through the composite between the plies of woven Nicalon. The volume fraction of the Nicalon was ~0.44. The carbon had a low volume fraction, below 8%..

Figure 3.56.a,b shows a metallographic section of the N100f composite. Second phases are clearly revealed and EDS showed them to contain aluminium and iron away from the fibres, figure 3.56.c, and aluminium, iron and silicon close to the fibres, figure 3.56.d. Quantitative analysis of the phases yielded the results given in table 3.11. The range of compositions found suggested that the composition of these intermetallics range from $FeAl_3$ to $FeAl_8$, the silicon level reaching only ~2 wt%. The SAD pattern taken in the TEM, figure 3.56.e, corresponds to $FeAl_3$, with a_0=6.743nm, b=1.545nm and c=0.807nm. The intermetallics were often observed at the fibres, with bridging only when fibres were close together. Figure 3.57 shows the deep-etched composite with the intermetallics on the fibre surface.

Porosity was a common feature of N100 composites, although the infiltration of N100f appeared greater than that of N100w. In figure 3.58 a large area (~1500mm^2) of the preform was not infiltrated. This was a problem with two out of the three N100w composites provided, which meant that only one sheet could be used for subsequent characterization. In the case of the N100f sheet the infiltration was generally fairly good.

The N100f composite showed a more even distribution of fibres with less high-density regions of fibre. The reinforcement was well aligned in the longitudinal orientation, and a single layer of woven Nicalon was present on one surface of the sheet. This layer had been added to restrict the movement of the preform during infiltration. The overall volume fraction of the fibres was approximately 0.43.

Figure 3.59 shows the interface in the N100 composite. Carbide needles were found to be present and were similar in morphology to those found in the N357

composite but fewer in number and not as large. Where they were present they were found in isolated groups which were densely packed. Only ~10% of the fibres showed any reaction and rarely did it surround completely a particular fibre.

In the specimens investigated no alumina was found at the interface of the aluminium and the Nicalon. Where intermetallics were present on the fibre it was common to find that the carbides were still present and of a similar size to those at the aluminium/fibre interface, figure 3.60.

3.1.5. Alumina/Borsic-357 Alloy Composite

Three distinct regions were present in this composite, figure 3.61, one reinforced with FP alumina, one reinforced with Borsic and a reinforcement-free layer. These regions have fairly consistent proportions and the thickness percentages are ~46% , ~1.5% and 52.5% respectively.

Figure 3.62 shows a polished section of a layer containing FP alumina. The diameter of the alumina fibres varied very little, the measured distribution, figure 3.63, giving 20 μm ± 8%; this compares with 20 μm ± 5% quoted by the manufacturer. The SAD, figure 3.64 gave the incomplete ring pattern characteristic of polycrystalline α-alumina with a_0 = 0.476 nm and c = 1.299nm. The infiltration of this region was complete and the fibre/fibre contact much lower than the Nicalon composite. Locally the alumina volume fraction was approximately 0.38, which equates to an overall volume fraction of ~0.17.

The Borsic fibres were in a nominal ply containing a monolayer of filaments, figure 3.61. The diameter of the Borsic was ~142μm, but a size distribution is not

given since too few fibres were present to provide a meaningful analysis.

Throughout the composite many "second" phases are present. These were silicon particles, intermetallics and impurity inclusions. The distribution of the silicon was similar to that for the Nicalon-alloy composite, with coarse particles close to the fibres. However, deep etching, figure 3.65 reveals that the presence of the networks of silicon is less extensive. A network of silicon and fibres still existed but only when the fibres are closely packed.

Figure 3.66 shows that the intermetallics are larger and more numerous than in the N357 composite; they were confirmed as $FeSiAl_5$, table 3.12. These were the only intermetallics found in this composite and were the predominant matrix bridging phase between fibres.

Figure 3.67.a is an x-ray map of the alumina region with intermetallic (pink) and silicon (blue) bridges evident. Little or no magnesium segregation is found, although the x-ray map, figure 3.67.b, shows a small but uniform level in the matrix. EDS in the TEM, figure 3.68, did find a very slight increase in the magnesium at the aluminium/alumina interface compared with the matrix level.

The third matrix constituent was the irregular phase marked X in figure 3.62; such phases varied in size from ~1μm to ~4mm. The composition also varied considerably, the major element present being iron although carbon was also common. Figure 3.69 shows a deep-etched structure in the FP alumina region with an inclusion. EDS of this phase shows the presence of iron, silicon, carbon with traces of other elements.

Figure 3.70.a shows an area containing Borsic fibres. An x-ray map of this region, figure 3.70.b, in addition to the matrix phase distribution shows silicon x-rays from the silicon carbide coating on the fibres. There are a large number of silicon- and magnesium-containing phases, shown yellow in the x-ray map which in some cases contained aluminium, iron and carbon. The same figure shows the titanium weft (blue), boron fibres (green) on the tungsten core (red). The aluminium is not shown in these figures but forms the remainder of the matrix, deep etching of the specimen reveals that the titanium weft is in the form of a strip 20 μm thick and 100 μm wide, figure 3.70.c.

Figure 3.71 is a DSC thermograph of the solution-treated F357 composite. This was taken from the alumina region and shows that the area of the endothermic peak, corresponding to the iron-rich intermetallics, is greater than that for the N357 composite. This is indicative of the greater quantity of iron-rich intermetallics which were present.

3.2. Mechanical Properties.

3.2.1. Unreinforced 357 Alloy

The stress response to applied tensile strain is shown in figure 3.72. Since the strain gauges used had a maximum capability of ~2%, the strain at which the material fractured was estimated from the chart recording. The results are given as engineering stress against measured strain.

The 357 alloy was found to yield at a stress of 38MPa and a strain of 0.06%. Fracture occurred at 64.6 ± 5.2MPa and 3.2%. The elastic (initial straight line)

modulus, as estimated from the slope of the stress/strain curve, was 62GPa.

The stress verses strain relationship for the peak-aged material, figure 3.72 showed higher yield stress and failure stress than the as-received material, 86MPa and 124 ± 8MPa respectively, but the strain to failure was less, at a value of 1.05 ± 0.03%. The modulus was the same as for the as-cast alloy, approximately 60 GPa. The results are summarized in table 3.13

Figure 3.73. shows the ageing response of the 357 alloy. The microhardness is seen to increase to a maximum of 140 ± 7Hv after 10 hours heat treatment at 160°C. This may be compared with the as-received hardness of the alloy of 84 ± 5 Hv.

3.2.2. Aluminium 1000

The aluminium was tested only in the as-cast condition since it showed no ageing response. Figure 3.74, a typical stress versus strain curve under tensile loading, shows a low yield point at 28MPa and 0.02%. The specimen underwent considerable necking during deformation and gave a fracture strength of 52MPa ± 13MPa The elastic modulus calculated from the initial linear section of the curve, was 68 ± 2MPa.

3.2.3 Nicalon-357 Composites.

Typical tensile stress versus strain curves for the specimens with fibres in longitudinal and transverse directions are given in figure 3.75.a. The failure point was found to be 132 ± 21MPa and 0.11 ± 0.02% for the longitudinal specimens and 54 ± 14 MPa at 0.10 ± 0.03 % for the transverse orientation, table 3.14. Figure 3.75.b summarises the strength data for all N357 specimens tested, in the form of a histogram. The modulus calculated from the linear section of the curve was ~120GPa.

Acoustic emission events occurring within the composite during straining are shown, for the N357 composite stressed in the longitudinal fibre orientation, in figure 3.76 . There was little increase in the event rate with increasing strain and the number of events to failure was low. Figure 3.77 shows a typical example for the transverse orientation. Here there was a more steady build up of events until failure was reached.

Figure 3.78 is a scanning electron micrograph taken from the fracture surface of a longitudinal specimen. The surface is characterised by large flat areas where the fibres had failed on the same plane and the glass weft is also visible. Figure 3.79 taken at higher magnification, confirms the absence of fibre pull out, although some debonding of plastically deformed aluminium from the fibres is observed, P. The aluminium suffered necking in all areas during failure. The feature marked D in figure 3.79 contains iron, silicon and aluminium indicating it was an intermetallic particle. These were common features on the fracture surface and figure 3.80 shows a back-scattered image of such an area. The lighter phase is the intermetallic and fracture of this phase passed through several fibres and was noted

to lie in a plane near to perpendicular to the loading direction (fibre length). Small fragments of material found to be silicon were located on the surface.

Figure 3.81 illustrates a fracture surface where the glass weft, G, is a prominent feature. There was a tendency for the fracture to pass through the weft fibres, an effect which led to the removal of infiltrated bundles from the fracture surface, bundles of Nicalon fibres also being found to be removed from the fracture surface. Both of these usually were held to the surface by a ligament of matrix material. The fibre fracture was brittle in nature, each tow appearing to fail at the same point. This was especially true in densely-packed regions but in the less densely packed regions and at the periphery of the tows the fracture sometimes passed onto another plane. This resulted in the stepped surface of some of the specimens.

Figure 3.82 shows a fracture surface from a tensile test with the fibres in the transverse orientation. There is a mixture of fibre splitting and debonding, the majority being the former. The debonding results in some retained matrix material. For the splitting, figure 3.83, the fibre fracture surface is very smooth as would be expected from a brittle material. The Nicalon fibres were often found to fail perpendicular to their length, figure 3.83. In some cases there appeared to be a combination of splitting and perpendicular failure, figure 3.84. Fractured intermetallic particles were again common, although not as large as in the longitudinal orientation. They were often found where a fibre bundle was removed from the surface or a fibre had split, figure 3.85. Small fragments of silicon are found all over the surface either attached to it or as debris on the surface. The weft fibres were parallel to the stressing direction and figure 3.86 shows that the interface had debonded at the edge of the wefts. The glass surface was damaged in most areas and showed little evidence of retained matrix material. Figure 3.87

shows a region where infiltration was poor. This was close to the sheet surface and shows the melt front solidified prior to infiltration.

Depending on the dimensions of the flexural test bar the fracture strength of specimens was higher than that for longitudinally-orientated specimens tested in tension, 340 ± 20 MPa (geometry C) and 232 ± 19 MPa. The notable exception is geometry B (see figure 2.4) where the failure stress is 116 ± 23MPa. The failure stress for the four point bend specimens was calculated using a geometric relationship which had the following form:

$$S = \frac{F.L}{b.d^2} \qquad \text{.....equation 3.1.}$$

where S is the stress in the outer "fibre" of the beam, F is the load, L the outer support span, b the beam width and d the beam depth, see figure 2.4. The standard (ASTM D790) suggests the use of a correction factor when the span to depth ratio was less than 16:1. Equation 3.1. becomes:

$$S = \frac{P.L.(1+(4.70.D^2/L^2)-(7.04.D.d/L^2))}{bd^2} \qquad \text{.....equation 3.2.}$$

This relationship was applied to the dimensions for geometries A, B and C but the change in the strength only increased the strength for geometry B by ~2% and did not affect either the strength for A or C. ASTM D790 also gives a relationship for the maximum strain (e) incurred.. All these calculations were based on an outer to

inner span ratio of 3:1. The maximum strain is given by the equation:

$$e = \frac{4.70.D.d}{L^2} \qquad \text{..... equation 3.3.}$$

where D is the deflection of the test machine cross-head. Strains were recorded from the tensile surfaces using strain gauges.

For geometry C it was possible to have the glass weft either in-the-plane or through-the-plane of the test specimen, figure 3.88. These bars were used to deduce the possible effect of the glass weft on the fracture behaviour of the composite. Four-point bend geometry was utilized because the dimensions of the sheet would not allow tensile test specimens to be prepared with the different weft orientations. The results are given in table 3.14. The in-plane-weft specimens showed a lower failure stress than those with the through-plane orientated weft, 305 ± 29 MPa compared with 358 ± 8 MPa.

The fracture surface of specimens tested in flexure differed from that tested in tension. Figure 3.90 shows that there was a considerable amount of "stepping" of the fracture plane. Closer examination revealed that this was associated with the glass weft material. Figure 3.91 shows that Nicalon tended to fragment and debonding of the matrix from fibres was also common. Although the debonding resulted in retained material on the fibre surface, this was found to be any of the matrix constituents.

Figure 3.92 shows a region with a "spiky" phase on the fibre surface. It is not clear what this phase is but EDS suggested that it may have contained magnesium and

aluminium. The infiltration in this area would appear to be poor or a large amount of matrix material had been removed.

Figure 3.93 shows a section through the fracture surface with the crack running from top to bottom. The brittle fracture of the fibre tows is evident and there is no fibre pull out. Examination of the matrix region, in the case of figure 3.94 an x-ray map of the same area, shows that silicon and intermetallics had failed and are present on the fracture surface. The fracture path followed these phases. Figure 3.95 shows a region of the same bar but away from the main crack front; the Nicalon tows have failed and the fracture passed through the glass weft. The same figure contains another feature; this was the matrix voiding at fractured second phases in the matrix. The path of the fracture, both the secondary cracking and the main fracture, is often altered by the weft; figure 3.96 is an example of the main fracture path deviating and diverging at a weft.

The fracture surface of the flexural test with fibres in the transverse orientation is given in figure 3.97; these surfaces were very similar to those of the tensile tests. The fibres failed predominating by splitting. Much of the splitting was associated with intermetallics; figure 3.98 shows an intermetallic which is attached to a split fibre. The second phases caused the fracture of the fibres perpendicular to their length, figure 3.99 showing an area with fragmentation. Figure 3.100 shows a feature not noticed in the tensile tests; this is the apparent "skinning" of the fibre. The fracture had passed through the outer layer of the fibre; the same micrograph shows fibre failure perpendicular to its length which is associated with bridging silicon phases. The silicon had become debonded from the fibre and had fractured. The areas of the fibre which have not peeled are covered with a small needle like phase; these phases were too small to allow EDS analysis. However, another area,

figure 3.101 showed this skinning effect; the phases which were present here contained aluminium, oxygen and magnesium; some carbon and silicon was detected as well but was thought to come from the fibre. Figure 3.102 shows an area where there was not complete infiltration, the fibres have a clean surface. The centre of this micrograph shows the presence of several iron rich phases, D; again these were associated with the fracture of the fibres.

The tensile stress versus strain curve after heat treatment is shown in figure 3.103. The fracture stress is now only 70 ± 9 MPa in the longitudinal fibre orientation and ~25MPa in the transverse fibre orientation, only a small number of these test results are available . The strain to failure for the heat treated specimens is similar to that of the as provided specimens, 0.09%.

In flexure the strength was lower after heat treatment; the bar geometry used was type C measured only for the longitudinal fibre orientation. The strength obtained was 119 ± 12 MPa with a strain to failure of ~0.14%. No difference in the fracture surface after heat treatment was noted.

The shear tests used proved to be unsuccessful for providing a value of the shear strength of the composite. The majority of the failure was localized to the region at the cut notches. In only a single case did failure occur in shear. The calculated results are given in table 3.15, shear failure gave an interlaminar shear strength ~16MPa. The values quoted for the specimens that did not fail by shear can be considered to be below the actual shear strength.

Examination of the shear failure showed a mixture of Nicalon and weft fibres on the fracture surface, figure 3.104. This shows much fracture of the Nicalon; this

was often associated with matrix or interphases, figure 3.105 shows a fibre where a number of phases containing aluminium, magnesium and oxygen were present. In some regions the fibres had no apparent matrix material on their surface, figure 3.106, this indicated that these were regions which had not been infiltrated.

Figure 3.107 is the age-response of the aluminium in the N357 composite and no change in hardness was observed. The microhardness of the α-aluminium dendrites was found to remain at 36 ± 4Hv in each sheet.

3.2.4. Pure Aluminium Composites

The woven fibre composite, N100w, gave the stress strain curves in figure 3.108 for the two orientations used and tested in tension. The failure stress in the 01 direction is 130 ± 12 MPa and 83 ± 8 MPa in the 02 direction. The failure strains were 0.19 ± 0.01% and 0.23 ± 0.01% respectively.

For the filament-wound specimens, N100f, there was a distinct change in the strength with orientation. The longitudinal strength is 149 ± 22 MPa and the transverse strength depended on whether the specimen was cut with or without the woven layer. The strength without the layer was ~20MPa and with the layer was ~90MPa. Stress versus strain curves are given in figure 3.109, and show yielding at low strains. The yield point is approximately 60 MPa and 0.02% for the longitudinal orientation and 30 MPa and 0.02% for the transverse. The transverse stress strain relationship, without the woven layer, is seen to be very similar to that observed in unreinforced aluminium, whereas the stress/strain relationship with the woven layer shows an improved strength. The results are summarized in table 3.13.

Figure 3.110 shows a typical example of the acoustic emission monitoring during straining for pure aluminium composite this shows a larger number of events prior to the final failure than the N357 composite, the event rate increased progressively.

The filament wound composite showed a less brittle failure than the alloy composite. Figure 3.111 shows a typical well infiltrated area with brittle fibre fracture and ductile matrix aluminium. When infiltration was poor, as in figure 3.112, the fracture still showed no pull-out of fibres. The feature near the centre of figure 3.112 shows the presence of aluminium and is thought to be a solidified melt front. The fibres were often split or fractured into segments ranging from 5 to 25 μm in length, figure 3.113.

The fracture surface of a specimen with fibres in the transverse orientation, tested in tension, is shown in figure 3.114. This shows clumps of infiltrated fibres partly removed from the surface, K, split fibres, J, and retained matrix phases. Figure 3.115 shows fibre failure perpendicular to the length; this was associated with the phases marked with arrows and these were found to be iron-aluminium intermetallics, the retained material on the fibre surface was shown to be aluminium and the small bright fragments silicon.

When tested in flexure the strength of the N100f composite was 176 ± 11MPa in the longitudinal orientation and 118 ± 16MPa in the transverse; geometry C was only used. The failure strains were 0.3 % and 0.79% respectively. Figure 3.116 shows the stress versus strain relationship for typical specimens.

The fracture surface of the bar with longitudinal fibres, figure 3.117, shows the consequence of a region without infiltration, there was a large area in the centre of

the bar which has fibre lengths of the order of 3mm exposed. This was not pull-out as the fibres were not infiltrated with matrix material. Much of the fracture surface shows, figure 3.118, fibre fracture perpendicular to their length. This is combined with the separation of matrix and fibre and the plastic deformation of the aluminium constituent. Well infiltrated regions show the brittle surface similar to the N357 composite.

In the bars which had a transverse fibre orientation the fracture was a combination of debonding and large regions which had no matrix, figure 3.119, the retained surface phase was invariably aluminium.

Table 3.15 indicates that the shear strength of the N100f composite was greater than that of the N357 material, the values being ~43MPa and ~16MPa respectively. The fracture surface for the shear geometry, figure 3.120 shows that the predominant failure was by fracture of the fibres. This was true unless the composite was not fully infiltrated when there was no load bearing ability, this is shown in figure 3.121.

3.2.5 Alumina-Borsic composite.

These specimens were tested in flexure only, with a span (inner to outer) ratio which was not 1:3, and equation 3.1 now becomes the following relationship:

$$s = \frac{3.F.l_1}{b.d^2}$$

Where l_1 is the distance from the outer to inner loading point. Testing was carried

out with the Borsic fibres in the 90° orientation in relation to the bar length, see figure 3.122. Heat treatment effects were also studied, the thermal history applied was the same as that described in section 2.2.

The results are given in table 3.16 and show only a very slight change in the strength with heat treatment. The value for the as provided composite was 202 ± 26 MPa and the aged composite 215 ± 30 MPa.

The fracture surface of the composite is shown in figure 3.123. The alumina region with the fibres aligned in the length of the bar was characterised by a flat fracture with a large number of iron containing phases evident; figure 3.124 shows an example where the intermetallics, marked D, were shattered. Fibre fracture itself shows the polycrystalline nature of the fibres. Where the alumina was perpendicular to the length of the bar debonding of the fibres and matrix was the usual form of failure, some fibre splitting is noted and usually associated with the presence of a second phase either silicon or more often an iron intermetallic. Figure 3.125 shows a transverse fibre region (alumina) where an intermetallic is seen to contact the fibre at a position where failure of the fibre perpendicular to its length had occurred, i.e. the fracture path has changed to pass through the fibre at the intermetallic; this is marked with the arrow.

The fracture in the Borsic area is shown in figure 3.126 this is for a longitudinal orientation and shows the observed stepped fracture. This was associated with the titanium weft, T. Figure 3.126 also shows that the Borsic fibres usually split along their length, S, the failure passing through the tungsten core. Transverse Borsic failure such as that shown in figure 3.123 was observed to be by fibre splitting.

The microhardness of the aluminium dendrites in the F357 composite achieved a maximum after approximately 6 hours and increased from the as-cast hardness of 65 ± 3 Hv to 95 ± 1Hv. The curve is shown in figure 3.127 with that for the unreinforced alloy. Although the peak occurs earlier than the parent alloy the maximum hardness achieved was lower.

The applicability to MMCs of dynamic modulus testing was investigated. The basic arrangement for the measurement of the material's dynamic response is shown in figure 3.128 The technique based on the method set out in ASTM 747[151] was utilized for the F357 composite only. A standing wave is produced in the material, by striking the specimen, the mode of oscillation will depend on the strike position and direction. The resulting oscillation will have a resonance frequency which is measured experimentally. The frequency depends on the material properties, density and stiffness. The frequency was calculated from the oscilloscope output via a pick-up stylus placed at one end of the specimen; using the following relationship the dynamic modulus, E_{dyn}, was calculated:

$$E_{dyn} = A_R.M.f^2/w$$

where A_R is a quantity dependent on the thickness to length ratio tabulated in ASTM 747, M is the mass of the bar, f the frequency measured and w the width of the bar.

The technique is non-destructive and the test bars used were those which were cut for the flexural tests. Testing was performed in the geometry described in figure 3.122. The dynamic modulus measured for the as received F357 given in table 3.16 show little difference between each heat treatment condition and with the

positioning of the test bar and the calculated value typically was found to be ~100 GPa.

3.3. Single Fibre Tests.

The strength of the Nicalon fibres from each environment. are given in table 3.17 and figure 3.129 these show a clear trend in the strength of the Nicalon fibres. The fibres in the as received condition gave the highest strength of 1513 ± 473 MPa, after the acid etch. Furthermore the strength of the as received fibres did not differ appreciably from this value either without the etch (1560 ± 536 MPa) or after a heat treatment at 540°C for 16 hours (1511 ± 523 MPa). The strength measured then depends on the environment from which they were extracted. Production of a preform reduces the observed strength to 1084 ± 395 MPa and incorporation into a composite further reduces the strength, those for fibres extracted from the N100 and N357 composite being 742 ± 299 MPa and 420 ± 174 MPa respectively. After exposure to a heat treatment of 540°C for 16 hours followed by 10 hours at 160°C, the strength of fibres extracted from the N357 composite was 279 ± 121 MPa. This final population of fibre strengths is thought to have a higher mean than is actually correct, this is due to the lower strength fibres having failed during mounting.

The fibres from each environment above were investigated in the SEM. Figure 3.130 shows the fibres as they were received, with the polymeric size easily visible on the surface. After desizing, either thermally or chemically, the fibres were found to have a clean surface, figure 3.131. A small number of surface flaws were found in some of the fibres but generally no obvious defects were present. The fibres extracted from the composites show a number of surface features. Figure 3.132.a shows a fibre which has a silicon containing phase on the surface,

S, fibres were found that had a large number of phases on the surface, figure 3.132.b. In certain cases such as figure 3.132.c there was some evidence of an interfacial reaction. Much of the material retained on the surface is the result of incomplete dissolution of the matrix, it is thought that this gave a more accurate measure of the fibre strength. Many of the matrix phases which may have had an effect on the fibre strength in the composite were still present.

3.4. Fibre/Matrix Interfacial Shear Tests.

The fibre interfacial shear strength for the N357 composite, as calculated from some 50 indents, was 58 ± 41 MPa. After heat treatment of the composite for 10 hours at 160°C, it fell to 37 ± 24 MPa. The figure calculated for the N100 composite was 12 ± 5 MPa. A noticeable feature of these tests was the amount of variation in the results. Using Student t-tests at a 95% confidence a difference was found between the N357, N357 after heat treatment and the N100. The results showed that interfacial shear strength (τ) for the N357 is greater than that for the heat treated N357 (N357ht) composite and greater also than the aluminium based composite (N100). If a 99% confidence limit is used there is no statistical difference between τ (N357) and τ (N357HT), whilst there was still a difference between the N357 and N100 values.

The values of τ calculated are given in table 3.18. It should be noted that these values are produced with knowledge that additional factors require consideration. These would include the amount of plastic deformation of the matrix local to the fibre and the effect of any sub-surface features, such as fibre breaks and matrix second phases.

The majority of the indents were made in isolated fibres, i.e. ones which were surrounded by sufficient matrix material to allow production of a clearly defined matrix indent. In addition some measurements were made on fibres in tows and in contact with other fibres, to give the values of the interfacial shear stress of 10 ± 8 MPa.

Figure 3.133 shows a scanning electron micrographs of typical indents. The deformation of the matrix is clear and in some examples fibre fracture was evident. Less fibre fracture has occurred in the N100 composite. Figure 3.133.b shows catastrophic failure of a fibre during indentation. The deformation of the matrix was common, with second phases often being found attached to the fibre, figure 3.133.c. In some cases the attached phase was found to have fractured and the crack to have continued into the surrounding brittle phases.

CHAPTER 4. DISCUSSION.

4.1. Effect of Fabrication Route on Microstructure of the Composite.

The detailed microstructural investigations in the present study provide essential data which can be used to elucidate the characteristics of preform infiltration and the subsequent solidification sequence of the composite. Starting with porosity, this was a feature common to both of the Nicalon-reinforced composite systems. It was related to the fibre packing and in turn to the manufacturing route. The infiltration of a fibre array which has an even spatial distribution should result in minimal porosity, but where fibres were in close contact and infiltration by liquid metal was inhibited, porosity could become a problem. Thus, since the pressure required to infiltrate the interstices between the fibres is a function of the radius of curvature of the melt front (as the radius of curvature of the melt front reduces the pressure necessary for infiltration increases), fibres in contact contained, not surprisingly, a small amount of porosity in the interstices.

The second type of porosity which was found resulted from the characteristics of freezing of the melt prior to complete infiltration. This was observed in the central regions of thick N357 sheet, but was more common in the N100 sheets where the use of aluminium metal required a higher melt temperature than the aluminium alloy. Figure 4.1.a shows this schematically; the melt may pass through and either side of the preform, but not above or below, and so there is more than one infiltration direction. The molten aluminium which travelled further will have had more time to cool, and thus the viscosity would have increased, impregnation would have been inhibited and porosity would have been increased. A third type of porosity, of a gross nature, may result when the melt front approached a region of densely packed fibres, figure 4.1.b. If the melt could not surmount this barrier and no other melt front could reach the uninfiltrated area, porosity will have resulted. Generally, porosity effects are accentuated in composites which have a high packing density of fibres, but shrinkage porosity is not thought to be a problem because of

the pressure applied during fabrication. Such porosity adversely affects the strength of the composite and clearly without contact between matrix and fibre no stress transfer is possible. Furthermore, transverse properties will be strongly affected by the reduced loading area associated with the presence of porosity, figure 4.1.c.

Once infiltrated the aluminium alloy solidifies, the resulting microstructure being strongly influenced by the presence of the fibres. In the case of the aluminium-silicon alloy the silicon particles were segregated to the fibres, see figure 3.11, a feature which has been noticed in other MMCs[41,50-54,153,154]. In particulate-reinforced composites, for instance, it has been reported that the degree of segregation is a function of the melt front solidification characteristics. Thus the solidifying aluminium dendrites drive the particulates and silicon-rich melt to the same area[101,152] and when the remaining melt solidifies, it will yield a region rich in both silicon and particulates. This is, however, unlikely to be the reason for the segregation of silicon in the present fibre-reinforced composite, although some movement of fibres has been observed by Yang and Scott[53] at the edge of similar tows in a carbon fibre-357 composite produced by the same method. The Nicalon fibres are much more massive and held tightly within their tows and no evidence that they were moved by the melt was observed. The segregation is a consequence of the solidification sequence in the composite, as shown schematically in figure 4.2. Hence upon cooling of the infiltrated preform the α-aluminium dendrites nucleate in the inter-fibre regions. As the dendrites develop they result in an enrichment of silicon in the liquid aluminium surrounding the fibres, examination of the phase diagram for Al-Si shows that the limit of the solubility of silicon in aluminium is only ~1.2 wt% and therefore silicon (as part of a silicon-containing eutectic) is the final constituent to solidify. This is also true of the Al-Si-Fe system, figure 4.3, a system which is more applicable to the composite (N357) studied here since iron was a common contaminant in the composites.

Once the melt is introduced into the preform, the fibres, having a low thermal mass, soon

attain the same temperature. However, the lower cooling rate of the fibres means that the dendrites nucleate in the inter-fibre regions. The dendrites started to form prior to full infiltration and they will extend until halted by some feature such as a fibre. As they grow the solidification front pushes melt enriched in silicon and iron towards the fibre. The iron-rich intermetallics start to nucleate at a temperature of approximately 884 K, the exact temperature being dependent on the iron and silicon content. Then, at the eutectic temperature of 576°C, the remaining melt solidifies.

A change in silicon morphology from the well known eutectic microstructure was characteristic of all composites. The presence of the reinforcing fibres locally modified the silicon structure, although in regions with no reinforcement the morphology was one with a coarse nature similar to that observed in hypereutectic aluminium-silicon alloys[58]. Similar observations were made by Gallerneault, Higgins and Lloyd[180] in studies on a 12% Si alloy with delta alumina fibres, where they reasoned that the acicular appearance of the silicon resulted from the heterogeneous nucleation of the silicon on residual silica from the binder material, followed by enhanced diffusion growth at the fibres.

Several elements have been proposed as nucleation agents for the silicon, including phosphorus, arsenic, sulphur, selenium and tellurium[59,61,63]. Phosphorus as aluminium phosphide is the element utilized in most commercial alloys to act as a nucleant for the silicon. In the composite it would appear that there was enhanced nucleation and growth at the fibres. The segregation of silicon would appear to be a consequence of two phenomena; (i) the nucleation of the aluminium in the interfibre regions "depositing" silicon rich melt at the fibre regions and (ii) the subsequent enhanced nucleation and growth of silicon at the fibres.

The glass weft, in the N357 composite, was known to contain many elements which could lead to heterogeneous nucleation and subsequent morphological modification of the silicon. No evidence that any of these elements were absorbed from the weft was found.

Indeed, if this had occurred a large number of nucleation sites would be expected which would then result in the formation of a large number of small silicon particles. The sodium in the weft might have been expected to modify the silicon but this was not observed.

The implication is that the modification of the silicon morphology is due mainly to the cooling rate. When slowly cooled the characteristic eutectic morphology of silicon is expected but with more rapid cooling the silicon assumes a coarse structure, which would explain the difference in the silicon morphology away from and at the fibres in the composite. There was slow cooling at the fibres due to their low thermal conductivity and this resulted in the more rounded form of silicon. Alloys which have the modified silicon morphology are known to have improved mechanical properties, although coarse silicon has been shown to embrittle the alloys. To modify the silicon morphology, therefore, sodium and phosphorus are often added to the unreinforced alloy, Das, Prasad, Dan and Rohatgi[156] showed an enhancement in the properties of a particulate reinforced aluminium-silicon alloy. Their work was carried out using low volume fractions of reinforcement and little has been reported concerning high volume fraction fibre composites. It remains to be seen if any such modification of the composite would result in an improvement in properties.

EPMA examination of the material showed that the most common type of intermetallic phase was $FeSiAl_5$ (β). It adopted a plate-like morphology and occurred also in the unreinforced alloy. DSC analysis located an endothermic peak at 576°C which was consistent with the presence of the $FeSiAl_5$ intermetallic. The quantity of intermetallic was greater in the N357 composite suggesting that contamination of the alloy occurred during manufacture of the composite. Wet analysis of the composites confirmed the presence of iron and in some composite sheets chromium and nickel were also found. The contamination was attributed to pick-up in the LMI apparatus, more particularly from the material used for the transfer tube. Those composites which contained chromium, nickel

and iron in levels above the specification for 357 were produced with a stainless steel transfer tube. Later composite sheets produced with a ceramic-lined transfer tube did not suffer from this contamination, although iron was still present as a melt impurity. Early production runs of FP-Borsic/357 composite showed even more iron contamination, and then the size of the DSC endotherm was found to be greater than that for the N357 composite, but this material was produced at a time when a cast iron feeder tube was used and large dross phases were picked up by the melt.

The iron-rich phase formed in 357 would be expected to be β ($FeSiAl_5$) although the non-equilibrium α (Fe_2SiAl_8) might possibly be present. The pseudo-binary phase diagram, figure 4.4 shows the effect that silicon in the alloy will have on the intermetallic phase formed. Above ~7.5% silicon the intermetallic would be the β phase but below this figure the α phase would first form, transforming to β at 884 K. It was difficult to obtain an exact figure for the silicon content of the matrix by wet analysis due to the presence of silicon in the Nicalon fibres, although the nominal silicon content in the 357 alloy was within the range 6.5 to 7.5 %. However, in studies on the same alloy reinforced with alumina fibres, Scott and Yang[54] and Durrant[158] observed the presence of both α and β intermetallic phases. It should be noted that an increase in silicon content would shift the cooling path into the β+Al+Liq phase field, figure 4.4, but that the glass weft, which contains silicon, was not dissolved in the matrix. Thus the glass weft was chemically stable in the metal and an alternative explanation for the presence of only the β intermetallic is required. If then the cooling rate is considered, a slow rate would be expected to form the equilibrium phase, β, but at rapid rates some α phase would be expected which had not transformed via the peritectic reaction to the β. Indeed the fact that Yang and Scott[54] found α and β in contact with one another, figure 4.5, and with a well defined orientation relationship between their lattices, suggests partial transformation. Although the conductivity of the alumina used in the work by Yang and Scott is greater than the Nicalon (38 cf 25 W/mK), this difference would not be expected to alter the cooling rate of the composite appreciably, which would imply that the cooling

rate was little affected by the type of reinforcement.

In the parent alloy the size of the intermetallics was limited to the inter-dendrite dimensions. In the composite the intermetallic extends through aluminium matrix regions to reach dimensions of the order of hundreds of micrometers. As with the silicon morphology the dimensions of the intermetallic phase varied between the composite sheets.

Contamination of the alloy by the chromium results in the formation of intermetallics with a range of compositions. Iron is known to replace the chromium in the lattice of $Cr_4Si_4Al_6$[59] and, if all but a single chromium atom per unit cell is replaced by iron, the weight percentages for each element become chromium 38.7%, iron 10.4%, silicon 20.9%, and aluminium 30%. These values correspond with those measured for the intermetallics in the N357 composite, section 3.1. Those intermetallics which contained nickel tended to be small in size and number and, consequently, were difficult to locate in the TEM for identification. There is, however, the possibility that nickel can form several phases in these composite systems, including $NiAl_3$ and $(FeNi)Al_9$.

The intermetallic phase present in the aluminium-based composite was $FeAl_3$ and this was segregated to the fibre regions. The presence of chromium or nickel was not observed in the N100, but here it was noted that the feeder tube used in producing this composite was ceramic lined. The iron is thought to be a melt pollutant.

EPMA investigation of the Nicalon fibres showed that there were three elements present, these being silicon, carbon and oxygen. Different batches of the Nicalon gave different weight percentages of these elements; the silicon was ~53 wt%, the carbon either ~31 or ~33 wt%, and oxygen ~14 or ~9 wt%. For each batch the total weight percentage was rarely 100 %. One implication, therefore was that some other element was present or that the measurement and/or the correction was inaccurate. Although the EPMA investigation

showed only silicon, carbon and oxygen, the possibility that hydrogen, undetectable by EPMA, may have been present had to be considered. In the DSC experiments, the temperature of the exothermic peak observed for both the N357 composite and the as-received Nicalon, corresponded to that observed using differential thermal analysis (DTA) by Hesegawa[157] for the curing of the polycarbosilane precursor fibre. This indicated that incomplete curing of the polycarbosilane had occurred and that a small amount of hydrogen was still present in the Nicalon fibres. However, this level of hydrogen does not account for the apparent discrepancy in the measured weight percentages, ~6 to 8 wt%. Different ZAF correction factors were also investigated and although the Scott and Love correction is considered to provide more accurate results than that used in the JEOL JXA 8600M, calculated weight percentages of elements were slightly lower, but this may be due to batch variability rather than the correction procedure. For example, the actual numerical value of the ZAF correction factors in each case was very similar and from the JXA 8600M were 1.01 for silicon, 1.01 for carbon and 1.42 for oxygen. The fluorescence factor, F, was unity in all cases, and the major difference (~3 % relative) lay in the absorption factor, which for oxygen was 1.42; the Scott/Love correction gave comparable correction factors, the absorption factor increasing by ~3%. One possibility is that the use of a non-conductive standard (silica) may be affecting the result and this is being further investigated. Another possibility was that the measured x-ray intensities were incorrect, and for this reason the x-ray emission peaks were studied in more detail. In the initial work, the silicon and oxygen x-ray peaks were recorded using analysing crystals which were insensitive to the chemical state, PET and LDE1 respectively. The carbon x-ray peak, however, showed a distinct variation in shape, the Nicalon giving a broader peak than the silicon carbide standard. The calculated peak areas showed a difference of approximately 6 % and whilst this can account for some of the inaccuracies it does not explain fully the discrepancy observed in total weight percentages. This work is being continued, but since the carbon x-ray peak has been shown to depend on the compositional state, the calculation of the k-ratio should be made with peak areas rather than peak heights.

Further investigation of the x-ray emission spectra from various carbon-containing compounds showed profound differences in shape. The difference in x-ray peak shape observed for different species of carbon has been noticed before[159-161], although, it has rarely been used as an aid to the identification of compounds as was carried out in this study. Both the first-order and second-order carbon x-ray peaks indicated that the Nicalon was a mixture of silicon-carbon bonding and free carbon. In addition to the variation in carbon x-ray emission spectra, x-ray emissions from the other elements, present in the Nicalon, were investigated using 'composition sensitive' detection crystals. In the current investigation, the dependence of the shape of the silicon Kβ x-ray emission peak on chemical bonding of the silicon gave evidence that this element was not present entirely as silicon carbide. It was deduced that a proportion of the silicon was bonded with oxygen, but that it was not in the form of silica. Difference in the shape of the oxygen Kα peak from Nicalon and from silica was also indicative of the presence of some other oxygen-containing phase. The possibility thus presented itself that the oxygen was combined as a silicon oxycarbide. Indeed, many structural investigations on Nicalon fibres[14-36] have reported excess carbon and the presence of oxygen and early work such as that by Yajima et al[16], suggested that the oxygen was present as a surface layer. However, as the present investigation and other studies utilizing EPMA have shown, there was an even distribution of oxygen across the fibre and only slight surface enrichment. Moreover, recent work using techniques such as nuclear magnetic resonance (NMR)[28] and x-ray photoelectron spectroscopy (XPS)[35], have suggested the presence of a ternary silicon oxycarbide phase in the form SiO_xC_y. Although the quantitative analysis of the Nicalon is still being investigated to ascertain the exact elemental break-down, the present EPMA data were used to produce an estimate of the composition percentages. The peak shape investigation has shown the probable presence of silicon carbide, a silicon oxycarbide phase and free carbon, and the calculations described in chapter 3 gave the proportions of each of these to be 59-68 wt% silicon carbide, 20-30 wt% silicon oxycarbide and 10-15 wt% free carbon.

The work carried to date indicates also that there was some oxygen enhancement in the surface region of the fibre and that its most probable form is as a silica layer. There was an indication, too, that the silica layer was patchy on the as-received fibres but was more continuous after flame desizing. This is in accord with other studies reporting a thin layer of silica on the surface, typically of thickness ~20nm[14], but which has been shown to thicken with further heat treatment in air[30,31]. The presence of the silica on the fibre surface is particularly pertinent to the interfacial reactions, as will be discussed later in this chapter.

The Nicalon fibres were circular in section with an average diameter of 14.8μm, but ranging widely from <8μm to >30μm. Variations, too in the local volume fraction of fibres were common, resulting from the fabrication route used for the fibre preform. Furthermore, the tendency of the glass weft, when used, to keep the fibres in tows resulted in closely-packed regions of fibre and areas between fibre tows with no reinforcement.

EPMA studies in the SEM revealed the presence of magnesium at the fibre matrix interface but the technique did not identify precisely the position or composition of the phase concerned. Higher resolution work using TEM showed that there was a zone at the fibre/matrix interface which ranged in thickness from 10 nm to 200nm. EDS indicated that the zone was enriched in magnesium and aluminium. Furthermore, the zone gave an electron diffraction ring pattern which corresponded to the β-silicon carbide of the bulk fibre, an observation which would indicate that the magnesium/aluminium was within the fibre. Although the position of the zone was clear, the exact nature of this region could not be ascertained. In aluminium-magnesium alloys it is commonly found[162] that the magnesium segregates to grain boundaries and this may be a contribution to the segregation to the fibre/matrix interface.

The composite sheets which showed higher magnesium content, according to wet analysis, were those which exhibited magnesium segregation at the fibre surface, and the higher the level of magnesium in the matrix alloy, the more marked the effect. For a magnesium zone of 200nm thickness, calculations based on the size of the fibre gave a magnesium content of ~0.6% by volume. The interfacial magnesium would have originally have been in the matrix, since the fact that no magnesium enrichment was found in the regions close to the glass weft removes it as a possible source of magnesium. Within a composite sheet the variation in the magnesium zone thickness was a result of the contact time with the melt. Initially the magnesium in solution in the aluminium component of the matrix would have been in contact with the fibres and thus the magnesium would be able to interact with the fibre. In regions where the silicon or an intermetallic came into contact with the fibre, the time for reaction to occur would be less which would explain the interaction zone thickness being smaller. The most likely situation is that the magnesium reacted with one or both of the oxygen-containing phases. Both the aluminium and the magnesium would be expected to reduce the silica to form their respective oxides by reactions such as:

$SiO_2 + 2Mg \rightarrow 2MgO + Si$ ..... 1.

and $3SiO_2 + 4Al \rightarrow 2Al_2O_3 + 3Si$ 2

The formation of spinels has also been reported, by reaction either with the silica layer or with alumina fibres according to:

$2SiO_2 + 2Al + Mg \rightarrow MgAl_2O_4 + 2Si$ 3

No evidence was obtained indicating that either the simple oxide or spinel oxide had formed in the outer zone of the fibre, despite the fact that the constituent elements were present. Nevertheless, since the magnesium is located within the fibres, even when

aluminium carbide was the interphase and the carbides do not form where the silica occurs, see later, the interaction is believed to be with a bulk fibre phase. The heats of formation for potential reaction products are seen to favour the formation of the spinel since the reaction

$$4Al + 2Mg + 4O_2 \rightarrow 2Al_2MgO_4$$

has a $\Delta G = -3900\ J\ K^{-1}\ mol^{-1}$, whereas the reaction:

$$2Mg + O_2 \rightarrow 2MgO$$

has a $\Delta G = -1020\ J\ K^{-1}Mol^{-1}$. Although both of these reactions involve the gaseous species of oxygen, the relative reactivity is assumed to hold with a solid state reaction via the oxygen in silicon oxycarbide. Girot, Albingre, Quinisset and Naslain[70] produced data on the interface between Nicalon and an Al-Si-Mg alloy, which suggested the formation of the spinel. In addition to magnesium penetration of the fibre a number of other interactions between the aluminium matrix and the Nicalon fibre were observed; these are summarized in figure 4.6.

With regard to the crystals of alumina which were found at the interface, these may have occurred by the reaction of the aluminium in the melt with the silica found to be present on the fibre, as indicated in equation 2. Such a reaction would require the transport of oxygen into the matrix and the dissolution of the liberated silicon in the remaining aluminium phase. Indeed, the formation of alumina has been reported when a silica coating is present but it is not usually found in other composite systems.

Groups of carbide crystals attached to the Nicalon fibre were a common occurrence. They may be formed by reaction with the free carbon or with the β-SiC, as follows

$4Al + 3C \rightarrow Al_4C_3$ ..... 6.

$4Al + 3SiC \rightarrow Al_4C_3 + 3Si$ ..... 7.

The first reaction has been noted in many carbon fibre reinforced composites. Work by Yang and Scott[53] on a composite based upon an aluminium-silicon matrix alloy and made by the LMI production technique, has shown the formation of a large number of carbide crystals where carbon fibre was in contact with aluminium metal, although no such reaction was detected at a fibre/silicon interface. The kinetics of the reaction have been studied by Okura and Motoki[137] for a carbon fibre coated with a pure aluminium, who showed that the formation of the carbide affected the fibre properties adversely, the more extensive the carbide layer the greater being the reduction in fibre strength. These authors found that the growth of the carbide was greater at higher temperatures and, using the data of Okura and Motoki, the parabolic rate constant at 1000 K was deduced to be 8.4×10^{-20} $m^2 sec^{-1}$. For example, the calculated reaction time to form a layer of carbide 100 nm thick would be approximately 16 hours.

The second carbide-forming reaction (reaction 7) is less often observed and many authors[47,55,94,100,123,127,133] find no reaction between the pure silicon carbide and aluminium alloys until temperatures of up to ~970 K are reached. Furthermore, when the silicon content of the alloy was above ~7.2 %, the reaction 4 was reversed to become:

$Al_4C_3 + 3Si \rightarrow 4Al + 3SiC$ ..... 8.

Another possibility is that the aluminium had reacted with the silicon oxycarbide in the

fibre to form the aluminium carbide by a reaction according to:

$$(2x + 4y)Al + 3SiO_xC_y \rightarrow xAl_2O_3 + yAl_4C_3 + 3Si \quad \ldots\ldots\ldots 9.$$

This is, however, considered unlikely since this would produce a number of different reaction products in the same area but this was rarely observed, generally alumina or aluminium carbide being found in isolation. Where both reaction products were found in close proximity, this would have been the result of aluminium reaction with the free carbon to form the carbide and with the silica to form the alumina but in very localized areas. Such interface reactions in the aluminium/Nicalon system have been observed before. Viala, Bosselet, Fortier and Bouix[41] found a reaction zone approximately 2μm thick for a pure aluminium matrix and between 4 and 7μm for an aluminium-14.5%silicon alloy, both zones being formed after 95 hours at 1000K. The morphology of the carbides would also indicate a reaction with the free carbon in the fibres. Yang and Scott[54] have shown similar needle-shaped carbides, figure 4.9, for carbon fibre reinforced 357 alloy, whilst the study by Hughes et al[134], for the formation of aluminium carbide by the aluminium/pure silicon carbide reaction, found a more regular shaped reaction product. Additional evidence that a reaction did not occur between silicon carbide and aluminium was provided by the lack of any small silicon particles, which should have been liberated during reaction and deposited heterogeneously at the interface, as reported by Peteves et al[126]. A further possibility was that a residual carbon layer on the surface, present due to the desizing prior to infiltration, was reacting with the aluminium to form the carbides but no evidence for such a layer was found. It is thus unlikely that either the aluminium/silicon carbide or aluminium/oxycarbide reactions were responsible for the aluminium carbide formation and that it was principally due to the aluminium/free carbon reaction.

An approximation of the reaction time for the present composites can be made by using

the results of Viala et al. These would indicate a reaction rate constant of 5.9×10^{-18} m^2 sec^{-1} for the pure aluminium and 3.65×10^{-17} m^2 sec^{-1} for the Al-14.5 wt%Si alloy at 1000°C; the variation of interfacial reaction product thickness with time being given in figure 4.7. For the alloy, the reaction zone was 100nm thick which, assuming a reaction temperature of 1000 K, gives a reaction time of approximately 2 minutes. This increases to 9 minutes for a zone size of 200nm. Both values are typical for the solidification times in the LMI process. In the alloy composite the aluminium carbide is a metastable phase, due to the presence of silicon in the matrix, reaction 8. The aluminium liberated in this reaction forms further aluminium carbide with the free carbon exposed in the fibre and then further dissolution of the Nicalon takes place. In the pure aluminium matrix composite, however, the aluminium carbide is a stable reaction product which acts as a barrier to further reaction with the fibre, the growth depending on the diffusion of carbon through the aluminium carbide.

As mentioned earlier the reaction rate decreases as the temperature of the reaction is reduced. The curve of Okura and Motoki[137] in figure 4.7 for the variation in parabolic rate constant with temperature would imply that the reaction effectively does not occur at lower temperatures below ~600°C. However, the interface in the heat-treated composite showed an extended reaction zone thickness. This occurred at a temperature of 540°C, and so was due to a solid/solid interaction. Coltters[163], in a review of the thermodynamic data on binary carbides, gave a relationship for the $Al_{(solid)}/C_{(solid)}$ interaction with a $\Delta G^\bullet$ for the formation of Al_4C_3 as -61 ± 3 kJ $mol^{-1}K^{-1}$. For the $Al_{(liq)}/C_{(solid)}$ reaction the thermodynamic relationship results in a $\Delta G^\bullet$ of -58 ± 3 kJ $mol^{-1}K^{-1}$, at ~700°C, showing there was very little difference in the heats of formation of the carbide during the casting and in the heat treatment.

The variability in the type of reaction product formed, either alumina or carbide, is thought to be due to the patchy nature of the silica on the Nicalon surface. Hughes et al[134] showed that when silica layers of thickness approximately 5nm on pure silicon carbide

were present, the only reaction product formed was alumina and/or alumino-silicates.

In certain non specific areas phases were found that had not formed by reaction between Nicalon and matrix components. The first example of this was a phase which showed a spinel type structure, the exact composition of these phases varied from that of $MgAl_2O_4$ to a similar phase which contained some additions of silicon. These were observed at, or close to, the fibre surface and usually of a typical dimension of 200nm square. There was no observable interaction, between the fibre and these phases. The implication was that they were deposited at the interface rather than the result of some reaction with the reinforcement. Further evidence of a deposition of phases at the interface was provided by the presence at the interfacial region of material which clearly came from the glass weft. The amorphous structure and presence of calcium, magnesium, oxygen and silicon corresponds very closely with the weft composition. Both these deposited phases would have been formed and/or transported from elsewhere in the fibre. The melt front carried them until they were arrested by the fibres, the remaining melt then solidifying around them; this is shown schematically in figure 4.10. The implication from the structure of the deposited phases is that the majority of the glass weft material remains in the fibres; however, some is ablated by the passing melt and transported physically to a position at the interface with the fibres. Most of this deposited weft material retains the morphology of its source but some is 'smeared-out' at the interface to form a very thin layer. A chemical interaction may occur to form the spinel type phase, it is possible that the surface oxide present on the molten aluminium reacts with the magnesium, in solution, to form the spinel. These smeared and bulk deposited phases explain the apparently high levels of magnesium segregation observed in many of the composites sheets in EPMA.

Apart from its good casting characteristics, another reason why 357 alloy was selected was its potential for age hardening to increase its hardness and yield strength. In particular, it was hoped that this would be beneficial in the improving transverse strength of the composite. Unfortunately the benefits of ageing were not realized in the N357

composite because Mg_2Si precipitates, responsible for the ageing response, did not form. Indeed, as discussed above, the magnesium was shown to segregate to the first 100nm of the Nicalon fibre. In the alumina-Borsic reinforced 357 composite there was, however, a small ageing peak but this was found to form in a shorter time. Such accelerated aging is often observed in MMCs[56,164-168] and is attributed to an increased number of nucleation sites such as interfaces or dislocations for the precipitate phase. The presence of a high density of dislocations in the composites, due to thermal contraction difference between fibre and matrix[165], can act as a hardening mechanism as well as a nucleation site for precipitates. In this connection Bhanu Prasad, Prasad, Kuruvilla, Pandey, Bhat and Mahajan[166], in work on a non age hardening Al-Mg alloy found an increased matrix hardness which was attributed to the heterogeneous nucleation of magnesium phases at the dislocations. Unfortunately, because of the complicated nature of the fibre distribution in the F357 composite, the effect of matrix strength on the transverse strength of the composite could not be evaluated. It should, however, be remarked that where MMCs are required for use at elevated temperature, there would be little advantage in utilizing an alloy with a metastable phase since the precipitate would coarsen prematurely and the composite become embrittled.

4.2. Effect of Microstructure on Mechanical Properties.

As was stated in the introduction, section 1.5, the tensile strength of a composite in the longitudinal orientation may be estimated using the rule of mixtures (ROM) which is of the form

$$\sigma_c=\sigma_f V_f + \sigma_m(1-V_f) \quad \text{..... equation 4.1.}$$

where σ_c, σ_f, and σ_m are stresses in composite, fibre and matrix respectively and V_f is

the volume fraction of the fibre and the response of the composite during straining is thus:

$\sigma_{c\varepsilon} = \sigma_{f\varepsilon} V_f + \sigma_{m\varepsilon}(1-V_f)$ ..... *equation 4.2.*

where $\sigma_{c\varepsilon}$, $\sigma_{f\varepsilon}$ and $\sigma_{m\varepsilon}$ are the stress levels at a given strain ε. The stress levels at a given strain, $\sigma_{m\varepsilon}$, for the matrix were taken from the measured stress strain curve, see section 3.2.3, these were used with the fibre properties obtained by assuming that quoted strength and stiffness values were correct for the Nicalon fibres, 2.0 GPa and 200 GPa. The stress strain curve calculated using equation 4.2, is given in figure 4.11, the failure point being ~1.4GPa at 1.0 % strain.

However, as discussed in section 3.3 the mechanical performance of the fibre depended upon its condition, and brittle materials such as silicon carbide are known to have strengths which follow a Weibull probability distribution (WPD). The WPD is a relationship which describes the distribution of flaws within a fibre volume, V, the volume being related to the length, L, by $V=\pi r^2 L$ where r is the fibre radius. The distribution may be represented by the relationship:

$P_f = 1 - exp[-V.(\sigma/\sigma_o)^m]$.....*equation 4.3.*

where P_f is the probability of failure, V is the sample volume loaded at a stress σ, and m is the Weibull modulus; the term σ_o represents a correction factor for the material in question. The equation has been expressed also in the form[158]:

$P_f = 1 - exp[-\alpha.l.\sigma^m]$ ..... *equation 4.4.*

where $\alpha = A/\sigma_o^m$ is a constant for a given fibre cross-sectional area A and l is the sample gauge length.

P_f may be estimated from:

$$P_f = \frac{n}{N_t+1} \qquad \text{.....equation 4.5.}$$

where N_t is the total number of specimens and n the strength ranked number of the specimen. The relationship may be re-written in the following form:

$$\ln\ln[1/(1-P_f)] = m.\ln\sigma - \ln[\alpha.l] \qquad \text{.....equation 4.6.}$$

The Weibull modulus, m, and α may be found from the gradient and intercept of the straight line, respectively. The value of m gives a measure of the scatter of the distribution, and the higher the value of m the less will be the amount of scatter. The fibre properties in a chemically reactive system, such as the aluminium/Nicalon composite, can however be expected to change. Values of m calculated for each set of results gave the curves in figure 4.12. The amount of scatter measured varied little between each set and the values of m are shown in table 4.1, as obtained from regression analysis of the curves. These Weibull shape factors have been shown to vary with the gauge length used in the fibre testing and indeed the type of Nicalon fibre. Bunsell and Simon[9] quote values which range from 2.2 to 3.6 for m and report that the Nicalon fibre type NLM 202 which was used in the present study gave some of the best properties. The above calculations do not, however, take into account the diameter variation of the fibres and a more rigorous form of equation 4.6 would be:

$$\ln\ln[1/(1-P_f)] = m.\ln\sigma - \ln A - \ln[l/\sigma_0^m] \qquad \text{.....equation 4.7.}$$

This was used for a set of the fibres from the 'bobbin' to produce the curve shown in figure 4.13, m was the same as that found using equation 4.6 and so the area correction was not necessary.

Using the mean value of σ_f to obtain an approximate value for the strength of the composite gave the values in qfigure 4.14 and summarized in table 4.2; this assumed that the fibre modulus was retained. Thus the calculated composite strength was found to be greater than that measured experimentally although the use of actual fibre strengths gives lower predicted values for the composites. However, no account of the fibre strength distribution has been taken.

The spatial distribution of the fibres in the composite also affected the strength since the statistical nature of the flaw distribution in fibres caused some to fail at a low load. The remaining unfailed fibres then shared an increased stress. Thus there may be a level of load where if one more fibre fails then the whole bundle will fail. Using the equation for the bundle strength, σ_b[88,89],

$$\sigma_b = (m\alpha)^{-1/m} \exp[-1/m] \qquad \text{..... equation 4.8}$$

and the ratio of bundle strength to mean strength ($\bar{\sigma}_f$) as:

$$\frac{\sigma_b}{\bar{\sigma}_f} = \frac{(m\alpha)^{-1/m} \exp[-1/m]}{[(\ln 2)/\alpha]^{1/m}} = (1.8884m)^{-1/m} \qquad \text{.....equation 4.9}$$

gave for the Nicalon fibres a bundle strength of ~0.56 of the mean fibre strength, a fibre bundle strength of 862MPa and a composite strength (based on ROM) of 410MPa. These values were based upon the strength of fibres from the as-received population and a volume fraction of fibres of 42%. If, however, the strength distribution of fibres extracted from the N357 composite was used the bundle strength became 235MPa and the composite strength 130 MPa. The matrix stress at the fibre failure strain was taken to be ~0.1% for this calculation.

Although a broken fibre in the dry bundle may no longer contribute to the load-bearing capability, a broken fibre in a composite would be expected to retain some load-carrying capability. Thus the ends of the broken fibre, corresponding to the ineffective length (δ), would have a decreased ability to carry stress, but beyond that distance from the ends the fibre could support a share of the applied load, (figure 1.16)

For infiltrated fibre bundles there will be a number of fibre breaks throughout the composite as the load is applied. The first fibre failure may result in catastrophic failure if the value of m is large and the scatter in fibre strengths is small. The redistribution of load may then be sufficient to break the neighbouring fibres, a process which will be repeated as the load is increased and, consequently, the section rapidly loses the ability to carry the load. Where there is a wide distribution of fibre strengths the failure process differs. The local redistribution of load about a failed fibre is unlikely to coincide with a weak point in the fibre and more scattered breaks occur and accumulate. Again the local fibres are required to carry an increased tensile stress and a localized shear stress concentration may develop which can lead to interfacial failure or to matrix yielding. An approximation of the failure stress of the first overloaded fibre has been proposed by Zweben[171] as:

$$\sigma_1 = \beta.[4.N.l.\delta.(k^m-1)]^{-1/2m} \qquad \text{..... equation 4.10}$$

where N is the number of filaments, l is the strand length, $\beta = \alpha^{-1/m}$ and k is a fibre tensile stress intensity factor for the array of fibres (1.146 for a square array); δ, the ineffective length, is given by:

$$\delta = D.[(V_f^{-1/2}-1).E_f/2.G_m]^{1/2} \qquad \text{..... equation 4.11}$$

where G_m is the shear modulus of the matrix and D is the fibre diameter.

For Nicalon-reinforced aluminium the value for the ineffective length was calculated to be

~21μm. This gives a first overloaded stress of ~710MPa using data for as-received fibres and ~180MPa for fibres extracted from the alloy composite. The values were calculated using β values obtained from the WPD intercept, E_f= 200GPa, G_m= 28GPa and N was estimated from the specimen cross sectional area as $6x10^4$ fibres, the gauge length was 30mm, and m taken from the relevant WPD, see table 4.1. If this fibre failure is assumed to result in composite fracture, the composite strength can be deduced from the ROM, the value for the as-received fibre based composite would be ~340MPa and the value based on the extracted fibres would be ~100MPa. This implies that there was some damage tolerance in the composite although only a small number of fibres will result in the total loss of strength.

If the fibre is considered as a brittle material containing a flaw of depth, a_f, the fracture behaviour may be related to the strength using knowledge of the fracture toughness of the fibre material in question. For bulk silicon carbide the fracture tougthness (K_{IC}) is $3MNmm^{-3/2}$. The following equation was used to calculated the flaw size responsible for the fibre failure:

$$K_{IC} = Y.\sigma.(\pi.a_f)^{1/2} \qquad \text{..... equation 4.12}$$

where Y is a geometrical factor, (1.12), σ is the failure strength of the fibre and a_f is the corresponding critical crack dimension. Calculations were performed using the mean fibre strengths measured for each set of fibres and the results are shown in figure 4.16. This shows that the predicted flaw size responsible for the fibre failure was often greater than the fibre diameter (15 μm), which is clearly not possible. It could be said, however, that the as-received fibre failure was due to the population of intrinsic flaws produced during manufacture, whilst the fibres taken from the preform possessed additional flaws due to the mechanical damage incurred whilst handling. The mechanical damage can account for some of the fall in strength of the fibres extracted from the composite, but not all.

To explain this apparent discrepancy the microstructure of the composite was considered. Figure 4.17 shows that as the thickness of the interface reaction product increased the fibre strength decreased. A similar trend was observed in the measured composite strength, although these were taken from three sets of tests. The curve shows both the as-received fibre strengths and the strength of the fibres extracted from the uninfiltrated preform, both of which gave a greater fibre strength than those fibres extracted from the composites. The variation in the reaction product thickness alone does not explain the reduction in strength of the fibres, if, however, we assume that the interface reaction product can be considered a stress enhancing mechanism further analysis may be made. For the as-cast N357 a typical size of the aluminium carbide is 250nm by 24nm. Using the simple Inglis relationship:

$$\sigma_{max} = k.\sigma = 2.\sigma.[a/\rho]^{1/2} \qquad \text{..... equation 4.13}$$

where σ_{max} is the stress at the tip of the feature with a length a and radius ρ, and taking an apparent load of 420 MPa giving a crack tip stress of ~2.7GPa. A similar calculation for the N100 material, with a mean fibre strength of 760MPa and where typical carbide lengths are ~70 nm, gave a value of ~2.8GPa. These values are close to the strengths measured for the as-received fibres. The calculated stress intensity factor, k, was 6.45.

Fractography of the composite showed that the intermetallic phases were often associated with the fracture, the failure initiating in the intermetallic and then passing to the fibre. If it is then assumed that the failure strain in the intermetallic is below that of the fibre, the intermetallic acting as a large matrix flaw, fracture mechanics can again be used to investigate fibre failure. The equation may be written in the form:

$$\sigma_f = K_{IC}/[1.06.\pi.c]^{1/2} \qquad \text{..... equation 4.14}$$

where c is the interphase zone size. The variation in the fibre strength and the composite

failure stress calculated using the equation is illustrated in figure 4.18. The curve makes no distinction between the type of brittle phase and the same analysis could be used for the Al_4C_3 and Al_2O_3. Below a value of interphase thickness of c_1 the fibre strength will be dependent on the intrinsic flaws and independent of the interface zone size. Above c_1 the failure is determined by the size of the interface phase zone and in the case of Al_4C_3 the stress concentration effect gave an apparent thickness of ~8μm. Consequentially up to a c value of 8μm the fracture may be due to either the carbide or the intermetallic but at higher values the intermetallics would control the initiation. For a continuous interphase there would be a critical thickness where the composite failure strength is dependent upon the failure strain of the interphase, $\sigma_c=\varepsilon_b E_c$. However, if the second phase is discontinuous, as is usually the case, this would not be so, although the loss of matrix strength would then be important. Additional factors would require consideration, these include any stress enhancement, the bond between the phase and the fibre and the orientation of the phase to the loading direction. Further evidence of the involvement of intermetallics in the fracture of the MMC is given by the fracture surface of the alumina/Borsic hybrid composite. The presence of extensive intermetallics resulted in the fracture of the alumina fibres and the same intermetallic could act as an initiation site for several fibres. It is possible also that the iron-rich intermetallics and other matrix phases act as flaws in the matrix; these then fail prematurely leading to an increased stress on the fibres due to loss of section area of the matrix.

The above analysis considered only the initiation of fibre and composite fracture. The propagation of the failure is important in determining the strength of the composite. Fracture initiation in the longitudinal orientation of the composite in tension is very dependent on the strength of the fibre. The measured composite tensile strength was within 1% of the predicted "bundle theory" value, the implication being that only very few fibre breaks are needed to produce complete failure of the N357 composite. Acoustic emission data are in accord with this. The count rate was shown to be low until a time very close to the failure point when a considerable number of events occurred in a small

increment of strain.

The fibre strength is strongly influenced by the method of incorporating fibres into the composite due, in turn the deterioration of the fibre properties caused by interfacial reactions. Whether the presence of the alumina or aluminium carbide is more severe is not clear since both probably contribute to the fracture. It would also appear that the magnesium/aluminium interaction zone in the outer surface regions of the fibre has some effect on the fibre fracture and in section 3.2 it was shown that the surface of the fibre can fail preferentially to the bulk. The initiation of the composite fracture is dependent on the fibre strength, which in turn is controlled by the interface phase or phases. Thus, the presence of the interfacial reaction product and intermetallics both contribute to the initiation, the silicon phases were shown to fracture from the fibres during TEM specimen preparation, it is likely therefore that they also cause premature failure. Schamm, Le Petitcorps and Naslain[172], have measured the strength of Nicalon fibres where a interfacial reaction has been enhanced by application of a wetting process with K_2ZrF_6; the interfacial product formed was deemed responsible for the loss in fibre strength observed.

Normally the matrix would be expected to redistribute the load after first fibre failure but if, as in this example, the matrix contained a large number of interlocked brittle phases, the fracture is likely to be catastrophic. Such embrittlement can arise in unreinforced alloys when second phases are present. For example Ritter and Briant[173] have shown that there is void formation around large iron- and silicon-rich inclusions resulting from the cracking of these particles. The larger inclusions are those which form voids first and these are therefore more deleterious. Subsequent failure would then depend on the ability of the surrounding aluminium to yield and thereby resist void coalescence. A large number of void nucleation sites are available in the composite and in section 3.2 it was shown that microvoiding occurred at silicon particles and that the fracture path through the matrix-rich regions was associated with their fracture. Such micro-voids may coalesce and

lead to crack propagation. The fracture of particulate and whisker reinforced MMCs is often explained in terms of void formation and coalescence[83,116,173,174]; the formation of these voids is attributed[174] to the localized plastic deformation at stress concentrations such as sharp corners of whiskers. Both the silicon and the intermetallics are very angular and a similar process of stress concentration-void formation is thought to occur in the present composite matrix areas. The weft material, both the glass in the N357 and the titanium in the F357, influenced the fracture path. The glass fibres were often not infiltrated with matrix and thus had no load bearing ability.

As a result of the brittle nature a Weibull probability distribution may be used to characterise the composite. Figure 4.19 shows the curves for longitudinal and transverse fibre orientations, It may be seen that the transverse failure stress has a larger scatter than the longitudinal failure stress, as expressed by the smaller *m* value, although it may be argued that there are too few test results to provide a rigorous Weibull analysis of the composite.

Much of the above analysis of the alloy composite may be applied to the composite based upon commercially pure aluminium (N100). Using the as-received fibre strength and measured matrix strength and applying the ROM gives a composite strength of 670MPa. This is not appreciably different from the alloy composite as the fibre properties dominate the approximation. However, if the measured strengths for fibres extracted from the N100 composite are used as the ROM value becomes 335MPa. These results are summarized in table 4.3.

The bundle strength is again calculated to be ~0.56 of the mean fibre strength. Since fibres extracted from the composite gave a mean strength of 740 MPa, the calculated bundle strength is 416 MPa. The corresponding fibre failure strain was 0.21% (E_f=200GPa), at which strain the pure aluminium stress (σ^*) was 26 MPa and thus the expected composite strength would be 194 MPa.

Using the first overloaded fibre failure approach the value of σ_1 was calculated to be 360 MPa and the corresponding composite strength to be 170 MPa. The calculations utilize the WPD functions for measured from fibre population and matrix properties. The higher observed mechanical strengths in the N100 composites may be thus explained in terms of the strength of the fibres.

Although the fibre distribution in the N100f composite was improved there were still areas of local high packing density. These fibres were still linked by brittle intermetallics which although small in dimensions could cause fracture of the fibres.

4.3. Factors Controlling the Interfacial Bond

The bond strength between the fibre and the matrix is of prime importance for the control of the composite properties. Fractographic studies of test specimens of all geometries have shown that the bond between fibre and matrix is strong, the transverse fibre orientation specimens showing preferential fibre splitting rather than interfacial failure. The shear tests rarely failed in shear and when they did it was as a result of a large amount of porosity. The best indicator of the bond strength was provided by the fibre/matrix interfacial shear tests, despite the reservations about the applicability of the technique to composites with a strong fibre/matrix bond and a plastic matrix. In the alloy-based composite the bond was found to be at least 3 times that in the pure aluminium material (58 ± 41 MPa and 12 ± 5 MPa respectively). However, both these represent a strong bond and are much greater than a non-reactive system, Bleay and Scott[175] have shown that for a Nicalon fibre/glass matrix composite the fibre/matrix interfacial shear strength is ~3MPa, measured in the same manner. The high bond strength is attributed to the reaction at the aluminium/Nicalon interface. In the study by Li, Arsenault and Jena[176] the Al/SiC bond is concluded to be stronger than the Al/Al bond which would indicate a very strong bond is formed in these composites between aluminium and silicon carbide as well

as the reactive aluminium/carbon interface.

Even allowing for the deformation of the matrix, the results are considered to provide a comparative measure of the bond strength in the composites, if not an absolute quantity. The interfacial shear strength here, is considered to be a combination of factors. These include the contribution from fracture of the fibre-matrix bond, interfacial sliding, and matrix deformation, figure 4.19. In certain fibres the bond does not fail, as evidenced in examples where either the fibre shatters or gross matrix deformation occurs. This means that the calculated value is lower than the actual bond strength. Since the measured deflection of the fibre is partly dependent on the matrix deformation, any comparison between interfacial bond strengths must take into account any difference in the yield stress of the matrix. If the difference is large it is likely to affect the measured result. In the composites used in this investigation the hardness of the aluminium dendrites was similar for both the N357 and the N100 (~38 Hv), and so the bond strength is considered a fair comparison for fibres isolated in the aluminium matrix constituent.

The bond is associated with the interface reaction, the second phases on the fibre surface and mechanical interlocking between matrix and fibre. The reaction zone size will only affect the interface strength when it becomes so large as to fail preferentially. The major difference between the N357 and N100 composites then becomes the presence of second phases and the diffion of magnesium into the fibre. In the pure aluminium only small 1-2 μm intermetallics are present on the fibres, whereas in the alloy composite a large number of silicon and intermetallic particles exist. These are seen (section 3.3) to be still be bonded to the fibre in the post-indented specimens. The usual case is that the matrix deforms or the second phase fails and therefore the volume of material associated with the indentation in the alloy composite is much larger than the N100 composite; this is shown schematically in figure 4.20.

In the heat treated alloy composite the measured bond strength is lower, the fibre/matrix

shear strength was ~36MPa; this is thought to be due to an enhanced interface reaction. The fibre failure noted during indentation would be due to a strong bond and preferential failure of the interphase, which in turn results in fracture of the fibre. The shear tests carried out on the composites showed that where the fibre/matrix bond existed the fibres failed rather than the bond.

4.4. Importance of Test geometry on Measured Strength.

For any material to be utilized it is necessary that the properties can be characterised with confidence and ideally a single strength or stiffness quoted and used in design criteria. The flexural strength was higher than the tensile strength, ~340MPa compared with ~130MPa, for the N357 composite. However, this was only for one geometry of flexural test bar and the strength was shown to vary depending on the geometry used. The worst case resulted in the measured flexural strength being below the tensile value, at 116MPa. The next section attempts to account for this discrepancy by investigating the statistical nature of the composite failure.

Simple relationships based on the dimensions of the bar do not explain the variation in the strength. The strengths were compared with the interspan area and no obvious dependence or trend found, figure 4.21. If the distribution of fibres is considered to be even through the sheet it is possible to consider a series of plies of single fibre depth equally distributed through the bar. Simple beam theory then would consider the maximum stress to be in the outer 'layer' (usually termed 'fibre', but this is thought confusing in the context of a composite). If the effective stressed volume of the outer layer is simply considered to have the same depth in each geometry, the relationship with the strength will be as that found for the inter-span area.

The tensile tests showed that the strength of the composite followed a Weibull probability distribution. If each of the layers was assumed to follow the same Weibull distribution

further analysis was made to find an effective geometrical dependence for the strength in flexural tests. The basic WPD for failure is given in the following form:

$$P_f = 1 - exp[-V.(\sigma/\sigma_0)^m]$$

If for the bend tests it is assumed that the composite has the same WPD as the tensile tests, so that $m = 6.11$ and $1/\sigma_0 = 9.39 \times 10^{-14}$, there may be considered some volume of material V which is associated with the fracture of the composite. This is assumed to be:

$$V = b.l.a_1$$

where a_1 is the apparent depth associated with fracture. This may approximated by assigning a probability of failure. If the mean strength value, $P_f = 0.5$, is used the variation in a_1 calculated is as shown in figure 4.22 for the experimental test results. This shows that the failure associated depth varies with the geometry of the bar.

The stress distribution through the bar is given by the relationship:

$$\sigma_y = 2.F_{max}.L.y/b.d^3$$

where y is the distance from the neutral axis of the test bar. This is calculated for each bar dimension and if the composite is assumed to act as a homogeneous material, the variation will be as given by the straight line in figure 4.23. As the composite follows a WPD it is possible to assign a failure probability through the depth of the bar, figure 4.23. These curves show that for geometry A and C the probability distribution varies from zero at the neutral axis to near unity at the surface; however, geometry B shows that the probability of failure only reached ~80%. In the investigation by Goda and Fukunaga[107] a separate Weibull parameter was ascribed to a certain type of flaw, and the composite was then described in terms of tri-modal Weibull distribution with parameters, m_1, m_2 and

m_3. A similar analysis is used to characterise hybrid composites such as the study by Kortschot and Beaumont[177]. It may be that in the different geometries different sets of flaws are responsible for the fracture of the composite; in geometry B the contribution of surface flaws may be greater but superimposed upon a set associated with the intermetallics or some other peculiarity. Since, in the present composites there were numerous flaws, which have been shown to contribute to the fracture, it is not clear which were responsible and further investigations are required before any conclusions can be drawn about the composite fracture in different geometries.

The comparison of the glass weft orientation related to the strength is now more complicated. The difference in the strength of the composite with the weft in-plane or through-depth is not sufficient to conclude that the weft does have an effect on the initiation of fracture. It has been shown that the fracture in the tensile tests initiates at the fibres and intermetallics and this is thought to be the case in the Flexural tests as well. Additionally the fracture surfaces of those specimens which failed in flexural tests, suggest that the glass weft did contribute to the initiation and propagation of the fracture.

CHAPTER 5. CONCLUDING REMARKS.

With the exception of the elastic modulus the mechanical properties of the composites were extremely disapointing. The longitudinal strength of the composite, in tension, was measured at ~10% of the predicted values by the rule of mixtures, indeed the figure of 130 MPa was not much improved on the strength of the unreinforced alloy, ~80 MPa. Even taking the most extreme case of the first fibre failure leading to complete composite failure over-estimates the strength. The present study has explained the poor mechanical performance in terms of the components and principally in relation to the microstructure which results from the interaction between them. Furthermore, the microstructure was shown to be the result of a specific set of fabrication parameters.

The quality of infiltration of the preforms was variable and although the majority of the fibres were well infiltrated, the close packing of tows resulted in localised porosity. The fact that the fibres were held in tightly packed tows by a glass weft used in preform manufacture, contributed to much fibre/fibre contact. Furthermore, phases derived from the glass weft were found to be carried to and trapped by the the fibre mass, where they then acted to hinder further penetration of the melt. Porosity was formed also by premature solidification of the melt front, an effect which was especially pronounced in the Nicalon-aluminium composite, where large volumes of material were not infiltrated. Such lack of infiltration will clearly provide large flaws in the composite with the reduction of bonded fibre/matrix and transverse loading areas.

A practical solution to improve the infiltration would appear to be to hold the metal at infiltration temperature for a longer time, until full infiltration had occurred, and then

allow the composite to solidify. However, it was found that even for the relatively short periods of time used to infiltrate the present composites, there was reaction between the Nicalon and aluminium. This would be undesirable to say the least.

The Nicalon fibre was shown, using EPMA studies, not to be a pure β-silicon carbide fibre but to contain a ternary Si-O-C phase and free carbon, typically in the proportions ~63 wt%, SiC, ~22 wt% silicon oxycarbide and ~15 wt% free carbon. These were obtained by carrying out a detailed analysis of the effects on soft x-ray emission spectra of chemical bonding. An enriched oxygen surface zone, which was thought to be silica rich, was observed but only on some fibres. It was found that the use of the x-ray peak intensity gave an underestimation of the carbon content; the utilization of the area of the characteristic x-ray emission peak improved the calculated results.

The molten aluminium reacts with the silicon carbide and free carbon in the Nicalon fibre to form aluminium carbide, Al_4C_3, according to:

$$4Al + 3C \rightarrow Al_4C_3$$
$$4Al + 3SiC \rightarrow Al_4C_3 + 3Si.$$

In the presence of silicon the latter reaction did not occur and the aluminium carbide was formed by the carbon reaction only. The reaction product in the alloy based composite is thus a metastable phase and the fibre continues to degrade with time at the elevated temperature. In the pure aluminium composite the carbide reaction forms by these reactions, but the phase was now stable. In the alloy composite a second reaction

occurred. This concerned the formation of alumina, Al_2O_3, by chemical reaction between the aluminium and the silica associated with the fibre.

As the extent of the interphase reaction increased the fibre strength and the composite strength decreased. The characteristic of the interfacial reaction has a bearing on the use of the composite at elevated temperatures, since if such a temperature was maintained for a prolonged time the interphase thickness will become excessive and gross deterioration of fibre properties result. As it is the fibre properties which control the composite behaviour it is paramount to control these interfacial reactions. Indeed it would be the situation with a gross interphase that embrittlement of the aluminium matrix would occur.

In addition to the matrix/fibre interphase, larger intermetallics phases in the matrix also resulted in the fibre fracture. Indeed, this was the main fracture process in the composite containing FP alumina. In this material little fibre/matrix interaction occurred but the intermetallics were commonly >200μm in length. The intermetallics were usually of the $FeSiAl_5$ type and resulted from contamination of the melt during infiltration. They formed a three-dimensional network with the silicon particles in the matrix to provide an easy path for the fracture to occur and some evidence of them failing ahead of the main fracture was found. The intermetallics in the aluminium-based composite were less extensive and bridged between fibres only when they were tightly packed. These intermetallics were $FeAl_3$.

The silicon and the intermetallic particles were formed ahead of the solidification front, resulting in preferential deposition in the fibre regions. The coarseness of the silicon and

intermetallics was due to the relatively slow cooling of the infiltrated composite.

An age-hardening alloy was used for the matrix because of the potential enhancement in transverse strength produced by the precipitation of Mg_2Si. However, fine-scale precipitates were not formed, and the magnesium was found to be present in the first 100-200 nm of the Nicalon, whether the composite was heat treated or not. The FP alumina reinforced composite showed a slight segregation of the magnesium to the interface between fibre and aluminium, but peak hardness was produced in a shorter time than in the unreinforced alloy. This accelerated ageing is thought to be due to enhanced heterogeneous nucleation in the composite compared with the unreinforced matrix. However, the use of an alloy that requires the formation of a thermally metastable precipitate to increase the transverse properties of the FRM will be beneficial only for room temperature applications. For elevated temperature applications a stable precipitate would be required, one such example being Al_3Ti formed by additions of titanium.

It is difficult to see where improvements could be made in the fabrication parameters since, despite the infiltration being incomplete, appreciable fibre/matrix reaction had nevertheless occurred. The application of some coating may aleviate the problem but this remedy would increase the cost of an already expensive reinforcement. Alternatively the use of an alloy which has a lower liquidus temperature may be beneficial, such as the aluminium-magnesium system which has a eutectic at 450°C.

The network silicon and intermetallics phases were influenced by the cooling rate and in

the present work resulted in a coarse structure. A more fracture-resistant form would be one which contains small evenly distributed particles. Quenching is a possible way of achieving this matrix structure but such treatment may cause fibre failure or high residual stresses due to differential contraction of fibre and matrix. The problem may also be alleviated by making additions to the alloy to promote nucleation sites. Furthermore, the deposited phases could be avoided by the use of preforming techniques which did not apply introduced additional constituents.

The glass weft acted as an easy path for failure and kept the fibres closely packed, both of which were undesirable. Filament winding was found to improve the distribution of fibres but because of the high volume fraction a large amount of contact between fibres still was present. A lower volume fraction of reinforcement, whilst theoretically giving poorer mechanical properties, may be worthwhile if improved infiltration can be achieved at a lower temperature together with a shorter solidification time to reduce detrimental fibre/matrix reactions.

There is clearly wide scope for further investigations into the relationships between manufacturing method, microstructure and properties of the composite. In particular, the deterioration of fibre properties with casting variables, such as the exposure time at elevated temperature, needs study, especially for the reinforcements which are reactive with the metal matrix. Control of the matrix chemistry to suppress the interfacial reaction may offer a route to achieve the desired bond between fibre and matrix and so realize the potentially good mechanical properties of the MMCs. Furthermore, since the mechanical properties of the MMC at elevated temperature will be affected by the growth of interphases, mechanical tests as well as structural examination need to be investigated at temperatures above ambient.

Finally, it is argued that the use of a lower volume fraction of more evenly distributed fibres may be benificial with regard to composite strength since the prospects of improved infiltration and the associated decrease in porosity may more than compensate for lose in potential reinforcement.

ACKNOWLEDGEMENTS

I am very grateful for the help and advice I have received from Prof. V.D. Scott during this work. In addition I would like to thank Mr R.L Trumper at A.R.E. Holton Heath for guidance and supply of materials.

The Science and Engineering Research Council provided the funds for my studentship and the electron optics equipment used in the work.

Finally, I acknowledge the help and support of members of the School of Materials Science at the University of Bath during the period I have been there.

REFERENCES

1. Feest,E.A. "Exploitation of the metal matrix composite concept." *Metals and Materials. May 1988 PP. 273-278.*

2. Dermarkar,S. "Metal matrix composites." *ibid. March 1986 PP. 144-146*

3. Trumper,R.L. "Metal matrix composites-applications and prospects." *ibid. Nov.1987 PP. 662-667*

4 "Metal matrix composites." *C.T.Lynch and J.R.Kershaw, Chemical Rubber Company 1972.*

5 "Composite materials vol.1 : Interfaces in Metal matrix composites." *Metcalfe,A.G. Ed., Academic Press 1974*

6 "Composite materials vol.4: Metallic matrix composites." *Kreider,K.G. Ed., Academic Press 1974*

7 Kreider,K.G. "Mechanical testing of metal matrix composites" *Composite materials: Testing and design, ASTM STP 460, 1969 pp. 203-214.*

8 Prewo,K. and McCarthy,G. "Interfacial characteristics of silicon carbide-coated boron-reinforced aluminium matrix composites." *J.Mater.Sci. 7 (1972) pp. 919-928*

9 Dhingra,A.K. "Alumina fibre FP." *Phil. Trans. R. Soc. Lond. A. 294, pp. 411-417 (1980).*

10 *Aluminium alloys- Contemporary research and applications. Treatise on Materials Science and Technology vol 31 eds. A.K. Vasudevan and R.D.Doherty. Acedemic Press (1989)*

11 Dhingra,A.K. "Metal matrix composites reinforced with fibre FP (α-Al2O3)."*Phil. Trans. R. Soc. Lond. A. 294. pp. 559-564 (1980).*

12 Mittnick,M "Continuous SiC fibre reinforced metals" *Developments in the science and technology of composite materials. Proc.Forth.Euro.Conf.Comp.Mater. Stuttgart FRG. Elsevier, Sept 1990 pp. 325-338.*

13 Champion,A.R., Krueger,W.H., Hartmann,H.S. and Dhingra,A.K. "Fibre FP reinforced metal matrix composites." *ICCC 2. pp. 883-906*

14 Bunsell,A.R., Simon,G., Abe,Y. and Akiyama,M. "Ceramic fibres" *Composite Materials Series, 2. Fibre reinforcements for composite materials. ed. A.R.Bunsell. Elsevier.* pp **427-478**

15 Handbook of composites: Strong fibres. vol 1 eds. W.Watt and B.V.Perov. Elsevier Science

16 Yajima,S., Okamura,K., Tanaka,J. and Hayase,T. "Synthesis of aluminium composite with continuous SiC fibre obtained from the precursor fibre of an organosilicon polymer." *J.Mater.Sci.Let. 15 (1980) pp. 2130-2131.*

17 Yajima,S. "Development of ceramic, especially silicon carbide fibres, from organosilicon polymers by heat treatment." *Phil. Trans. R. Soc. Lond. A 294 (1980) pp. 419-426.*

18 Soraru,G.D., Babonneau.F. and Mackenzie.J.D. "Structural evaluations from polycarbosilane to SiC ceramic." *J.Mater.Sci. 25 (1990) pp 3886-3893.*

19 Simon,G. and Bunsell,A.R. "Mechanical and structural characterization of Nicalon silicon carbide fibre." *J.Mater.Sci. 19 (1984) pp 3649-3657.*

20 Simon,G. and Bunsell,A.R. "Creep behaviour and structural characterisation at high temperatures of Nicalon SiC fibres." *J.Mater.Sci. 19 (1984) pp 3658-3670.*

21 Andersson,C-H, and Warren,R. "Silicon carbide fibres and their potential use in composite materials. Part 1." *Composites vol 15 Jan. 1984. pp 16-24.*

22 Yajima,S. Okamura,K. Tanaka,J. and Hayase,T. "High-temperature strengths of aluminium composite reinforced with continuous SiC fibre." *J.Mater.Sci. 16 (1981) 3033-3038.*

23 Carlsson,D.J. Cooney,J.D. Gauthier,S. and Worsfold,D.J. "Pyrolysis of silicon-backbone polymers to silicon carbide." *J.Am.Ceram.Soc., 73 [2] pp 237-241.*

24 Warren,R. and Andersson,C-H. "Silicon carbide fibres and their potential use in composite materials. Part 2" *Composites vol 15 no 2 April 1984. pp 101-111*

25 Stacey,M.H. "Production and characterisation of fibres for metal matrix composites." *Mater. Sci. & Tech. 1988 vol.4. p. 227.*

26 Carduner,K.R. Shinozaki,S.S. Rokosz,M.J. Peters,C.R. and Whalen,T.J. "Characterization of β-silicon carbide by silicon-29 solid-state NMR, transmission electron microscopy, and powder x-ray diffraction." *J.Am.Ceram.Soc. 73 [8] 2281-2286.*

27 Ichikawa,H., Machino,F., Mitsuno,S., Ishikawa,T., Okamura,K. and Hasegawa,Y. "Synthesis of continuous silicon carbide fibre. Part 5. Factors affecting stability of polycarbosilane to oxidation." *J.Mater.Sci. 21 (1986) pp. 4352-4358.*

28 Hasegawa,Y. and Okamura,K. ""Synthesis of continuous silicon carbide fibre. Part 3. Pyrolysis process of polycarbosilane and structure of the products." *J.Mater.Sci 18 (1983) pp. 3633-3648.*

29 Mah,T., Hecht,N.L., McCullum,D.E., Hoenigman.J.R., Kim.H.M., Katz.A.P. and Lipsitt.H.A. "Thermal stability of SiC fibres (Nicalon)." *J.Mater.Sci. 19 (1984) 1191-1201.*

30 Clark,T.J., Prack,E.R., Ishaq,M. and Sawyer,L.C. "Oxidation of SiC fibre" *Ceram.Eng.Sci.Proc. 8 pp. 717-731 (1987)*

31 Maniette,Y. and Oberlin,A. "TEM characterization of some crude or air heat-treated SiC Nicalon fibres." *J.Mater.Sci. 24 (1989) pp. 3361-3370*

32 Yajima,S., Okamura,K., Matsuzawa,T., Hasegawa,Y. and Shishido,T. "Anomalous characteristics of the microcrystalline state of SiC fibres." *Nature vol. 279 June 1979 pp. 704-707.*

33 Okamura,K. "Ceramic fibres from polymer precursors." *Composites. vol 18. 2 1987 pp. 107-120*

34 Nicalon product information. *Nippon Carbon Company, Japan.*

35 Porte,L. and Sartre,A. "Evidence for a silicon oxycarbide phase in the Nicalon silicon carbide fibre." *J.Mater.Sci. 24 (1989) pp. 271-275.*

36 Laffon,C., Flank,A.M., Lagarde,P., Laridjani,M., Hagege,R., Olry,P., Cotteret,J., Dixmier,J., Miquel,J.L., Hommel,H. and Legrand,A.P. "Study of Nicalon-based ceramic fibres and powders by EXAFS spectrometry, x-ray diffractometry and some additional methods." *J.Mater.Sci. 24 (1989) pp. 1503-1512.*

37 Kim,W.H., Koczak,M.J. and Lawley,A. "Interface reaction and characterization in B/Al composites." *ICCC 2 pp. 487-505*

38 Chenfu,W., Meifang,Y. and Shaoping,Z. "Carbon fibre reinforced pure lead composite used for tubular positive grid in lead-acid battery." *Proc.Seventh.Int.Conf.Comp.Mater. Nov 1989, Guangzhou, China vol 1. pp. 184-187.*

39 Lee,G-G. and Kim,J. "Mechanical behavior of squeeze casted continuous SiC/Al composites." *ibid* pp447-451.

40 Arsenault,R.J. and Pande,C.S. "Interfaces in metal matrix composites." *Scripta Metallurgica. vol. 18 1984. 1131-1134*

41 Viala,J.C., Bosselet,F., Fortier,P. and Bouix,J. "Chemical interaction between silicon carbide Nicalon fibres and liquid aluminum or aluminum-silicon alloys." *ICCM 6/ECCM 2, eds. F.L. Matthews, N.C.R. Buskell, J.M. Hodginson and J. Morton (Elsevier Applied Science: London and New York) vol.2. (1987) pp146-155*

42 Lee,D-J., Vaudin,M.D., Handwerker,C.A. and Kathner,U.R. "Phase stability & interface reaction in the Al-SiC system." *High temperature/High performance composites: Materials research society symposium proceedings. vol.120 Nevada 1988 p.357.*

43 Madeleno,U. Liu,H. Shinoda,T. Mishima,Y. and Suzuki,T. "Compatibility between alumina fibres and aluminium." *J.Mater.Sci. 25 (1990) pp. 3273-3280.*

44 Lloyd,D.J. and Chamberlain,B. " Properties of shape cast Al-SiC metal matrix composites" *Cast reinforced metal composites, proceedings of the International Symposium on advances in cast reinforced metal matrix composites. Chicago. sept 1988 eds. Fishman.,S.G. and Dhingra.,A.K. ASM international. pp. 263-269*

45 Yang,M. and Scott,V.D. "Interface and fracture of carbon fibre reinforced Al-7% Si alloy." *J.Mater.Sci. 26 1991 pp. 1609-1617*

46 Lloyd,D.J., Lagrace,H., Mcleod,A. and Morris,P.L. "Microstructural aspects of Al-SiC particulate composites produced by a casting method." *Mater.Sci. & Eng. A107 (1989) pp.73-80*

47 Henriksen,B.R. "The microstructure of squeeze-cast SiCw-reinforced Al4Cu base alloy with Mg and Ni additions." *Composites vol 21 No. 4 1990 pp.333-338*

48 Saggese,M.E. Scott,V.D. and Trumper,R.L. "Characterisation of interfaces in Al-Zn-Mg alloy reinforced with Sicabo fibres." *Mater. Sci. and Tech. Oct 1988 vol 4. pp. 871-875.*

49. Umekawa,S., Wakashima,K., Yoda,S., Takahashi,R. and Ioka,I. "Effect of thermal cycling on the interface of fibre-reinforced metallic composites." *Composite Mater., Kawata,K. & Akasaka,T. Ed., Proc. Japan-U.S. Conf., Tokyo 1981.*

50. Maniette,Y. and Oberlin,A. "Interphase phenomena in silicone carbide single filament composites." *J.Mater.Sci 25 (1990) pp. 3864-3874.*

51. Quanwu,S. Wenxu,G. and Shuqi,G. "The interface structure in C/Al composite without any coating." *Proc.SeventhInt.Conf.Comp.Mater. Nov 1989,Guangzhou, China vol 1. pp. 458-462.*

52 Chapman,A.R., Scott,V.D. and Yang,M. "Interface characteristics in fibre-reinforced aluminium alloy-Microstructure, micromechanics and manufacture." *ICCM.8 Honolulu 1991.*

53 Yang,M. and Scott,V.D. "Microstructural studies of alumina fibre reinforced aluminium alloy." *Developments in the science and technology of composite materials. Proc.Forth.Euro.Conf.Comp.Mater. Stuttgart FRG. Elsevier, Sept 1990 pp.261-266.*

54 Yang,M. and Scott,V.D. "Microstructural studies of aluminium-silicon alloy reinforced with alumina fibres." *J.Mater.Sci. 26 (1991) pp.2245-2254*

55 Nutt,S.R. "Interfaces and failure mechanisms in Al-SiC composites". from *Interfaces in metal-matrix composites. Proc. symp. AIME New Orleans 1986. eds. A.K.Dhingra and S.G.Fishman. pp.157-167*

56 Ribes,H. Salvo,L. and Suery,M. "Interface characteristics and age hardening behaviour of SiC reinforced Al-based alloys." *Proc.SeventhInt.Conf.Comp.Mater. Nov 1989,Guangzhou, China vol 1. pp.518-522*

57 "Equalibrium diagrams of aluminium alloy systems." *Aluminium Development Association, 1961.*

58 Metals Handbook. vol 7: Atlas of microstructures of industrial alloys. *American Society of Metals.*

59 "Aluminium alloys: Structure and properties." Mondolfo, *L.F., Butterworths, 1976.*

60 "Metallurgy of aluminium alloys." van Lancker,M. *Chapman and Hall.*

61 Lu,S.Z. and Hellawell,A. "Mechanisms of eutectic modification in the Al-Si system." *Aluminum alloys- Physical and mechanical properties. Eds. Starke,E.A. and Sanders,T.H. Papers presented at Int. conf. Virginia, USA 1986 pp.81-94*

62 Metals handbook: vol 6. Heat treatment. *American Society of Metals.*

63 Fat-Halla,N. Secordel,P. and Suery,M. "Microstructure and mechanical properties of modified and non-modified stir-cast Al-Si hypoeutectic alloys." *J. Mater. Sci. 23 1988 pp. 2419-2423.*

64 Dhingra,A.K. "Inorganic alumina fibres for reinforcement of metal castings." *Composite materials, Kawata,K and Akasaka,T. Ed., Proc. Japan-U.S. Conference, Tokyo, 1981 pp. 239-244.*

65 "Inorganic fibres and composite materials: a survey of recent developments." *Eds. Bracke,P., Schurmans,H. and Verhoest,J. European Patent Office applied technology series. vol.3. Pergaqmon International Information Corporation*

66 Wawner,F.E. "Boron and silicon carbide/carbon fibres" *Fibre reinforcements for composite materials. Composite Materials Series. vol. 2. Ed. A.R.Bunsell pp. 371-426*

67 De,A.K. and Phani,K.K. "Gauge length effect on strength of silicon carbide and sapphire filaments." *J.Composite Mater. vol 24 Feb 1990 pp. 220-231.*

68 Harris,S.J. "Cast metal matrix composites." *Mater. Sci. and Tech. March 1988 vol. 4 p 231*

69 Chou,T.W., Kelly,A. and Okura,A. "Fibre reinforced metal matrix composites." *Composites. vol.16. No.3. July 1985. pp. 187-206.*

70 Girot,F.A., Albingre,L., Quenisset,J.M. and Naslain,R. "Rheocasting Al matrix composites." *J. Metals. Nov.1987 pp. 18-21.*

71 Girot,F.A., Quenisset,J.M. and Naslain,R."Discontinuously reinforced aluminum matrix composites." *Compo. Sci. & Tech. 30 1987 pp. 155-184.*

72 Harris,S,J, "Fiber-Reinforced aluminum alloys" *In Aluminum alloys- Contemporary research and applications: Treatise on materials science and technology vol 31. eds A.K.Vasudevan and R.D.Doherty 1989 pp. 255-294*

73 Ibrahim,I.A., Mohamed,F.A. and Lavernia,E.J. "Particulate reinforced metal matrix composites- a review." *J.Mater.Sci. 26 (1991) pp. 1137-1156*

74 Bader,M.G., Clyne,T.W., Cappleman,G.R. and Hubert,P.A. "The fabrication and properties of metal-matrix composites based on aluminium alloy infiltrated alumina preforms." *Composite Sci. & Tech. 23 1985 pp. 287-301.*

75 Clyne,T.W. and Mason,J.F. "The squeeze infiltration process for fabrication of metal-matrix composites." *Metallurgical Trans.A. vol.18A. Aug.1987. pp. 1519-1530.*

76 Ward-Close,C.M. and Partridge,P.G. "A fibre coatinng process for advanced metal-matrix composites." *J.Mater.Sci. 25 (1990) pp. 4315-4323.*

77 White,J., Darby,N.A., Hughes,I.R., Jordan,R.M. and Willis,T.C. "Metal matrix composites produced by spray deposition." *Proc.Seventh.Int.Conf.Comp.Mater. Nov 1989,Guangzhou, China vol 1. pp.509-517.*

78 Chadwich,G. "Production, properties and applications of metal matrix composites." *Developments in the science and technology of composite materials. Proc.Forth.Euro.Conf.Comp.Mater. Stuttgart FRG. Elsevier, Sept 1990 pp.3-13.*

79 Bhagat,R.B. "High pressure squeeze casting of stainless steel wire reinforced aluminium matrix composites." *Composites. vol.19. No.5. Sept 1988 pp. 393-399*

80 Rabinovitch,M., Daux,J-C., Raviart,J-L. and Mevrel,H. "Carbon-reinforced magnesium and aluminium composites fabricated by liquid hot pressing." *Developments in the science and technology of composite materials. Proc.Forth.Euro.Conf.Comp.Mater. Stuttgart FRG. Elsevier, Sept 1990 pp. 405-411*

81 Tellesbo,H. Guldberg,S. Westengen, and Johnsen,T.E. "Characterisation of the squeeze cast M6-alloy AS41 with Al2O3 fibres." *ibid. pp249-254.*

82 Fukunaga,H. "Squeeze casting processes for fiber reinforced metals and their mechanical properties." *Cast reinforced metal composites, proceedings of the International Symposium on advances in cast reinforced metal matrix composites. Chicago. sept 1988 eds. Fishman.,S.G. and Dhingra.,A.K. ASM international. pp. 101-107*

83 Kobayashi,T., Yosino,M., Iwanari.,H., Niinomi. and Yamamoto,K. "Mechanical properties of SiC whisker reinforced aluminum alloys fabricated by pressure casting method." *ibid pp205-210*

84 Sample,R.J., Bhagat,R.B. and Amateau.M.F. "High pressure squeeze casting of unidirectional graphite fiber reinforced aluminum matrix composites." *ibid. pp. 179-183*

85 Diwanji,A.P. and Hall,I.W. "Effect of manufacturing variables on the structure and properties of squeeze cast C/Al MMCs." *ibid. pp. 225-230*

86 Mykura,N., "Liquid pressure forming of engineered metal matrix composites." *ibid. pp. 173-178*

87 Yu,K. Dollhopf,V. and Kochendorfer,R "Wettability and mechanical properties of CVD SiC filament and reinforced aluminium in a vacuum suction casting process." *Developments in the science and technology of composite materials. Proc.Forth.Euro.Conf.Comp.Mater. Stuttgart FRG. Elsevier, Sept 1990 pp399-404.*

88 Engineering Composite Materials. Harris,B.H. *Institute of Metals*

89 An Introduction to Composite Matreials. Hull,D. *Cambridge University Press*

90 Analysis and Performance of Fibre Composites. Agenwall,B.D and Broutman,L.J. *Wiley-Interscience Publications*

91 Li,Q., McCartney,D.G. and Walker,A.M. "Influence of safimax fibres on microstructure and microsegregation in an aluminium alloy." *Developments in the science and technology of composite materials. Proc.Forth.Euro.Conf.Comp.Mater. Stuttgart FRG. Elsevier, Sept 1990 pp. 351-356.*

92 Arsenault,R.J. "The strengthening of aluminum alloy 6061 by fibre and platelet silicon carbide." *Mater.Sci & Eng. 64 1984 pp. 171-181*

93 Grimes,H.H. Lad, R.A. and Maisel,J.E. "Thermal environment effects on strength and impact properties of boron-aluminum composites." *ICCC 2 PP. 555-566*

94 Ohori,K., Watanabe,H. and Takeuchi,Y. "Silicon carbide whisker reinforced aluminium composites- fabrication and properties." *Mater.Sci.& Tech. Jan 1987. vol.3. pp.57-60.*

95 Tsangarakis,N., Andrews,B.O. and Cavallaro,C. "Mechanical properties of some silicon carbide reinforced aluminum composites." *J.Comp.Mater. vol.21. May 1987. pp. 481-492.*

96 Favry,Y. and Bunsell,A.R. "Characterisation of Nicalon (SiC) reinforced aluminium wire as a function of temperature." *Comp.Sci.& Tech. 30. 1987 pp. 85-97.*

97 Skinner,A., Koczak,M.J. and Lawley,A. "Work of fracture in aluminum metal-matrix composites." *Metallurgical Trans A. vol.13A. Feb 1982 pp. 289-297.*

98 Buchheit,R.G., Ruch,W. and Wawner,F.E. "Processing and properties of aluminum alloys reinforced with Saffil alumina fibres." *Aluminum alloys-physical and mechanical properties. Eds. Starke,E.A. and Sanders,T.H. Papers presented at Int. conf. Virginia, USA 1986 pp. 181-198*

99 Friend,C.M. "The effect of matrix properties on reinforcement in short alumina fibre-aluminium metal matrix composites." *J. Mater. Sci. 22 1987 pp. 3005-3010*

100 Brown,L.D., Maruyama,B., Cheong,Y.M., Rabenberg,L.K. and Marcus,H.L. "Metal matrix interfaces and their impact on mechanical behavior of composites." *Proc. first Int.Conf. on Comp.Interfaces. Ed., Ishida and Keanny. (ICCI-1) May 1986. pp. 27-35*

101 McMinn,A., Page,R.A. and Wei,W. "The effect of processing parameters on the tensile properties of alumina fibre reinforced magnesium." *Metallurgical Trans.A. vol.18A. Feb. 1987. pp. 273-281.*

102 Saganuma,K. Okamoto,T. Hayami,T. Oku,Y. and Suzuki,N. "Influence of high temperature exposure on the properties of alumina short fibre reinforced AA6061 alloy." *J.Mater.Sci. 23 (1988) pp1317-1323.*

103 Rohatgi,P.K. Das,S. and Asthana,R."Synthesis, structure, properties and applications of cast Al-ceramic particle composites." *Aluminum alloys-physical and mechanical properties. Eds. Starke,E.A. and Sanders,T.H. Papers presented at Int. conf. Virginia, USA 1986 pp. 169-180*

104 Wisnom,M.R. "Factors affecting the transverse tensile strength of unidirectional continuous silicon carbide fibre reinforced 6061 aluminum." *J. Comp.Mater. vol.24 July 1990 pp.707-726.*

105 Ochiai,S., Osmura,K. and Murakami,Y. "Effects of interfacial reaction on fracture mode and tensile strength of fibres in metal matrix composites." *ICCM-4. eds. T.Hayashi, K.Kawata, and S.Umekawa. Tokyo 1982. pp. 1331-1338.*

106 Tsangarakis,N., Andrews,B.O. and Cavallaro,C. "Mechanical properties of some silicon carbide reinforced aluminum composites." *J.Comp Mater. vol.21. May 1987 pp.481-492.*

107 Goda,K. and Fukunaga,H. "Considerations of the reliability of tensile strength at elevated temperature of unidirectional metal matrix composites." *Comp. Sci. & Tech. 35 (1989) pp. 181-193*

108 Lee,C.H., Lee,D.Y. and Kim,H.S. "Interfacial reaction and tensile strength of monofilament composites with Al-base matrix." *Proc.Seventh.Int.Conf.Comp.Mater. Nov 1989, Guangzhou, China vol 1. pp. 484-490*

109 Levi,C.G., Abbaschian,G.J. and Mehrabian,R. "Interface interactions during fabrication of aluminum alloy-alumina fibre composites." *Metallurgical Trans. A. vol.9A, May 1978. pp. 697-711*

110 Johnston,W.D. and Greenfield,I.G. "Effect of magnesium concentration on the shear strength of unidirectional alpha-alumina/aluminum composites." *Cast reinforced metal composites, proceedings of the International Symposium on advances in cast reinforced metal matrix composites. Chicago. sept 1988 eds. Fishman.,S.G. and Dhingra.,A.K. ASM international. pp. 335-340*

111 Yajima,S., Okamura,K., Matsuzawa,T., Tanaka,J. and Hayse,T. "Contiuous SiC fibre reinforced aluminum." *Composite materials. Proc. Japan-U.S. Conf., Tokyo, 1981. Kawata and Akasaka, Ed.*

112 Skibo,M., Morris,P.L. and Lloyd,D.J. "Structure and properties of liquid metal processed SiC reinforced alumminum." *Cast reinforced metal composites, proceedings of the International Symposium on advances in cast reinforced metal matrix composites. Chicago. sept 1988 eds. Fishman.,S.G. and Dhingra.,A.K. ASM international. pp. 257-261*

113 Skinner,A.R. "The effect of heat treatment on the mechanical properties and microstructure of aluminium alloy MMC's." *abstracts; Metal matrix composites: Property optimisation and Applications. The Institute of Metals. Nov 1989 pp.F1-F4*

114 Schueller,R.D. and Wawner,F.E. "An analysis of high-temperature behavior of AA2124/SiC whisker composites." *Comp. Sci. & Tech. 40 (1991) pp. 213-223.*

115 Saganuma,K., Okamoto,T., Hayami,T., Oku,Y. and Suzuki,N. "Influence of high temperature exposure on properties of alumina short fibre reinforced AA 6061 alloy." *J.Mater. Sci. 23 1988 pp. 1317-1323.*

116 Da Silva,R., Caldemaison,D. and Bretheau, T. "Interface strength influence on the mechanical behaviour of Al/SiC particle metal matrix composite". *Interfacial Phenomena in Composite Materials '89. Proc. int. conf. Editor F.R.Jones. Butterworths. pp. 235-241.*

117 Li,C.-H., Nyborg,L., Bengtsson,S., Warren,R. and Olefjord,I. "Reactions between SiO_2 binder and the matrix in d-Al2O3/Al-Mg composites." *ibid. pp. 253-257.*

118 Gungor,M.N., Cornie,J.A. and Flemings,M.C. "The response of microstructures of metal matrix composites to solidification time." *from Interfaces in metal-matrix composites. proc. symp. AIME New Orleans. 1986 eds. A.K.Dhingra and S.G.Fishman pp.121-135*

119 Gungor,M.N., Cornie,J.A. and Flemings,M.C. "Solidification processing of an aluminum/alumina composite." *Cast reinforced metal composites, proceedings of the International Symposium on advances in cast reinforced metal matrix composites. Chicago. sept 1988 eds. Fishman.,S.G. and Dhingra.,A.K. ASM international. pp. 39-45*

120 Honjo,K. and Shindo,A. "Interfacial behavior of aluminum matrix composites reinforced with ceramic-coated carbon fibres." *Composite Interfaces. Proc. First Int.Conf.Comp.Interfaces (ICCI-1) May 1986 Cleveland, USA, eds. H. Ishida and J.L. Koenig. Elsevier Science Publishers pp. 101-107.*

121 Munitz,A. Metzger,M. and Mehrabian,R. "The interface phase in Al-Mg/Al2O3 composites." *Metallurgical Trans.A. vol.10A., Oct 1979, 1491-1497.*

122 Fox,S. and Flower,H.M. "Structure of aluminium alloy metal matrix composite incorporating alumina fibres." *abstracts, Metal matrix composites: Structure and property assessment. 23-24 Nov 1989 The Inst.Metals & Royal Aeronautical Society. pp. 18.1-18.3*

123 Le Petitcorps,Y., Stephenson,T., Girot,F. and Naslain.R. "Chemical analysis and bonding at the fibre-matrix interface in model aluminum matrix composites." *Cast reinforced metal composites, proceedings of the International Symposium on advances in cast reinforced metal matrix composites. Chicago. sept 1988 eds. Fishman.,S.G. and Dhingra.,A.K. ASM international. pp 67-70*

124 Laurent,V., Chatain,D., Eustathopoulos,N. and Dumant,X. "The wetting kinetics of aluminium and its alloys on single-crystal SiC." *Cast reinforced metal composites, proceedings of the International Symposium on advances in cast reinforced metal matrix composites. Chicago. sept 1988 eds. Fishman.,S.G. and Dhingra.,A.K. ASM international. pp27-31*

125 Quigley,B.F. Abbaschian,G.J. Wunderlin,R.and Mehrabian,R "A method for fabrication of aluminum-alumina composites" *Metallurgical Trans. vol.13A. Jan 1982. pp. 93-100.*

126 Peteves,S.D., Tambuyser,P., Helbach,P., Audier,M., Laurent,V. and Chatain,D. "Microstructure and morphology of the Al/SiC interface." *J. Mater. Sci. 25 (1990) r pp 3765-3772.*

127 Kohara,S. "Compatiblity of SiC fibers with aluminum." *Composite materials, Proc. Japan-U.S. Conf., Tokyo, 1981. 224-227. Kawata and Akasaka. Ed.*

128 Hall,I.W. Kyono,T. and Diwanji,A. "On the fibre/matrix interface in boron/aluminium metal matrix composites." *J. Mater. Sci. 22 1987 1743-1748.*

129 Fox,S. Flower,H. and West,D. "TEM characterisation of fibre-matrix interactions in light alloy MMC containing alumina fibres." *Developments in the science and technology of composite materials. Proc.Forth.Euro.Conf.Comp.Mater. Stuttgart FRG. Elsevier, Sept 1990 pp. 243-248*

130 Neite,G. Dudek,H.J. Kleine,A. and Borath,R. "Interfaces in Al2O3 fibre reinforced aluminium alloys." *ibid pp.237-242.*

131 Stephenson,T., LePetitcorps,Y. and Quenisset,J.M. "The interfacial role of silica on ceramic fibre-reinforced aluminium alloy composites." *ibid pp.255-260*

132 Fu,L.J., Schmerling,M., and Marcus,H.L. "Interface studies of aluminium matrix composites." *Composite Materials: Fatigue and Fracture, ASTM STP 907, H.T.Hahn, Ed., American Society for testing and Materials, Philadelphia 1986 pp. 51-72.*

133 Johnson,P.K., Flower,H.M. and West,D.R.F. "The interaction between liquid aluminium and particulate silicon carbide in Al-SiC metal matrix composites." *abstracts; Metal matrix composites: Property optimisation and Applications. The Institute of Metals. Nov 1989 pp. 16.1-16.3*

134 Hughes,A.E., Hedges,M.M. and Sexton,B.A. "Reactions at the Al/SiO2/SiC layered interface." *J. Mater. Sci. 25 (1990) pp 4856-4865.*

135 Tafto,J., Kristiansen,K., Westengen,H., Nygard,A., Borradaile,J.B. and Karlsen,D.O. "Studies of interfaces in light metal matrix composites by transmission electron microscopy." *Cast reinforced metal composites, proceedings of the International Symposium on advances in cast reinforced metal matrix composites. Chicago. sept 1988 eds. Fishman.,S.G. and Dhingra.,A.K. ASM international. pp. 71-75*

136 Choh,T. and Oki,T. "Wettability of SiC to aluminium and aluminium alloys." *Mater. Sci. & Tech. vol.3. 1987 pp. 378-385.*

137 Okura,A. and Motoki,K. "Rate of formation of intermetallic compounds in aluminium matrix-carbon fibre composites." *Comp.Scie. & Tech. 24 (1985) pp. 243-252*

138 Liu,H., Madaleno,U., Shinoda,T., Mishima,Y and Suzuki,T. "Interfacial reaction and strength of SiC fibres coated with aluminium alloys." *J.Mater.Sci 25 (1990) pp. 4247-4254.*

139 Henriksen,B.R. "The effect of Mg on the interface in an Al/SiCw composite". *Interfacial Phenomena in Composite Materials '89. Proc. int. conf. Editor F.R. Jones. Butterworths. pp. 242-245.*

140 Yoon,H-S. Okura,A and Ichinose,H. "Study of the interface of carbon fibre reinforced aluminium composite materials." *ibid. pp258-263.*

141 Nutt,S.R. "TEM characterisation of aluminum-base composites." *In Aluminum alloys- Contemporary research and applications: Treatise on materials science and technology vol 31 eds A.K.Vasudevan and R.D.Doherty 1989. pp.389-408*

142 Standard test method for tensile properties of fiber-reinforced metal matrix composites. *ASTM D 3552-77 American Society for testing and materials*

143 Roebuck,B. Gorley,T.A.E. and McCartney,L.N. "Mechanical property test procedures for metal matrix composites." *Mater.Sci & Tech Feb 1989 vol. 5 pp105-117.*

144 Standard test method for- Flexural properties of plastic and electrical insulating materials. *ASTM D790-80*

145 Standard test method for- Interfacial shear strength of polymeric composites. *ASTM D3846-79*

146 Standard test method for Tensile strength and Young's modulus for high-modulus single-filament materials. *ASTM D3379-75 pp.*

147 Marshall,D.B. and Evans,A.G. "Failure mechanisms in ceramic-fibre/ceramic-matrix composites." *J.Am.Ceram.Soc. 68 [5] May 1985 pp. 225-231*

148 Marshall,D.B. and Evans,A.G. "Measurement of interfacial mechanical properties in fibre-reinforced ceramic composites." *J.Am.Ceram.Soc. 70 [8] (1987) pp.542-548*

149 Marshall,D.B. "An indentation method for measuring matrix-fibre frictional stresses in ceramic composites." *Comm.Am.Ceram.Soc. Dec 1984 pp.C-259-C-260*

150 Scott,V.D. and Love,G. "The prospects of a universal correction procedure for quantitative EPMA." *Scanning vol. 12, (1990) pp. 193-202*

151 "Moduli of elasticity and fundamental frequencies of carbon and graphite materials by sonic resonance: standard test method of." *ASTM standard C.747.*

152 Das,S., Asthana,R. and Rohatgi,P.K. "Solidification of aluminium in presence of suspended graphite particles." *Aluminum alloys-physical and mechanical properties. Eds. Starke,E.A. and Sanders,T.H. Papers presented at Int. conf. Virginia, USA 1986 pp. 95-109*

153 Otani,T. "Corrosion behaviour of metal matrix composites." *PhD Thesis University of Bath 1989*

154 Trumper,R.L. and Scott,V.D. "Matrix solidification and segregation effects in fibre reinforced metals." *Proc.Seventh.Int.Conf.Comp.Mater. Nov 1989, Guangzhou, China vol 1. pp. 585-591.*

155 Prasad,B.K., Dan,T.K. and Rohatgi,P.K. "Pressure-induced improvement in interfacial bonding between graphite and the aluminium particle composites." *J. Mater. Sci. letters 6 1987 1076-1078*

156 Das.,S., Prasad.,S.V., Dan.,T.K. and Rohatgi.,P.K. "Modification and refinement of silicon in cast Al-Si-graphite particle composites" *Cast reinforced metal composites, proceedings of the International Symposium on advances in cast reinforced metal matrix composites. Chicago. sept 1988 eds. Fishman.,S.G. and Dhingra.,A.K. ASM international. pp 243-248.*

157 .Hasegawa.,Y. "Synthesis of continuous silicon carbide fibre. Part 6 Pyrolysis process of cured polycarbosilane fibre and structure of SiC fibre." *J.Mater.Sci. 24 (1989) pp. 1177-1190.*

158 Durrant, G. *Private comunacation*

159 Scott,V.D. "Electron Probe Microanalysis using soft x-rays" *paper presented at a meeting on electron beam techniques held at the Royal Society, London May 14-15, 1974.*

160 Sewell,D. *PhD Thesis University of Bath, 1984*

161 Bastin,G.F. and Heijlingers,H.J.M. "Quantitative electron probe microanalysis of carbon in binary carbides" *Publication of the Laboratory for Physical Chemistry, University of Technology Eindhoven. April 1985.*

162 Malis,T. and Chaturvedi,M.C. "Grain boundary segregation in an Al-8 wt% Mg alloy." *J.Mater.Sci. 17 (1982) pp.1479-1485.*

163 Coltters,R.G. "Thermodynamics of binary metallic carbides: A review." *Mater.Sci & Eng, 76 (1985) pp. 1-50*

164 Friend,C.M., Horsfall,I., Luxton,S.D. and Young,R.J. "The effect of fibre/matrix interfaces on the age-hardening charcteristics of d-alumina fibre reinforced AA6061." *Cast reinforced metal composites, proceedings of the International Symposium on advances in cast reinforced metal matrix composites. Chicago. sept 1988 eds. Fishman.,S.G. and Dhingra.,A.K. ASM international. pp. 309-315*

165 Vogelsang,M., Arsenault,R.J. and Fisher,R.M. "An in situ HVEM study of dislocation generation at Al/SiC interfaces in metal matrix composites" *Met.Trans A. vol 17A March 1986 pp. 379-389*

166 Bhanu Prasad,V.V., Prasad,K.S., Kuruvilla,A.K., Pandey,A.B., Bhat,B.V.R. and Mahajan,Y.R. "Composite strengthening in 6061 and Al-4Mg alloys." *J.Mater.Sci. 26 (1991) pp. 460-466*

167 Friend,C.M. and Luxton,S.D. "The effect of d-alumina fibre arrays on the age-hardening characteristics of an Al-Mg-Si alloy." *J. Mater. Sci. 23 1988 pp. 3173-3180.*

168 Dutta,I. Bourell,D.L. and Latimer,D. "A theoretical investigation of accelerated aging in metal matrix composites." *J.Comp.Mater. vol.22. Sept 1988 829-850.*

169 Prangnell,P.B. and Stobbs,W.M. "The effect of SiC particle reinforcement on the age behavior of aluminium based matrix alloys." *Proc.Seventh.Int.Conf.Comp.Mater. Nov 1989, Proc.Seventh.Int.Conf.Comp.Mater. Guangzhou, China vol 1. pp.573-578.*

170 Bader,M.G. and Pitkethly,M.J. "Probalistic aspects of the strength and modes of failure of hybrid fibre composite." *Mechanical characterisation of fibre composite materials. Ed. R.Pyrz Proc.Symposium. Aalborg University pp. 1-24*

171 Zweben,C. "Tensile strength of hybrid composites." *J.Mater.Sci. 12 (1977) 1325-1337.*

172 Schamm,S. Le Petitcorps,Y. and Naslain,R. "Compatibility between SiC filaments and aluminium in the K2ZrF6 wetting process and its effect on filament strength." *Compos.Sci. & Tech 40 (1991) pp193-211.*

173 Ritter,A.M. and Briant,C.L. "Effect of second phase particles on fracture in engineering alloys." *Treatise on Materials Science and Technology. vol 25. Embrittlement of Engineering alloys. eds C.L.Briant and S.K.Banerji. Academic Press (1983) Chapter 3. pp. 59-119*

174 Ma,Z.Y., Liu,J. and Yao,C.K. "Fracture mechanisms in a SiCw-6061 Al composite." *J.Mater.Sci. 21 (1991) pp. 1971-1976*

175 Bleay,S.M. *PhD Thesis 1991 University of Bath*

176 Li,S., Arsenault,J. and Jena,P. "Bonding of SiC and aluminium." *Cast reinforced metal composites, proceedings of the International Symposium on advances in cast reinforced metal matrix composites. Chicago. sept 1988 eds. Fishman.,S.G. and Dhingra.,A.K. ASM international. pp. 33-37*

177 Kortschot,M.T. and Beaumont,P.W.R. "Damage mechanics of composite materials: II- A damage-based notched strength model." *Composite Sci. & Tech. 39 (1990) pp. 303-326.*

178 Love,G. "The technique of electron probe x-ray microanalysis." *Microscopy and Analysis Jan 1991 pp 9-12.*

179 Mortensen,A., Michaud,V.J., Cornie,J.A., Flemings,M.C. and Masur,L. "Kinetics of fibre preform infiltration." *Cast reinforced metal composites, proceedings of the International Symposium on advances in cast reinforced metal matrix composites. Chicago. sept 1988 eds. Fishman,S.G. and Dhingra,A.K. ASM international. pp.7-13*

180 Gallerneault,M., Huggins,U. and Lloyd,D.J. "The microstructure of the aluminum-silicon eutectic solidification in the presence of d-Alumina fibre." *Metallography of Advanced Materials: Microstructural Science vol. 16. Cialone,H.J., Johnson,G.W.E., Blum,M.E. and Vander Voort,G.F. eds. pp75-84*

	DIAMETER (μm)	COST (£ kg^{-1})	Ultimate Tensile Strength (MPa)	Modulus (GPa)	Density (g cm^{-3})
BORON					
Boron	140	400	3500	438	2.49
Borsic	142	1430	3100	400	2.71
SILICON CARBIDE					
SiC on C	140	890	4000	430	3.04
SiC on W	100	1250	3500	420	3.32
Nicalon	15	400	2500	190	2.55
Tyranno	10	470	2900	210	2.4
CARBON					
T300	8	120	2000	330	1.74
P100	10	1200	2200	690	2.10
P120	10	1600	2200	820	2.18
Alumina					
Saffil	3	25	2000	300	3.3
Saffimax (SD)	3	75	2000	300	3.3
Saffimax (LD)	3.5	75	2000	300	2.0
FP Alumina	20	450	1800	380	3.96

Table 1.1 Summary of properties for fibres which have potential use in metal matrix composites.

ELEMENT	SILICON	CARBON	OXYGEN
WEIGHT PERCENT	55.5	28.4	14.9

Table 1.2 Average elemental composition of Nicalon fibres reported in literature.

CONSTITUENT	β-Silicon Carbide	Silica	Free Carbon
WEIGHT PERCENT	61	28	10

Table 1.3 Proposed composition of Nicalon fibre by various authors.

Reference	Reinforcement	Matrix Alloy	Reaction Product
24.	SiC	Aluminium Magnesium	Al_4C_3 Mg_2Si
39.	Nicalon	Pure Al Al-13.5%Si	No reaction
40.	SiC whisker	Aluminium	Diffusion of Al into SiC
41.	Nicalon	Pure Al Al-14.5%Si	Al_4C_3, Al_2O_3
42.	Beta SiC (CVD)	99.98 Al	Al_4C_3
43.	Al_2O_3/SiO_2 fibres	99.99%Al	volatile Al_2O Al_2O_3 (with silica)
44.	SiC particulate	6061 A356	No carbide Al_4C_3, Mg_2Si
45.	Carbon	Al-7%Si-0.4%Mg	Al_4C_3
47.	SiC whisker	Al-Cu with Mg or Ni	MgO, Al_2O_3 and $MgAl_2O_4$
54.	Alumina	Al-7%Si-0.4%Mg	seg of Mg
55.	SiC whisker	2124-6061	MgO
56.	SiC particulate	Al-&%Si-0.3%Mg	$MgAl_2O_4$
70.	Nicalon	Al alloy	$MgAl_2O_4$, Spinel silica reaction.
85.	Carbon Fibre	Al alloys	Al_4C_3
94.	Beta SiC	AA6061	No reaction

Table 1.4 A summary of the interfacial interaction between fibre and matrix for a number of metal matrix composites. Continued on the next page.

Reference	Reinforcement	Matrix Alloy	Reaction Product
100.	Carbon SiC	Aluminium "	Al_4C_3 no reaction
110.	FP-alumina	Al-Mg	$MgAl_2O_4$
112.	SiC	Aluminium	Al_4C_3
121.	FP Alumina	Al-4%Mg	MgO fine dispersion $MgAl_2O_4$ discrete crystals.
122.	Alumina	Al-10%Mg	Al_3Mg_2 mixed oxide Al_2O_3 MgO
123.	SiC	Al-7%Si-0.6%Mg	Mg_2SiO_4, Al_2O_4Mg MgO, Mg_2Si
124.	SiC single crystal	Al alloys	Al_4C_3, supressed by additions of Si
125.	FP alumina	Al-Mg alloy	$MgAl_2O_4$
126.	α-SiC	99.9999%Al	Al_4C_3
127.	Nicalon	Aluminium Al-1%Si	not identified no reaction
128.	Boron	Aluminium	Several borides Al_2O_3 acting as a diffusion barrier.
129.	Alumina	Al-10%Mg Magnesium	Mg penetration MgO
130.	Al_2O_3 (Saffil) silica binder	AlSi12CuMgNi piston alloy	Segregation of Mg,Si with high oxygen. $MgAl_2O_4$
131.	Fibres with SiO_2 layer Silica rod	Al-(Mg,Cu)	$MgAl_2O_4$ MgO, Al_2O_3, CuAlO2
132.	SiC fibre Particulate Carbon	6061 7075 both the above	γ-Al_2O_3 γ-Al_2O_3 & $MgAl_2O_4$ Al_2O_3 Al_4C_3

Table 1.4 cont'd A summary of the interfacial interaction between fibre and matrix for a number of metal matrix composites. Continued on the next page.

Reference	Reinforcement	Matrix Alloy	Reaction Product
133.	SiC particulate	Al Al-Si LM13	Al_4C_3 No carbide below below 970°C
134.	SiC SiC/SiO_2	Aluminium	Al_4C_3 Al_2O_3 + alumina silicate, Al_4C_3 when silica <5nm.

Table 1.4 cont'd A summary of the interfacial interaction between fibre and matrix for a number of metal matrix composites.

Sheet Number	Fibre Type	Matrix Type	Preform Construction	Sheet Dimensions (mm)	Sheet Designation
200	FP-alumina Borsic	357	3 plies FP Borsic with Woven Ti weft strip	100x100x10	F357
300	Nicalon	357	Glass weft	100x100x13	N357
400	"	"	"	150x150x3	N357
500	"	"	"	---"---	N357
600	"	Commercially Pure Al	Plain Weave	150x150x3	N100w
700	"	"	"	"	N100w
800	"	357	Glass weft	"	N357
900	"	"	"	"	N357
1000	"	"	"	150x150x4	N357
1100	"	Commercially Pure	Filament Wound	150x150x6	N100f

Table 2.1 Sheet descriptions of the composites used in the present investigation.

Alloy	Composition (wt %)				
	Silicon	Magnesium	Iron	Chromium	Nickel
357	6.5-7.5	0.3-0.38	0.38	<0.05	<0.05
Al	—	—	0.3	—	—

Table 2.2 The nominal compositioal ranges of the two matrix alloys used in the production of the metal matrix composites.

Crystal Name	Type	Lattice Plane Spacing. 2d. (nm)
LIF	Lithium Fluoride	0.4027
PET	Pentaerythritol	0.874
TAP	Thallium acid Phthalate	2.58
LDE1	Multilayer Device	6.0
STE	Lead Stearate	10.04

Table 2.3 The wavelength dispersive spectrometer analysing crystals fitted to the JEOL JXA 8600M electron probe microanalyser

Material	Weight Percent Element in Matrix*			
	Magnesium	Iron	Chromium	Nickel
357	0.38	0.13	<0.01	<0.01
1000	<0.01	0.86	<0.01	<0.01
N357				
300	0.29	1.02	0.06	0.03
400	0.05	1.04	0.02	0.07
500	0.09	0.98	0.03	0.07
1000	0.58	0.60	<0.01	<0.01
N100	<0.01	0.75	<0.01	<0.01

* - For the composites the wet analysis data was calculated to account for the fibre volume fraction.

Table 3.1 Wet chemical analysis data provided by ARE Holton Heath, for matrix materials and composites.

Element	Iron	Silicon	Aluminium
Weight Percent	25.4 ± 0.4	15.0 ± 0.5	63.9 ± 0.5

Table 3.2 Data from the quantitative electron probe microanalysis of the intermetallic, marked D in figure 3.1, in the 357 alloy.

Element	Iron	Silicon	Aluminium
Weight Percent	24.2 ± 0.3	23.6 ± 0.5	54.2 ± 0.4

Table 3.3 Data from the quantitative electron probe microanalysis of the intermetallic, marked E in figure 3.3, in the 357 alloy.

Element	Silicon	Oxygen	Carbon	Total
Batch 1	53.2 ± 1.2	14.4 ± 1.8	30.7 ± 1.5	98.3
Batch 2	53.2 ± 1.4	9.0 ± 0.4	32.9 ± 2.2	95.2

Table 3.4 Elemental composition of the Nicalon fibre in the alloy composite measured using the quantitative analysis in the JEOL JXA 8600M. The data are corrected using the ZAF factors in the electron-probe.

Standard	k-ratio, Nicalon/standard		
	Silicon	Oxygen	Carbon
SiC	0.77	-	0.99
SiO_2	1.25	0.17	-
Silicon	0.51	-	-
Graphite	-	-	0.09
Glassy C	-	-	0.07

Table 3.5 The difference in the ratio of x-ray intensity from specimen and standard, for different standards used for silicon, oxygen and carbon in the EPMA of Nicalon fibres.

Element	Silicon	Oxygen	Carbon
Weight Percent	52.6 ± 0.6	11.8 ± 0.5	26.8 ± 0.4 (27.9 ± 0.5)*

* - Includes a correction for the broader x-ray peak measured for the Nicalon.

Table 3.6 Calculated weight percentages of the elements in the Nicalon fibre, using the ZAF correction of Scott and Love.

Material	Full Width At Half Maximum (Å)			
	Carbon, Kα	Carbon, Kβ	Oxygen, Kα	Silicon, Kβ
Nicalon	1.278	0.867	0.148	0.028
Graphite(i)	1.978	1.60	-	-
Graphite(ii)	1.869	-	-	-
Glassy C	1.869	-	-	-
SiC	1.2	0.711	0.021	0.021
SiO_2	-	-	0.111	0.017

Table 3.7 The full width at half maximum for the x-ray peaks found in the electron-microprobe.

Material	Nicalon	Silicon Carbide	Glassy Carbon	Graphite
Shape Factor (eV)	8.82	7.25	10.95	10.65 (11.27)*

* - Calculated for the broad carbon x-ray peak from the graphite.

Table 3.8 The carbon Ka x-ray peak area to peak height ratio, shape factor, from the EPMA investigation.

Compound	Silicon Carbide		Silicon Oxycarbide		Free Carbon	
	wt %	vol %	wt %	vol %	wt %	vol %
Batch 1	59.4	54.1	29.5	31.3	11.2	14.6
Batch 2	67.9	62.5	19.5	20.9	12.6	16.6
Batch 3	64.5	59.6	26.9	29.0	8.6	11.4

Table 3.9 Estimated composition of the Nicalon fibre batches in the metal matrix composites.

Element	Silicon	Iron	Aluminium
Weight Percent	14.7 ± 1.3	24.4 ± 2.4	66.5 ± 1.8

Table 3.10 Weight percentage of the elements in the intermetallics found in the Nicalon-357 composite, measured in the EPMA.

Element	Silicon	Iron	Aluminium
Intermetallic 1	-	29.1 ± 1.8	70.2 ± 2.1
Intermetallic 2	2.13 ± 0.4	27.6 ± 0.9	71.3 ± 1.8

Table 3.11 Weight percent of elements in the intermetallics, away from the fibre , 1, and close to the fibre, 2, in the Nicalon-aluminium composite.

Element	Silicon	Iron	Aluminium
Weight Percent	14.63 ± 0.6	25.3 ± 0.5	59.6 ± 0.7

Table 3.12 Weight percent of elements in the intermetallics in the Alumina/Borsic-alloy composite.

Material	Fracture Stress (MPa)	Fracture Strain (%)	Initial Modulus (GPa)
357 as cast	64 ± 5	3.2	62 ± 4
357 heat-treated	124 ± 8	1.05 ± 0.03	60 ± 2
Aluminium	52 ± 13		68 ± 8
N357 as cast long	132 ± 21	0.11 ± 0.02	~120
N357 as cast trans	54 ± 14	0.10 ± 0.03	-
N357 ht long	70 ± 9	0.11 ± 0.02	~120
N357 ht trans	~35	~0.06	-
N100w 01	130 ± 12	0.19 ± 0.01	-
N100w 02	83 ± 8	0.23 ± 0.01	-
N100f long	149 ± 22	0.08 ± 0.01	-
N100f trans (a)	~20	-	-
N100f trans (b)	~90	-	-

long - tested with fibres in the longitudinal orientation
trans - tested with fibres in the transverse orientation
ht - heat treated, 540°C for 16 hours followed by 10 hours at 160°C
01 - major reinforcement orientation
02 - weft fibre orientation
(a) - transverse Nicalon only
(b) - transverse Nicalon and single woven layer

Table 3.13 Mechanical properties of the unreinforced metals and the composites tested in tension.

Material	Fracture Stress (MPa)	Fracture Strain (%)
N357 as cast long		
A	232 ± 19	-
B	116 ± 23	-
C(weft through-plane)	358 ± 8	~0.17
C(weft in-plane)	305 ± 29	~0.16
C(total)	340 ± 20	-
N357 ht long	119 ± 12	~0.14
N100f long	176 ± 11	~0.3
N100f trans	118 ± 16	~0.79

Table 3.14 Mechanical properties of composite materials tested in flexure, four point bending geometries shown in figure 2.4.

Nicalon-alloy composite		Nicalon-aluminium composite	
Specimen Number	Shear Strength (MPa)	Specimen Number	Shear Strength (MPa)
1*	16.4	1*	42.7
2	17.8	2	48.4
3	9.4	3	50.2
4	7.2	4	52.5
5	10.4	5	22.3

Table 3.15 Interlamina shear strength for the composite materials, only those specimens marked * failed in shear.

Composite condition	Strength of Fracture. (MPa)	Dynamic Modulus (GPa)
As Cast	202 ± 26	97 ± 7
Solution Treated	205 ± 50	101 ± 4
Aged 10 hours	215 ± 30	102 ± 5

Table 3.16 Mechanical properties of the Alumina/Borsic-alloy composite after different heat treatments. Solution treating was for 16 hours at 540°C and ageing undertaken at 160°C.

Condition	Strength (MPa)
Bobbin(as-received)	1560 ± 536
Bobbin(acid etch)	1513 ± 473
Bobbin(heat treated)	1511 ± 523
Preform	1084 ± 395
N100	742 ± 299
N357	420 ± 174
N357(heat treated)	279 ± 121

Table 3.17 Strength of single fibres extracted from different 'environments'. The heat treatment was 16 hours at 540°C.

Material	Fibre/Matrix interfacial shear strength (MPa)
N357	58 ± 41 (10 ± 8)*
N357(heat treated)	37 ± 24
N100	12 ± 5

* - Sub-set of fibres tested within the fibre tows.

Table 3.18 Fibre/matrix interfacial shear strength measured for the composite.

Condition	Strength (MPa)	m	Intercept
Bobbin	1560 ± 536	2.27	-16.95
Bobbin(heat treated)	1511 ± 523	2.94	-21.84
Bobbin(acid etch)	1513 ± 473	2.58	-19.34
Preform	1084 ± 395	3.00	-21.33
N100	742 ± 299	2.54	-17.09
N357	420 ± 174	2.38	-14.72
N357(heat treated)	279 ± 121	2.36	-14.08

Table 4.1 Single fibre Weibull analysis results for the Nicalon after extraction from different environments.

Fibre Condition	Predicted Composite Strength		
	Rule of Mixtures (MPa)	Bundle Strength (MPa)	First Fibre Failure (MPa)
Manufacturers Data	1400	-	-
Bobbin Fibres	720	410	340
Preform Fibres	470	-	-
As Cast 357	218	130	100
Heat treated 357	61	-	-

Table 4.2 Predicted composite strength using the measured fibre data and simple theories.

Fibre Condition	Predicted Composite Strength (MPa)		
	Rule of Mixtures	Bundle Strength	First Over-loaded
Bobbin Al matrix	670 335	416 194	- 170

Table 4.3 Predicted composite strength for the Nicalon-aluminium composite, based on the measured fibre properties of fibres extracted from different environments.

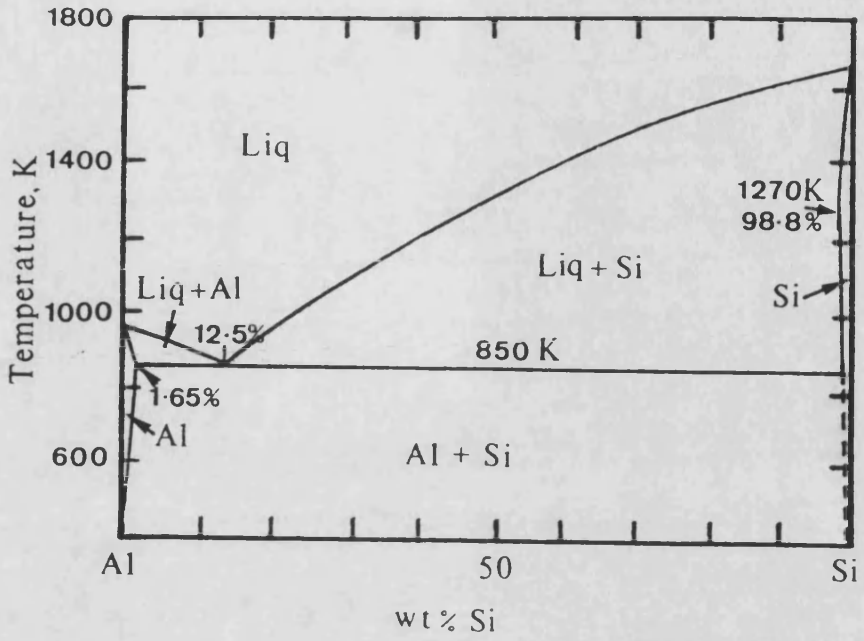

Figure 1.1 Aluminium-Silicon equilibrium phase diagram

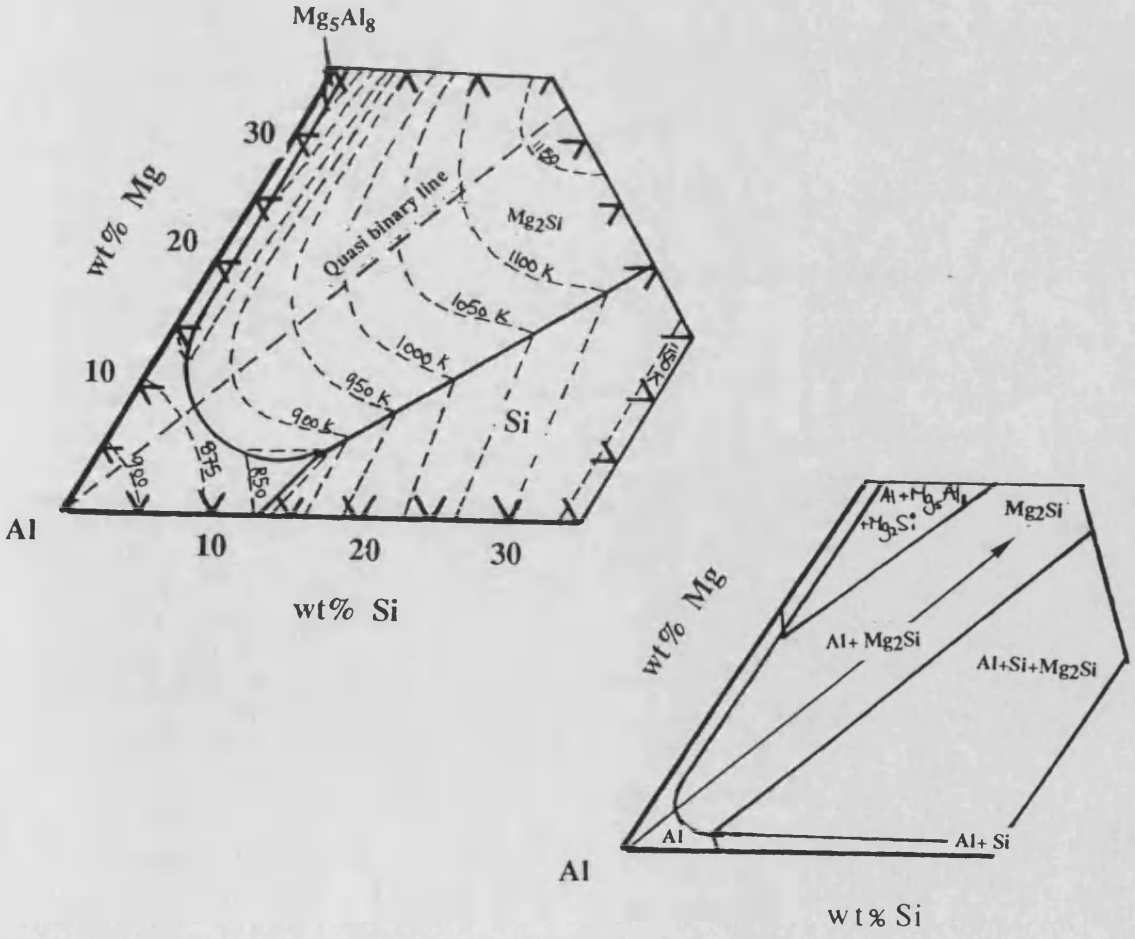

Figure 1.2 The aluminium corner of the Al-Mg-Si phase diagram (a) liquidus and (b) the phase distribution in the solid.

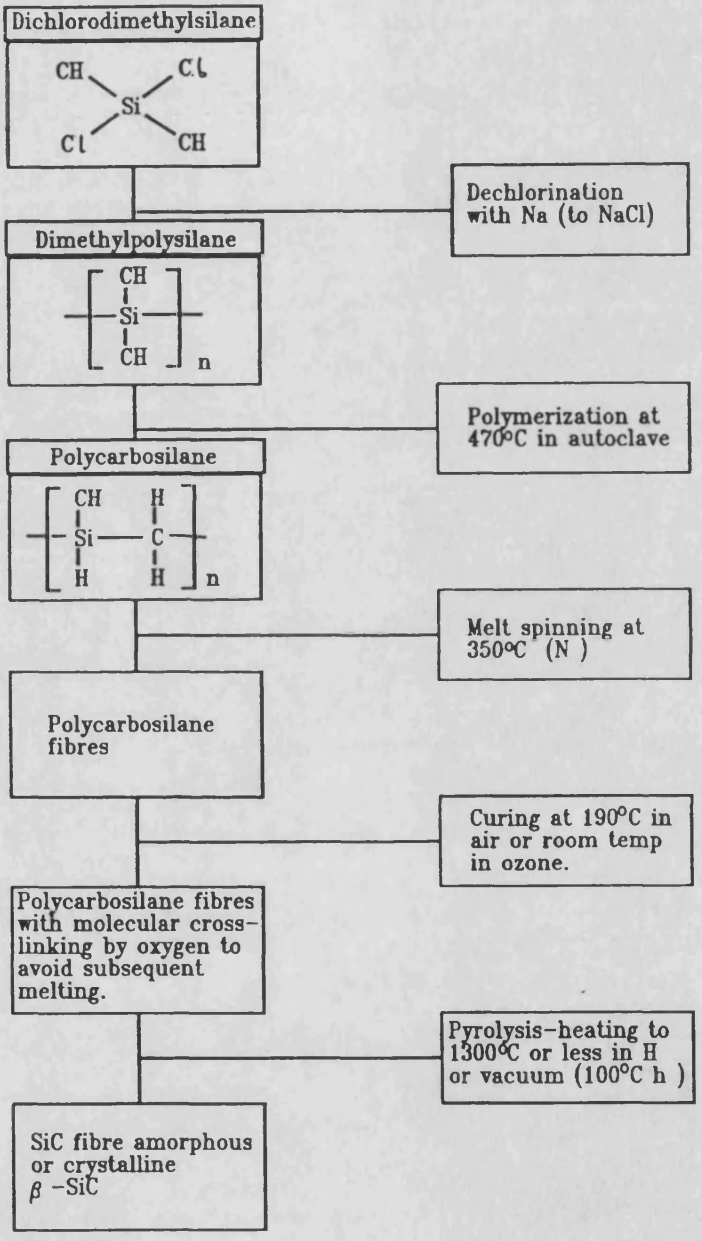

Figure 1.3 Basic steps in the fabrication of Nicalon fibres.

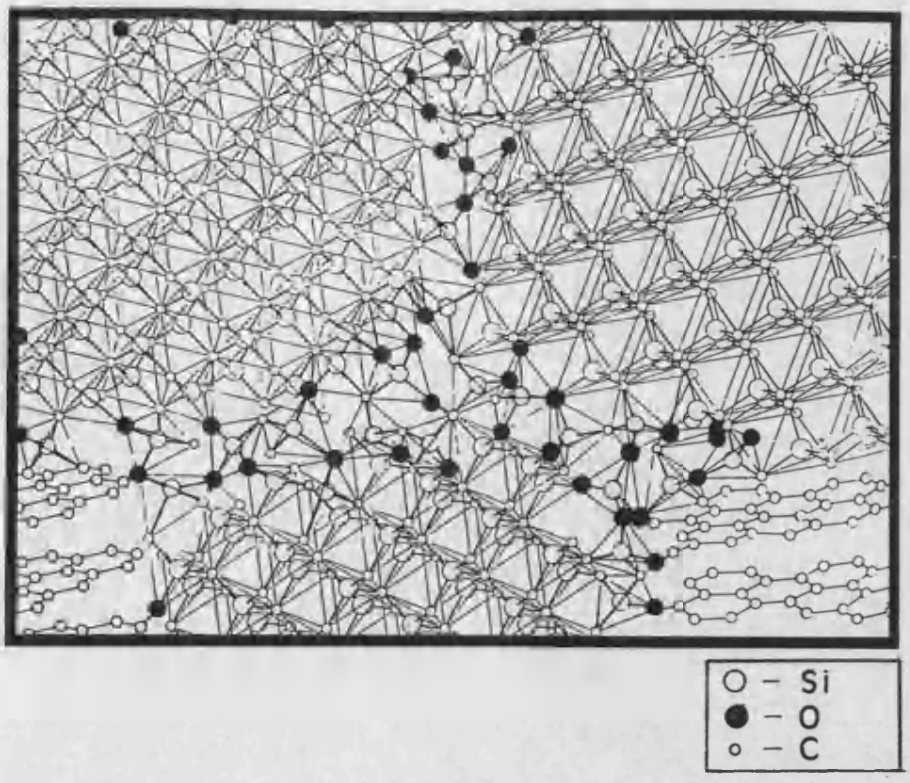

Figure 1.4 The proposed structure of the Nicalon fibre, from ref.

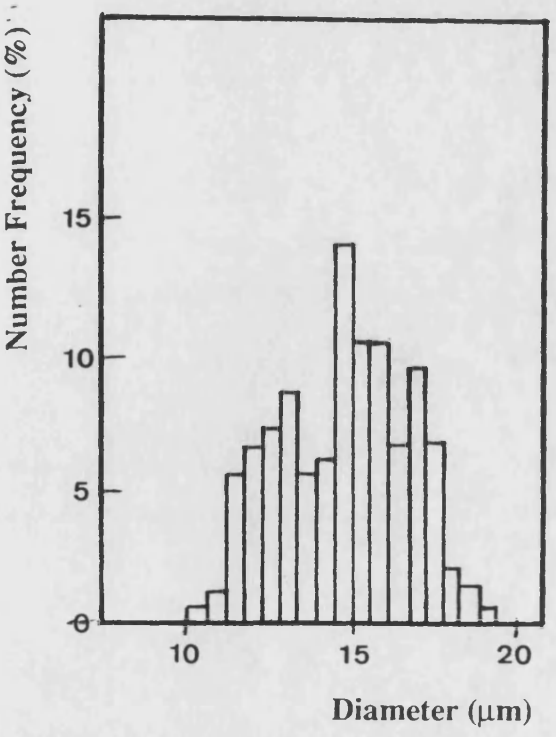

Figure 1.5 The diameter distribution for Nicalon fibres, after Anderson and Warren.

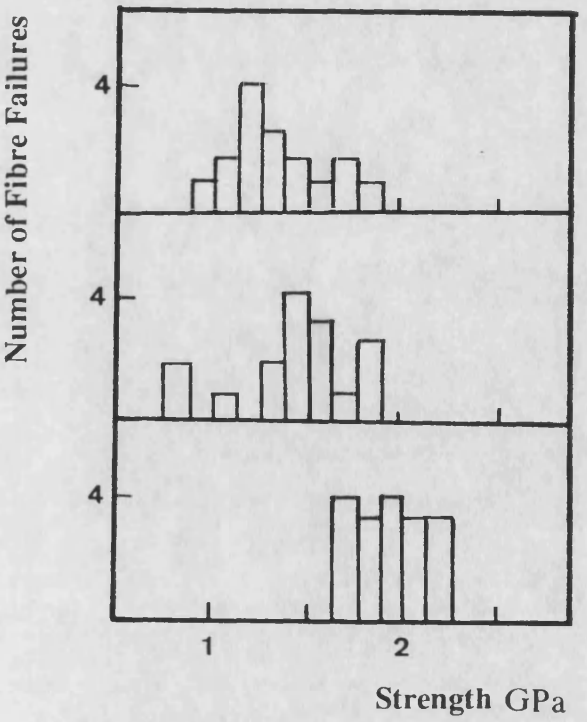

Figure 1.6 The tensile strength distribution for Nicalon fibres with three different gauge lengths, after Anderson and Warren.

Ref ? what of ?

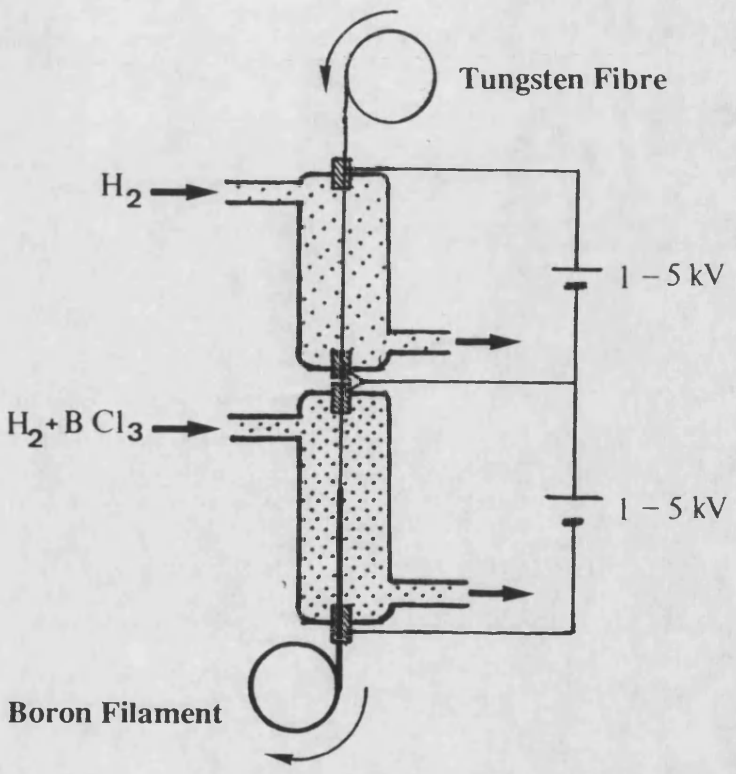

$$2BX_3(g) + 3H_2(g) \xrightarrow{\text{heat}} 2B(s) + 6HX(g)$$

where X may be Cl, Br or I.

Figure 1.7 Schematic diagram of the chamber used for chemical vapour deposition of boron.

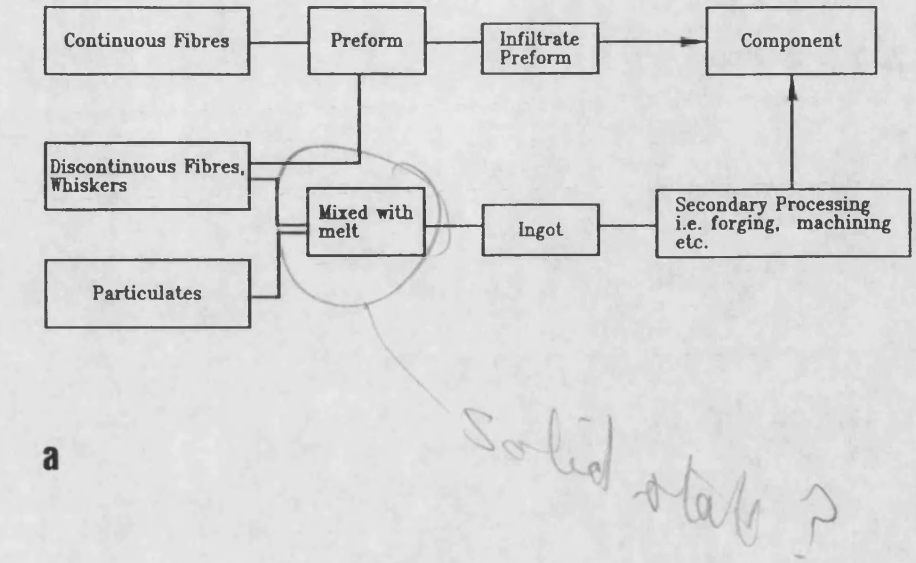

Figure 1.8 Main stages in the production of metal matrix composites by a. solid state methods and b. liquid state techniques.

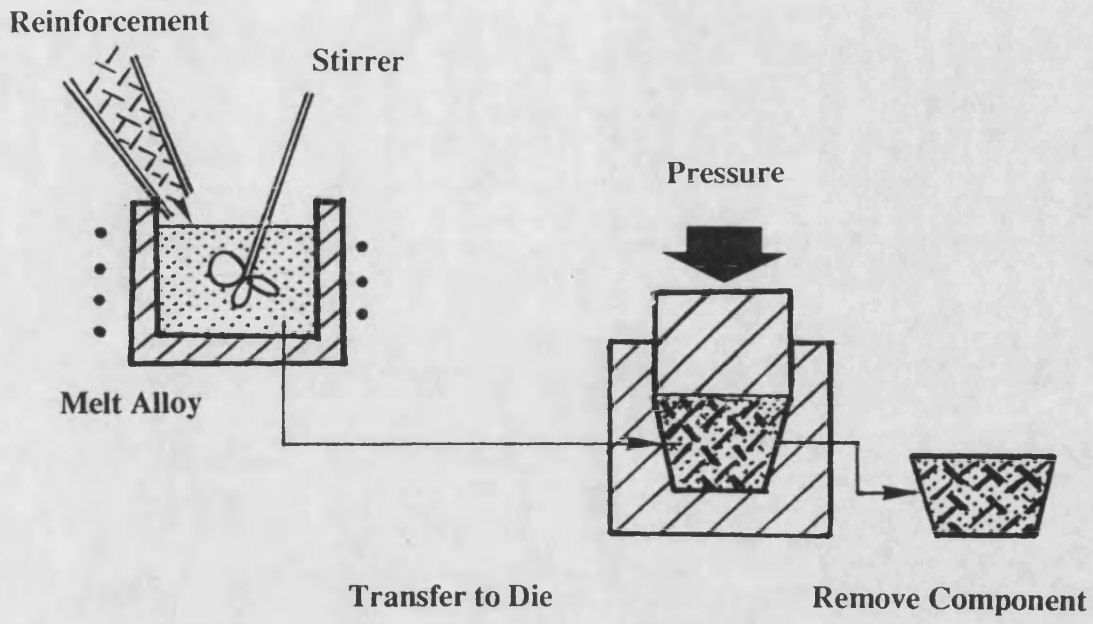

Figure 1.9 Schematic diagram of the compocasting forming of metal matrix composites.

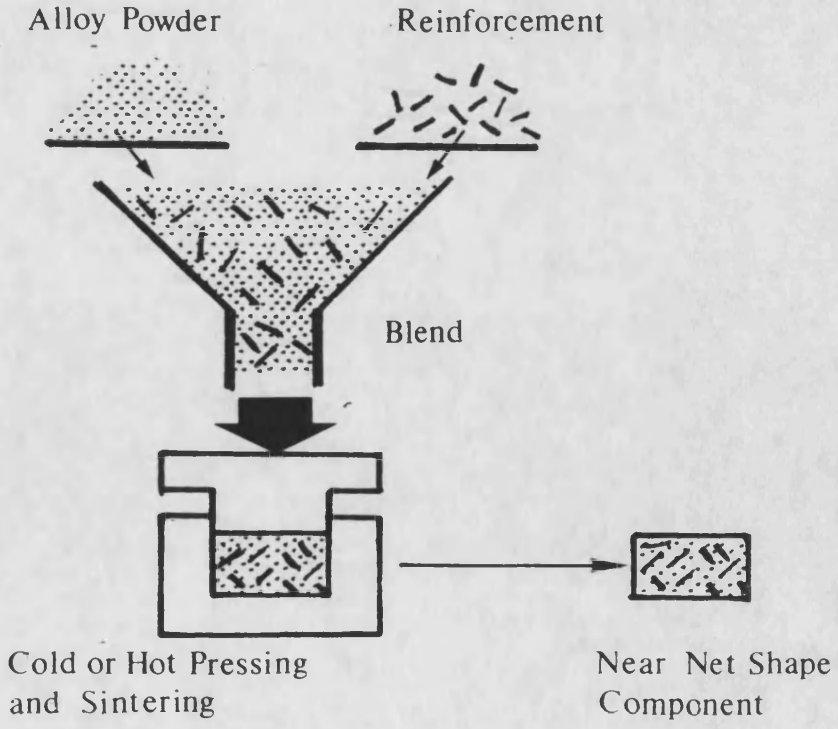

Figure 1.10 Basic stages in the forming of metal matrix composites by powder metallurgy.

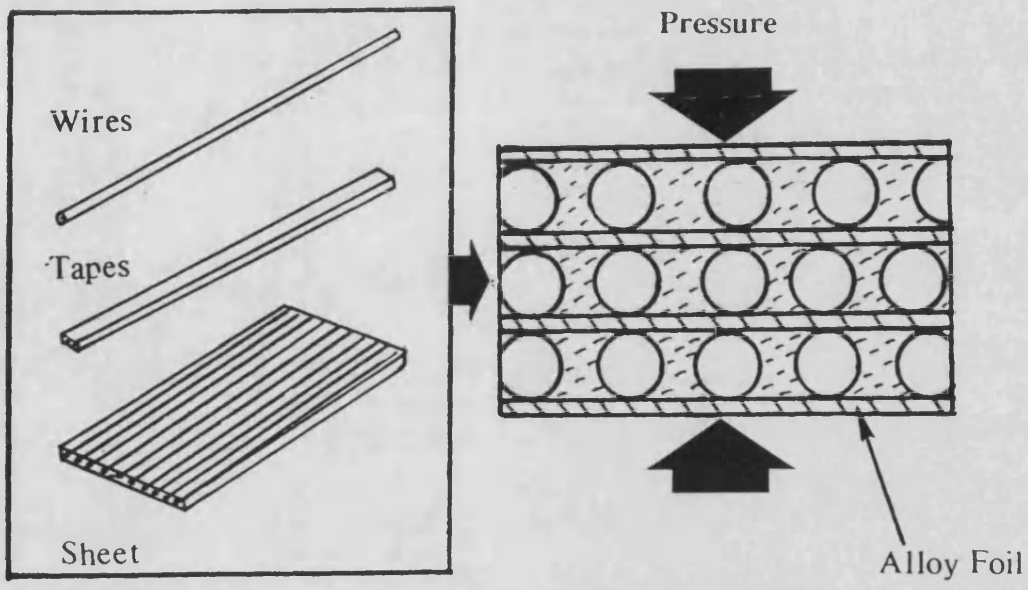

Figure 1.11 Basics of the diffusion bonding process for the fabrication of metal matrix composites.

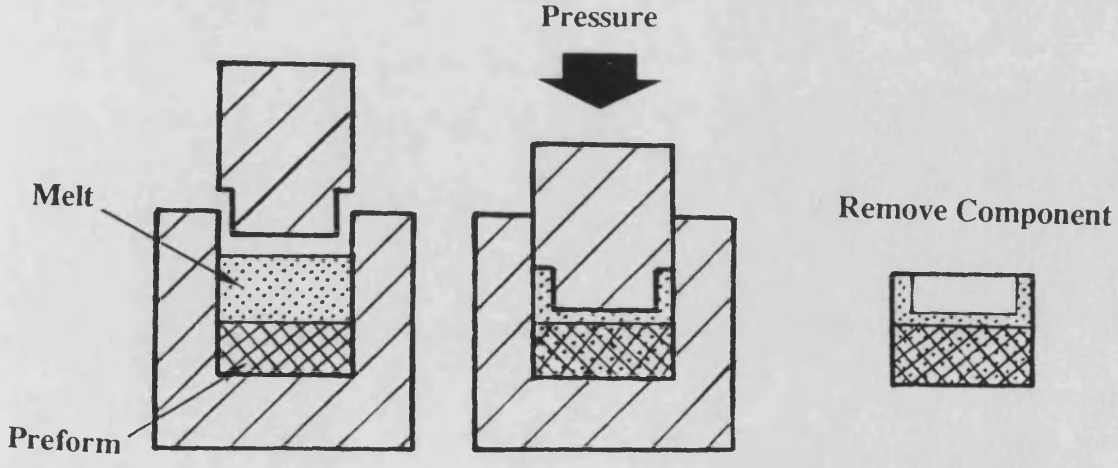

Figure 1.12 Schematic of the major stages in the squeeze cast forming of metal matrix composites.

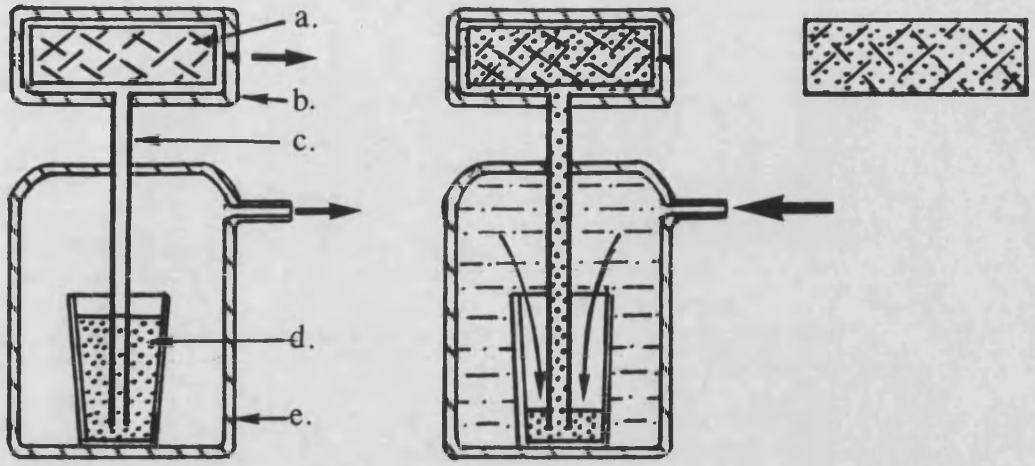

A. **Insert preform and evacuate die and chamber.**

B. **Apply inert gas pressure.**

C. **Remove near-net-shape component.**

a. Preform
b. Split Die
c. Melt Transfer Tube
d. Melt Alloy
e. Pressure Chamber

Figure 1.13 Main stages in the fabrication of metal matrix composites by the technique of liquid metal infiltration.

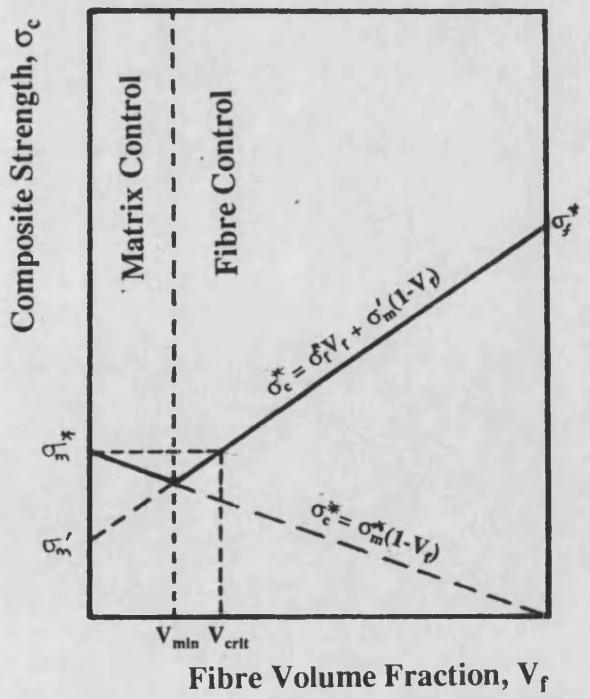

Figure 1.15 Variation of the composite strength with the volume fraction of a unidirectional material with the matrix yield point below the fibre yield stress.

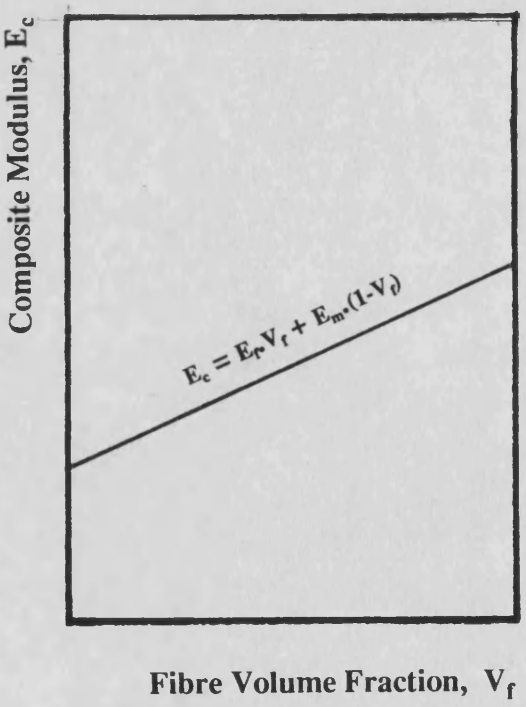

Figure 1.14 Theoretical variation of the composite modulus with the volume fraction of fibres.

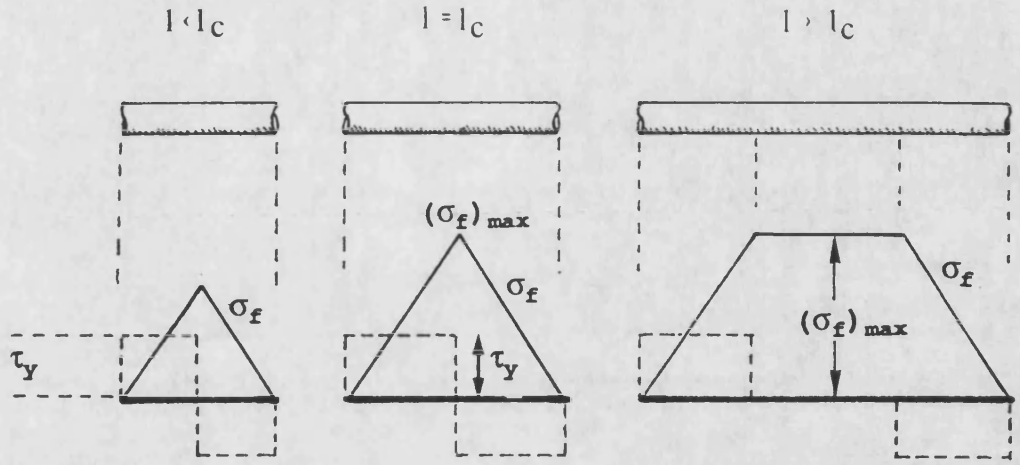

Figure 1.16 Variation of the tensile strength, σ, and the interface shear stress, τ, along the length of a short fibre in a matrix under tensile load.

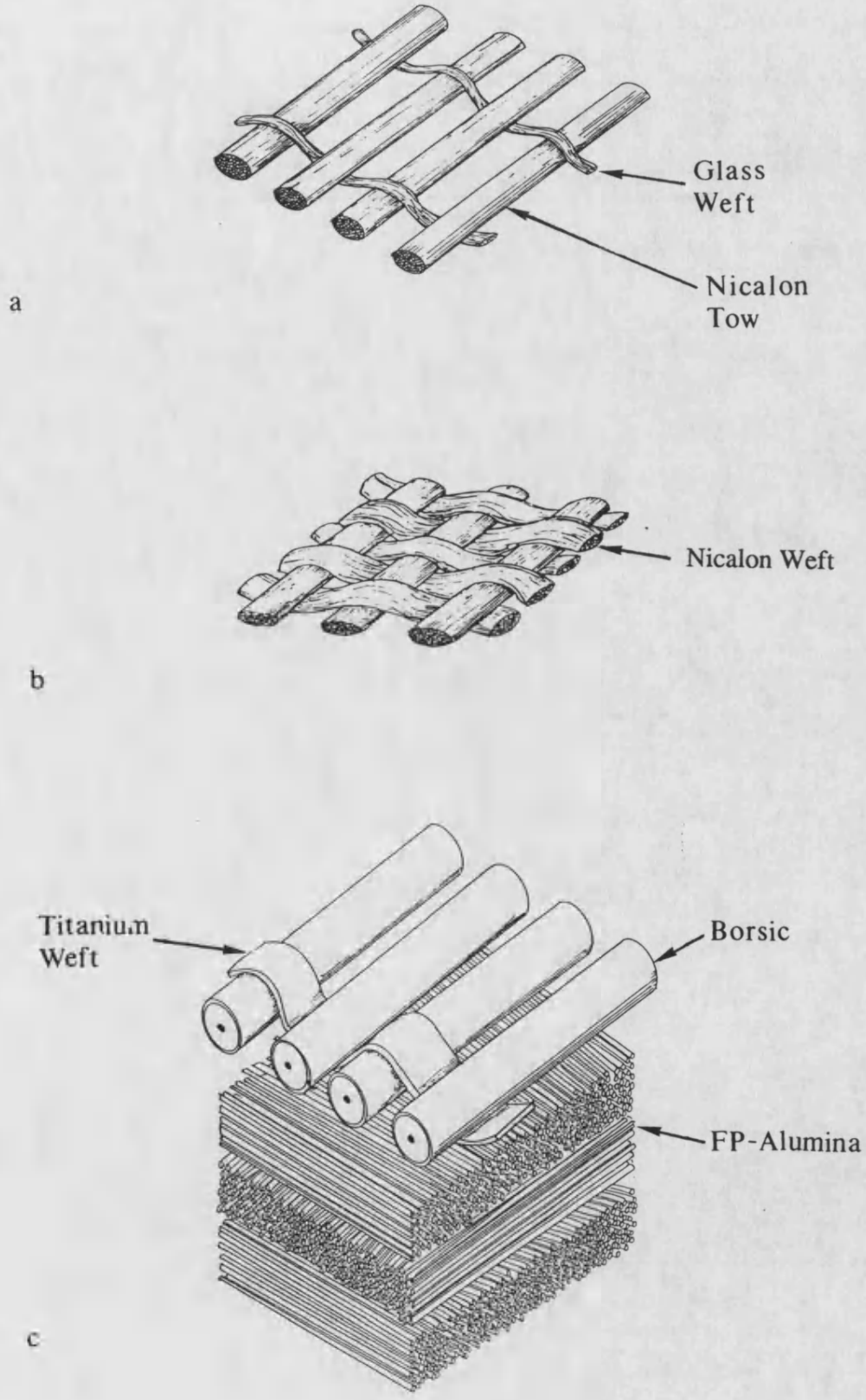

Figure 2.1 Schematic diagram of the preform structure for a. the Nicalon/aluminium-silicon alloy composite, b. the Nicalon/aluminium composite and c. the alumina-Borsic/alloy composite.

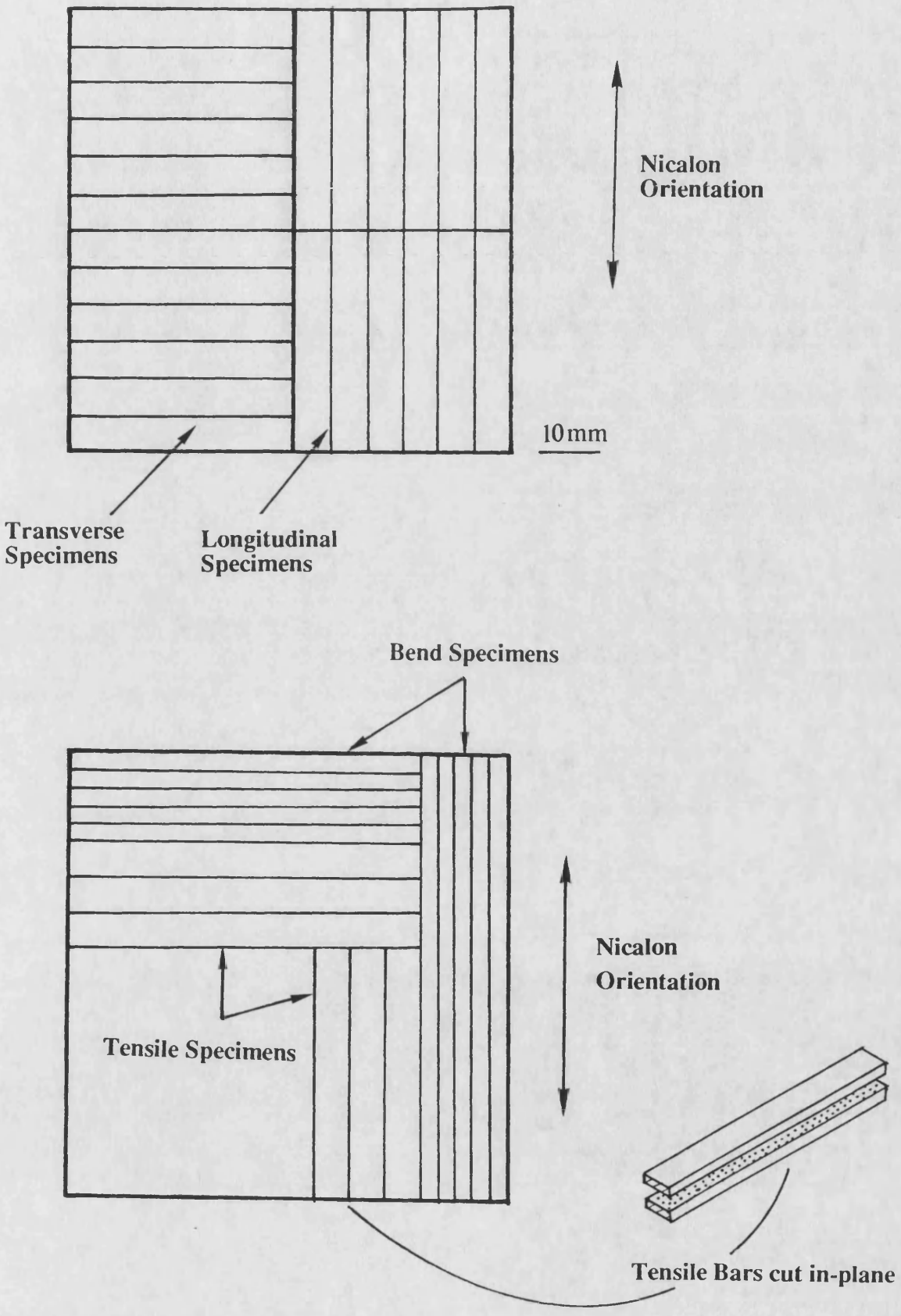

Figure 2.2 Cutting plan for test specimens of Nicalon composites based on a. 357 alloy and b. commercially pure aluminium (sheet 1100).

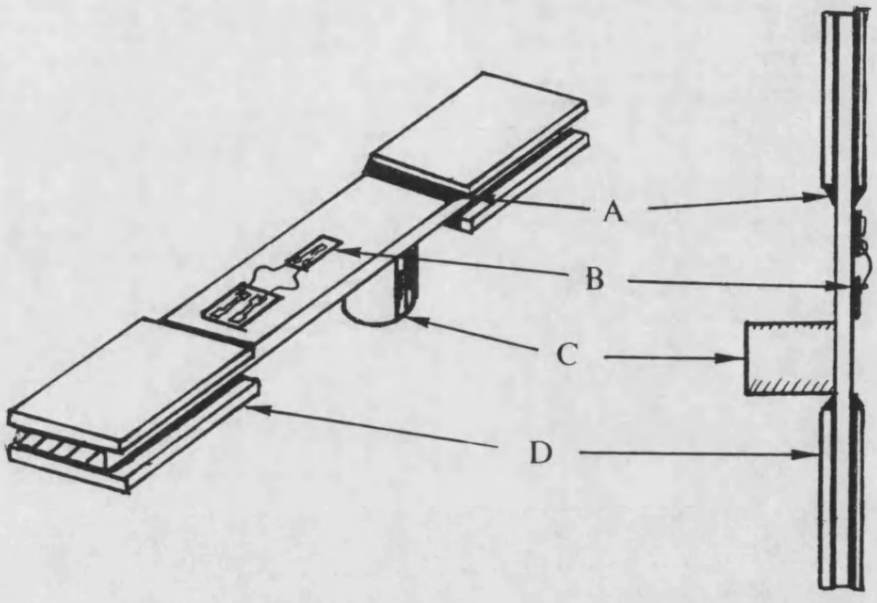

A- Adhesive
B- Strain Gauge
C- Acoustic Emission Transducer
D- End Tabs

Figure 2.3 Tensile test specimen showing the position of the strain gauge and acoustic emission transducer.

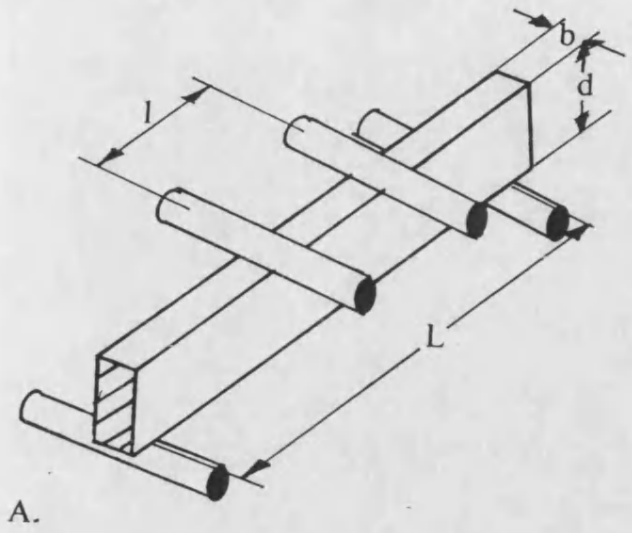

A.

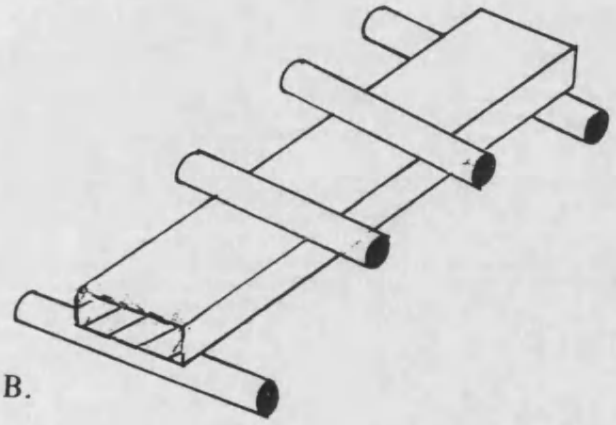

B.

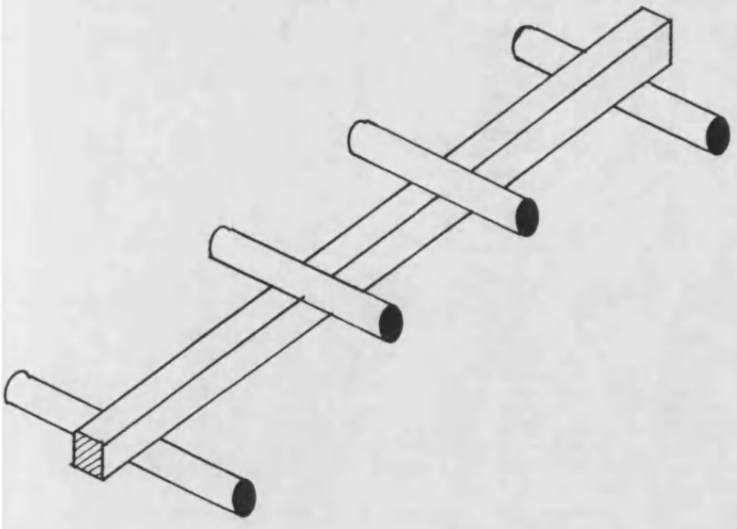

C.

	L (mm)	b (mm)	d (mm)
A	60	5	13
B	60	13	5
C	120	4	4

Figure 2.4 Geometry of the three types of flexural test bars.

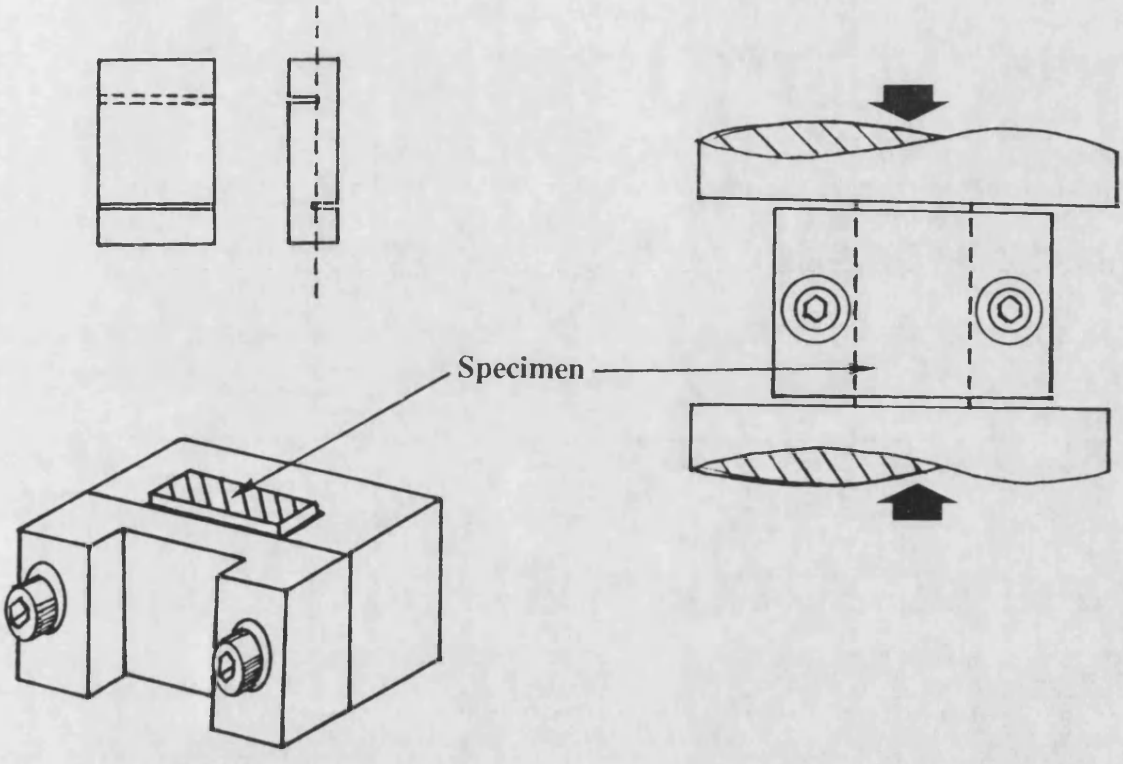

Figure 2.5 Shear test geometry and the constraining jig used.

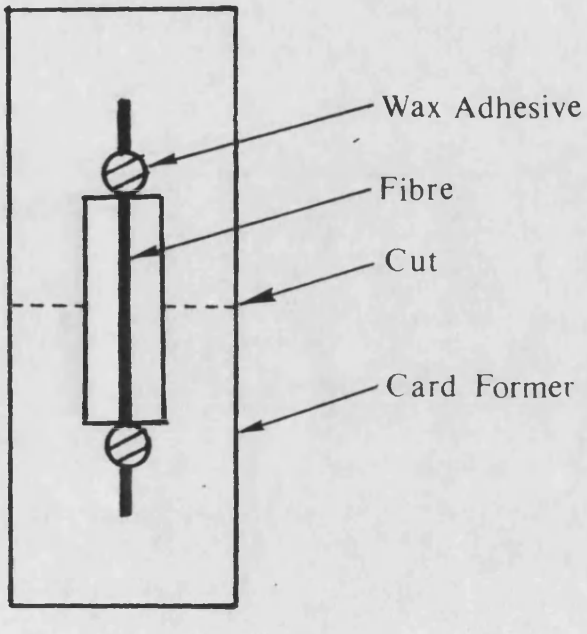

Figure 2.6 Schematic diagram of the single fibre test method, after ASTM D3379-75.

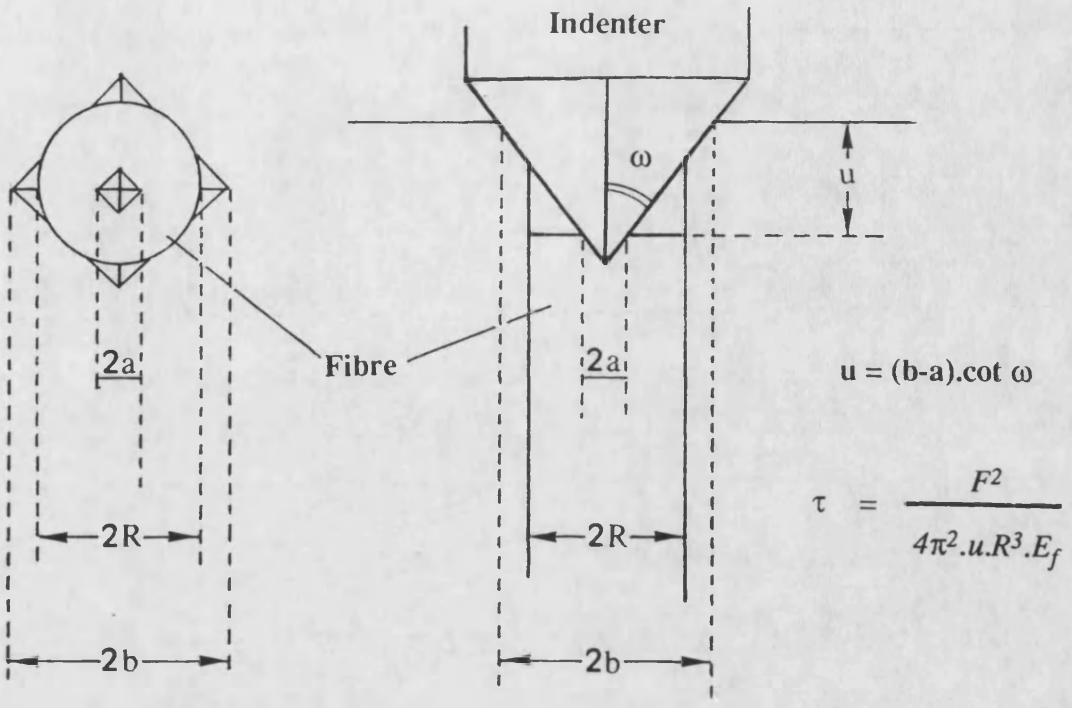

Figure 2.7 Basic geometrical features of the fibre/matrix interfacial shear test and the basic relationships used in calculating the fibre/matrix interfacial shear strength.

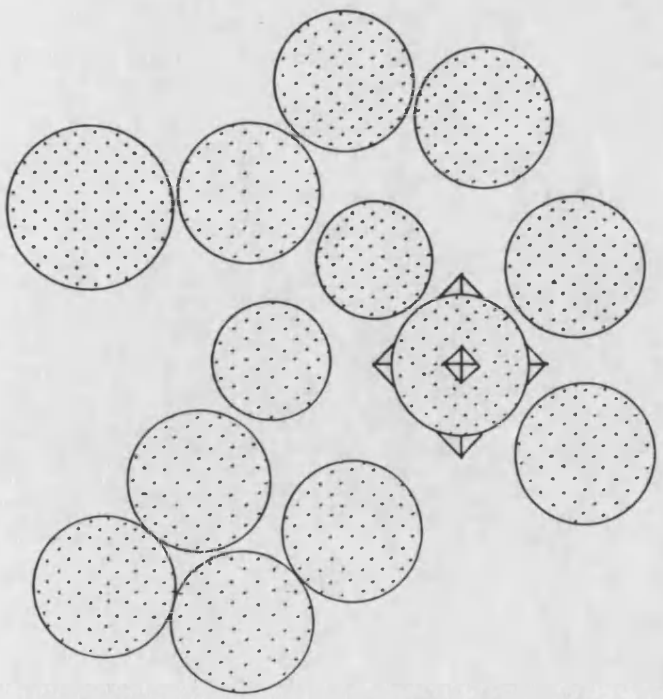

Figure 2.8 Schematic diagram of the positioning of the indenter for a fibre within a tow.

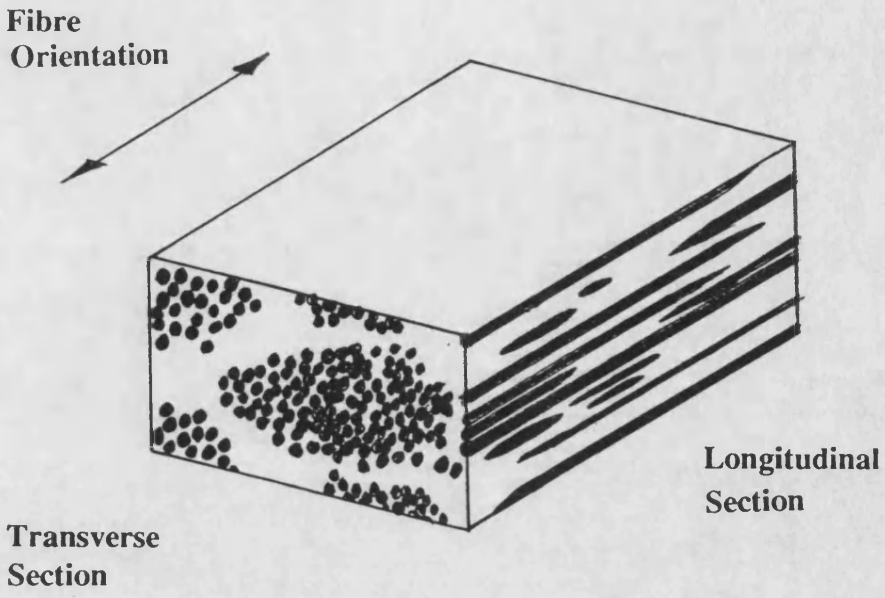

Figure 2.9 Representation of the composite sections used to investigate the microstructure.

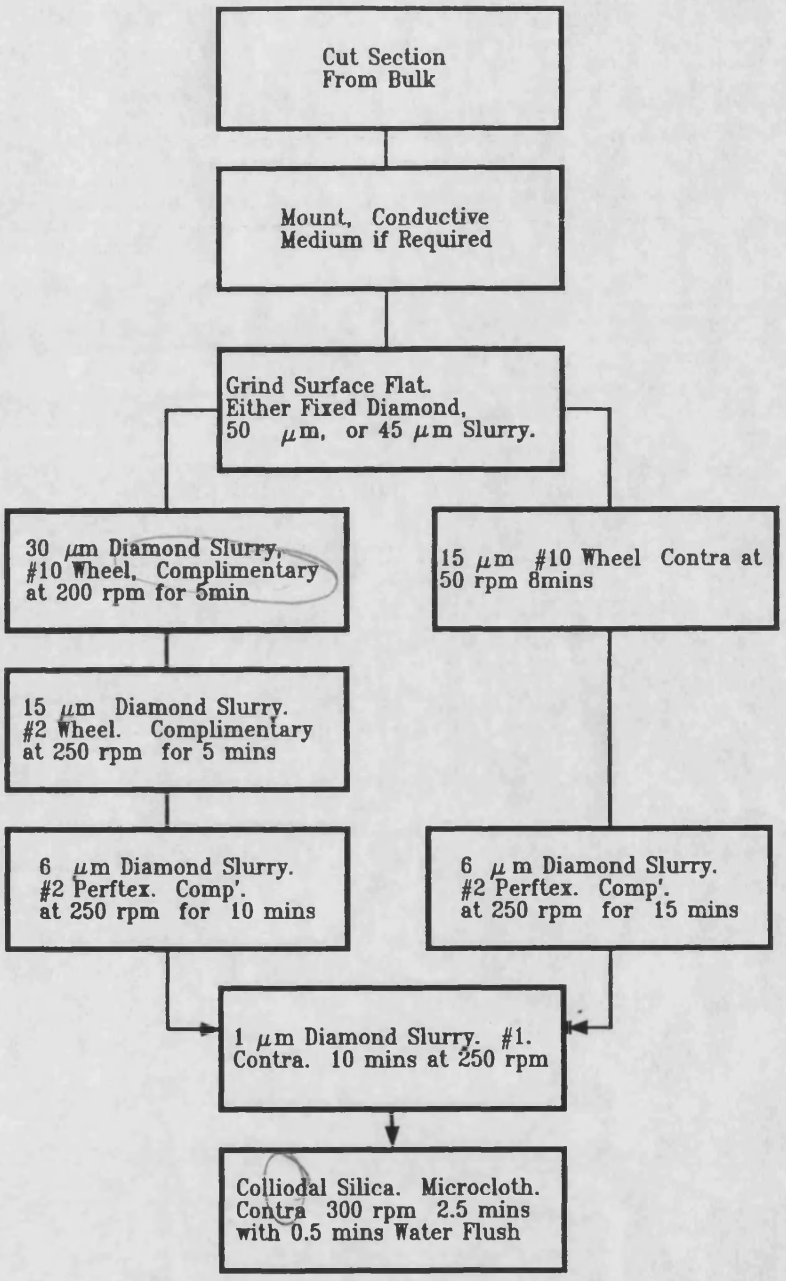

Figure 2.10 Stages in the preparation of a polished section of metal matrix composites, the quoted times are given only as a guide and were controlled by intermittent inspection.

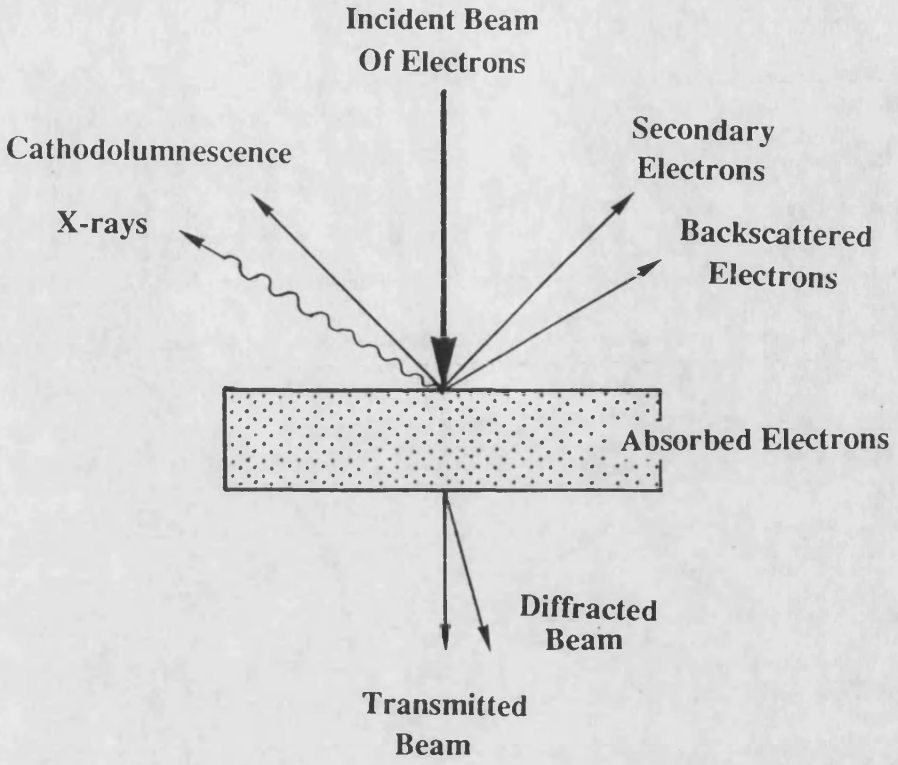

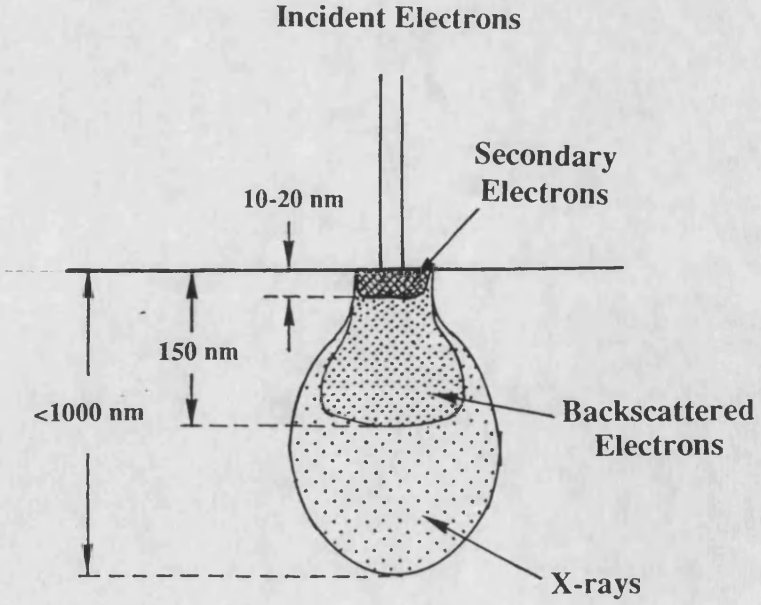

Figure 2.11 Interactions of an electron beam with the specimen and the size of the x-ray generation volume.

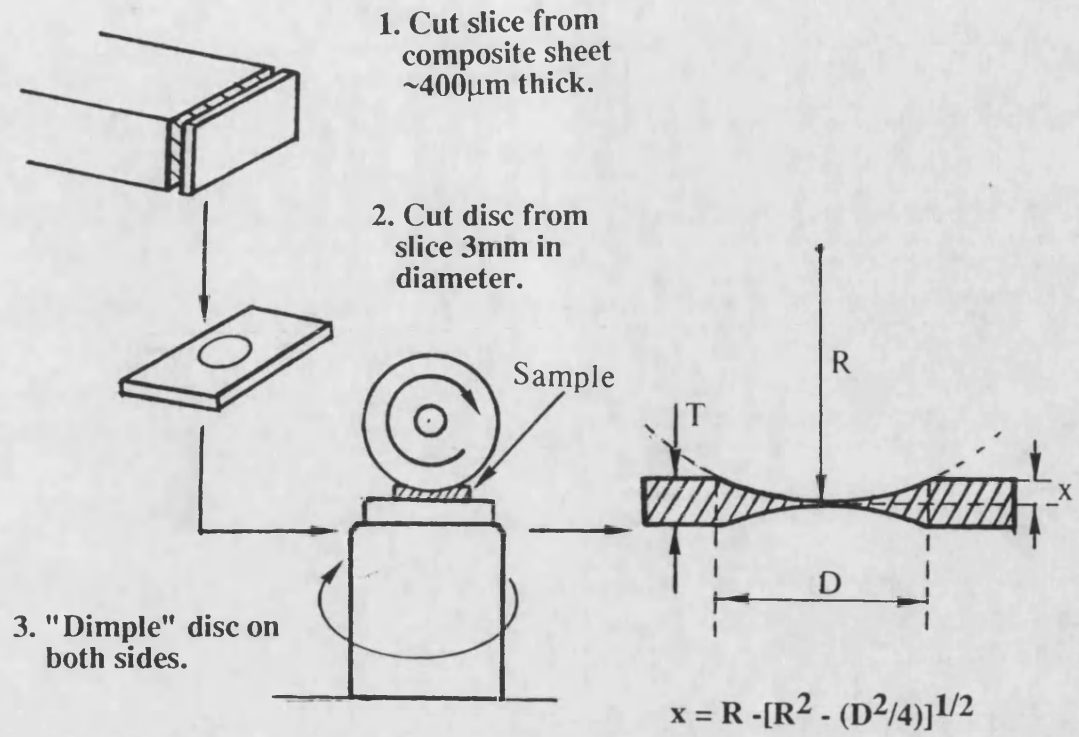

Figure 2.12 The main stages in the "dimpling" technique to produce thin sections of a specimen for transmission electron microscope specimens.

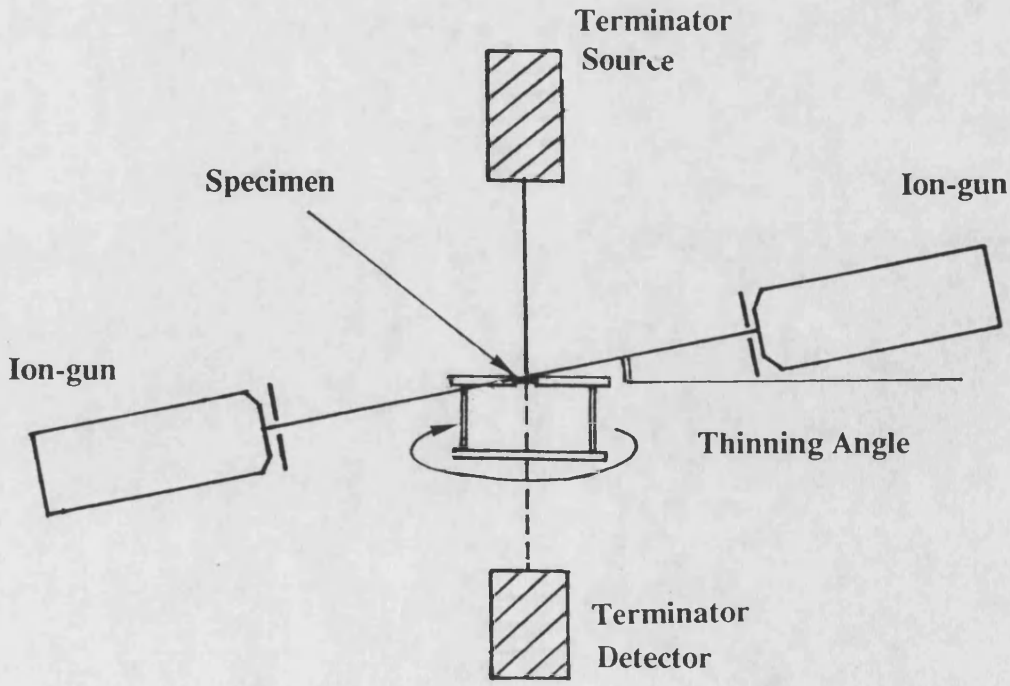

Figure 2.13 Main features of the ion-beam mill used for final thinning of TEM specimens.

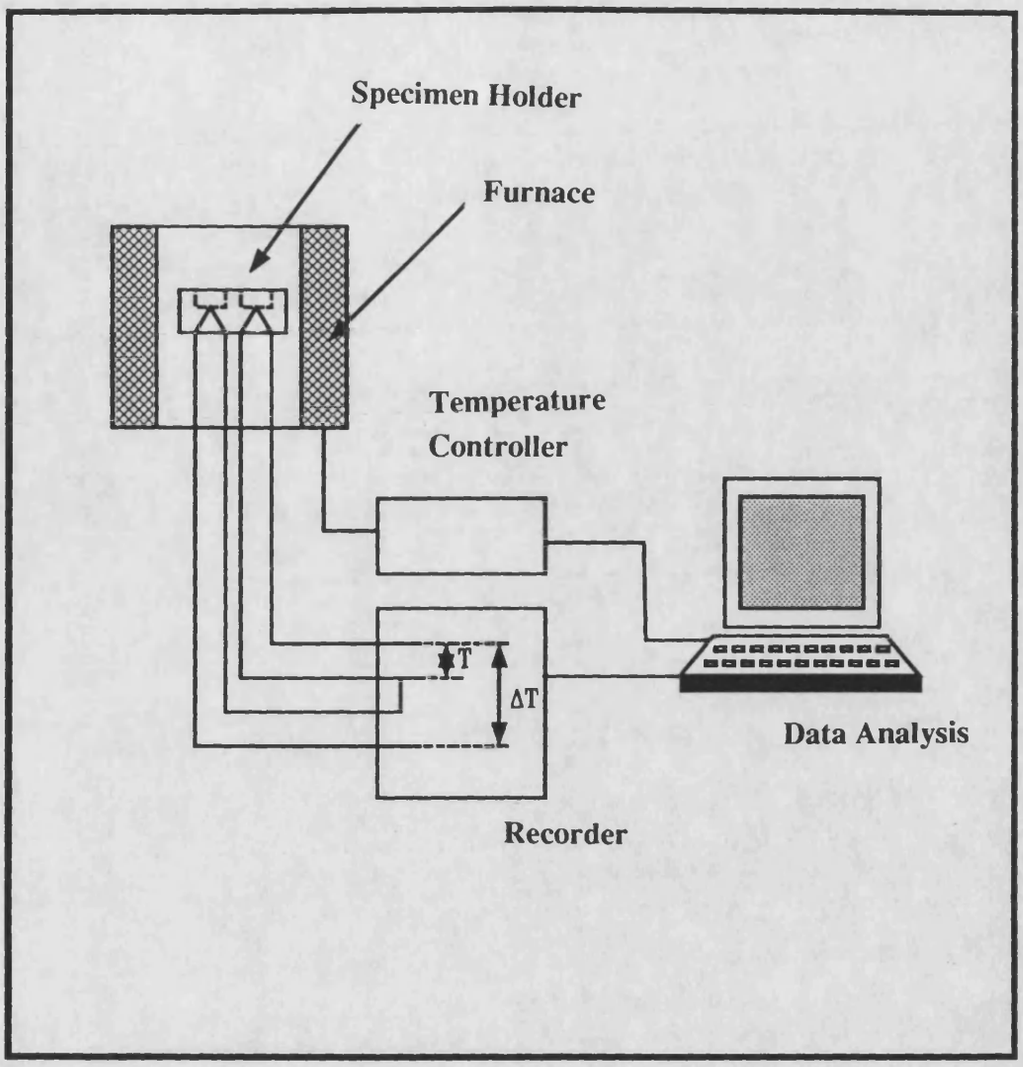

Figure 2.14 Schematic diagram of the main features in the differential scanning calorimetry technique.

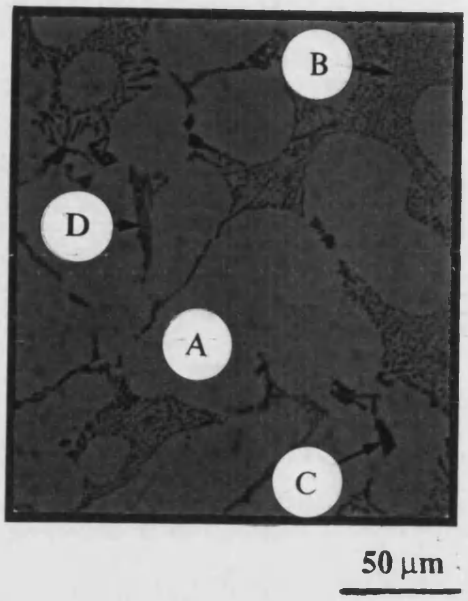

Figure 3.1 An optical micrograph of a prepared section of 357 alloy in the as cast state showing A α-aluminium, B eutectic mixture of Al and Si, C primary silicon and D iron rich intermetallic.

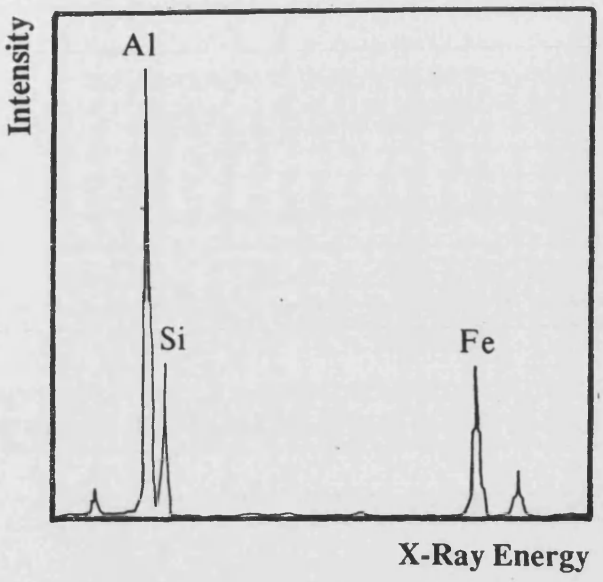

Figure 3.2 Energy dispersive x-ray spectra of the intermetallic phase marked D in 3.1. Found to be $FeSiAl_5$

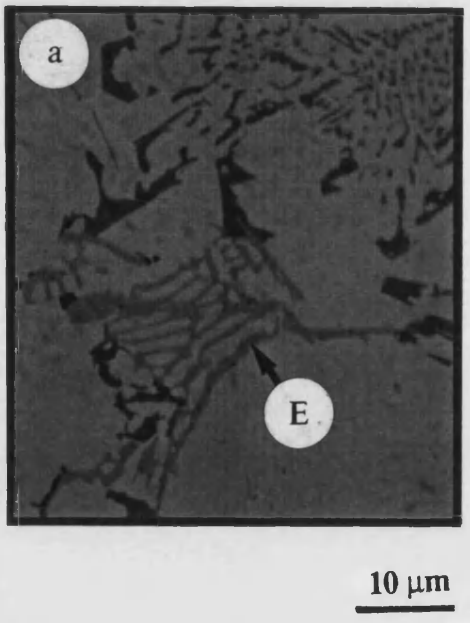

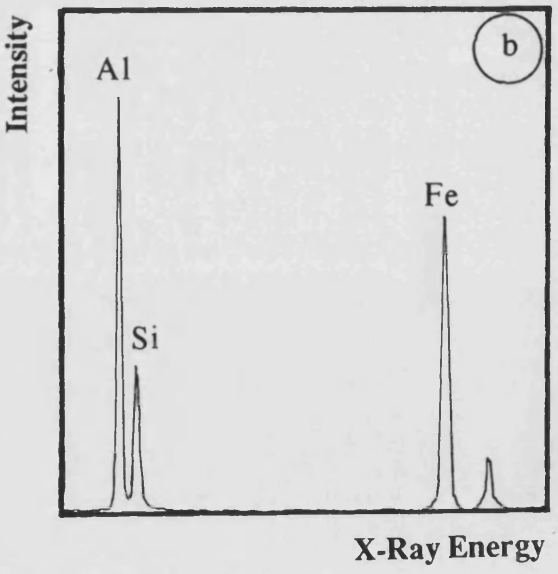

Figure 3.3 a. The optical micrograph of a second type of iron rich intermetallic which has a 'script' morphology and b. the corresponding EDS of the phase ($FeSi_2Al_4$)

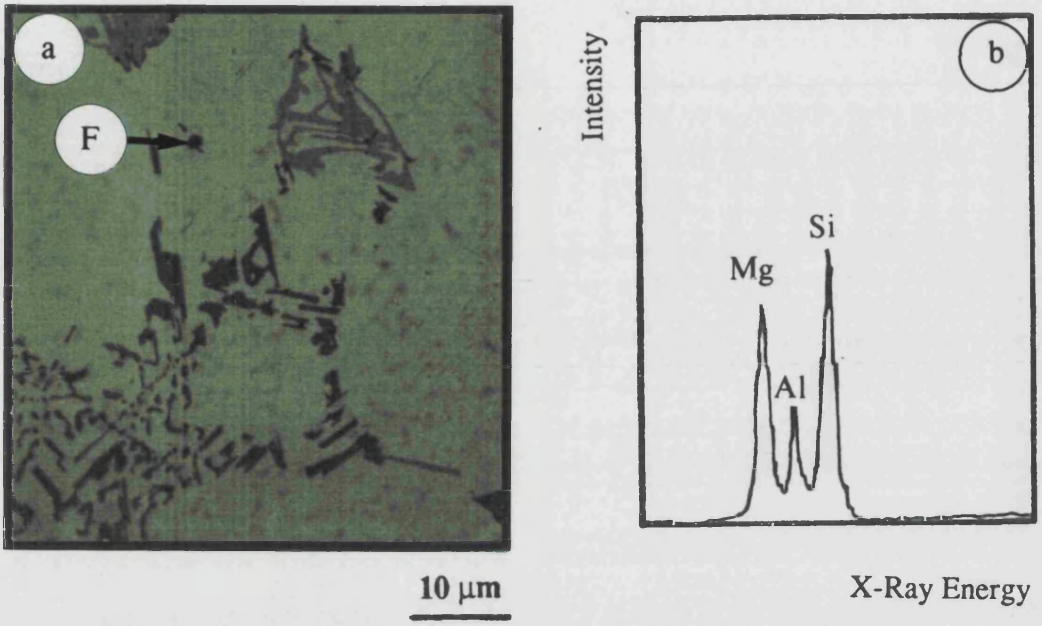

Figure 3.4 a. As cast 357 with a dark phase in the aluminium dendrite arms with the EDS trace b. showing the presence of magnesium and silicon.

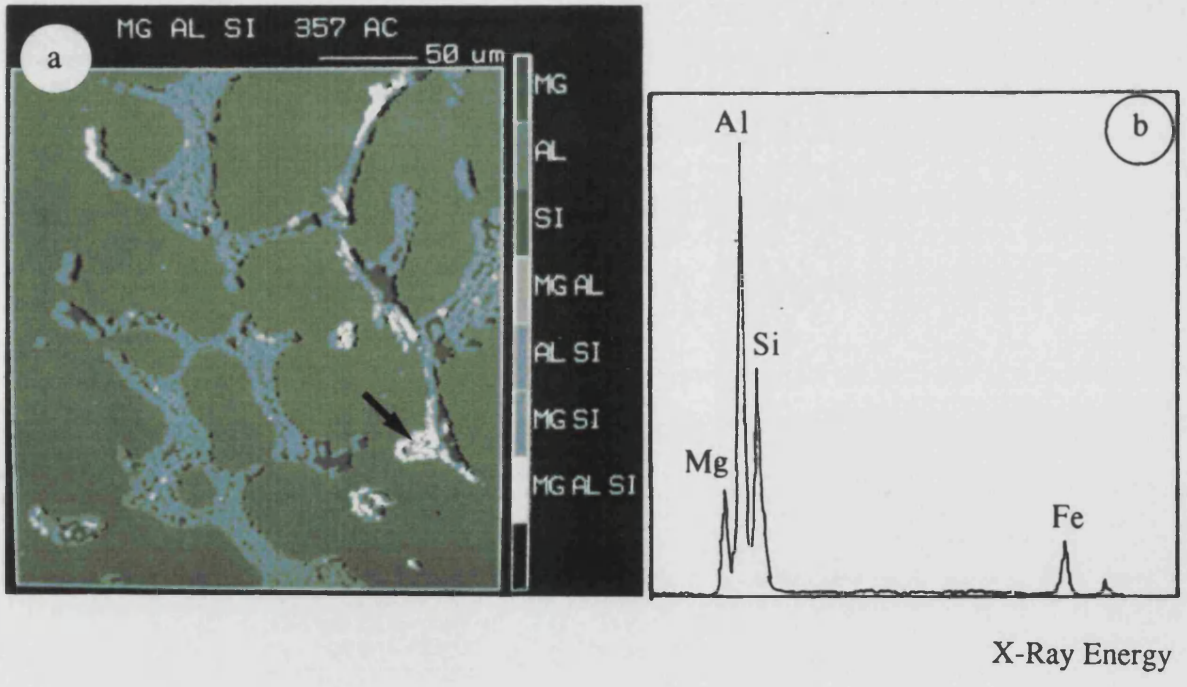

Figure 3.5 A x-ray combination map of the as cast 357 alloy showing the magnesium present in bulk phases, a, and the EDS trace of a similar bulk phase, b.

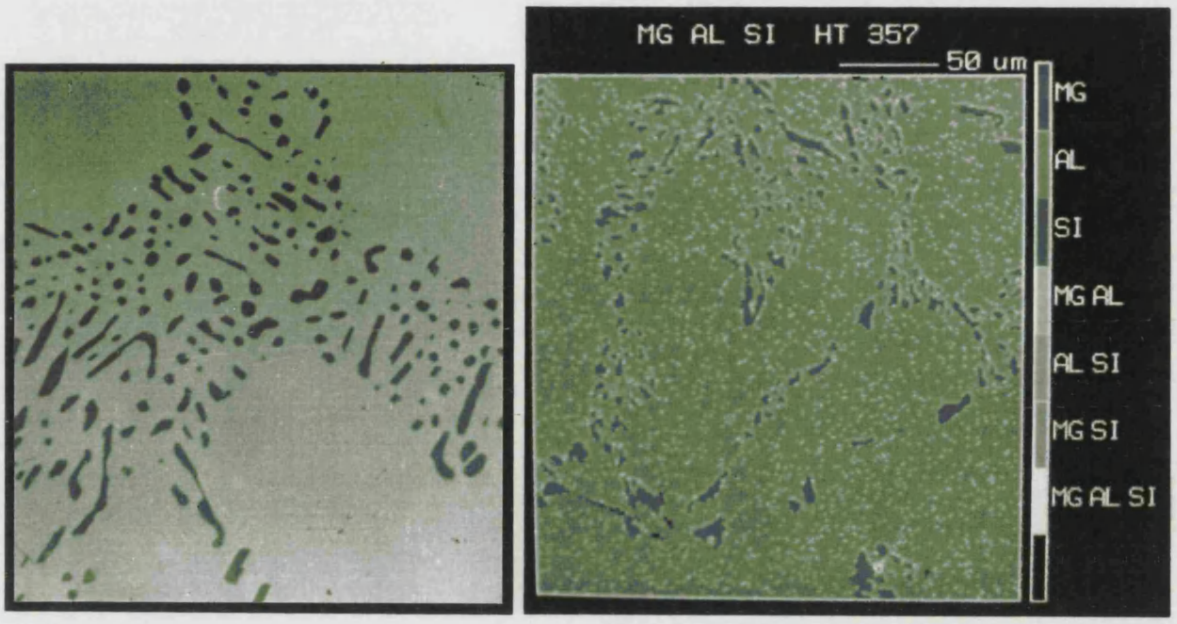

Figure 3.6 The microstructure of the 357 alloy after heat treatment with spheriodized silicon.

Figure 3.7 An x-ray combination map of the heat treated 357 showing the homogeneous distribution of magnesium.

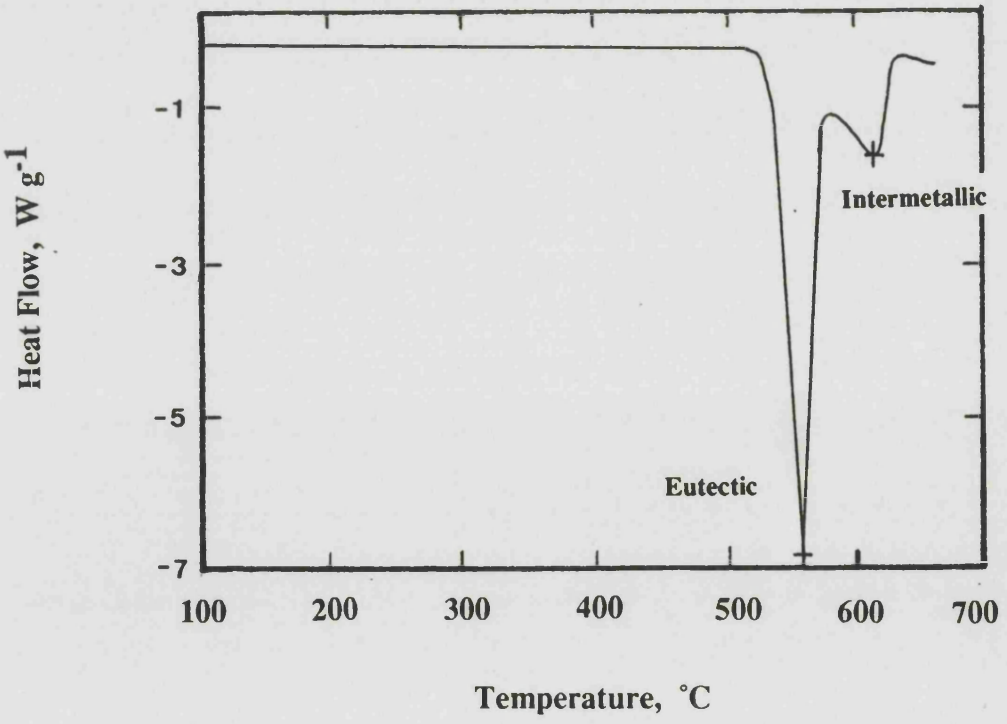

Figure 3.8 The DSC thermogram for the 357 alloy heated at a rate of 10° min^{-1} with twin endotherm.

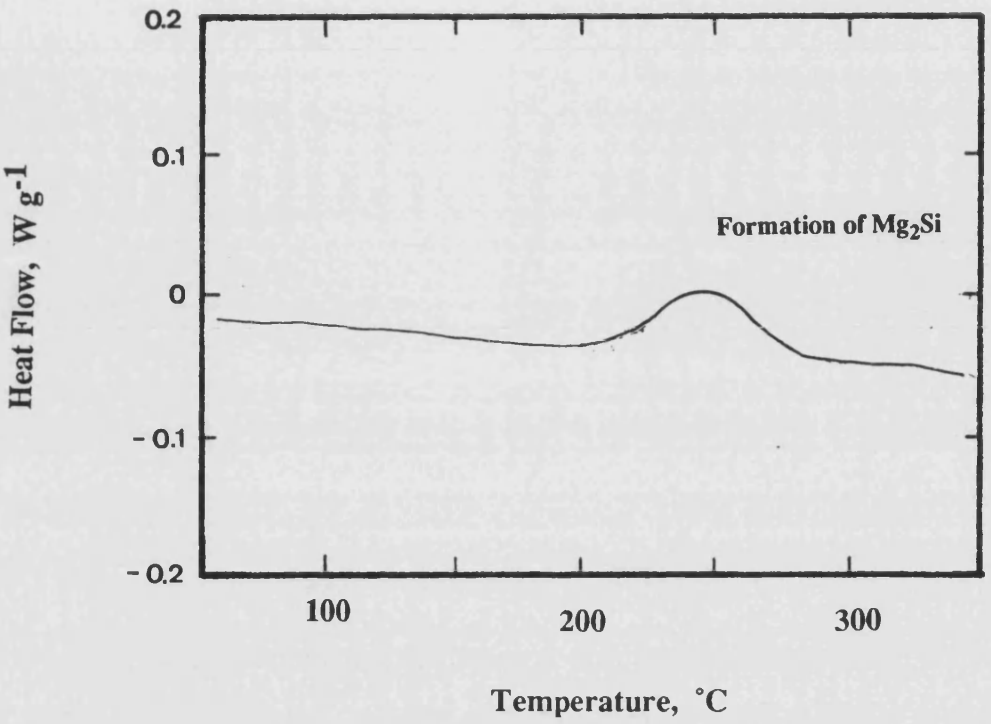

Figure 3.9 Detail of the DSC trace showing a exothermic peak.

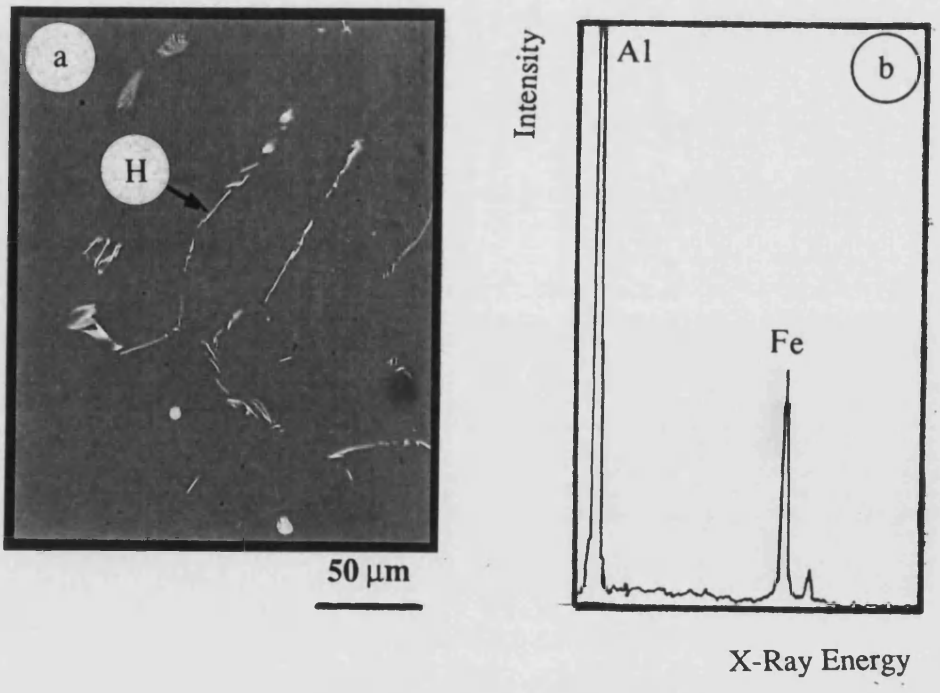

Figure 3.10 A back scattered electron image of a prepared section of the pure aluminium, a, with the EDS of the second phase, H, b.

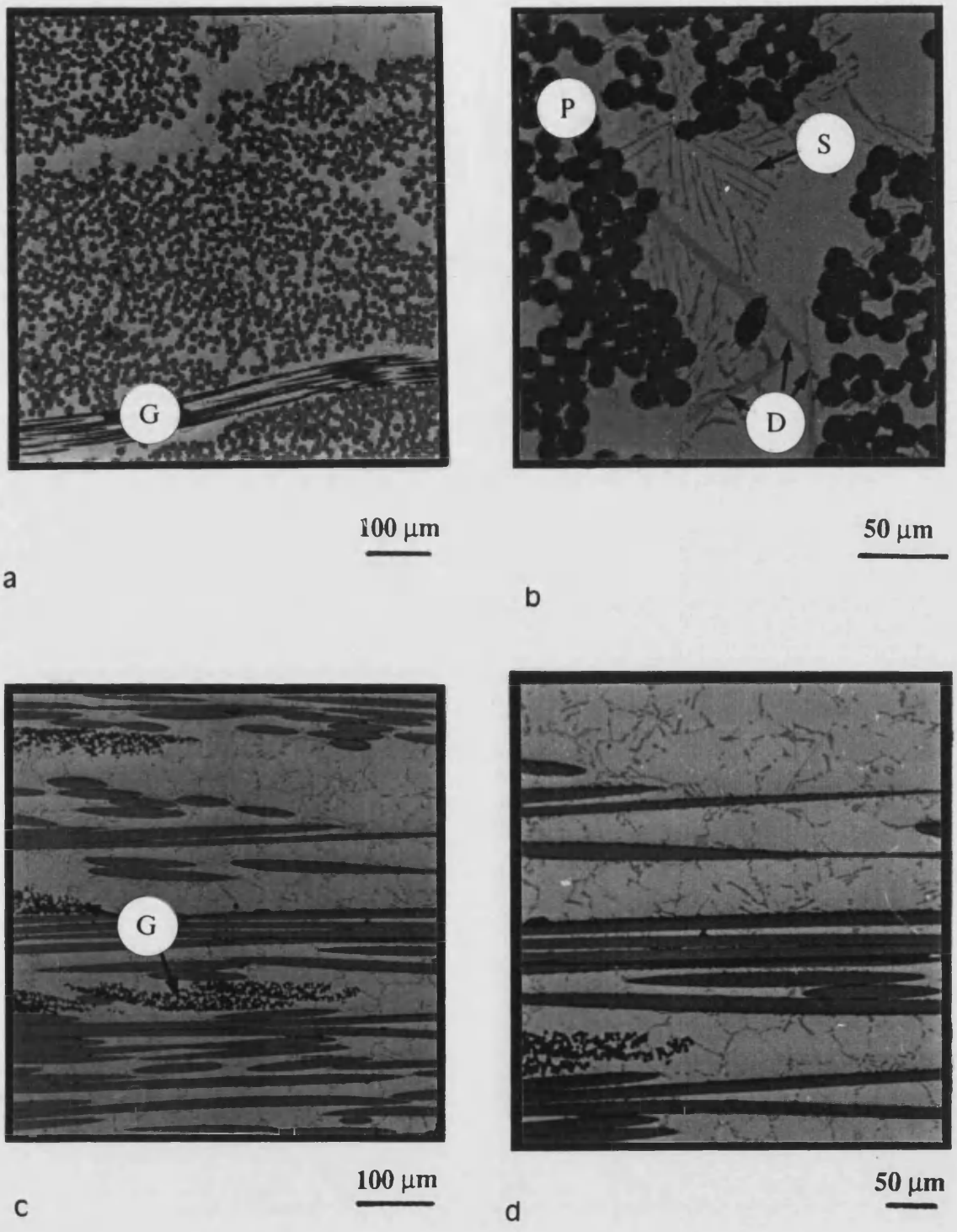

Figure 3.11 Optical microstructure of the Nicalon-alloy matrix composite in transverse section, a, b, and longitudinal section, c, d.

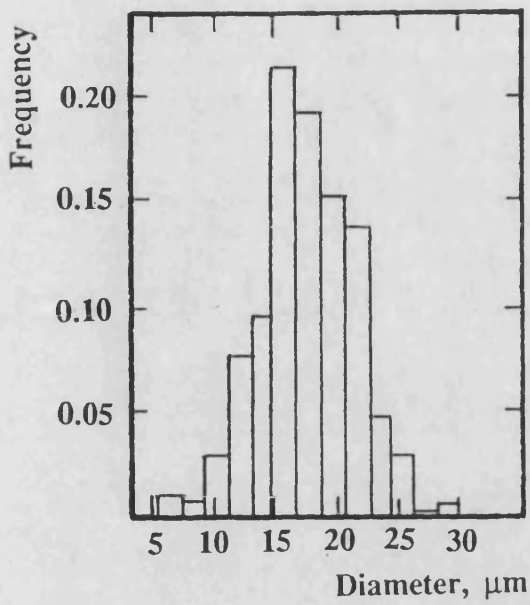

Figure 3.12 Measured fibre diameter distribution for the Nicalon, with a mean of 14.8μm, measured from ~800 fibres.

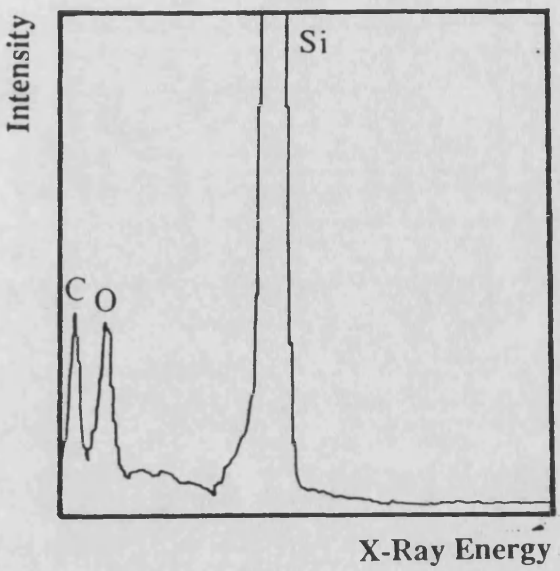

Figure 3.13 The EDS trace revealing the only elements in the Nicalon fibre were silicon, carbon and oxygen.

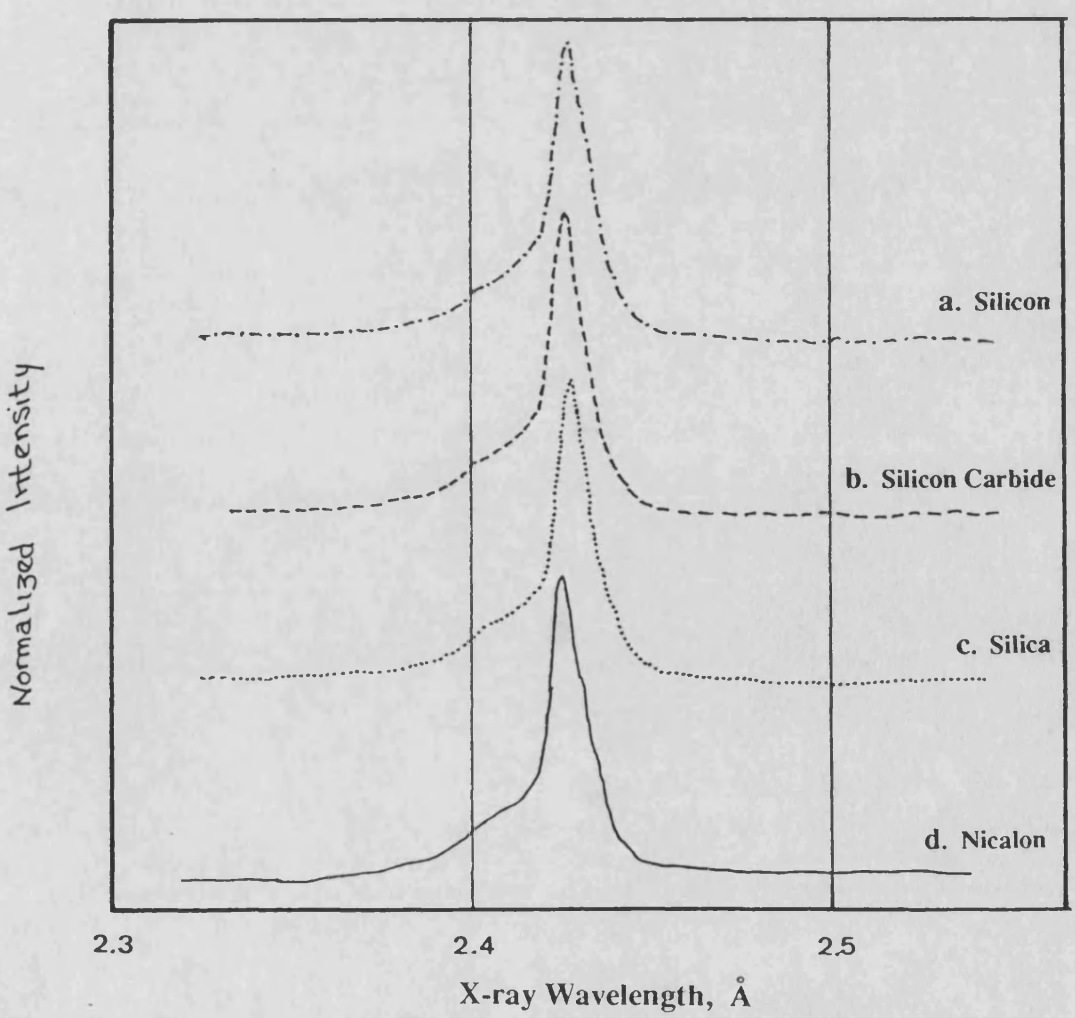

Figure 3.14 Silicon K_α x-ray emission peaks measured on the PET crystal, for pure silicon, a, silicon carbide, b, silica, c and Nicalon, d. All are normalized to the same peak height and separated to allow comparison.

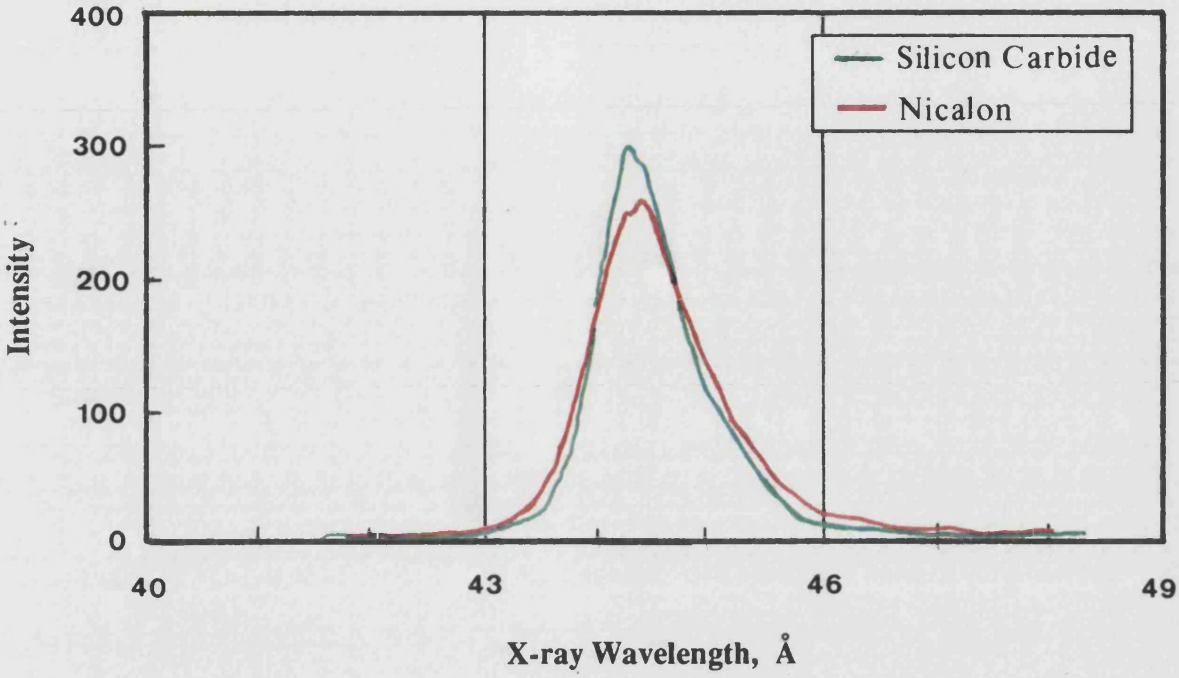

Figure 3.15 Carbon K_α x-ray emission peaks measured on the STE crystal for silicon carbide, a, and Nicalon, b.

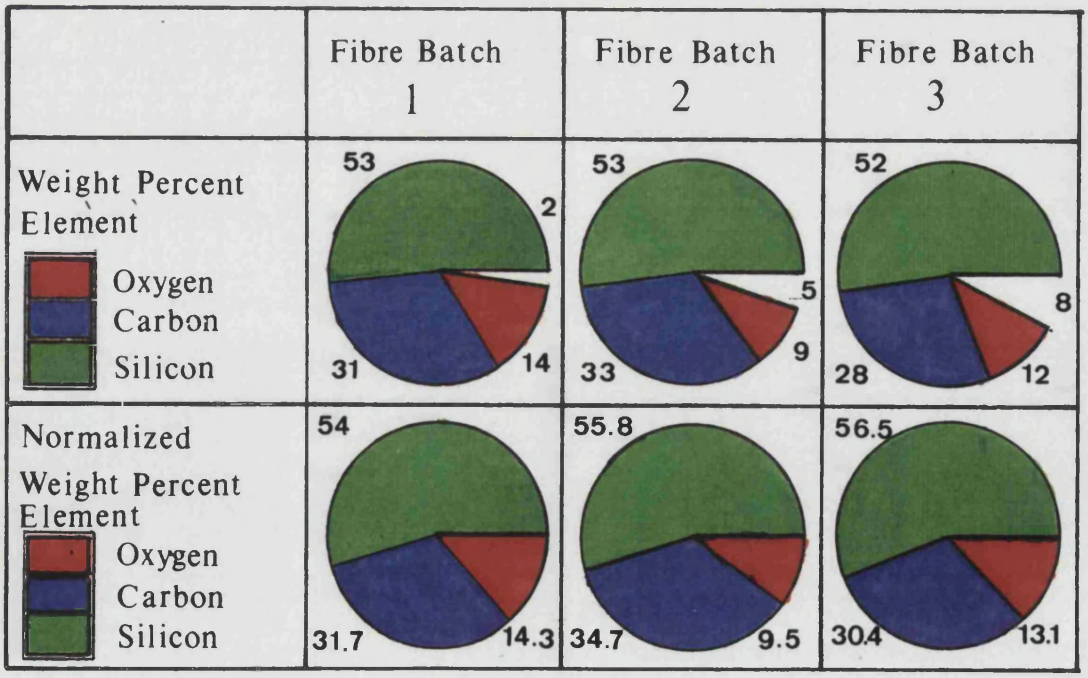

Figure 3.16 Pie chart showing the percentages of each element in the Nicalon fibre before, a, and after, b, normalization to 100 wt%.

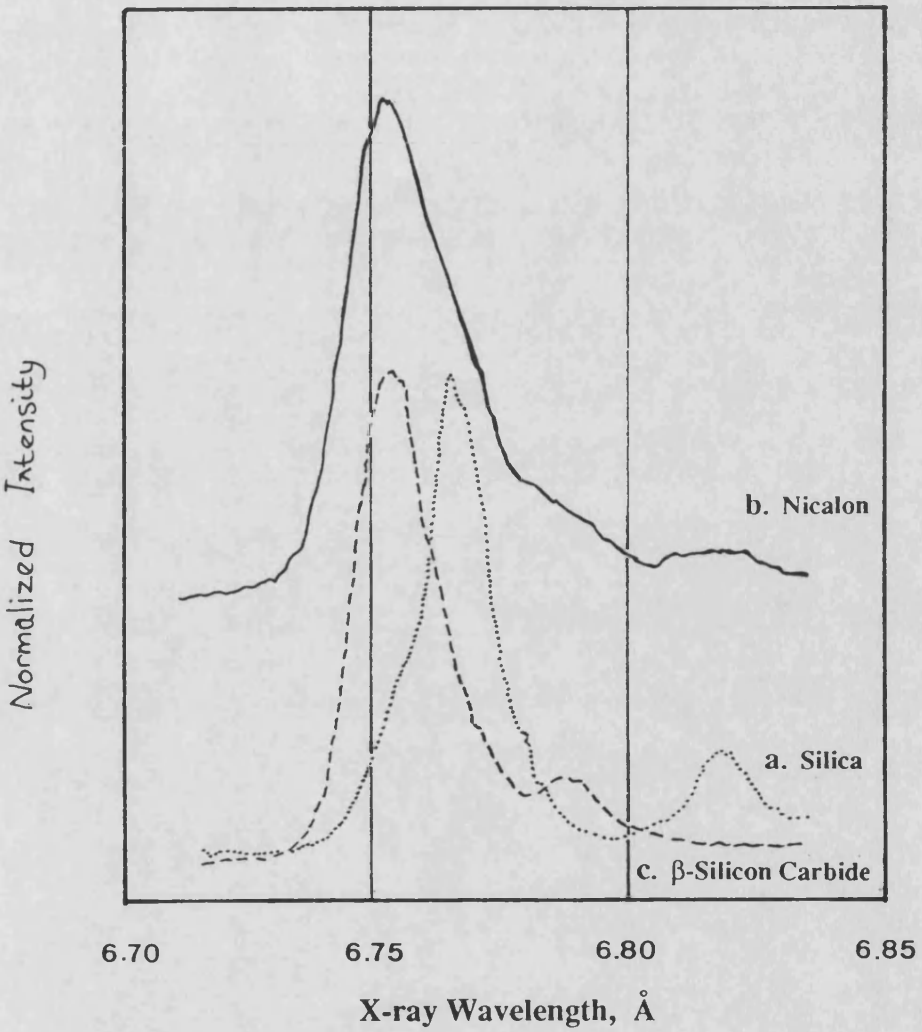

Figure 3.17 Silicon K_β x-ray emission peaks for silicon carbide, a, silica, b and Nicalon fibre, c. All the curves have been normalized to the same height and separated for clarity.

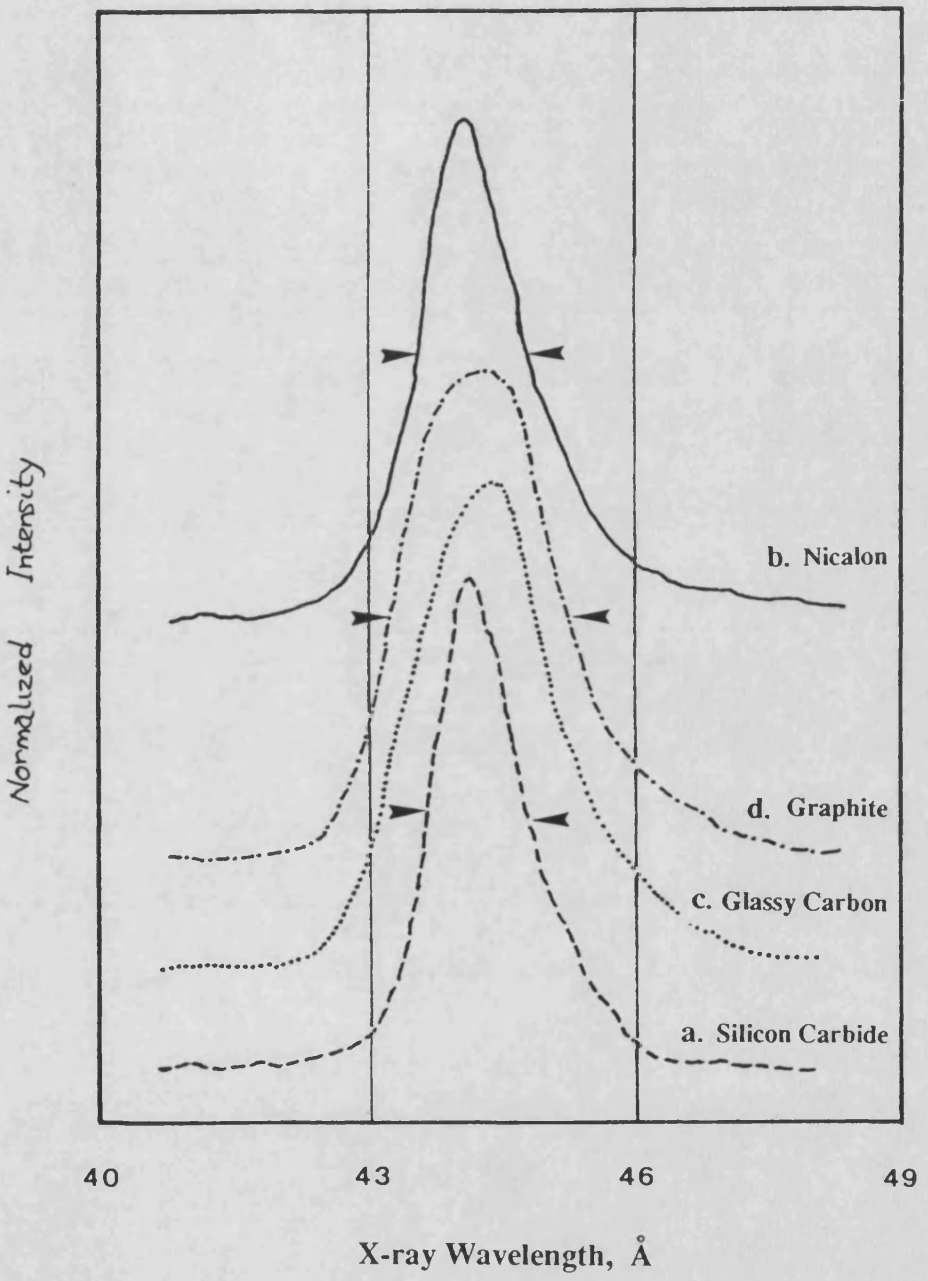

Figure 3.18 Normalized carbon K_α x-ray emission peaks for silicon carbide, a, Nicalon, b, glassy carbon, c and graphitic carbon, d. The arrows on each curve represent the full width at half maximum (FWHM) values.

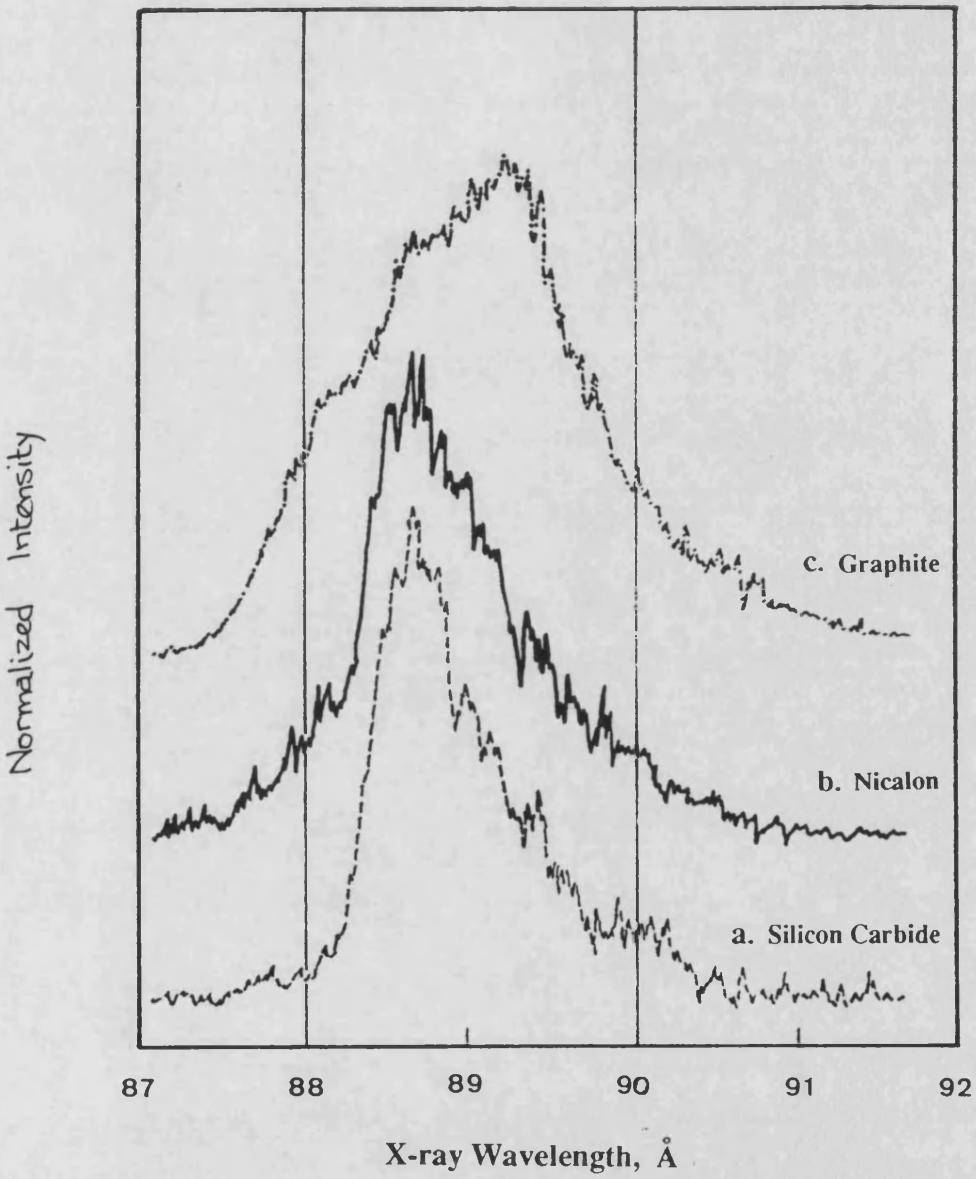

Figure 3.19 Normalized carbon K_α second order x-ray emission peaks, for silicon carbide, a, Nicalon, b, and graphite, c.

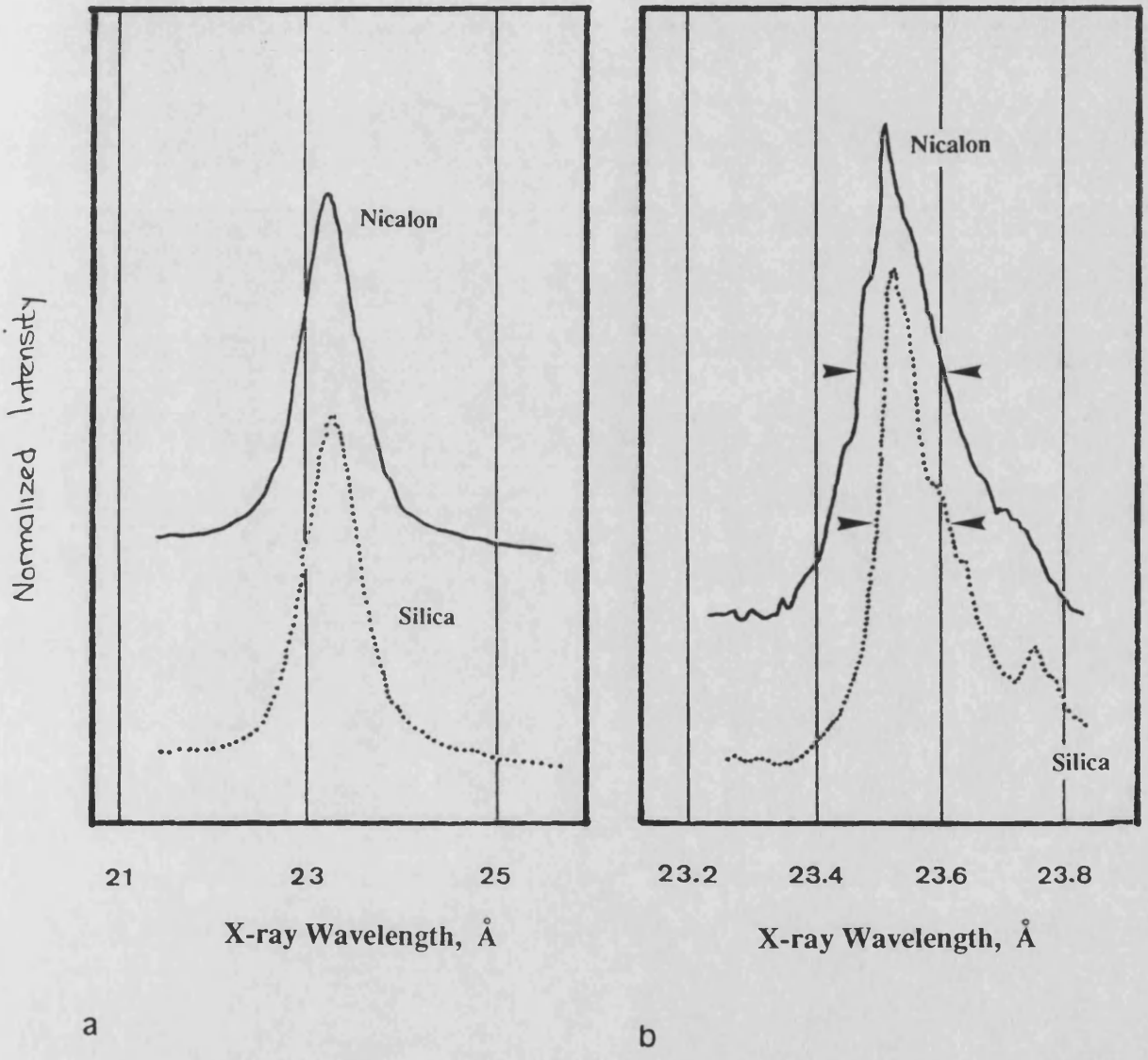

Figure 3.20 Normalized x-ray emission peaks for oxygen K_α measured using, a, the LDE1 and b, TAP analysing crystals, for silica and Nicalon.

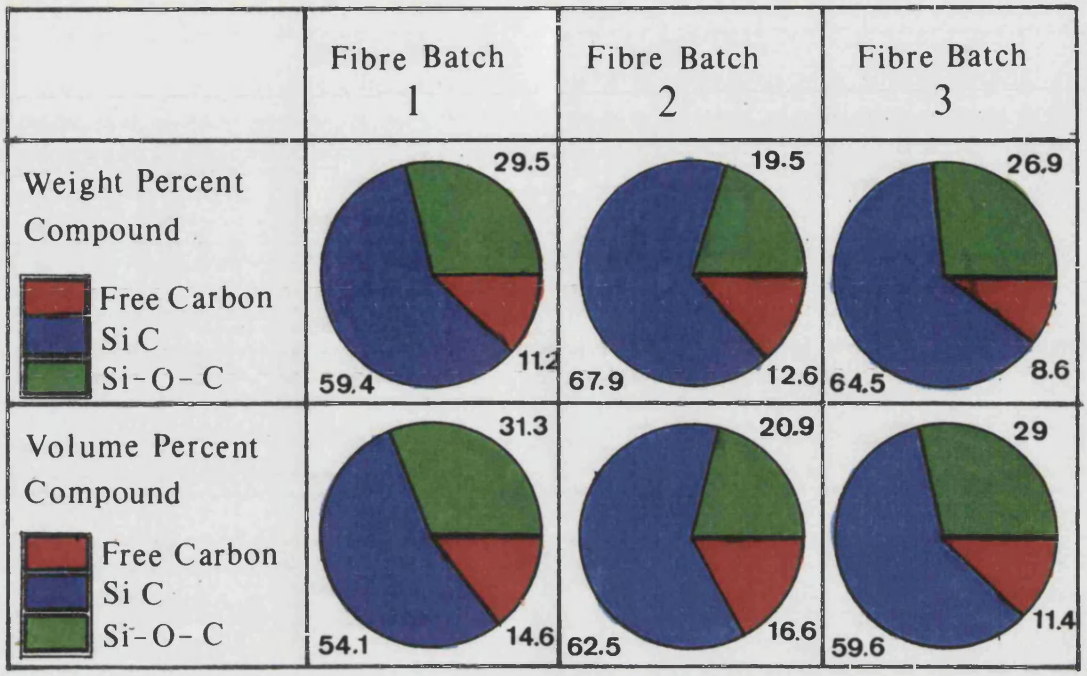

Figure 3.21 Calculated composition of the Nicalon material based on the normalized weight percentages given in figure 3.16.

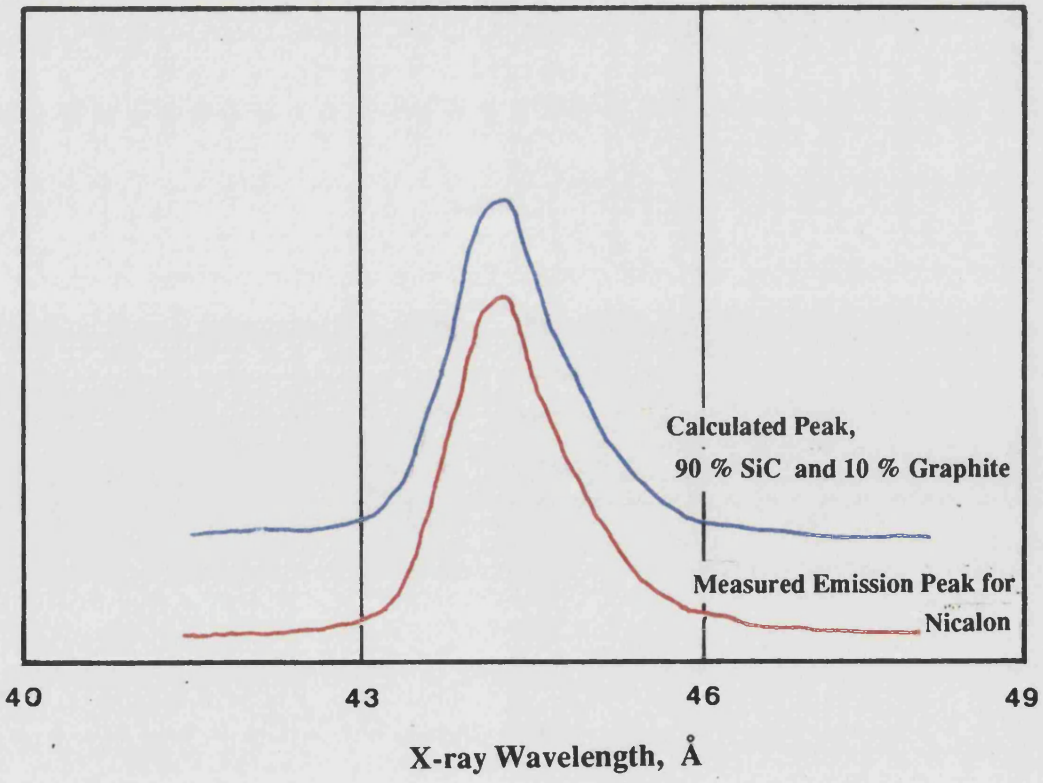

Figure 3.22 Carbon K_α x-ray peak as measured for the Nicalon fibre, a, and calculated using 10% of the graphite peak and 90% of the SiC peak, b.

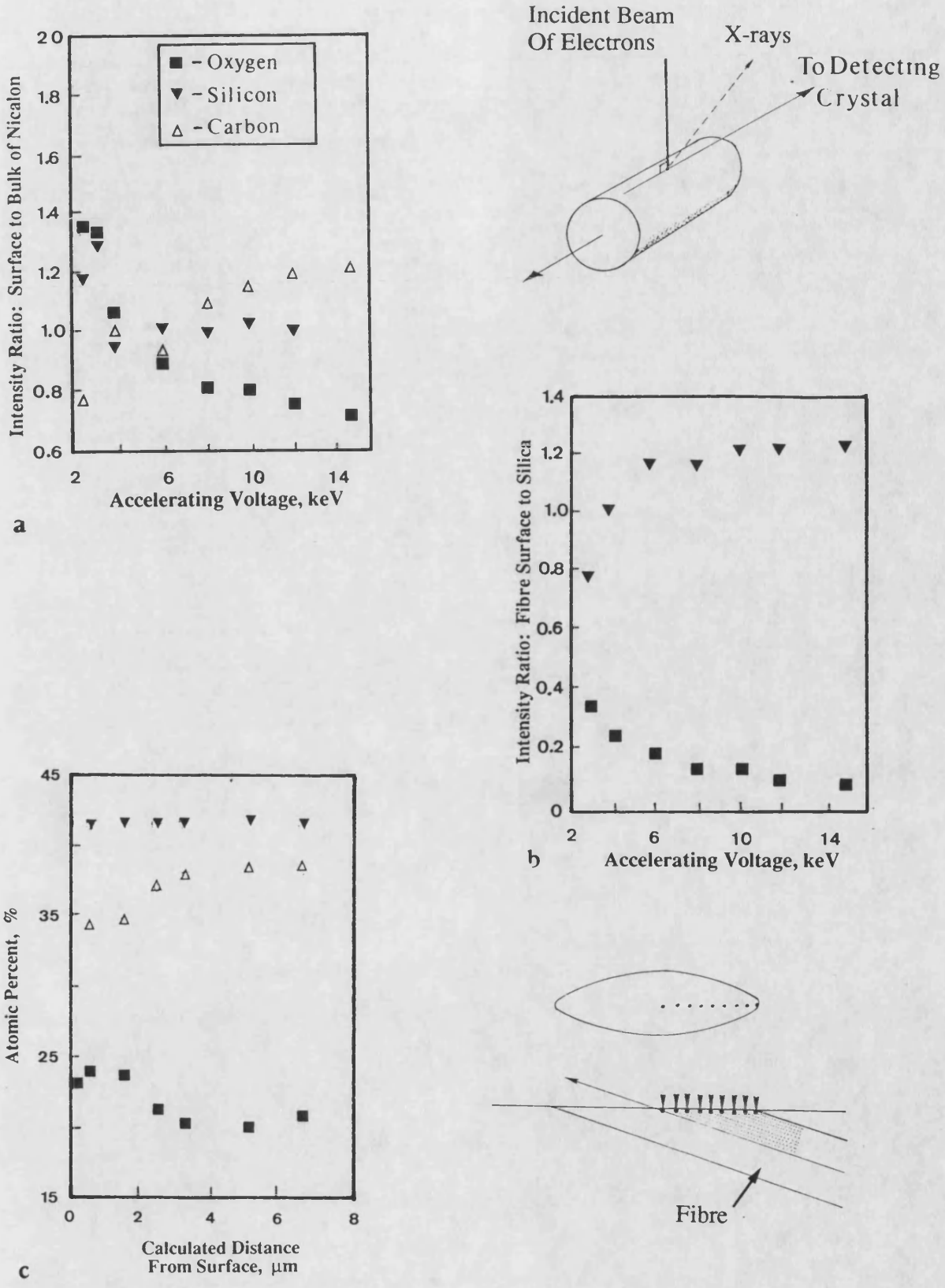

Figure 3.23 Surface analysis of the Nicalon fibre; a, comparing the intensity of x-rays emitted from the fibre surface with the bulk at different accelerating voltages, b, the intensity from fibre surface compared with a silica standard and c, stepped quantitative analysis across a low angled section fibre.

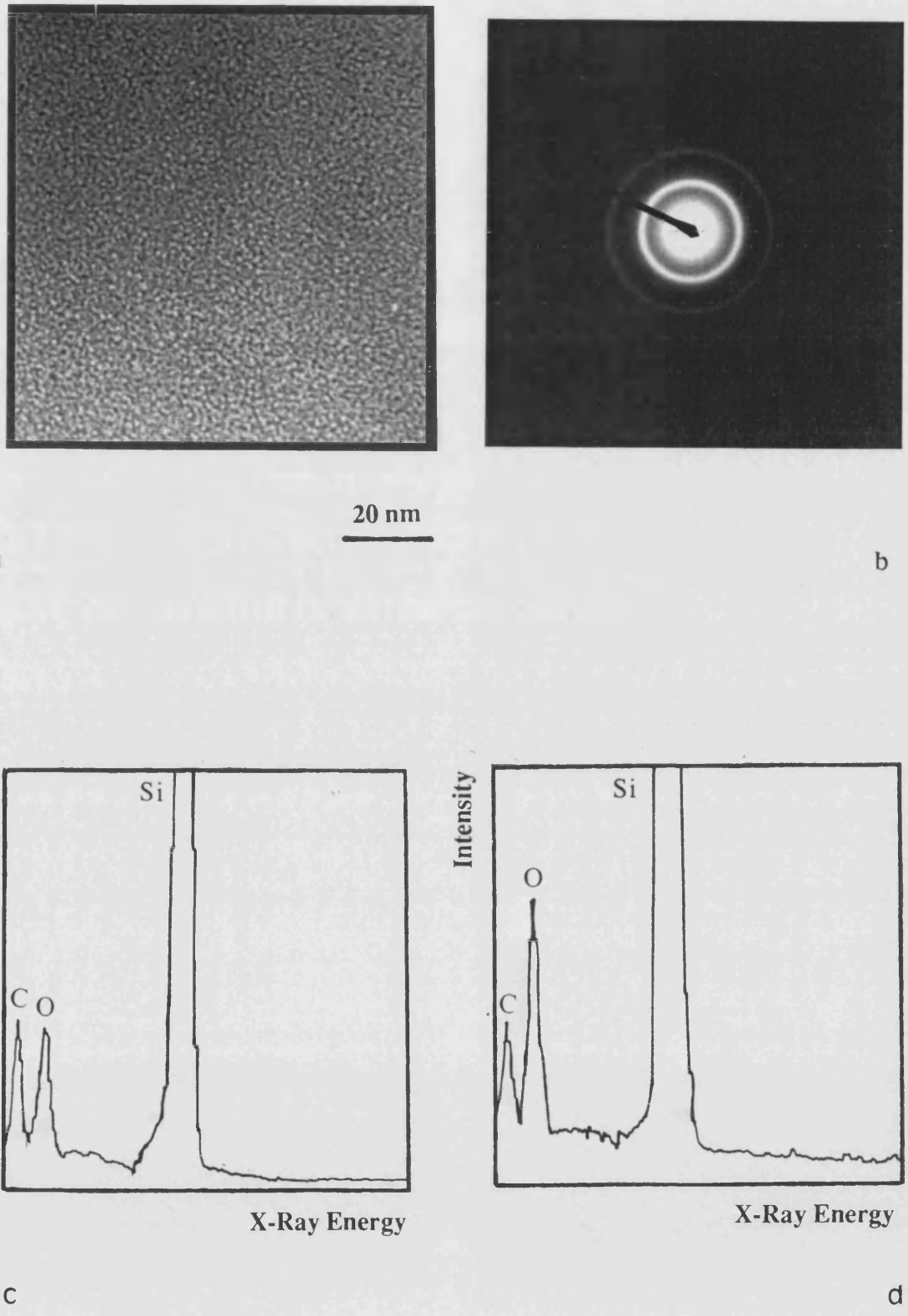

Figure 3.24 Transmission electron microscope image of the Nicalon fibre, a, with the corresponding selected area diffraction pattern, b, and the EDS spectra from the bulk fibre, c, and from the surface region of a fibre in an uninfiltrated region, d.

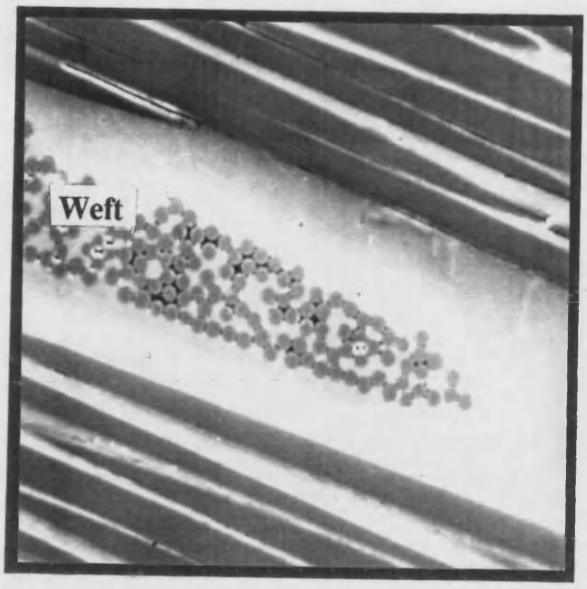

b

50 μm

a

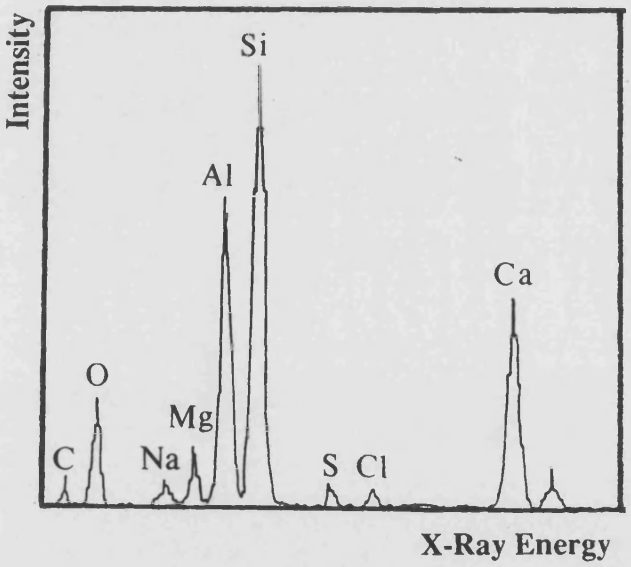

c

Figure 3.25 Prepared surface in the SEM showing the glass weft, a, the EDS trace for the weft, b, and the SAD pattern showing the amorphous nature of the weft, c.

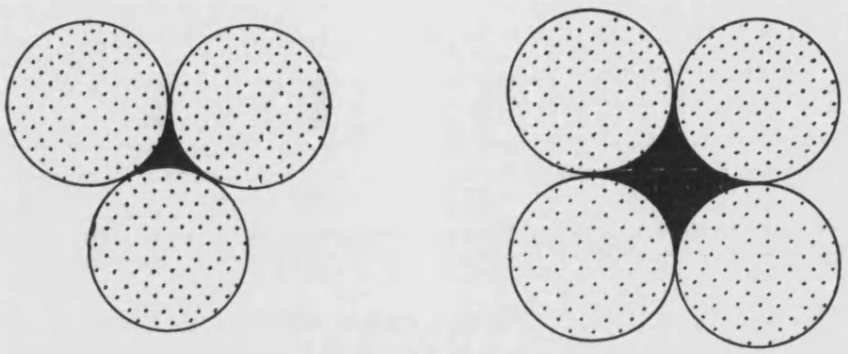

a

Figure 3.26 The types of porosity in the composite due to the fibre packing.

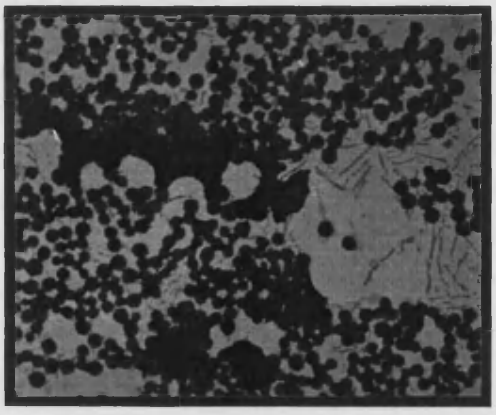

100 μm

Figure 3.27 Optical micrograph of the gross porosity found in the centre of thick Nicalon/Al-Si composite sheets.

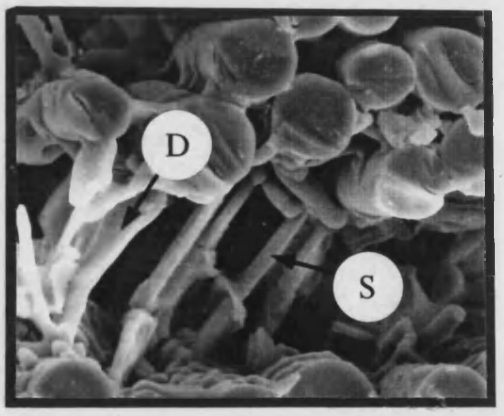

20 μm

Figure 3.28 Scanning electron micrograph of a Nicalon/Al-Si composite after selective removal of the aluminium matrix constituent, revealing the three dimensional networks of silicon, S, and intermetallics, D, which connect fibres.

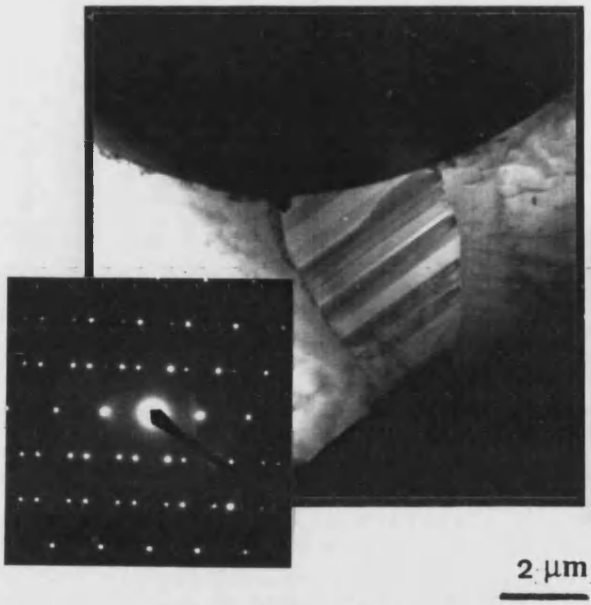

Figure 3.29 Transmission electron micrograph of a twinned silicon particle bridging between two fibres in the Nicalon/Al-Si composite.

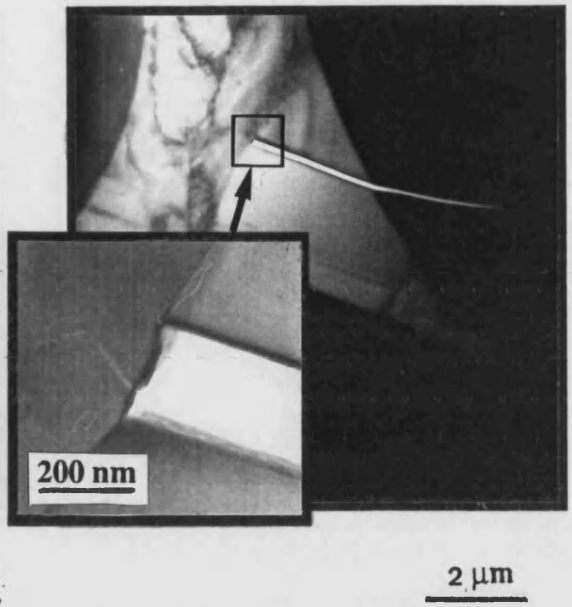

Figure 3.30 Transmission electron micrograph of a fractured silicon particle. The point at which the crack contacts the aluminium shows the presence of iron.

Figure 3.31 Fracture of silicon particle/fibre interface with the aluminium phase between showing a large number of dislocations but still attached to the fibre and silicon.

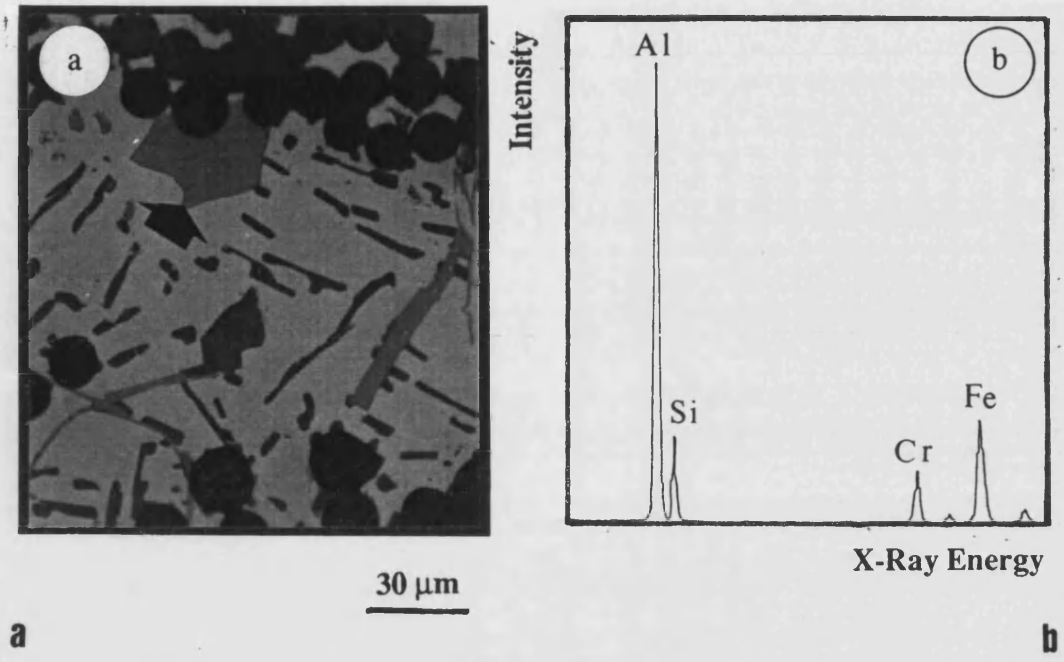

Figure 3.32 Optical micrograph, a, of an intermetallic in the Nicalon-357 composite which the EDS, b, shows to contain chromium in addition to iron, aluminium and silicon.

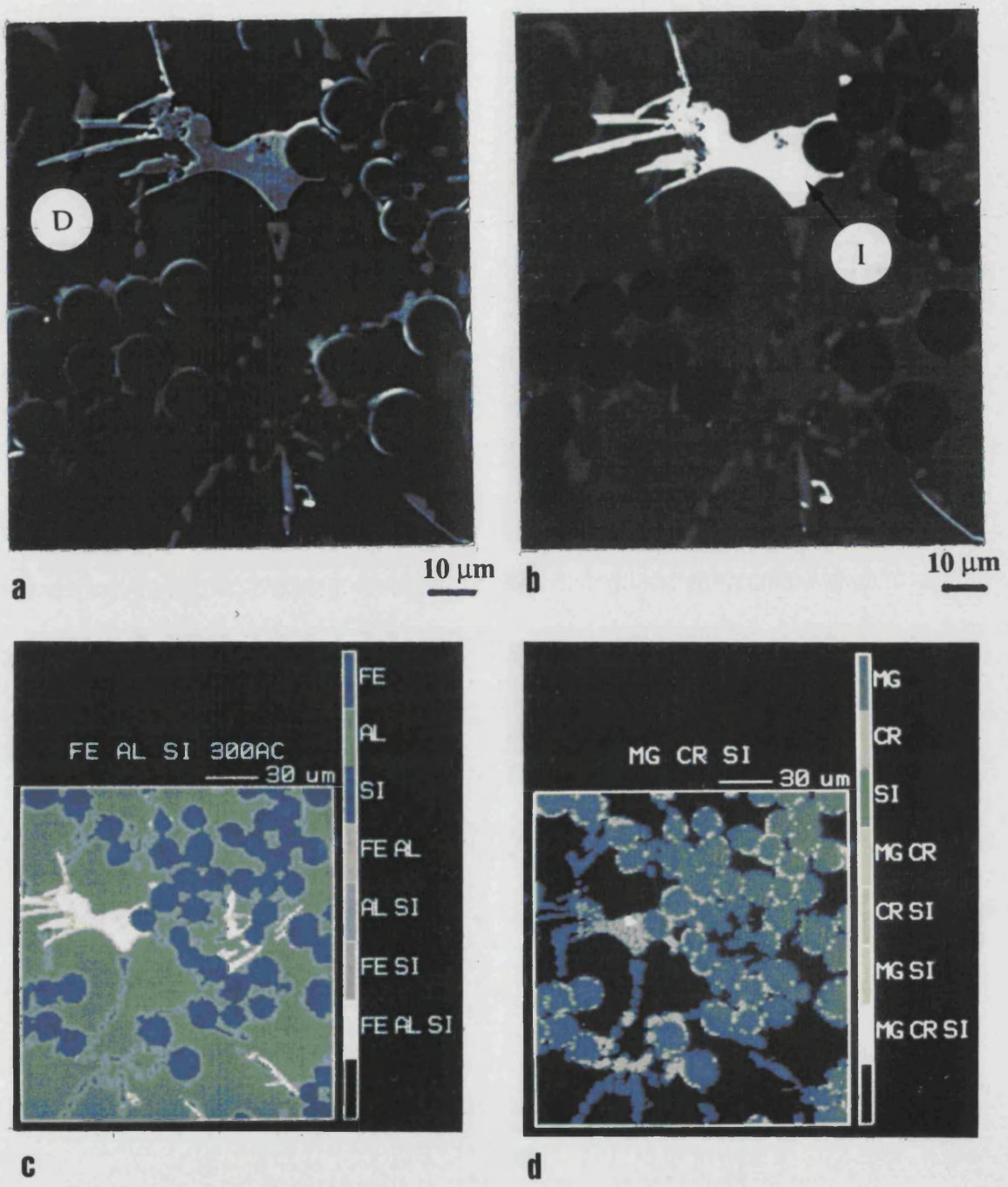

Figure 3.33 The as cast Nicalon-357 composite viewed in the SEM, with a, a secondary electron image, b, a back scattered image, c, an x-ray combination map of the region for iron, aluminium and silicon, and d, the x-ray combination map for magnesium, chromium and silicon. These micrographs show the presence of two intermetallics, D shows iron, aluminium and silicon, whereas I shows chromium in addition.

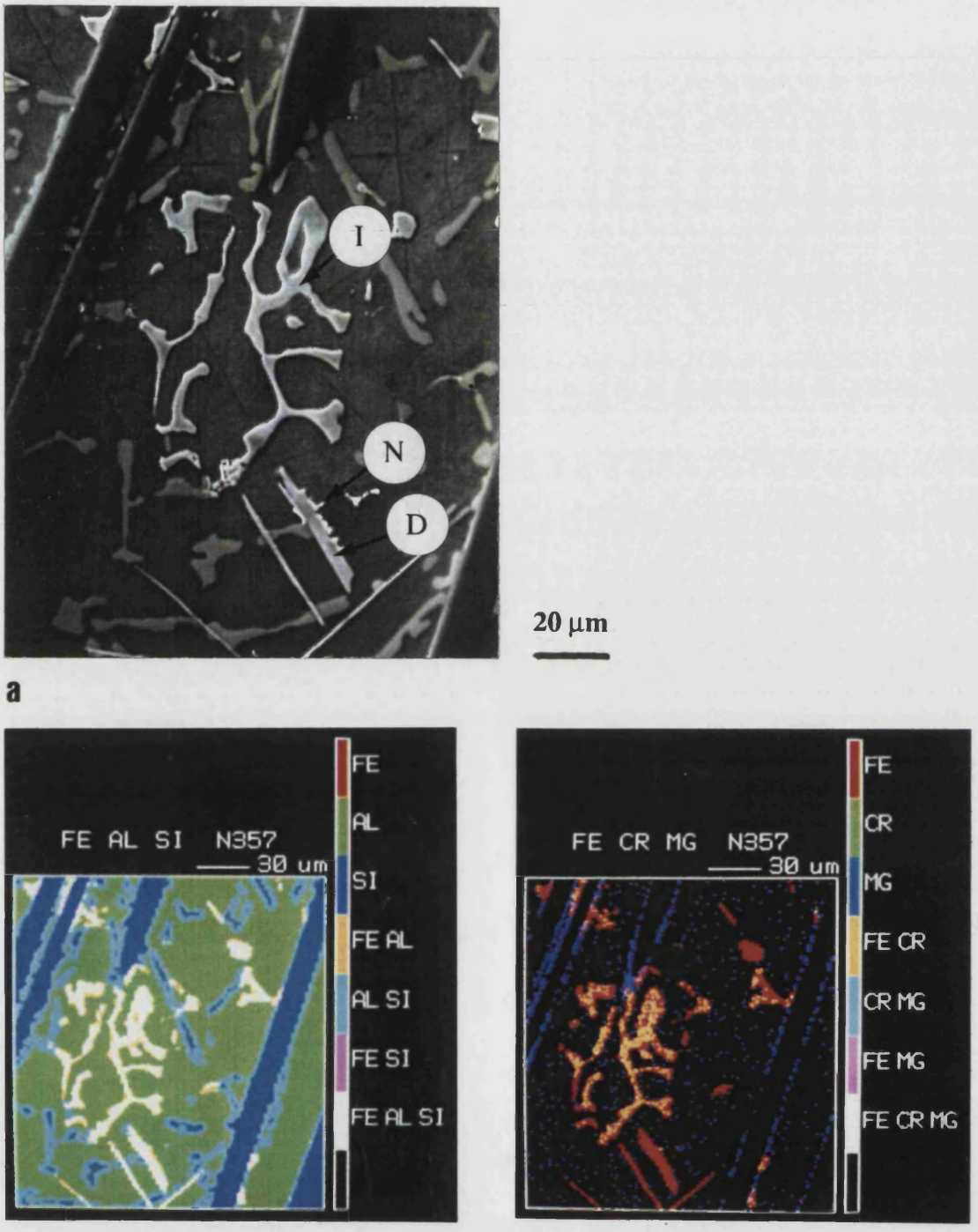

Figure 3.34 An SEM, a, of a region of the matrix which shows large intermetallics which the WDS x-ray combination maps for, b, iron, aluminium and silicon, and, b, iron, chromium and magnesium, revealed to be either Fe-Al-Si or Fe-Al-Si-Cr.

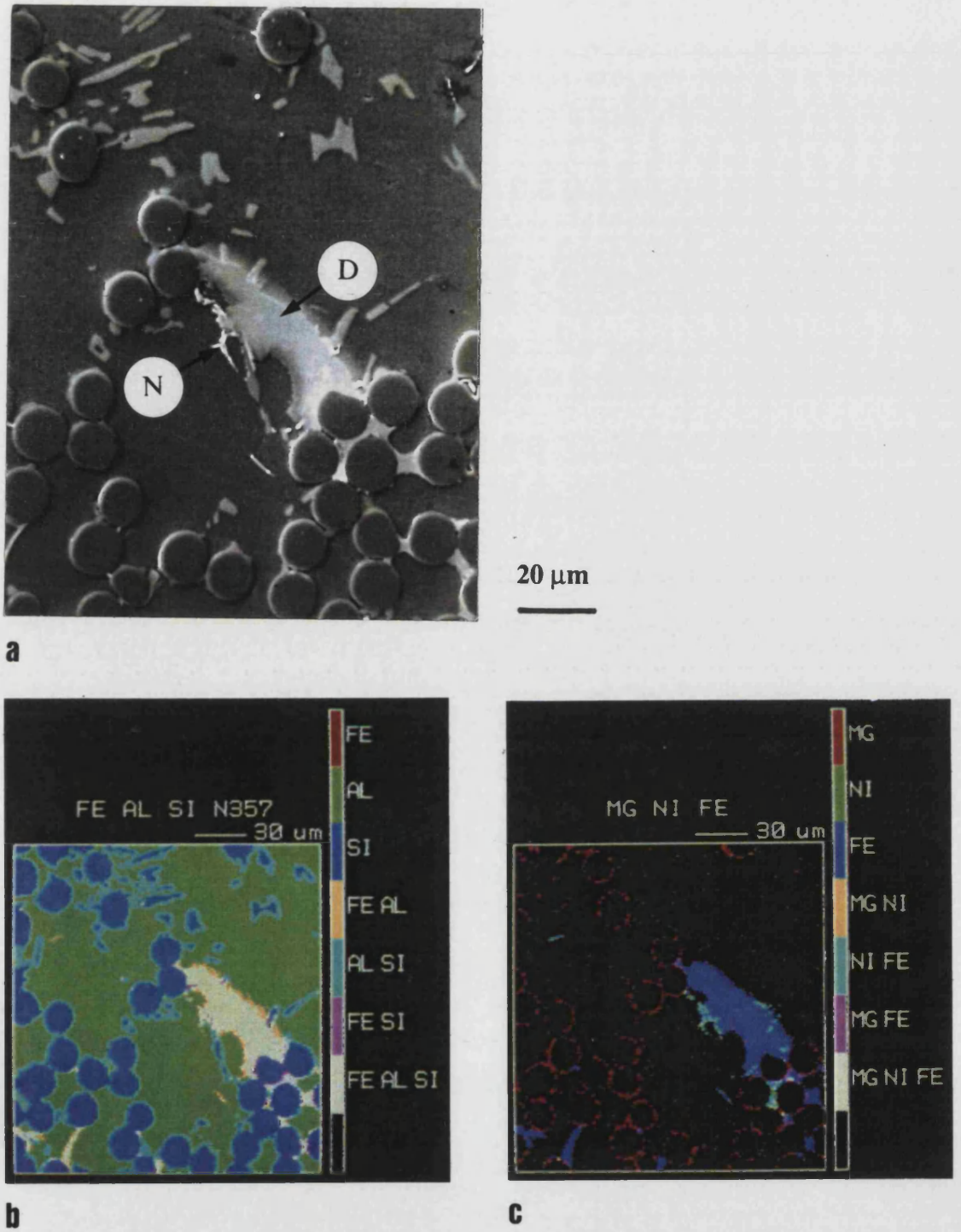

Figure 3.35 WDS x-ray combination maps for, b, iron, silicon and aluminium and, c, magnesium, nickel and iron , from a region which contains two types of intermetallic, the first, D, contains only aluminium, silicon and iron, the second, N, shows the additional presence of nickel.

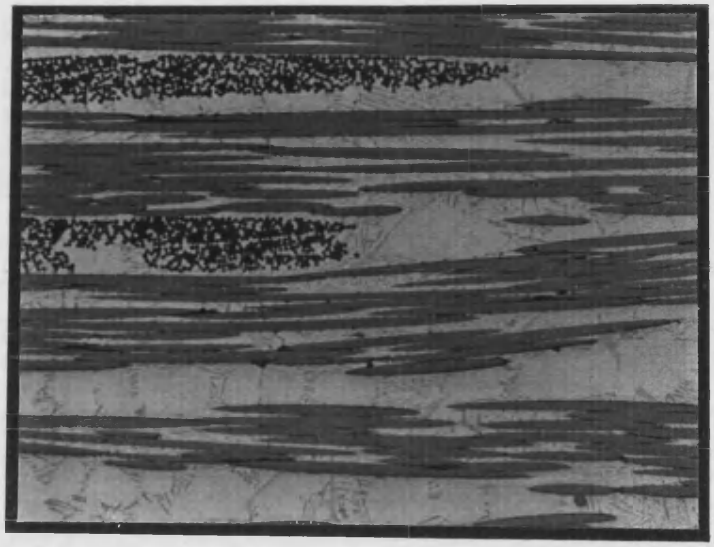

100 μm

a

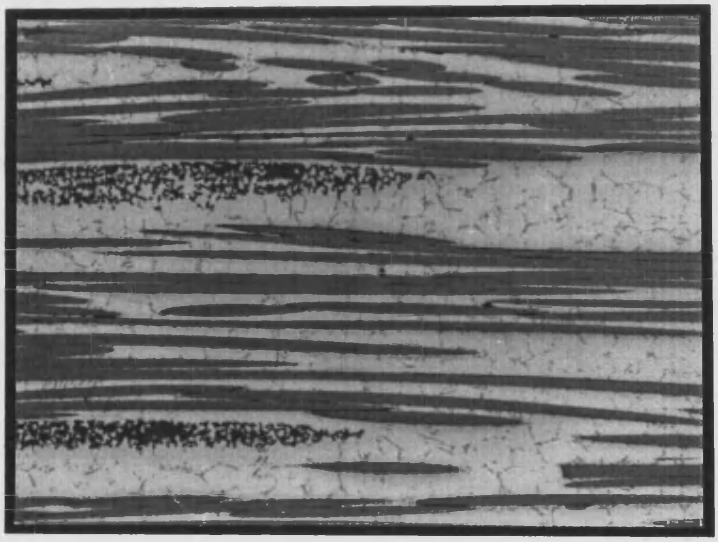

b

100 μm

Figure 3.36 Prepared sections of the Nicalon-357 composite taken from a, a sheet produced early in the investigation which has a large number of coarse second phases and b, a more recently fabricated sheet containing lower numbers of intermetallics of a smaller size.

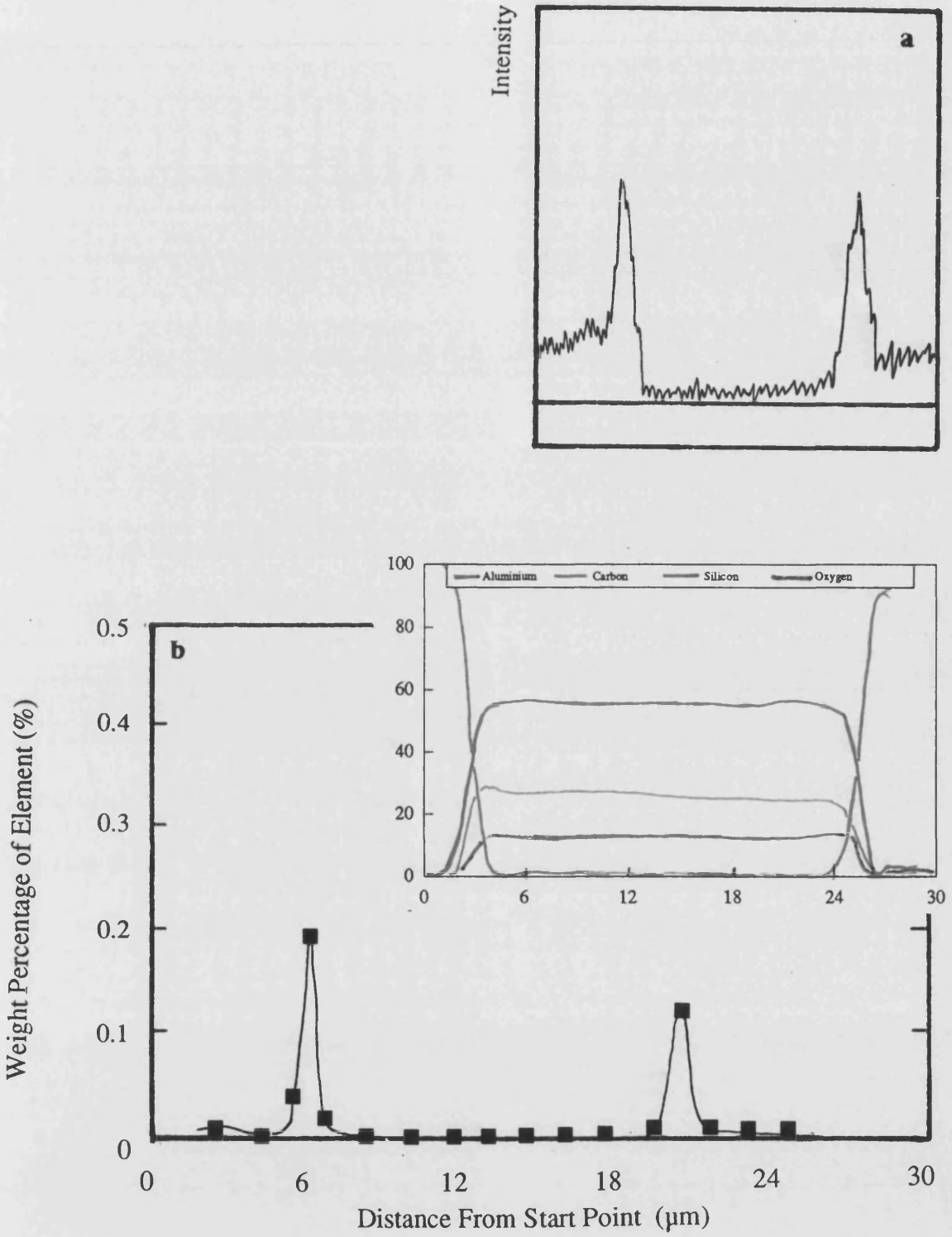

Figure 3.37 The variation of the magnesium across the Nicalon/matrix interface measured by, a, a line scan in the EPMA and, b, by stepped quantitative analysis. The latter was produced using a $MgAl_2O_4$ standard for the magnesium, aluminium and oxygen, and SiC for the silicon and carbon.

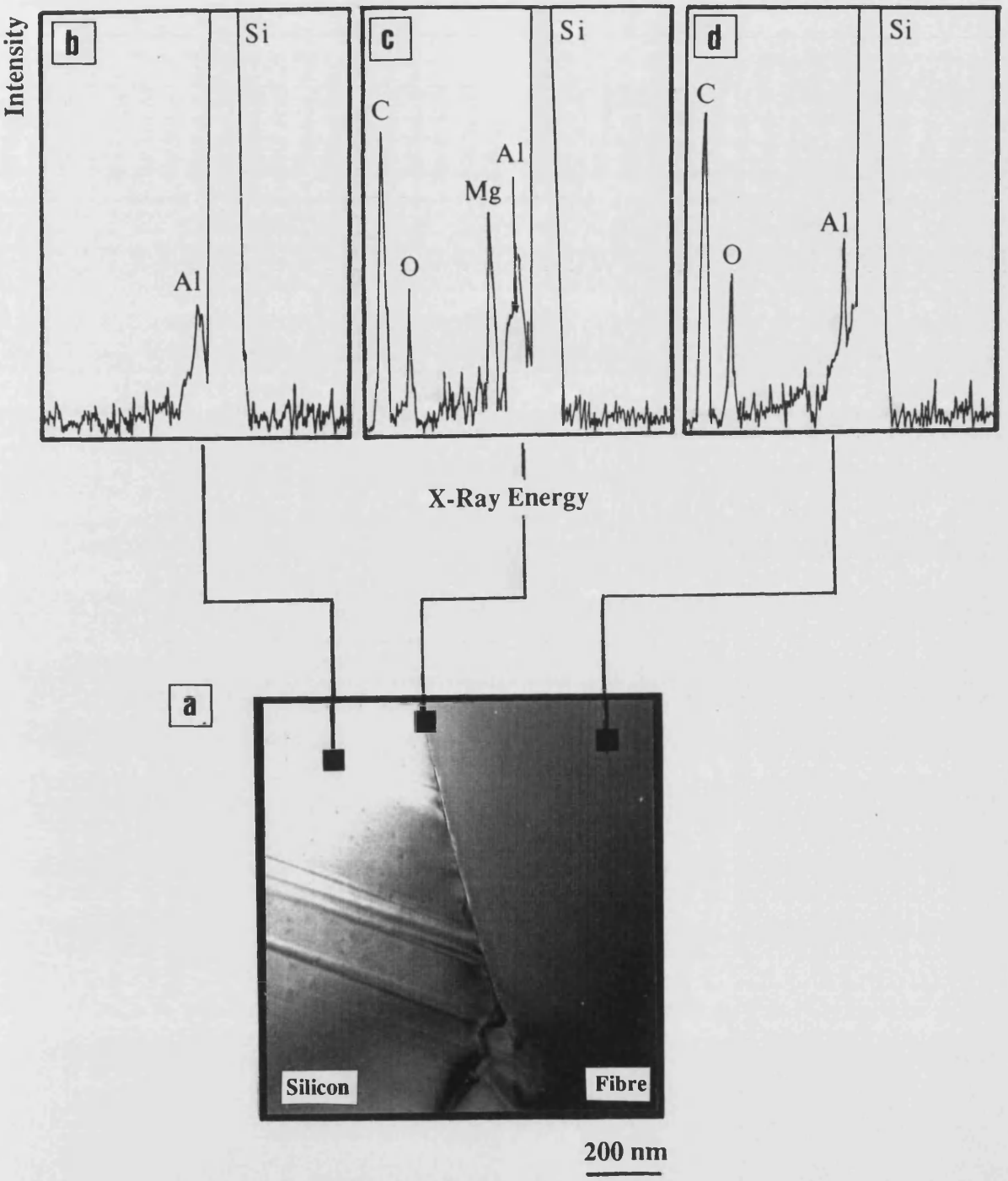

Figure 3.38 The interface between a silicon particle and the Nicalon fibre in the as cast condition, as viewed in the TEM, a, with the EDS traces taken from the silicon, b, at the interface, c and within the fibre bulk, d.

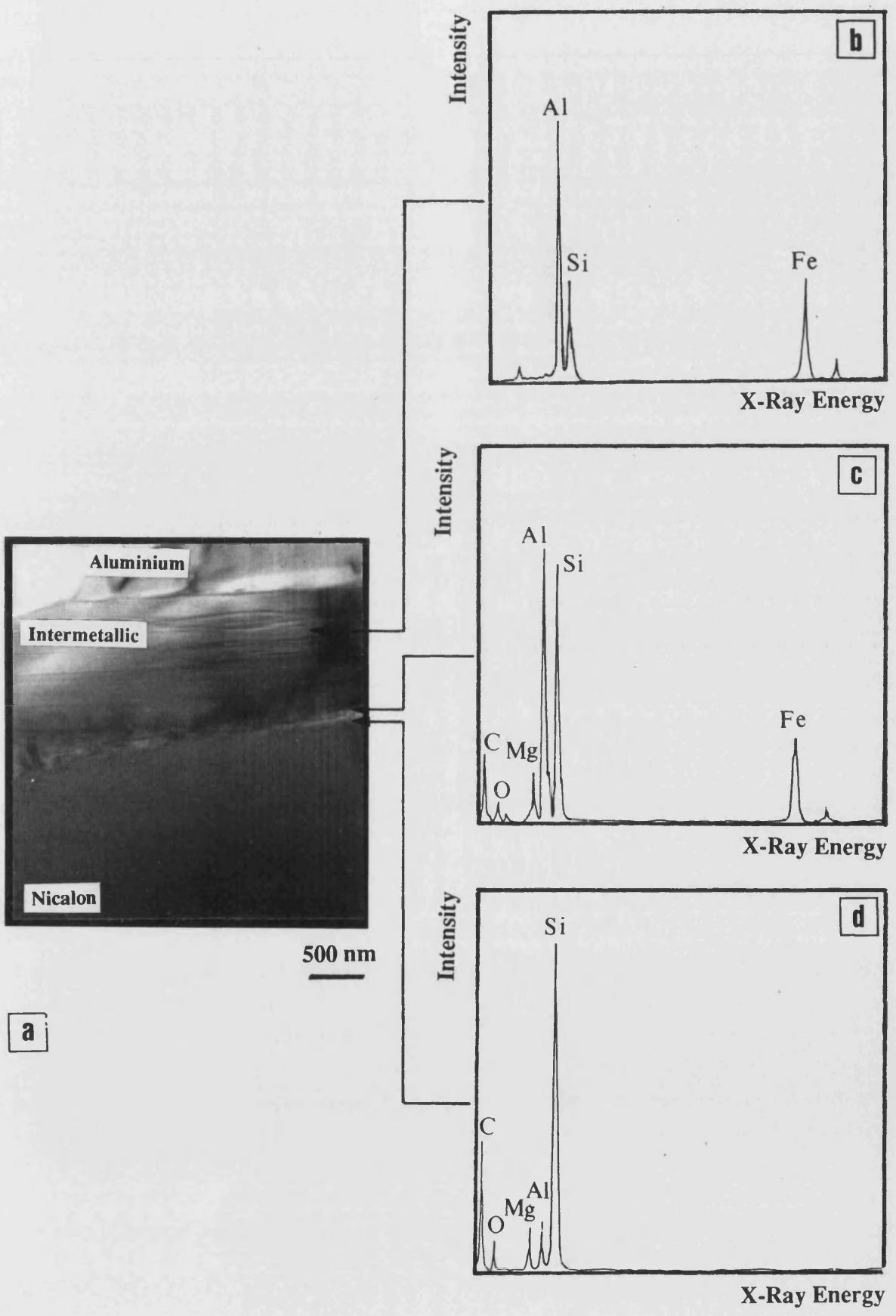

Figure 3.39 The interface between an iron-rich intermetallic of the $FeSiAl_5$ type, with the Nicalon fibre as seen in the TEM, a, with the EDS traces from the intermetallic, b, the interface region, c, and the surface region of the fibre, d.

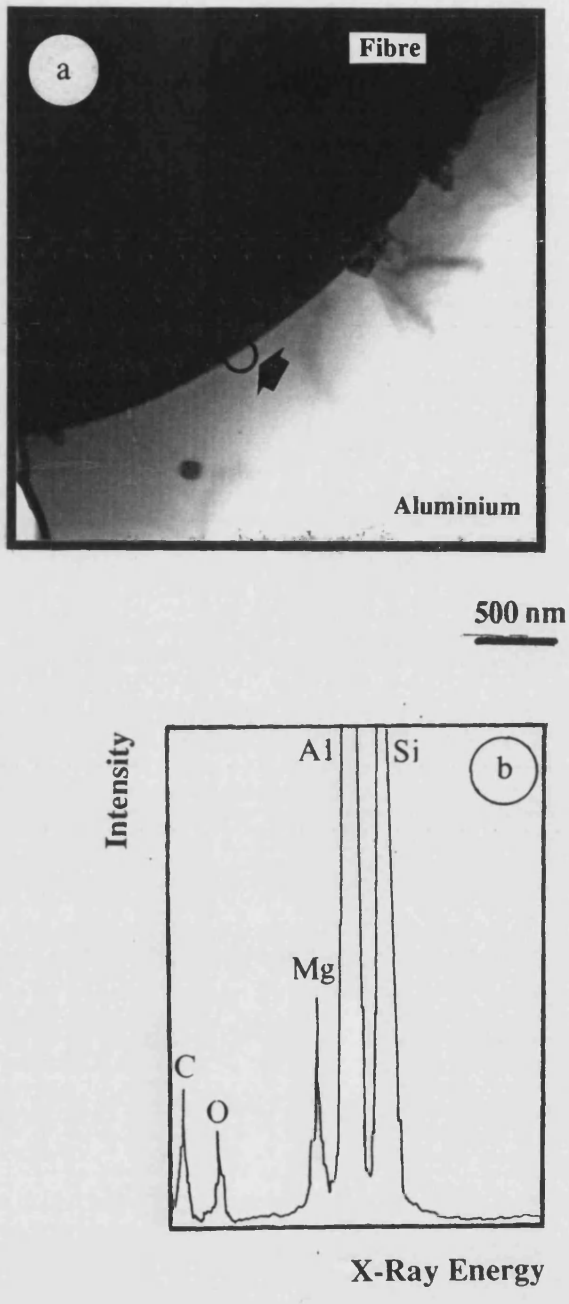

Figure 3.40 The interface between aluminium and Nicalon which TEM, a, shows to have little or no reaction, but the EDS, b, shows the presence of magnesium which was in neither the matrix or fibre.

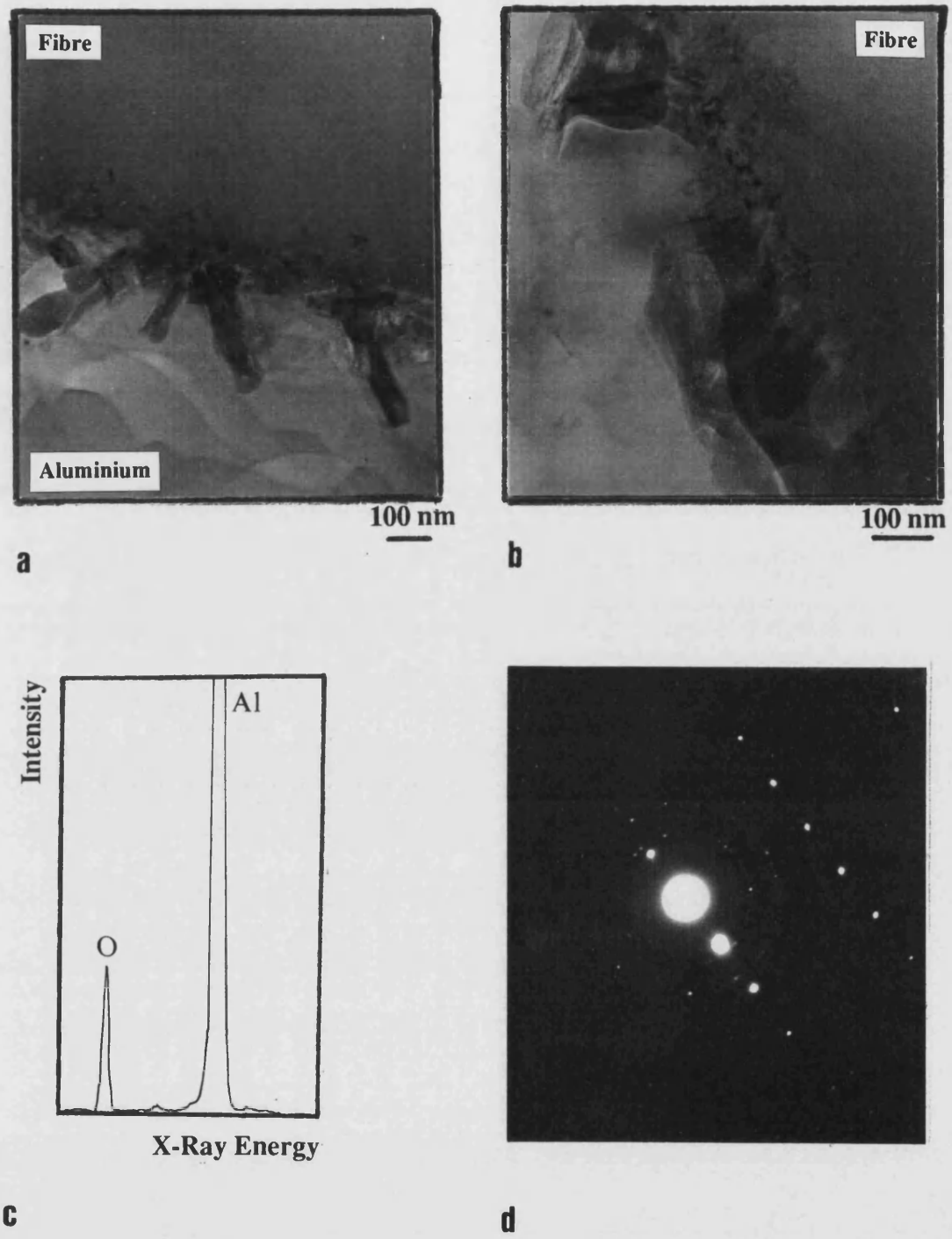

Figure 3.41 An interface between the aluminium and Nicalon fibre in the Nicalon-357 composite. As viewed in the TEM, a, a more bulky form, b, the EDS trace taken from an interphase, c, and the corresponding selected area diffraction pattern, d, indicate that these phases are alumina (Al_2O_3).

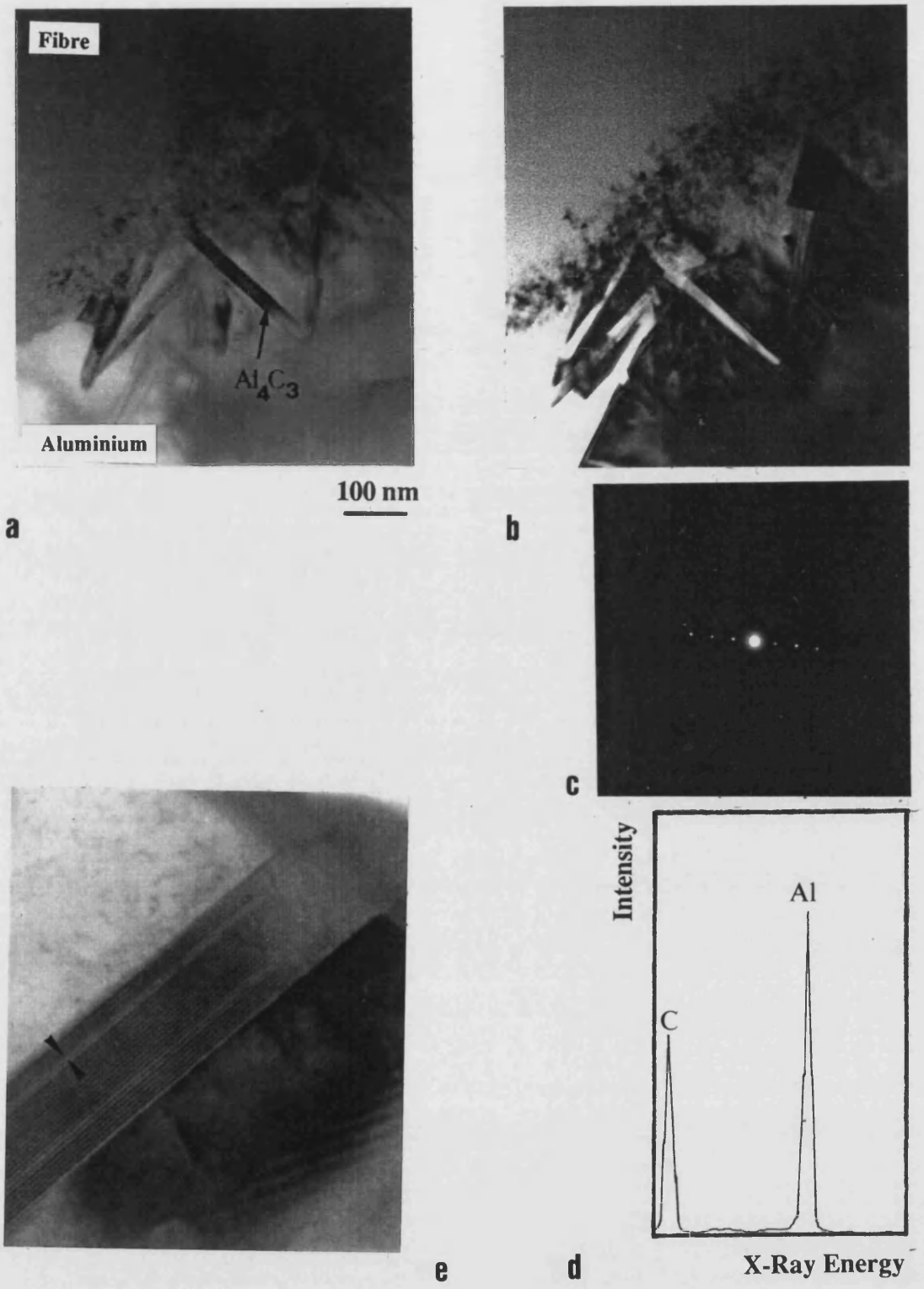

Figure 3.42 An aluminium/Nicalon interface in the as cast Nicalon-357 composite in, a, bright field and b, dark field. The SAD of the interphase, c, and the EDS trace, d, show these to be aluminium carbide (Al_4C_3) the lattice planes of which can be seen at high magnification, e.

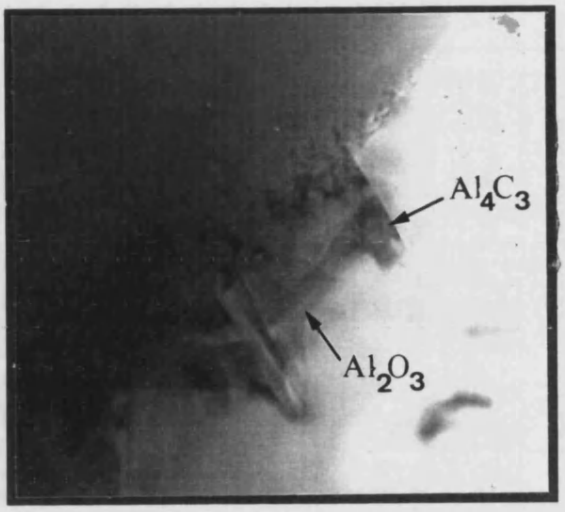

Figure 3.43 An interface between aluminium and Nicalon viewed in the TEM which shows the presence of both aluminium carbides and aluminium oxide in close proximity.

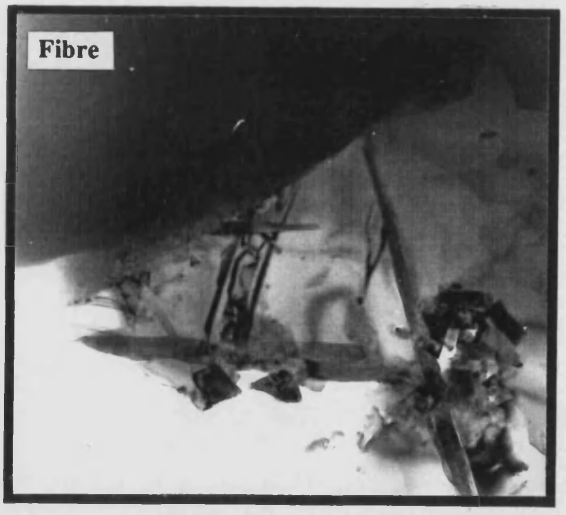

Figure 3.45 TEM of a region which has magnesium, aluminium and oxygen containing phases deposited close to but not on the fibre.

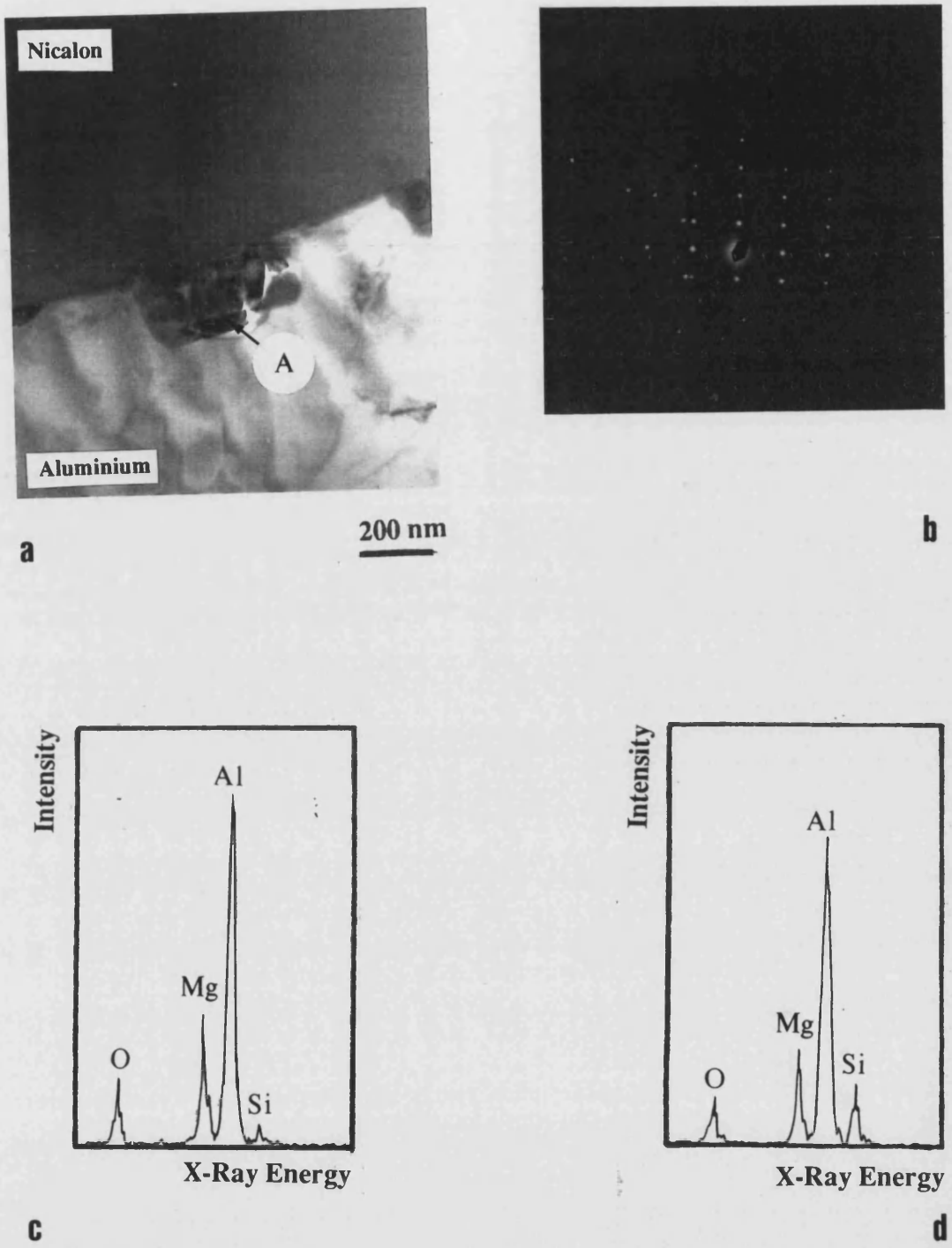

Figure 3.44 The fibre/matrix interface in an as cast Nicalon-357 composite with a bulky phase, A, observed in TEM, a. These phases show a range of compositions, revealed by EDS, from those containing little or no silicon, c, to those which have an appreciable level of silicon, d. The SAD for a typical phase of this type is given in b, indicates a spinel ($MgAl_2O_4$).

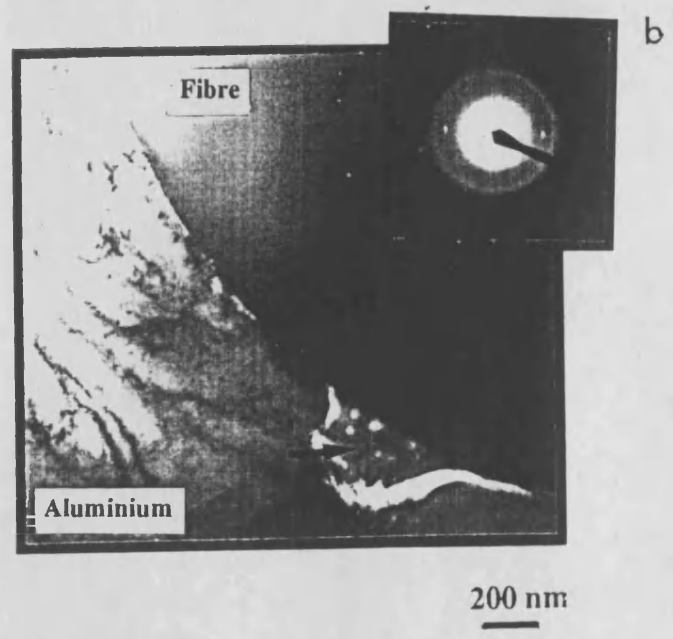

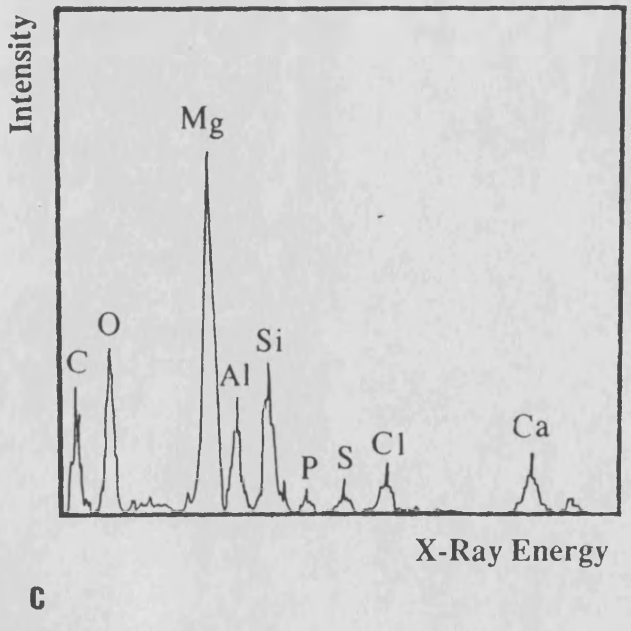

Figure 3.46 Interface between Nicalon and a matrix phase viewed in the TEM, a, with an amorphous structure revealed in the SAD, b, and the corresponding EDS, c.

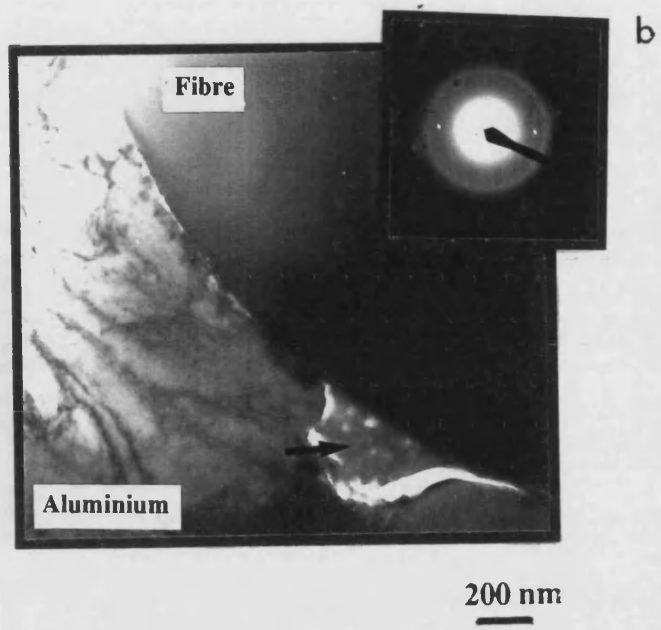

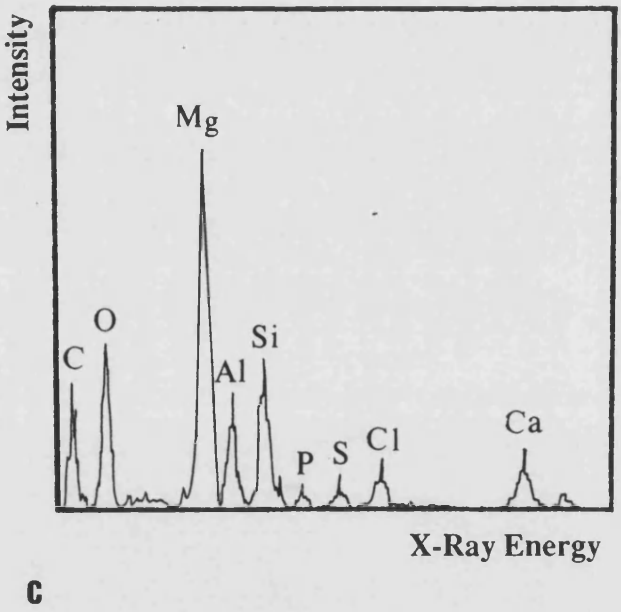

Figure 3.46 Interface between Nicalon and a matrix phase viewed in the TEM, a, with an amorphous structure revealed in the SAD, b, and the corresponding EDS, c.

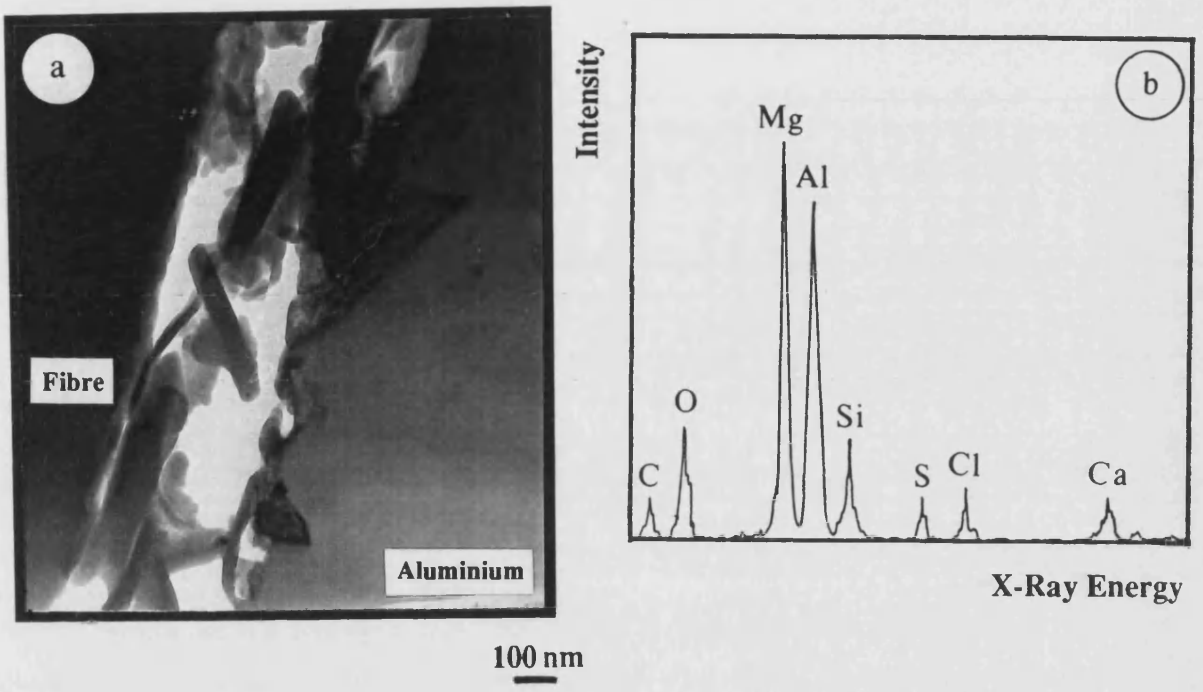

a b

Figure 3.47 A fibrous phase found to be present at the fibre/matrix interface in the TEM, a, with the corresponding EDS, b.

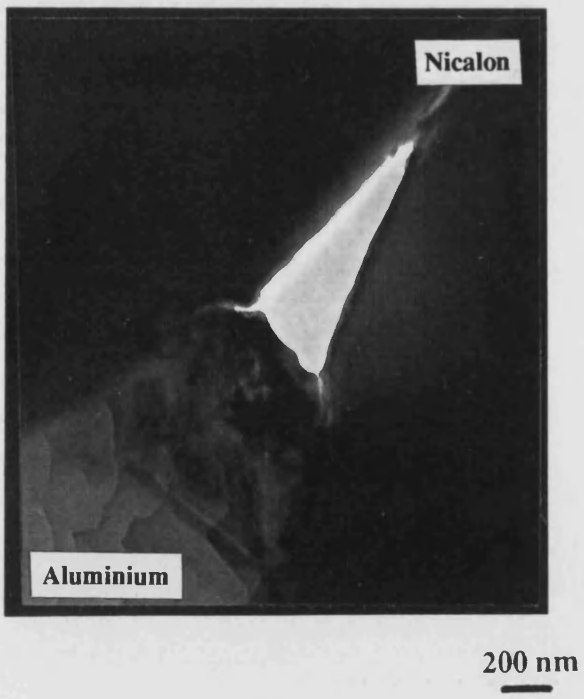

Figure 3.48 A TEM image of a second phase trapped in the interstices of closely packed fibres.

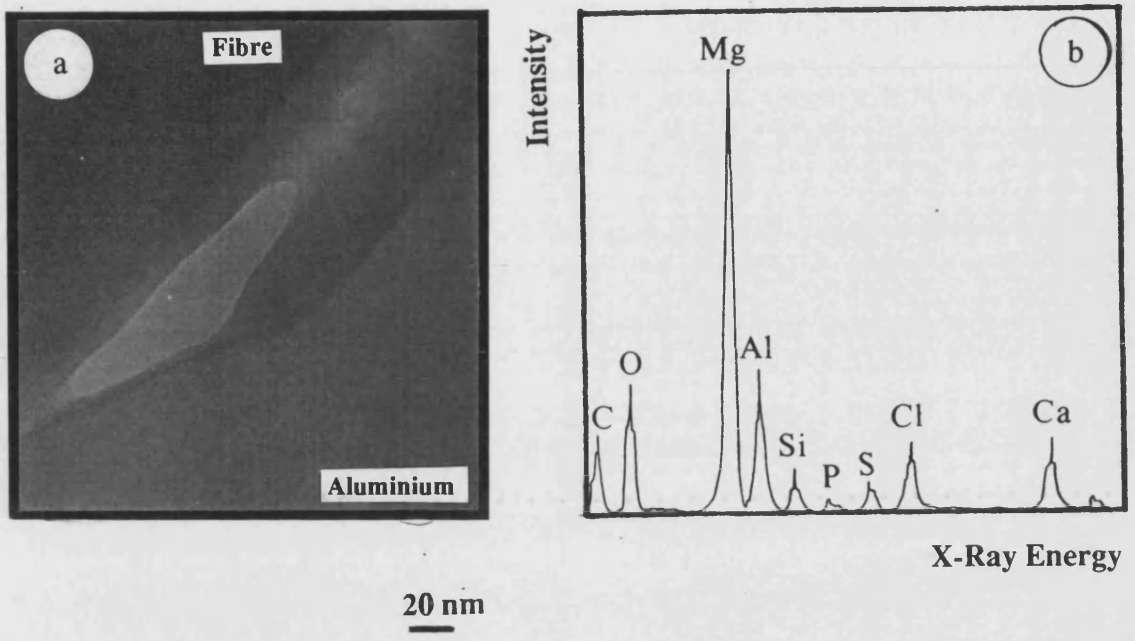

a b

Figure 3.49 A thin interfacial phase observed on some of the fibres. This had a composition which showed the presence of magnesium, aluminium, calcium and oxygen, b, the other elements emanating from the fibre and matrix constituents.

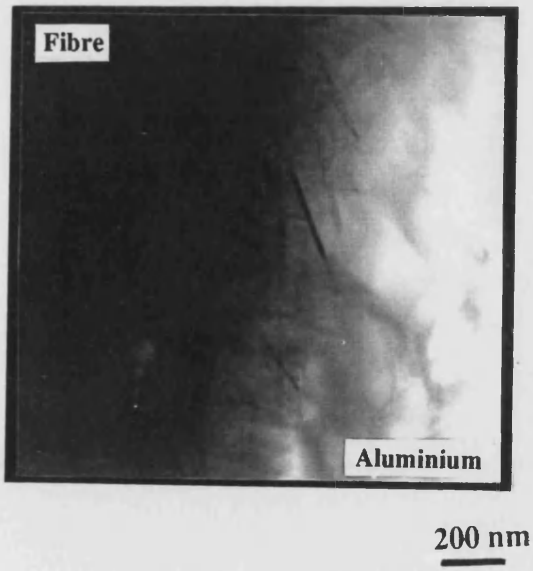

Figure 3.50 The interface between Nicalon and aluminium formed in the heat treated Nicalon-alloy composite, showing enlarged aluminium carbide formation.

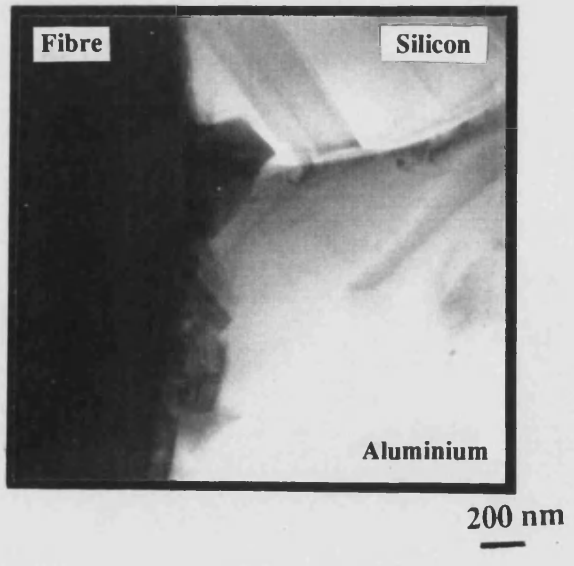

Figure 3.51 A TEM of a heat treated interface showing a silicon particle partially regrown over the interfacial reaction product.

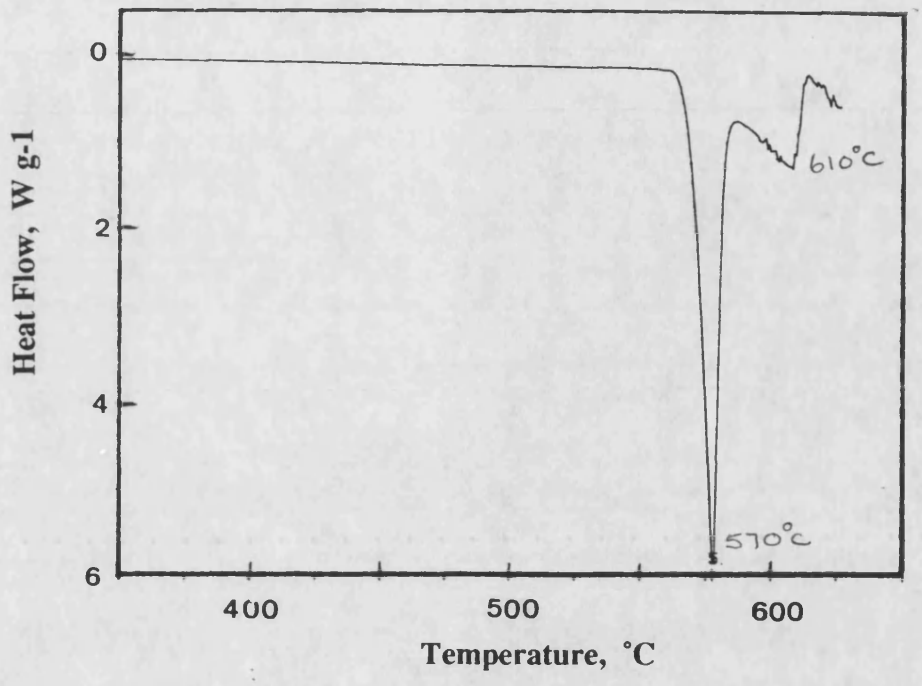

Figure 3.52 A DSC trace for the Nicalon-357 composite with the endotherms due to matrix components.

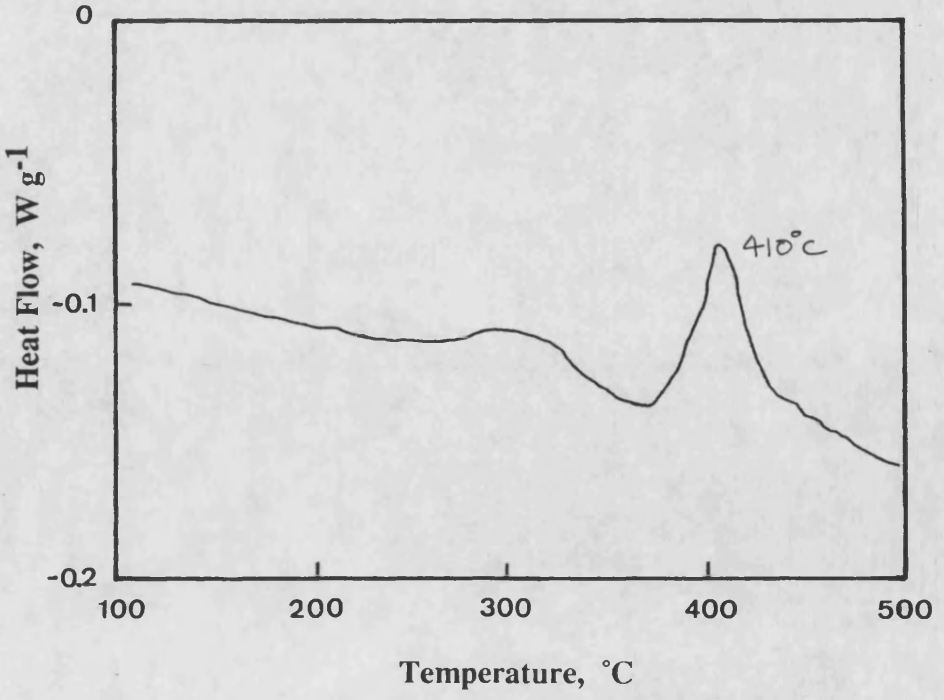

Figure 3.53 DSC trace for the N357 showing the double exothermic peak at 300 - 410°C.

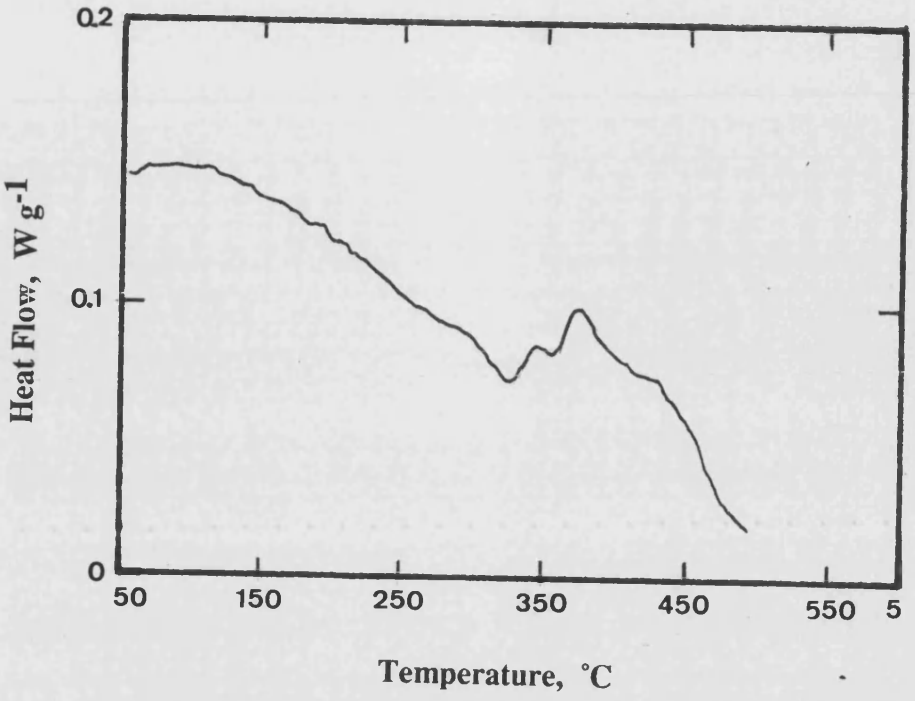

Figure 3.54 The DSC trace for a sample of Nicalon fibres showing a similar exotherm to that observed for the Nicalon-357 composite (figure 3.53)

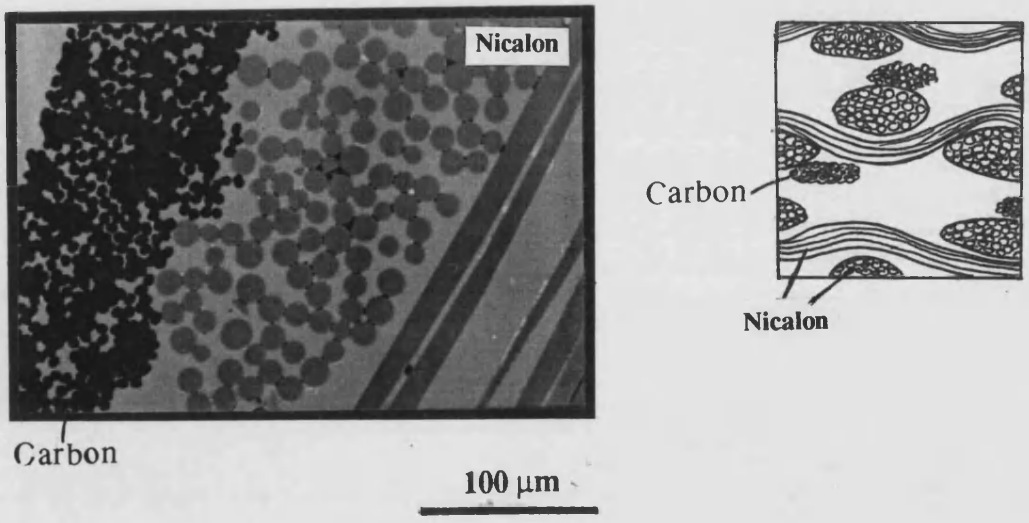

Figure 3.55 A SEM of the commercially pure aluminium matrix composite with the woven Nicalon reinforcement and also some carbon fibres.

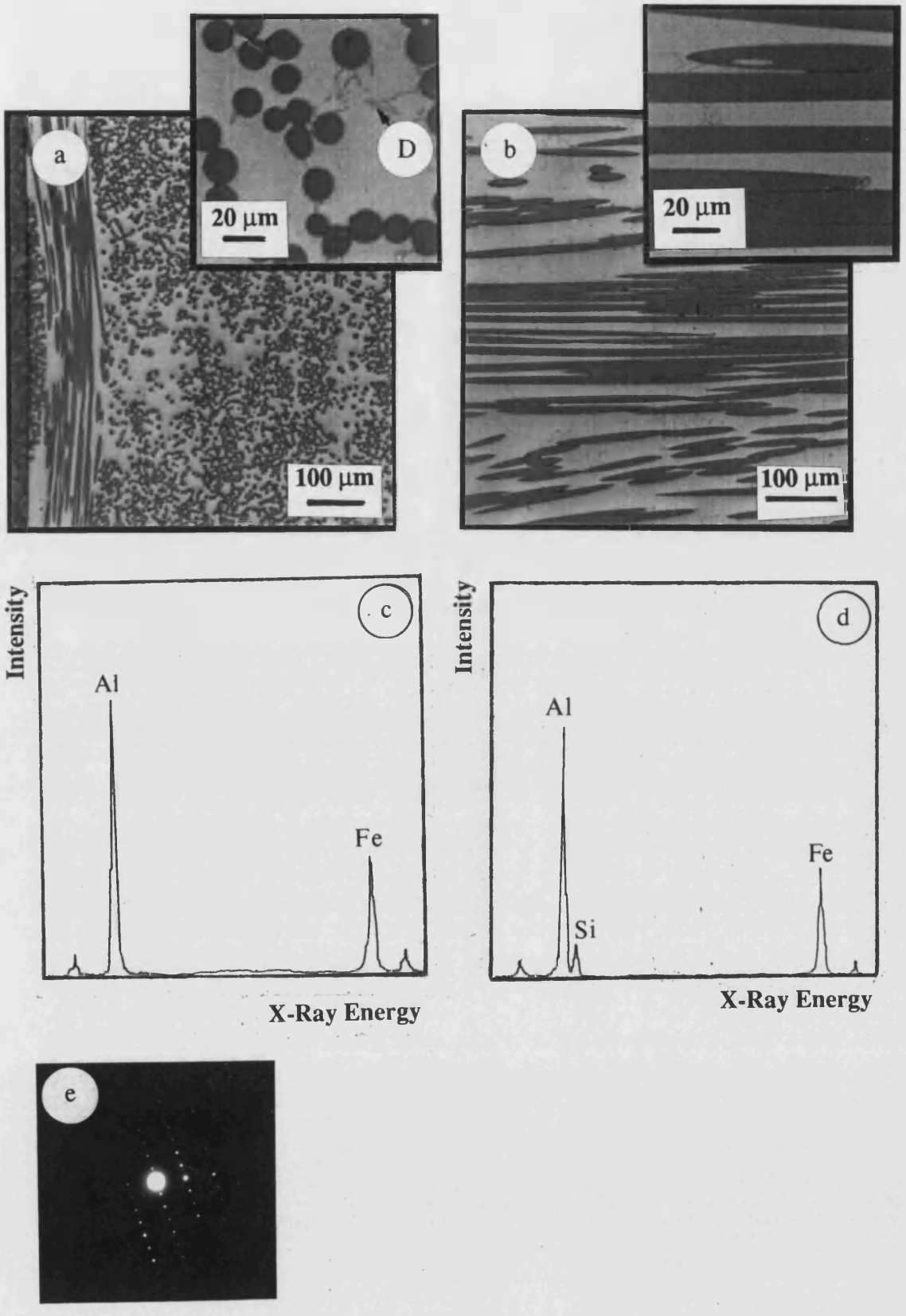

Figure 3.56 A optical micrograph of the filament wound Nicalon-aluminium composite (N100f) in transverse section, a, and longitudinal section, b. The intermetallics, D, either show the presence of iron and aluminium only, c, or silicon in addition, d, both of which give the same SAD pattern, e, which corresponds to $FeAl_3$.

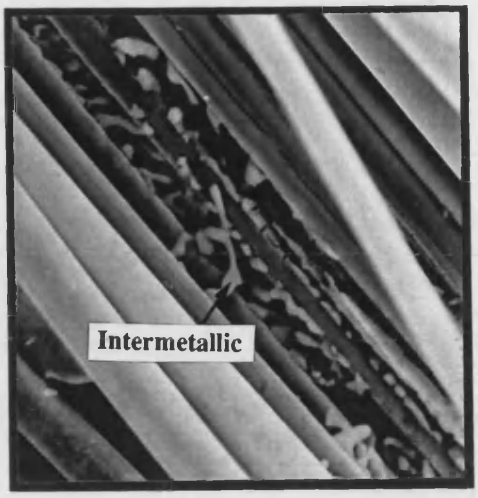

Figure 3.57 A SEM image of the Nicalon-aluminium composite after selective removal of the aluminium constituent, revealing the fibre bridging by the intermetallics.

Figure 3.58 A Nicalon-Al (N100w) composite with a large volume of the fibres not infiltrated.

Figure 3.59 The Nicalon/matrix interface in the Nicalon-Al composite in the TEM with a closely packed aluminium carbide interphase.

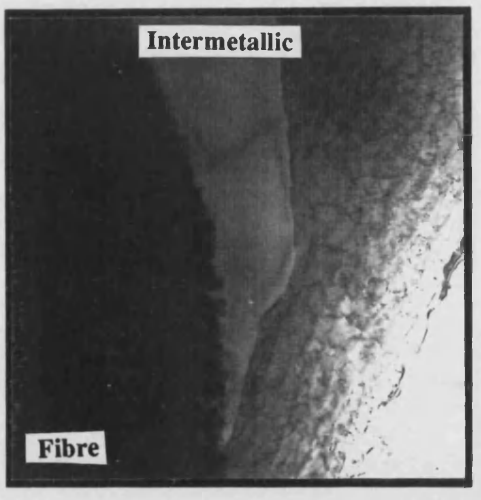

Figure 3.60 A Nicalon/matrix interface, in the TEM, of the Nicalon-Al composite with the carbide still present on the fibre with a intermetallic in contact.

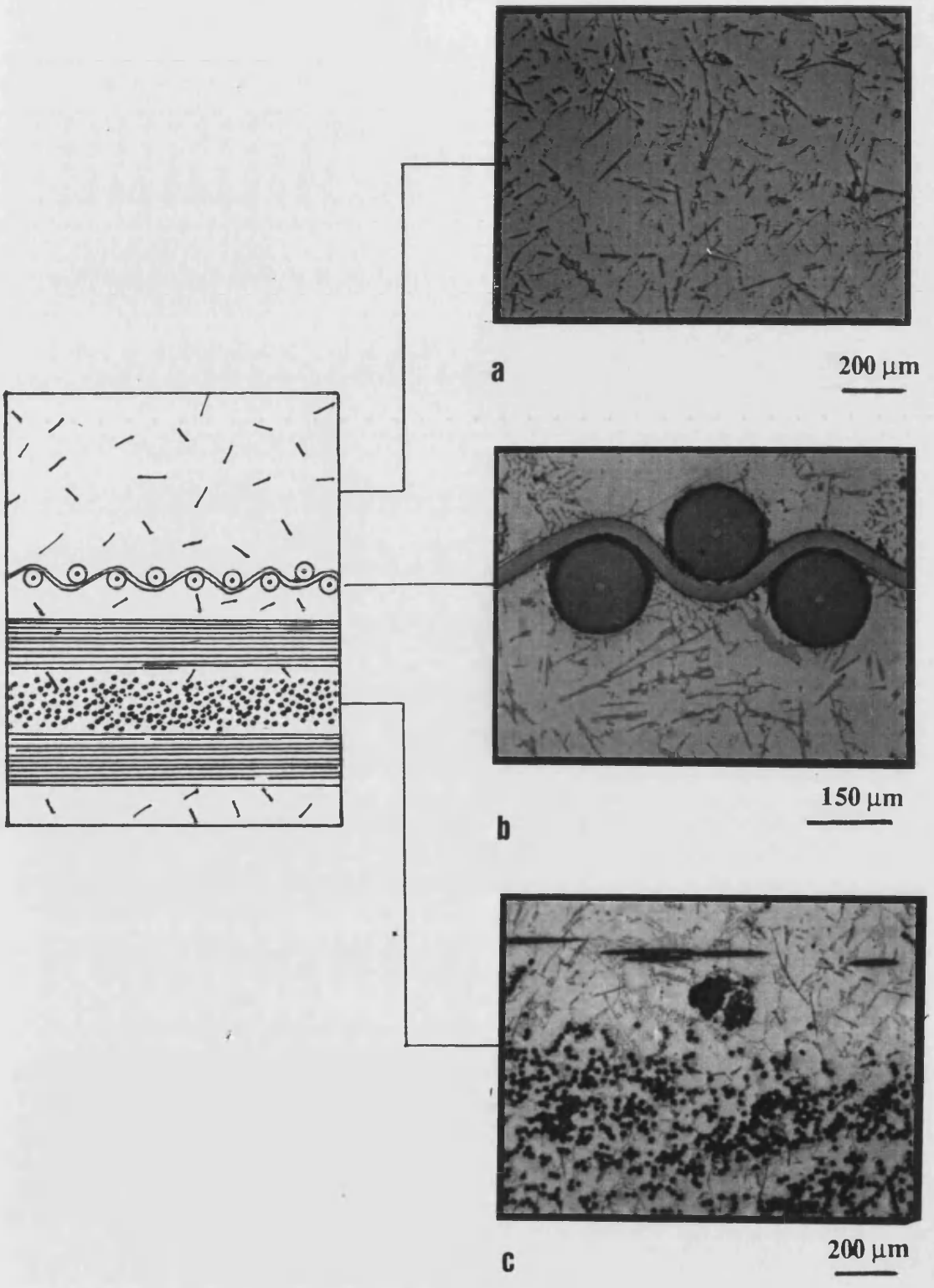

Figure 3.61 The three regions observed in the FP alumina/Borsic hybrid composite. These being a, a region which has no reinforcement, b, a monolayer of Borsic fibres in the 0° orientation and c, three plies of FP-alumina fibres arranged in 90-0-90° orientation.

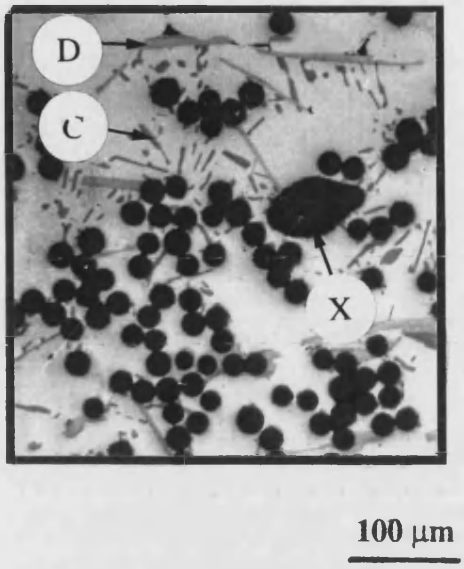

Figure 3.62 An optical micrograph of the alumina fibre region with intermetallics, D, silicon, C, and a dross particle, X.

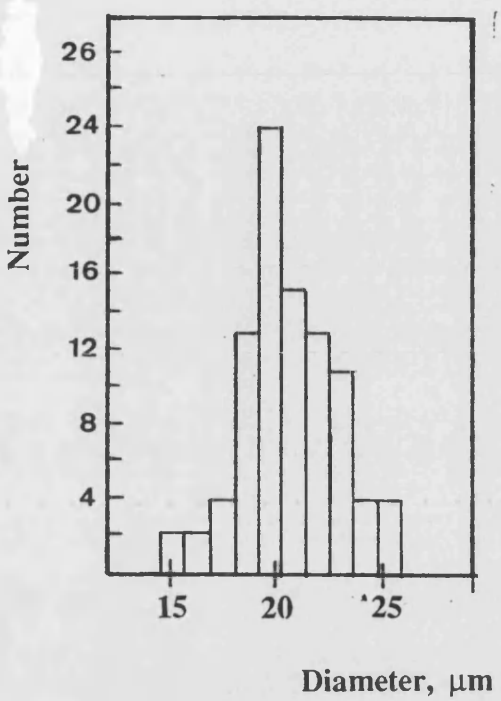

Figure 3.63 The measured diameter distribution for the alumina fibres in the composite.

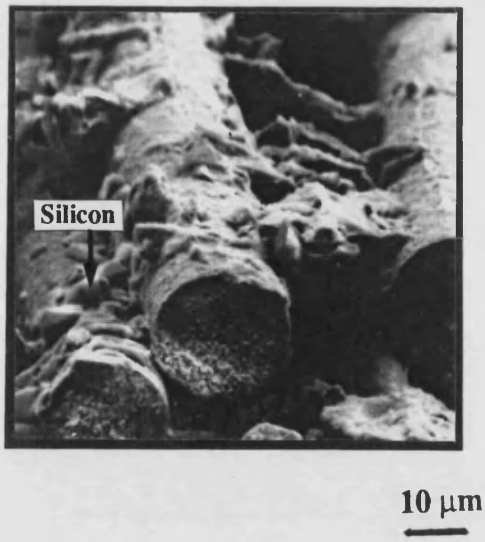

Figure 3.65 A SEM of the alumina region showing large intermetallic bridges between fibres and silicon bridging where fibres are closely packed.

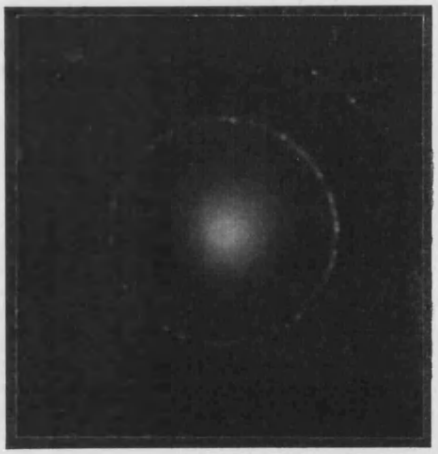

Figure 3.64 A SAD pattern of the alumina fibre showing the polycrystalline nature of the fibre.

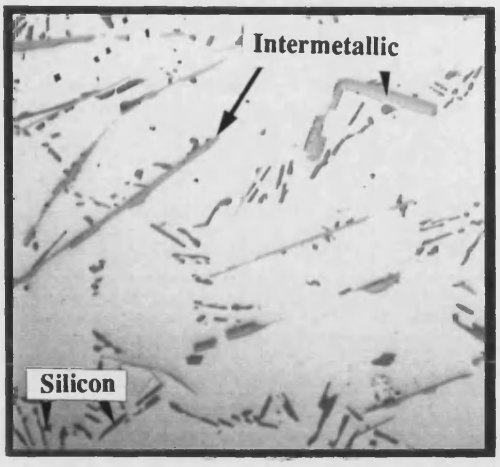

Figure 3.66 The unreinforced region of the Hybrid composite showing a large number of iron-rich intermetallics ($FeSiAl_5$) and coarse silicon.

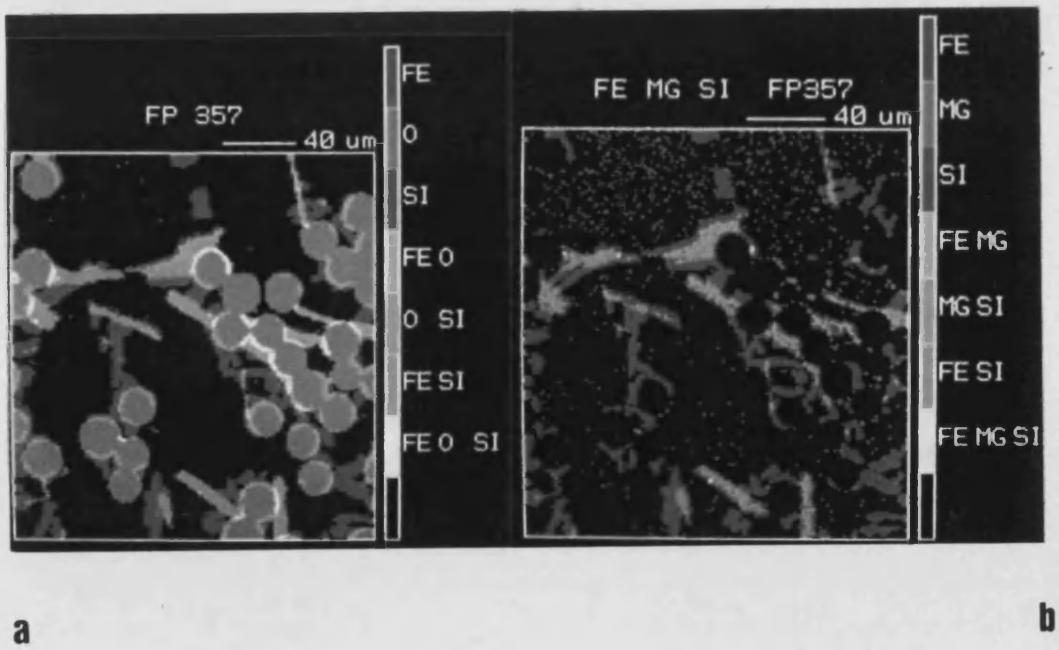

Figure 3.67 WDS combination map of an as cast alumina fibre area of the F357 composite with iron, oxygen and silicon, a, and iron, magnesium and silicon, b.

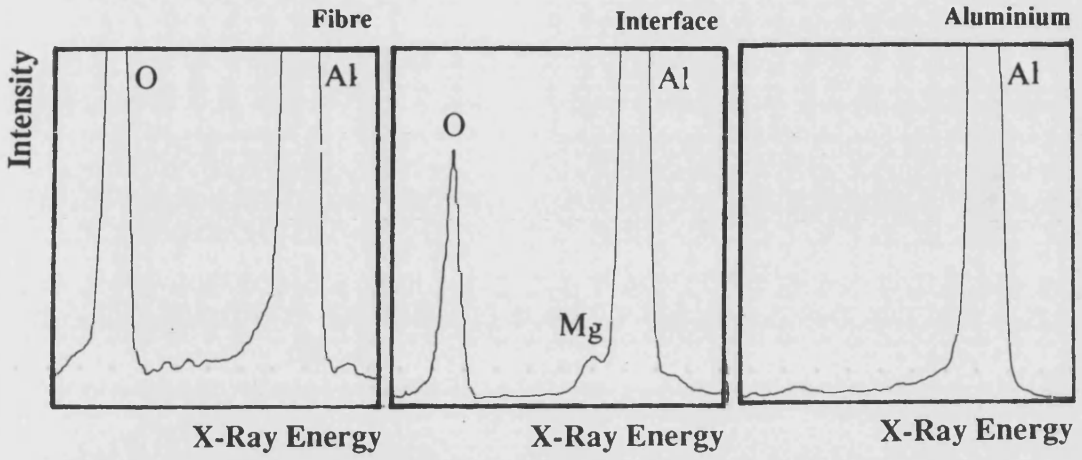

Figure 3.68 EDS in the TEM of the alumina/aluminium interface showing the slight segregation of magnesium to the interface.

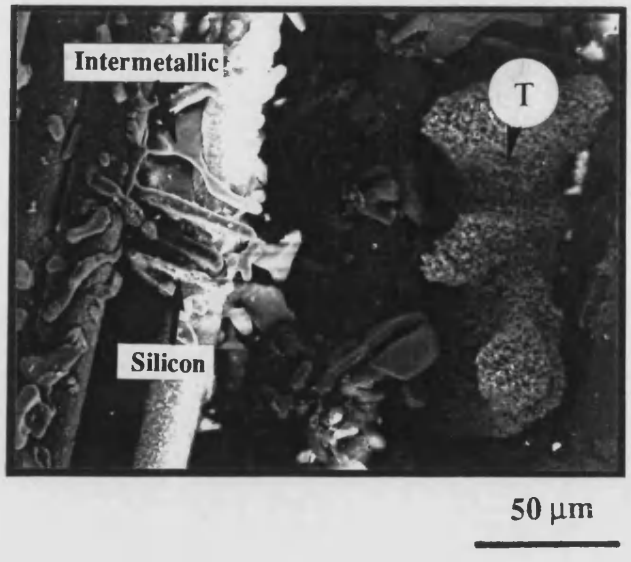

Figure 3.69 SEM of a deep-etched specimen in the alumina region, with a dross phase marked T.

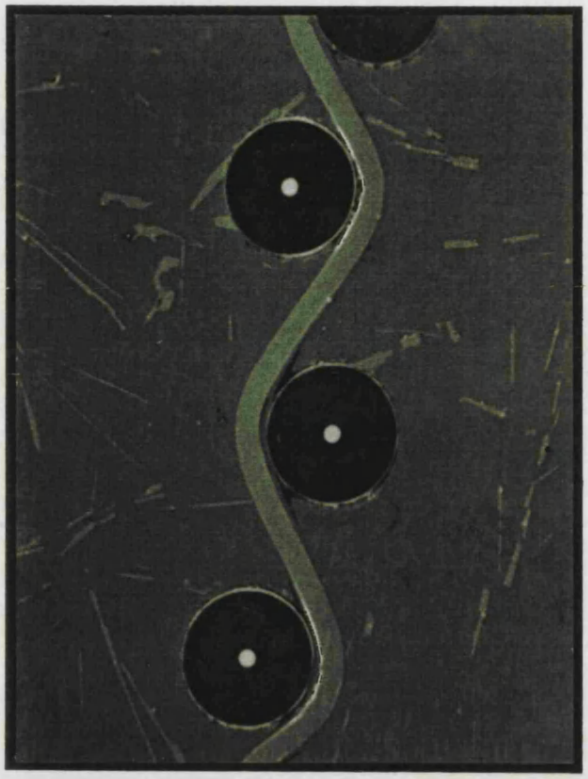

a

100 μm

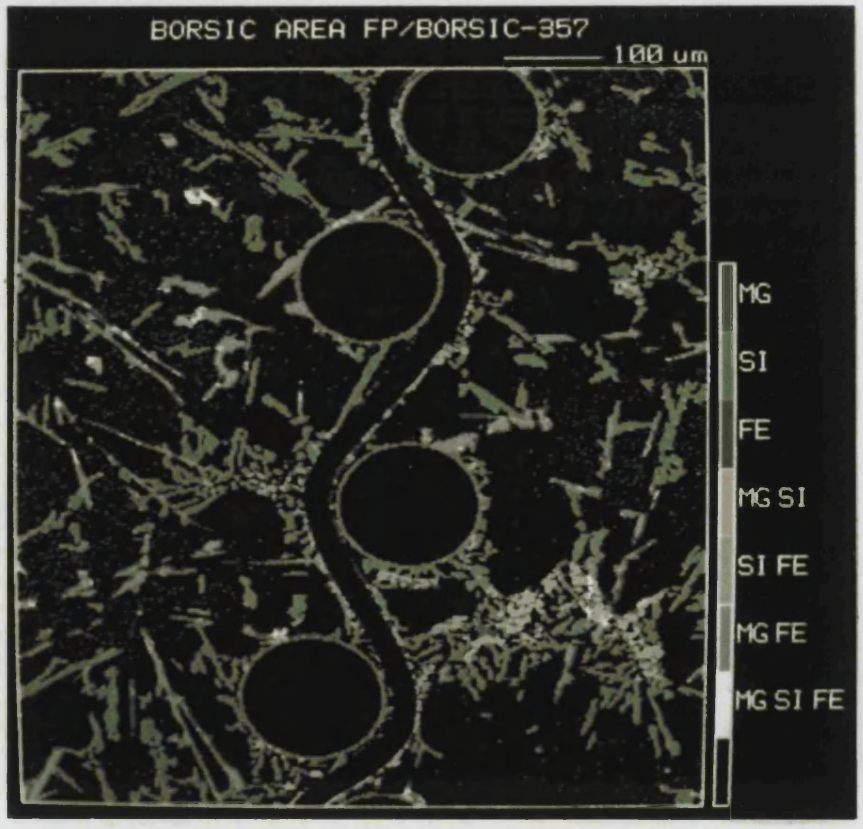

b

Figure 3.70 The Borsic fibre containing region of the hybrid composite, a, the SEM of the area, with, b, the combination map for magnesium, silicon and iron,

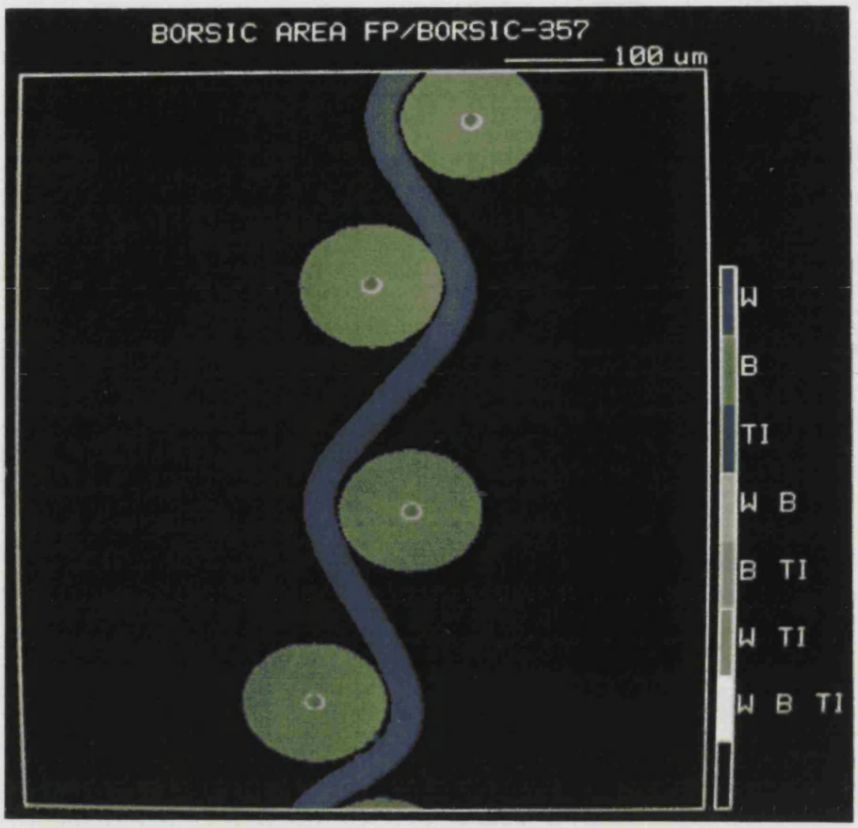

c

d

100 μm

Figure 3.70 c A x-ray combination map of the Borsic fibre containing region for tungsten, boron and titanium, and d. the titanium weft revealed in the SEM by selective removal of the aluminium by etching.

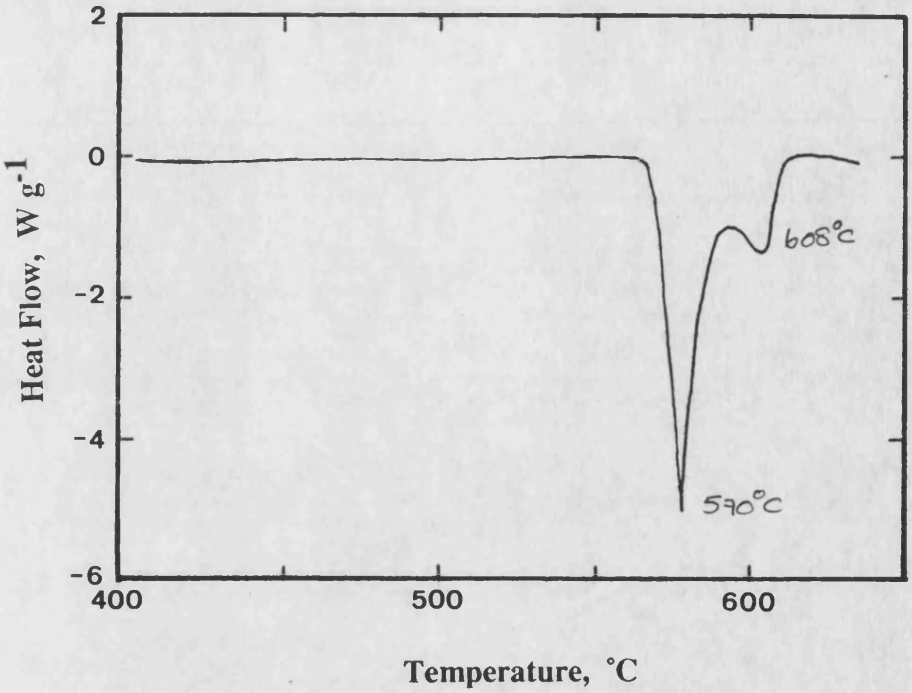

Figure 3.71 The DSC thermograph obtained from the alumina reinforced alloy composite.

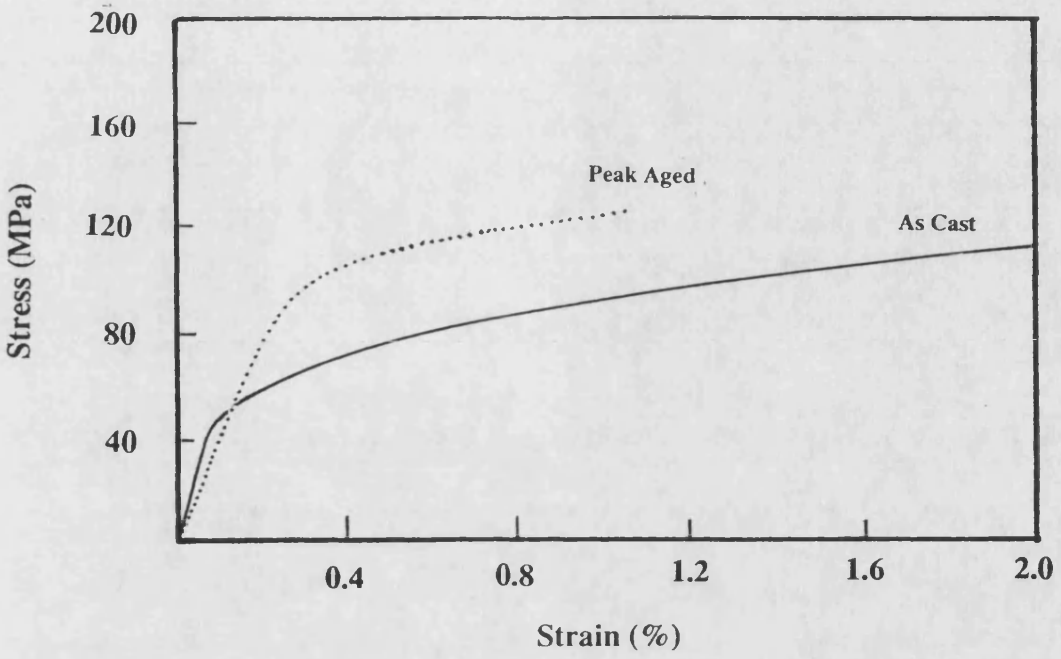

Figure 3.72 The tensile stress versus strain curve for the as cast and peak aged 357 alloy.

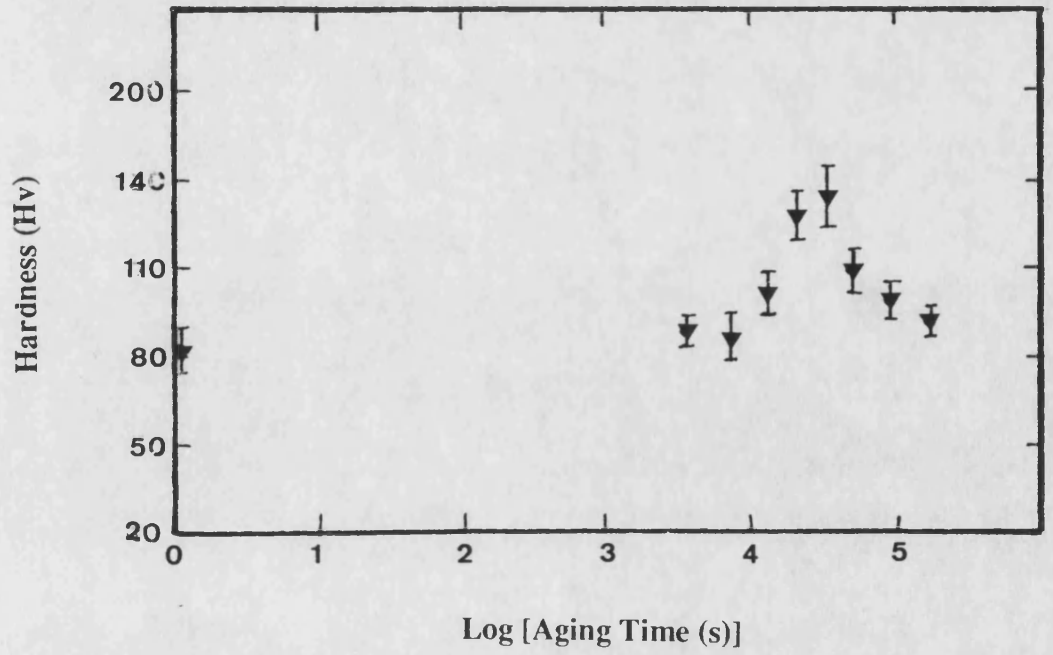

Figure 3.73 The variation of α-aluminium dendrite microhardness, with post solution treatment ageing time for the unreinforced alloy. (solution treatment at 540°C for 16 hours; age heat treatment temperature, 160°C)

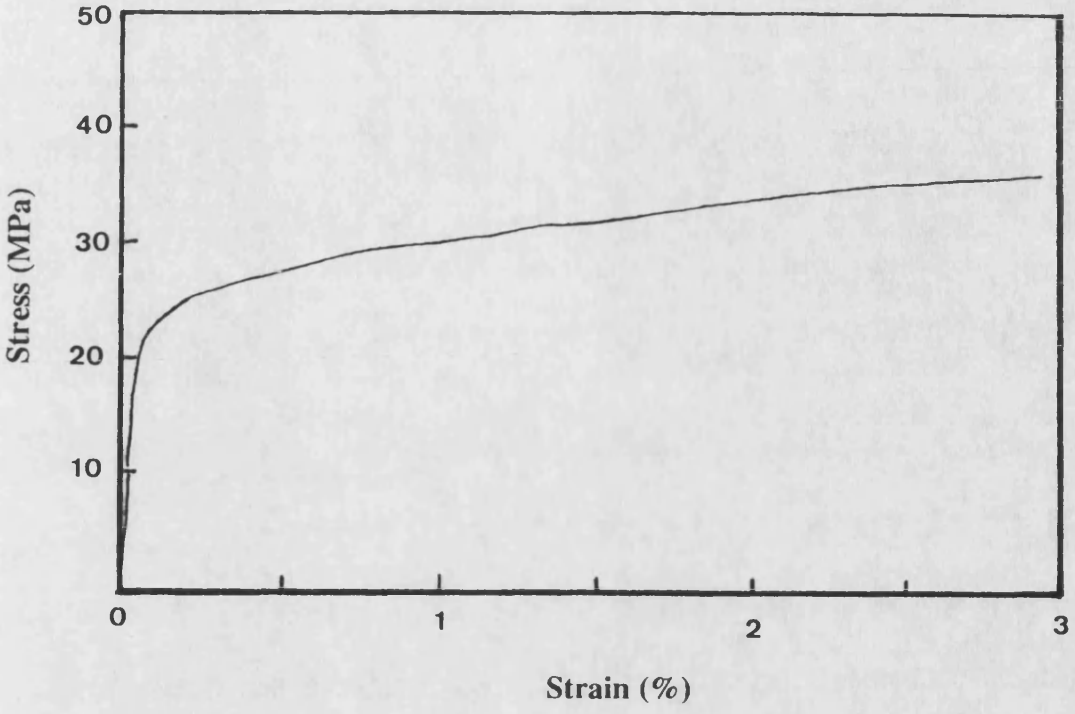

Figure 3.74 Tensile stress versus strain curve for the unreinforced commercially pure aluminium.

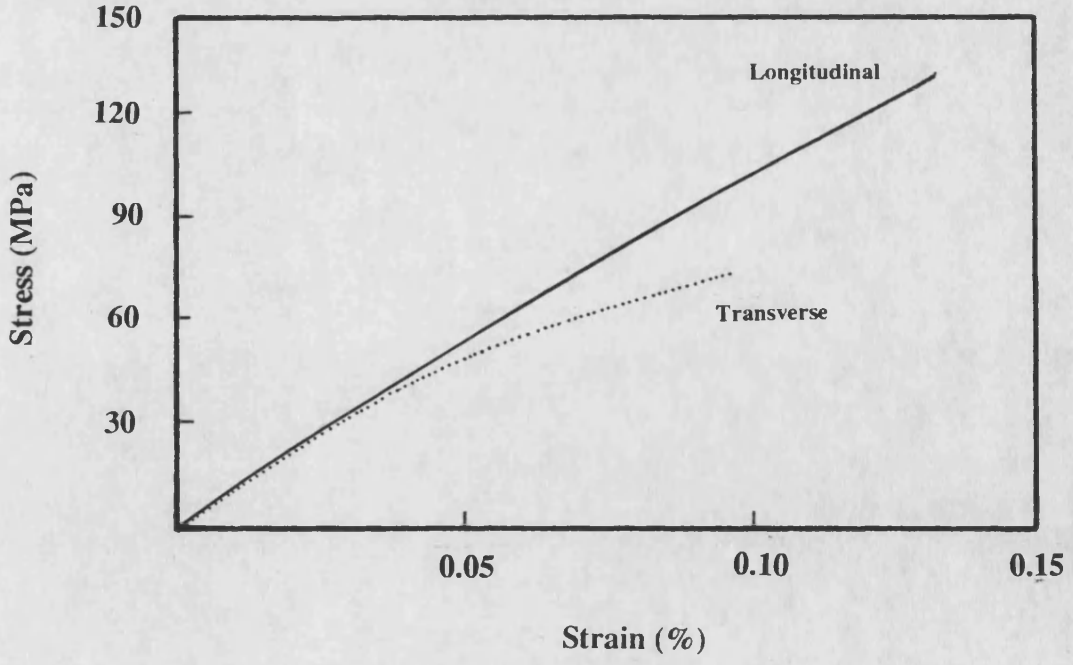

Figure 3.75a Tensile stress versus strain curve for the Nicalon-357 composite in both longitudinal and transverse orientations.

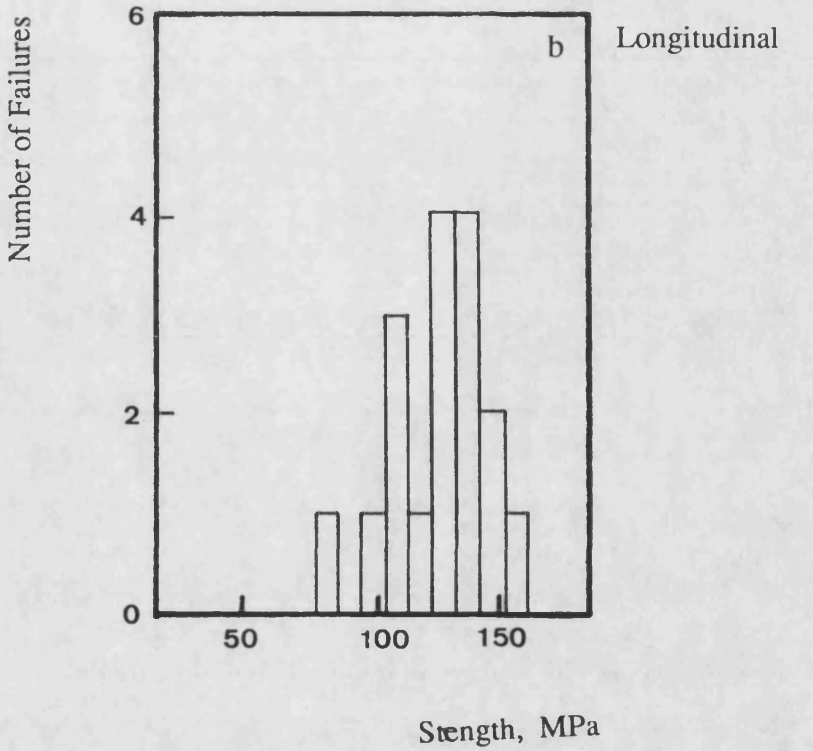

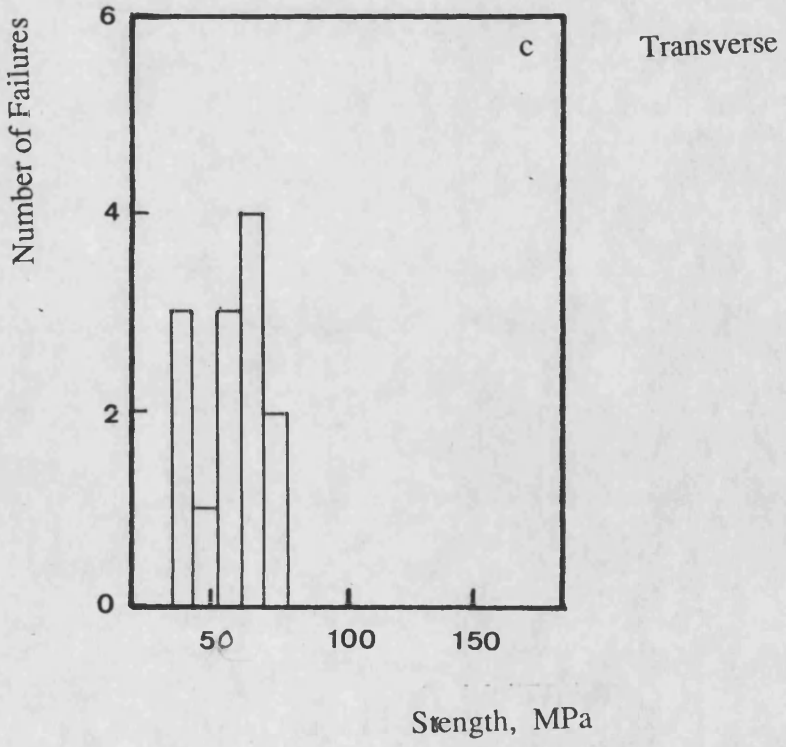

Figure 3.75. Summary of the tensile strength data for the Nicalon-alloy composite with the fibres in the longitudinal, b, and transverse, c, orientation.

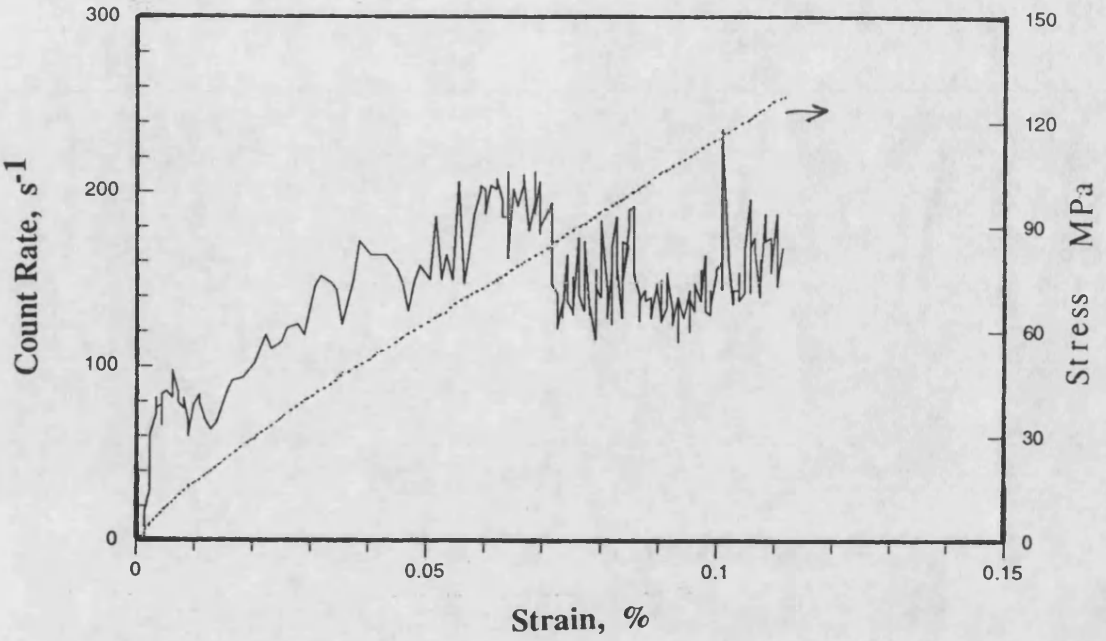

Figure 3.76 The acoustic emission event rate versus strain curve for the Nicalon-357 composite in the longitudinal fibre orientation.

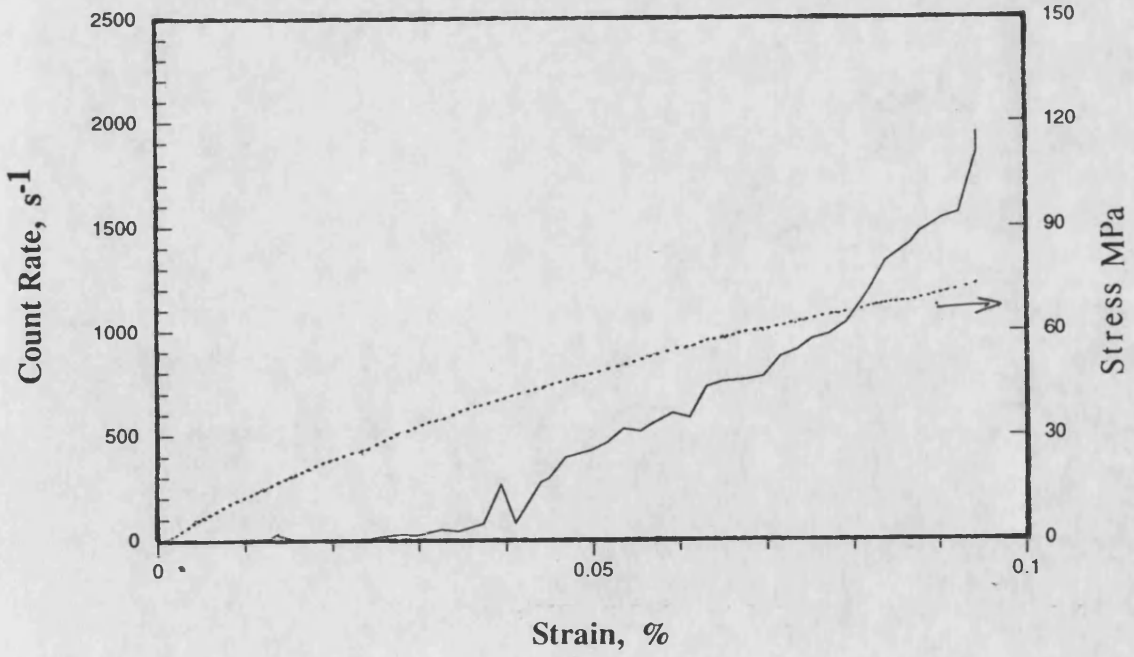

Figure 3.77 The acoustic emission event rate versus strain curve for the Nicalon-357 composite in the transverse fibre orientation.

500μm

Figure 3.78 A tensile fracture surface of Nicalon-357 composite, viewed in the SEM, of the longitudinal specimen, with large flat areas and the glass weft notable.

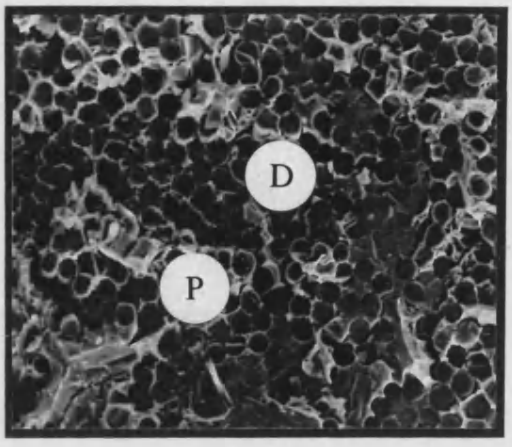

100 μm

Figure 3.79 Tensile fracture surface, of Nicalon-357 composite, showing the lack of fibre pull out, the presence of fractured intermetallics, D, and plastically deformed aluminium, P.

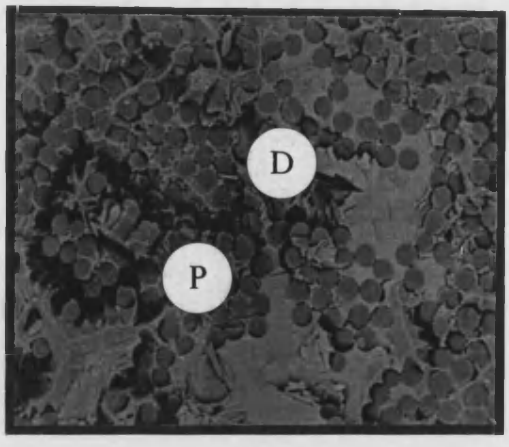

100 μm

Figure 3.80 The same area as figure 3.79, but a back scattered electron image. The lighter area is iron-rich intermetallic.

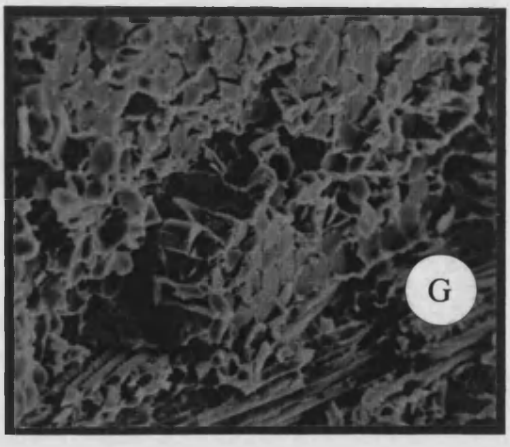

50 μm

Figure 3.81 Tensile fracture surface of a Nicalon-357 specimen with longitudinal fibre orientation, showing the partial removal of a fibre bundle associated with a glass weft. G

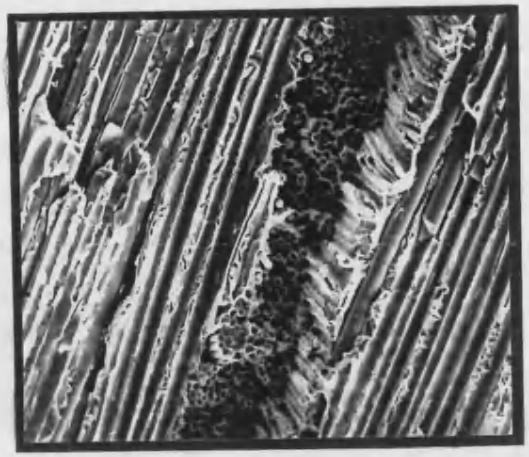

Figure 3.82 Tensile fracture surface of a Nicalon-357 composite, with transverse fibre orientation, showing fibre splitting and debonding of the glass weft fibres from the aluminium.

Figure 3.83 Failure of Nicalon fibres perpendicular to their length, on the fracture surface of a transverse fibre orientation Nicalon-357 composite, tested in tension.

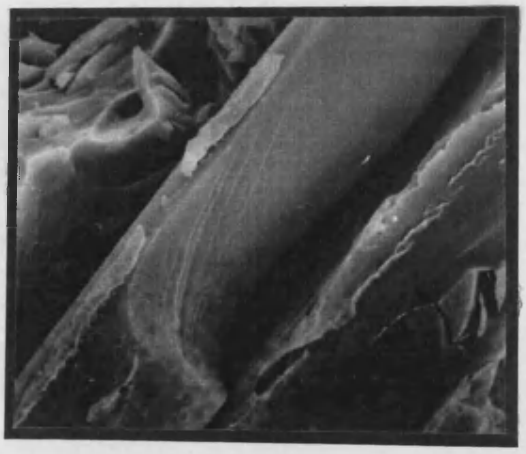

Figure 3.84 Fracture of a Nicalon fibre, from the transverse tensile specimen, with a combination of splitting and transverse fracture.

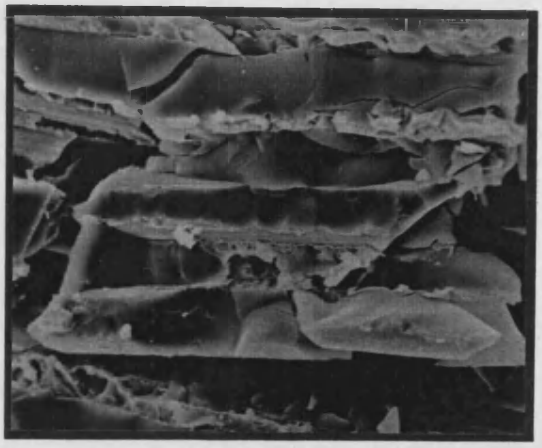

Figure 3.85 The fracture surface of a transverse tensile Nicalon-357 composite, showing the partial removal of a split bundle of Nicalon fibres.

50 μm

Figure 3.86 The fracture surface of a transverse tensile Nicalon-357 composite, showing the glass weft separation from the matrix and damage to the fibres.

100 μm

Figure 3.87 The surface of a tensile test bar with transverse Nicalon fibres, which shows a volume of incomplete infiltration.

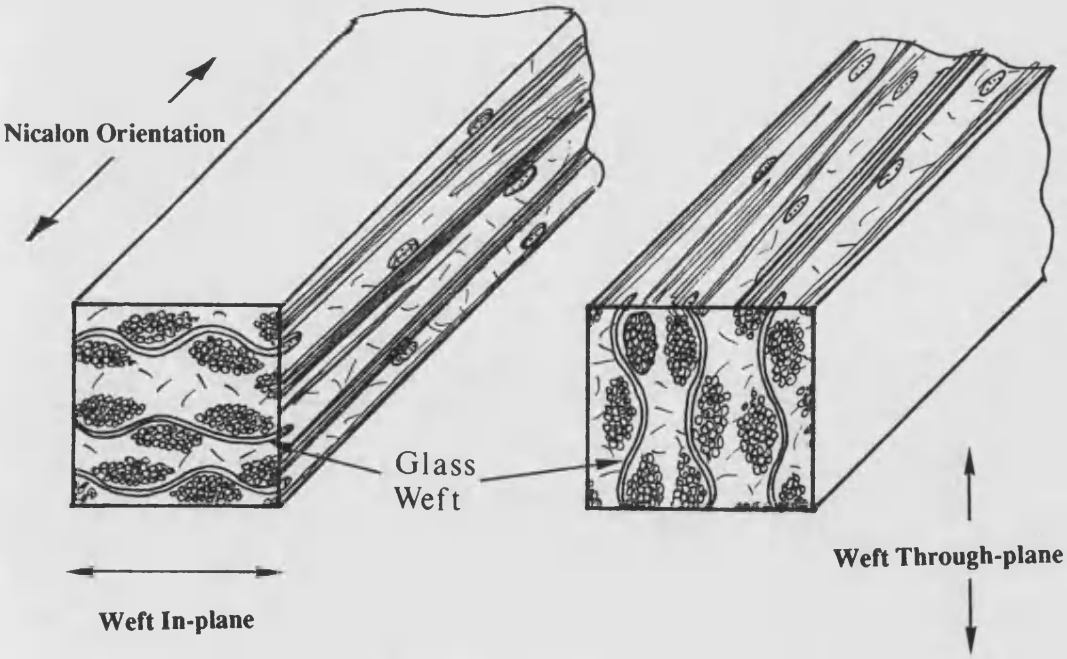

Figure 3.88 A schematic of the flexural test bars with, a, the glass weft in-plane and, b, through-plane of the composite.

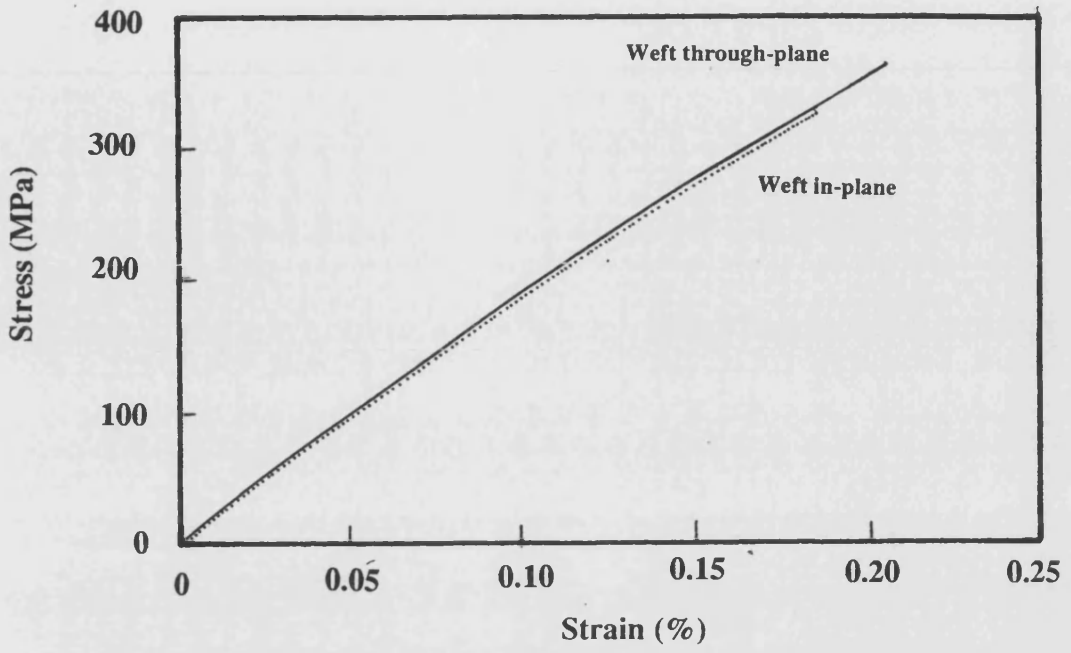

Figure 3.89 The stress versus strain curve for the Nicalon-357 composite tested in flexure, with the glass weft through- and in-plane.

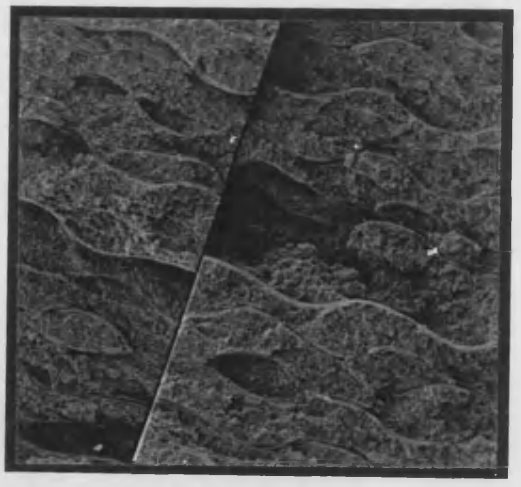

Figure 3.90 Fracture surface of the flexural test specimen with longitudinal fibre orientation. Nicalon-357 composite, shows stepping of the fracture path at the glass weft and brittle fracture of Nicalon areas.

Figure 3.91 Fracture surface of Nicalon-357 composite with fibres in longitudinal orientation and tested in flexure, fibre fragmentation.

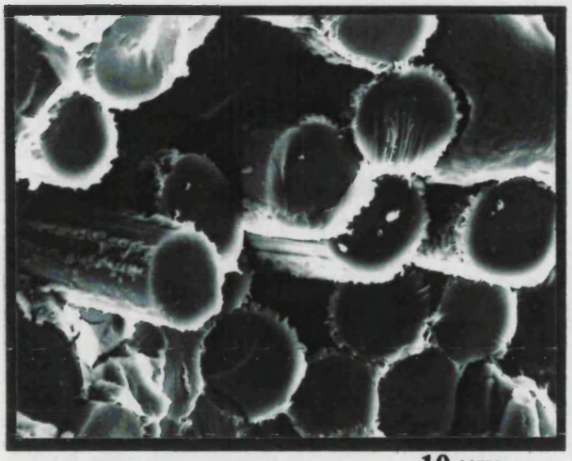

Figure 3.92 Fracture surface of Nicalon-357 composite with fibres in longitudinal orientation and tested in flexure, with 'spikey' phase on the fibre surface.

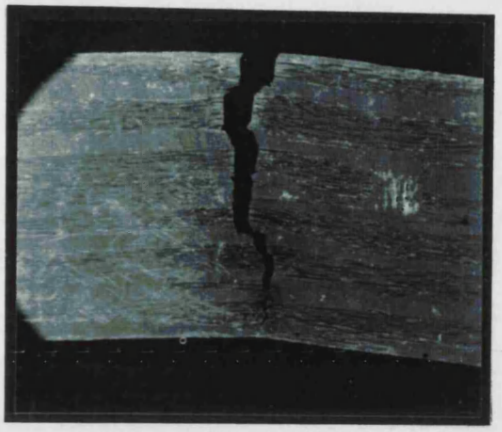

Figure 3.93 Section through the fracture surface of a Nicalon-357 composite tested in flexure, with the fibres in the longitudinal orientation, showing the brittle nature of the failure of tows.

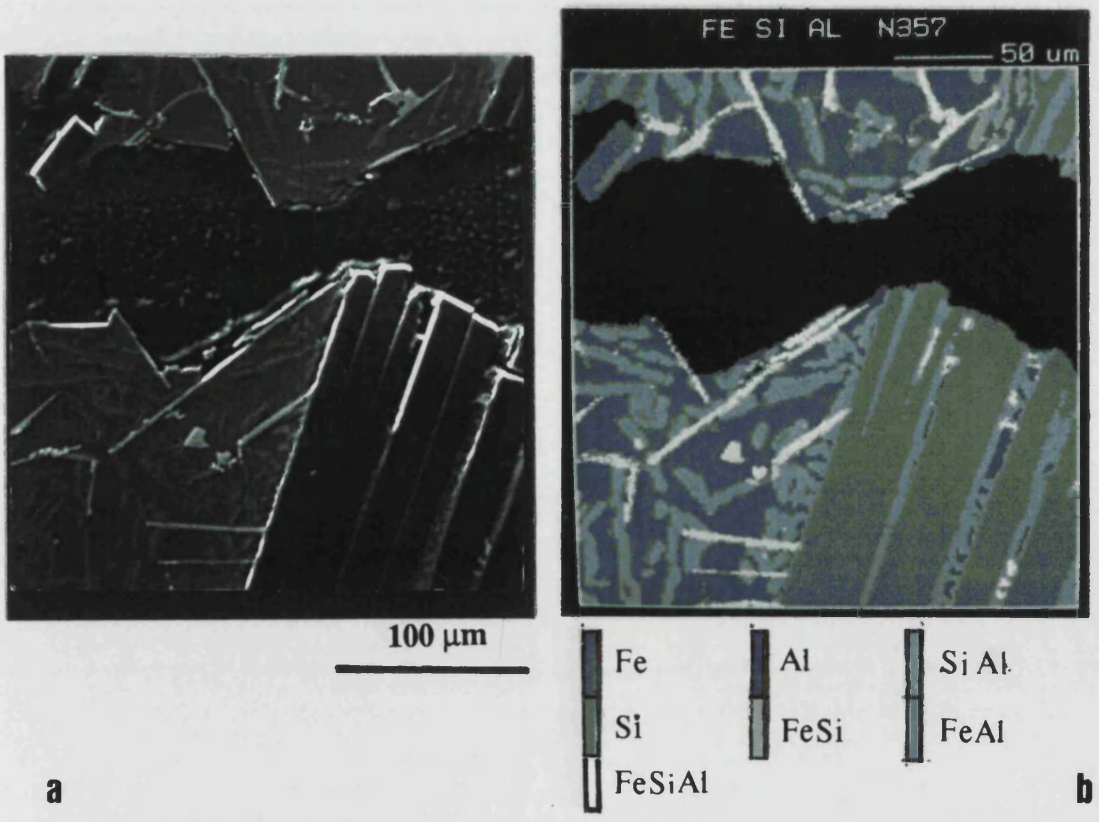

Figure 3.94 The matrix region from the section through the fracture surface of a flexural test bar of Nicalon-357 composite with longitudinal fibre orientation. The features in the fracture path in the SEM, a, are shown to be either silicon or intermetallics in the WDS x-ray combination map for iron, silicon and aluminium, b. The crack is running from left to right.

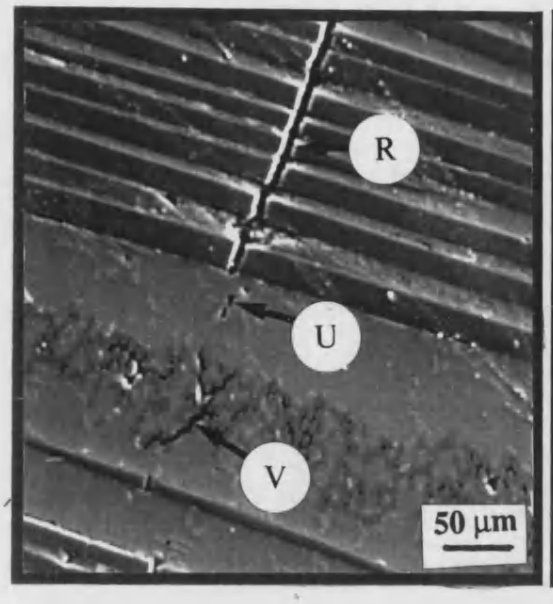

Figure 3.95 Section through the fractured flexural test bar of Nicalon-357 composite away from the main crack path showing complete Nicalon tow failure, R, advance failure of the glass weft, U, and matrix voiding at second phase particles, V.

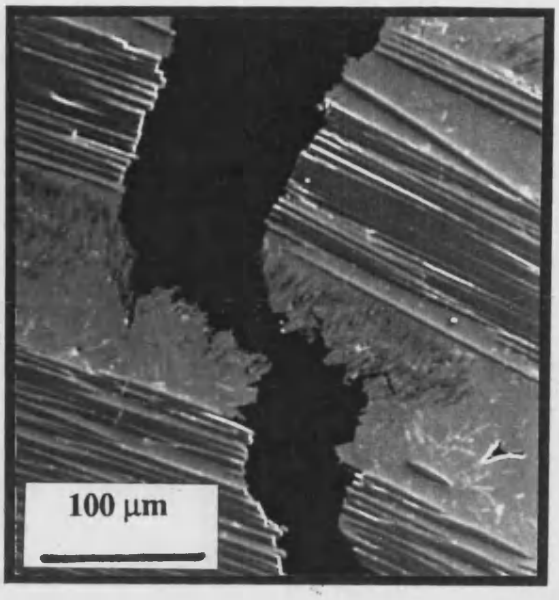

Figure 3.96 Section through the main crack path of the Nicalon-357 composite, with a change in the fracture path due to the glass weft.

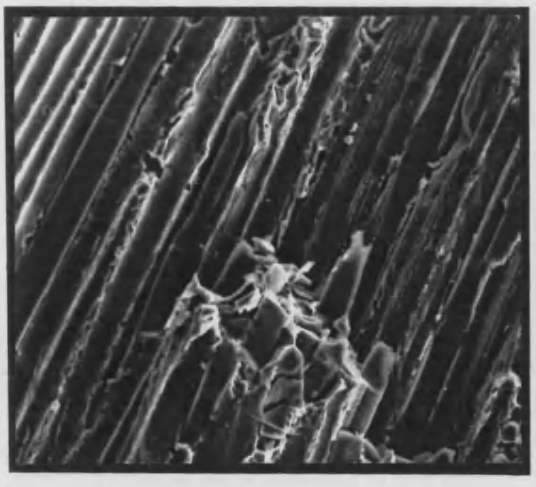

Figure 3.97 Flexural test fracture surface for the Nicalon-357 composite with the fibres in the transverse orientation, with much fibre splitting.

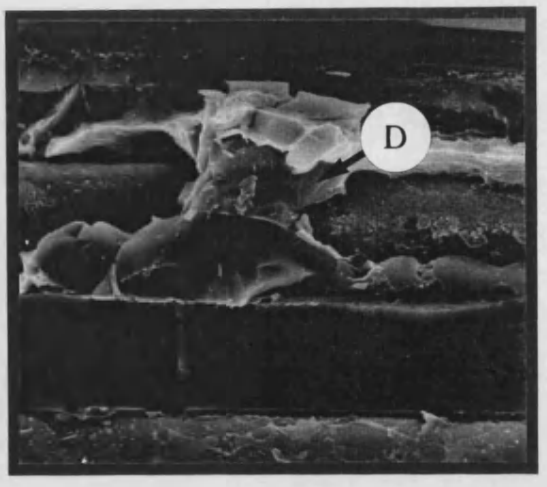

Figure 3.98 Fibre splitting associated with an intermetallic phase, D, on the fracture surface of a Nicalon-357 composite tested in flexure with the fibres in the transverse orientation.

10 μm

Figure 3.99 Nicalon fibre failure perpendicular to their length in a transverse oriented fibre Nicalon-357 composite tested in flexure.

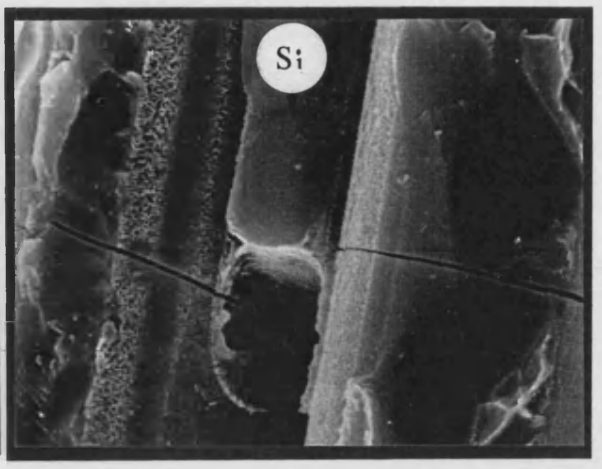

5 μm

Figure 3.100 Apparent "skinning" of Nicalon fibres when tested in flexure, with the fibres in the transverse orientation, for the Nicalon-357 composite. The failure of the fibres perpendicular to their length is associated with the silicon in the centre.

10 μm

Figure 3.101 A bulk interphase resulting in the "skinning" of the Nicalon in flexural tests of the transverse orientation Nicalon-357 composite, the bright phase Q shows x-rays from magnesium, aluminium and oxygen, in addition to fibre elements.

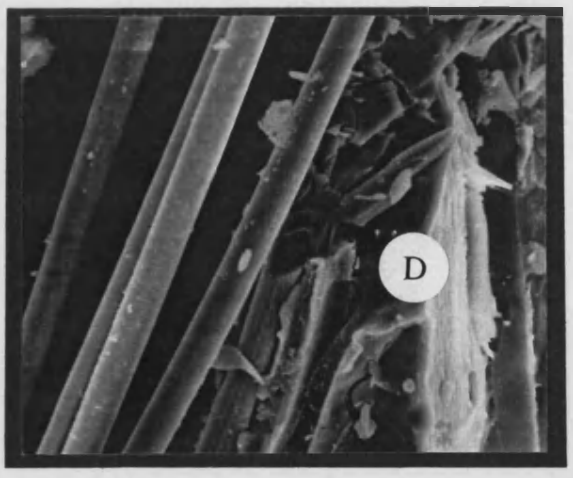

10 μm

Figure 3.102 Transverse fracture surface of a Nicalon-357 composite flexural test, with a region that was not fully infiltrated. The feature marked, D, is an iron-rich intermetallic and has caused fibre failure.

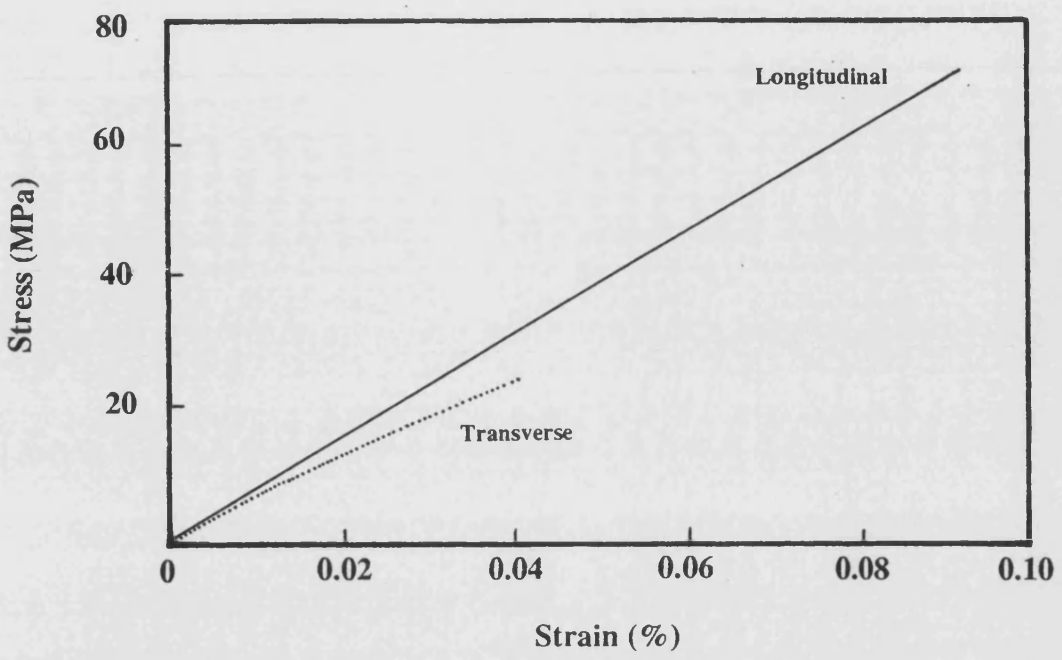

Figure 3.103 The stress versus strain curve for the heat treated Nicalon-357 composite.

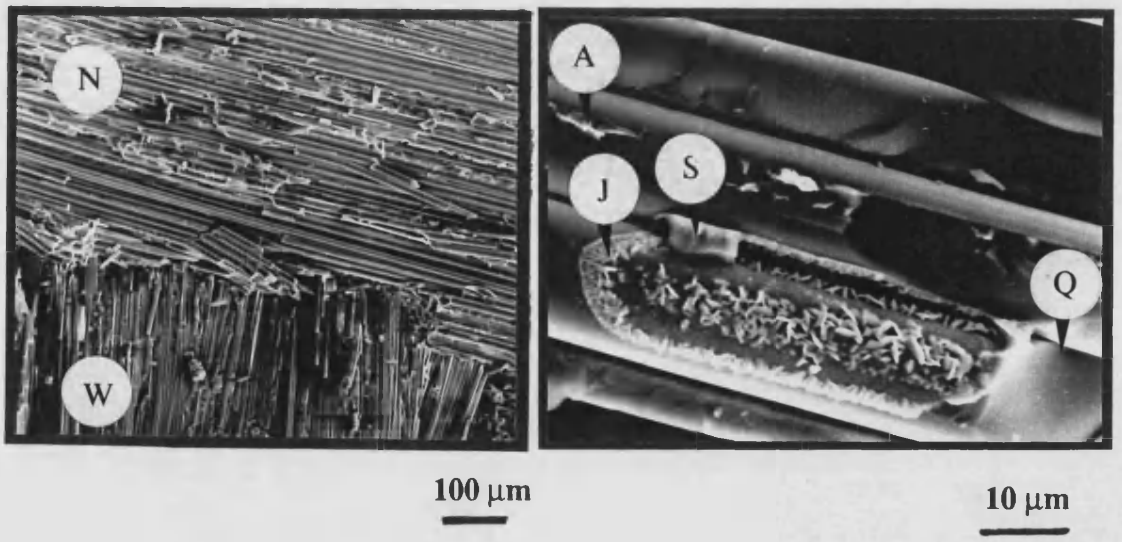

Figure 3.104 The shear fracture surface of the Nicalon-357 composite, with both Nicalon, N, and weft, W, fibres shown.

Figure 3.105 Shear fracture surface of the Nicalon-357 composite with fibre splitting, Q, retained matrix phases, aluminium, A, and silicon, S. The fibrous interphase, J, contains aluminium, magnesium and oxygen.

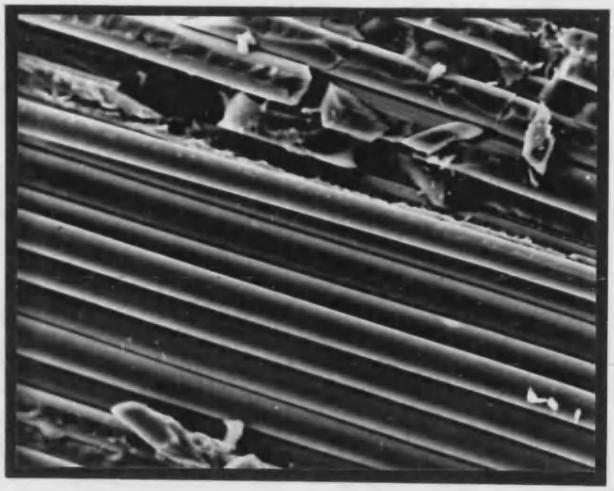

Figure 3.106 Fracture surface of a Nicalon-357 composite tested in shear, showing a region which had not been infiltrated with clean fibre surfaces and fibre splitting.

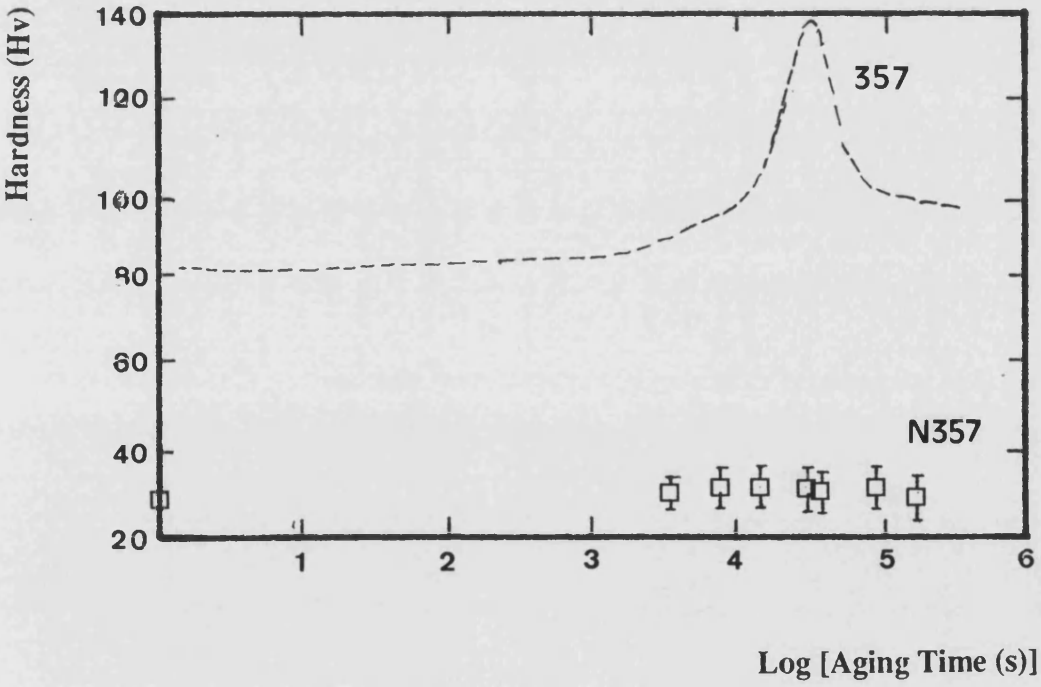

Figure 3.107 The hardness versus post-solution treatment heat treatment time for the Nicalon-357 composite. The heat treatment was carried out at 160°C.

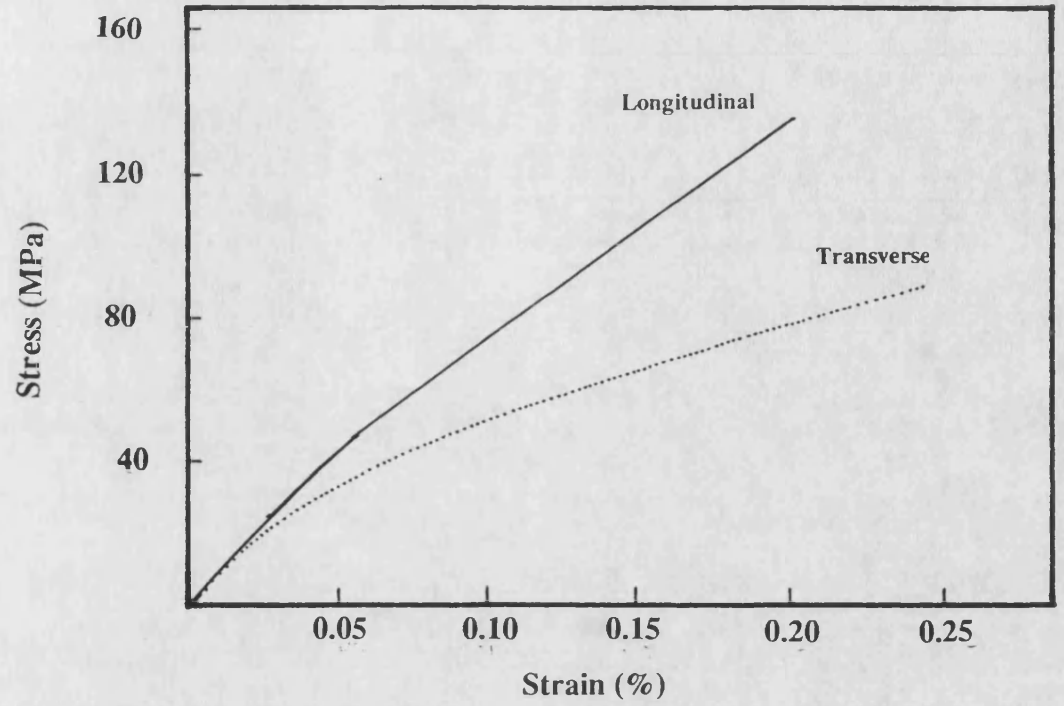

Figure 3.108 A typical tensile stress versus strain curve for the Nicalon-commercially pure aluminium composite with the woven Nicalon reinforcement. With both the 01 and 02 curves.

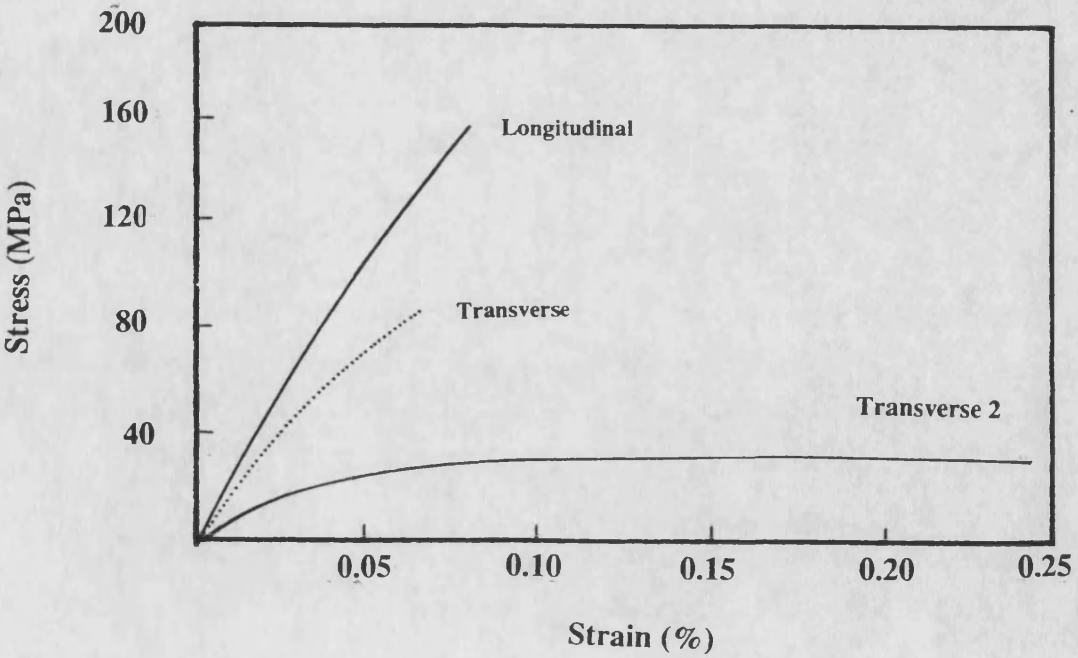

Figure 3.109 A typical example of the stress versus strain curve for the Nicalon-commercially pure aluminium composite with the filament wound reinforcement, tested in tension, for both the longitudinal and transverse orientations. Two transverse curves are given because of the presence of a woven Nicalon layer in some specimens.

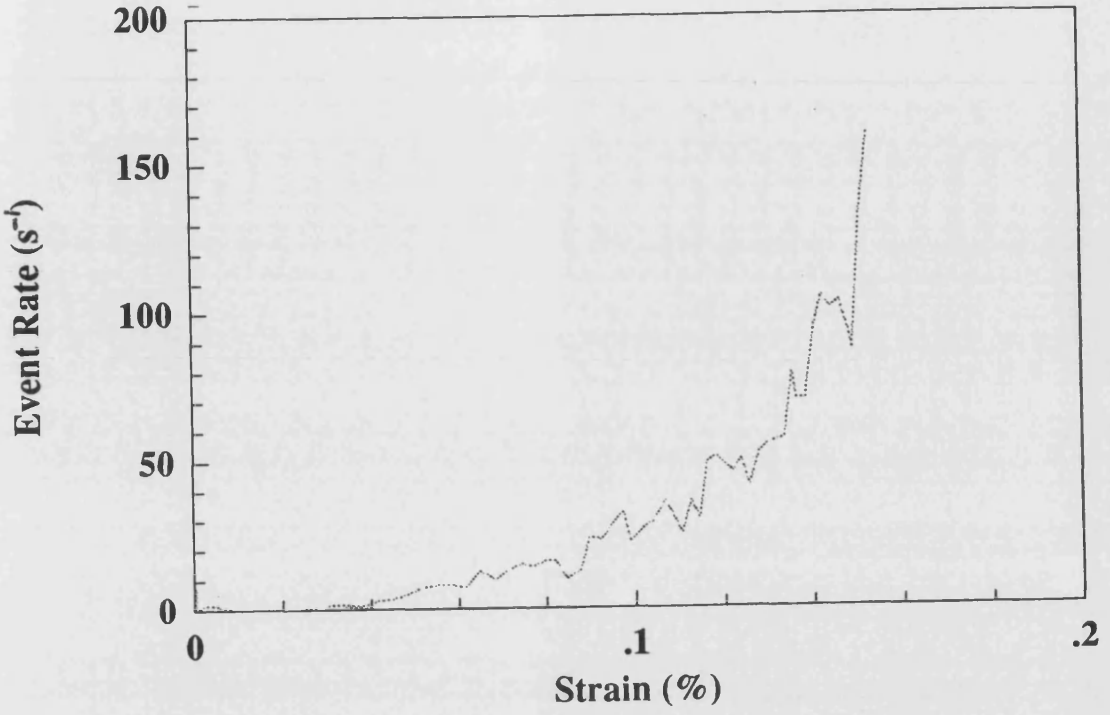

Figure 3.110 A typical acoustic emission event rate versus strain plot for the Nicalon-commercially pure aluminium composite tested in tension.

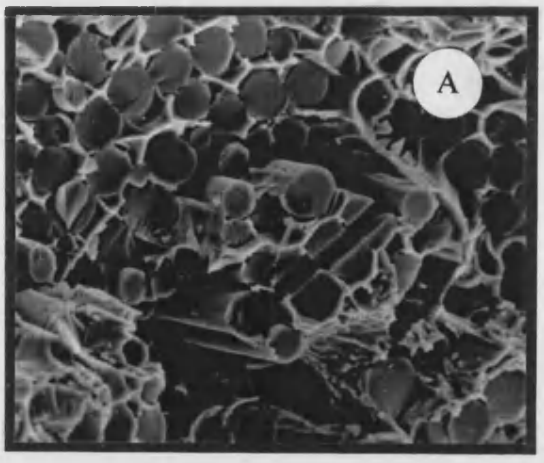

Figure 3.111 Fracture surface of a Nicalon-commercially pure aluminium composite, tested to failure in tension, with longitudinal fibre orientation. A well infiltrated region with plastically deformed aluminium, A, brittle fibre failure and fibre splitting.

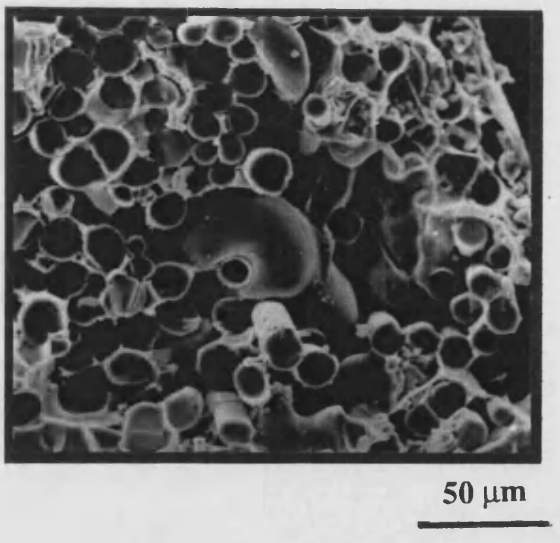

Figure 3.112 A poorly infiltrated region of the Nicalon-commercially pure aluminium composite revealed on the fracture surface of a tensile test specimen. The feature in the centre is prematurely solidified aluminium.

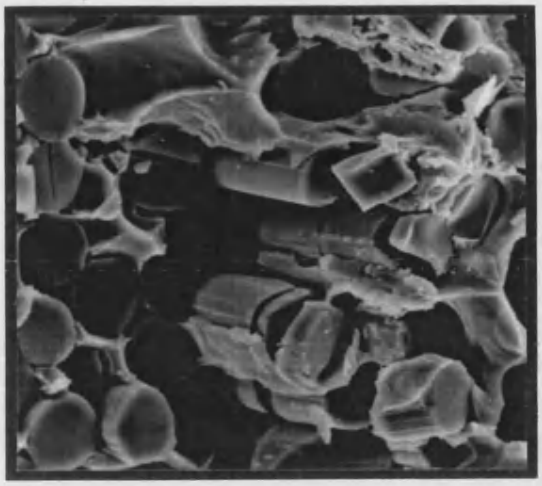

10 μm

Figure 3.113 Segmentation of the Nicalon fibre in a tensile test specimen of the commercial pure aluminium composite.

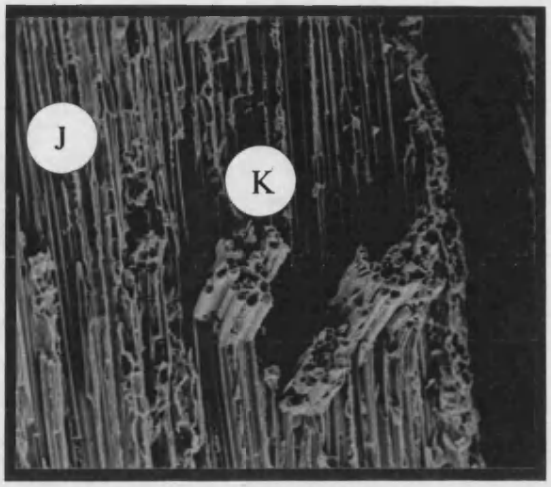

100 μm

Figure 3.114 Fracture surface of a Nicalon-commercially pure aluminium composite, tested in tension, with the fibres in the transverse orientation. Fibre splitting is common, J, and clumps of infiltrated fibres partially removed from the surface, K.

10 μm

Figure 3.115 A transverse ıracture surface from a Nicalon-commercially pure aluminium composite tested in tension, showing fibre failure perpendicular to its length and retained aluminium on the surface.

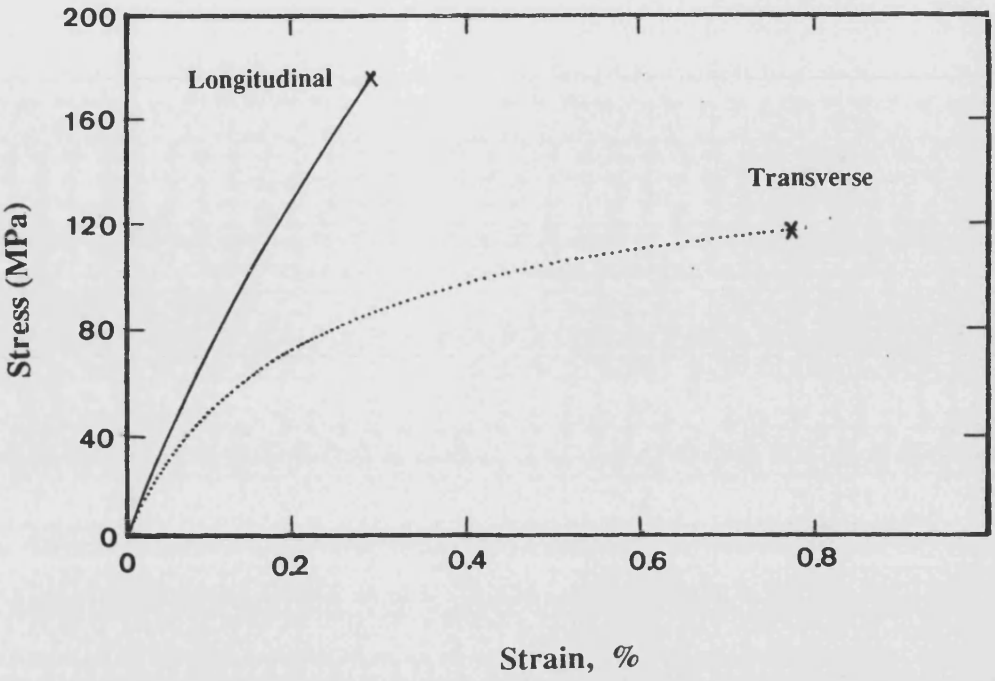

Figure 3.116 A typical stress versus strain curve for the Nicalon-commercially pure composite tested in flexure. With curves for both fibre orientations.

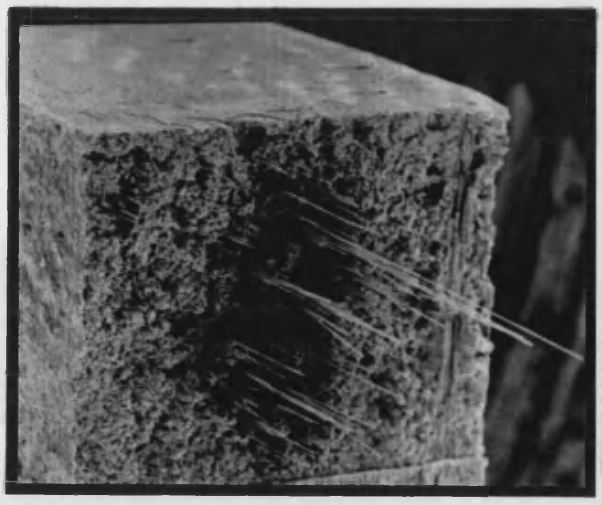

Figure 3.117 The flexural test fracture surface for the commercially pure based composite with an extensive volume of non infiltrated fibres, resulting in pseudo-pullout.

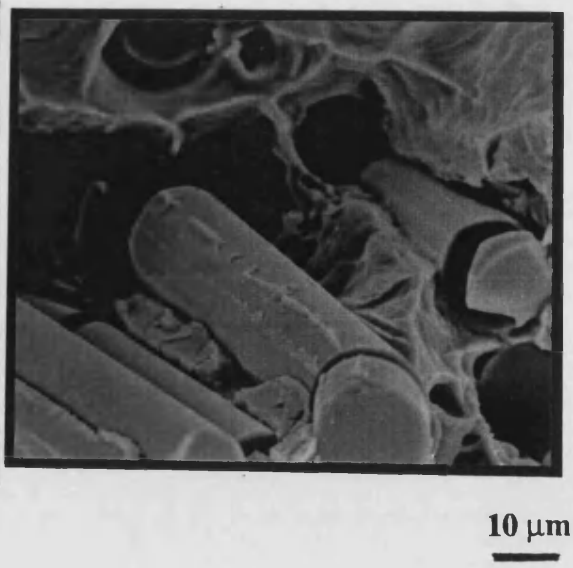

Figure 3.118 Fracture surface from a Nicalon-commercially pure aluminium composite with longitudinal fibres, showing the failure of the fibres perpendicular to their length and retained surface aluminium.

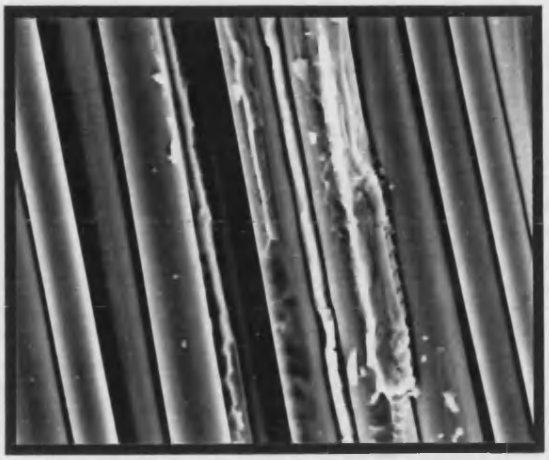

Figure 3.119 Fracture surface of a Nicalon-commercially pure aluminium composite with transverse fibres and tested in flexure, showing the clean fibre surface of a non infiltrated composite.

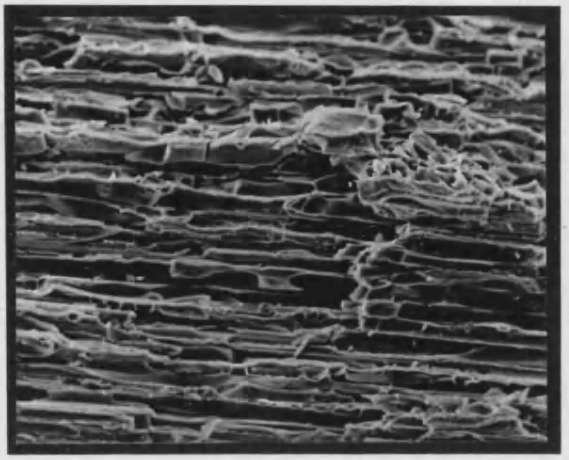

Figure 3.120 The shear fracture surface of a Nicalon-commercially pure aluminium composite, with a well infiltrated region, showing fibre splitting.

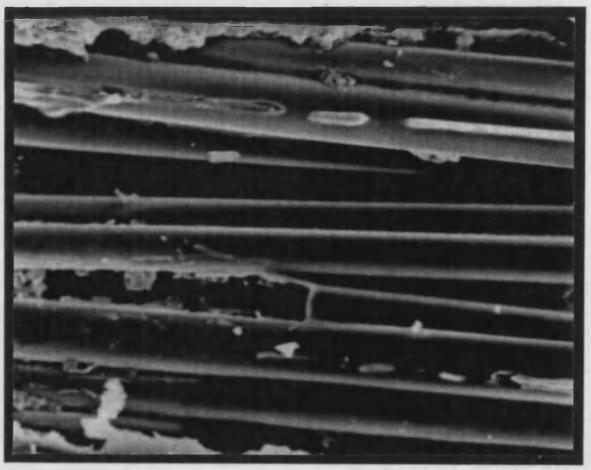

Figure 3.121 An area of the shear fracture surface which was not infiltrated where the fibres are undamaged.

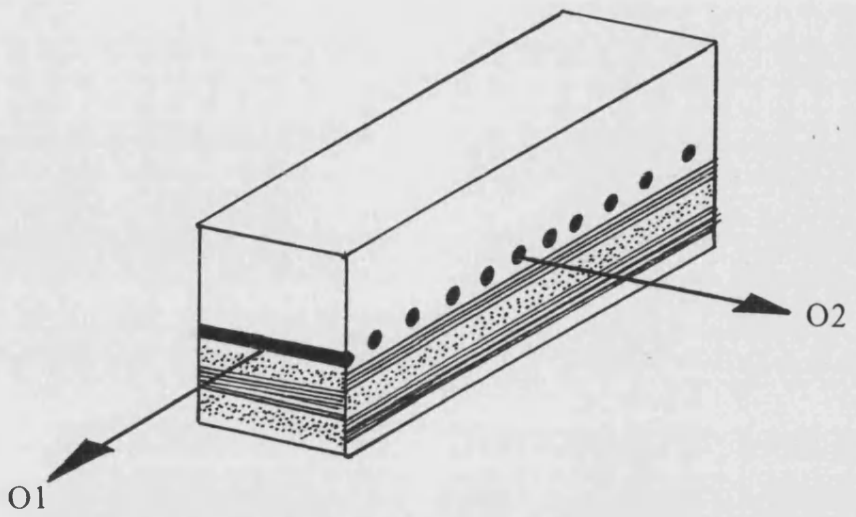

Figure 3.122 Schematic diagram of the orientations in the FP-alumnia/Borsic-357 alloy composite.

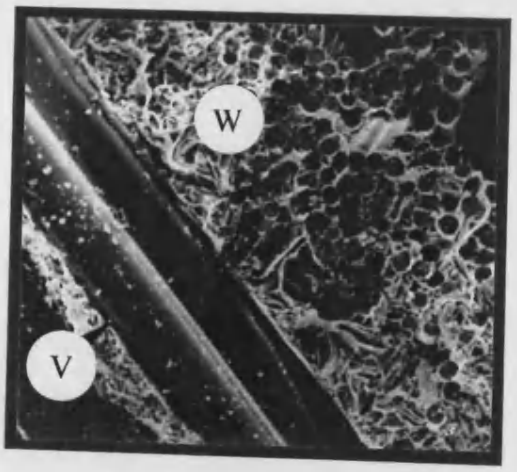

Figure 3.123 Fracture surface of the hybrid composite showing the Borsic fibre splitting, V, and the fibre failure of the alumina region, W.

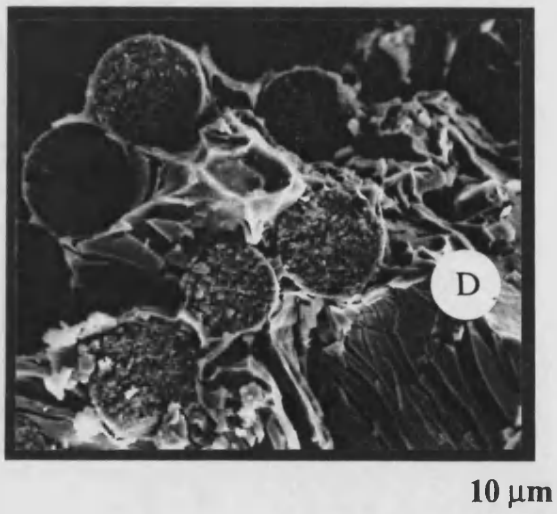

Figure 3.124 Fracture surface of the alumina region of the hybrid composite with the longitudinal orientated fibre fracture associated with a number of shattered intermetallics, D. The fracture of the fibres shows their polycrystalline nature.

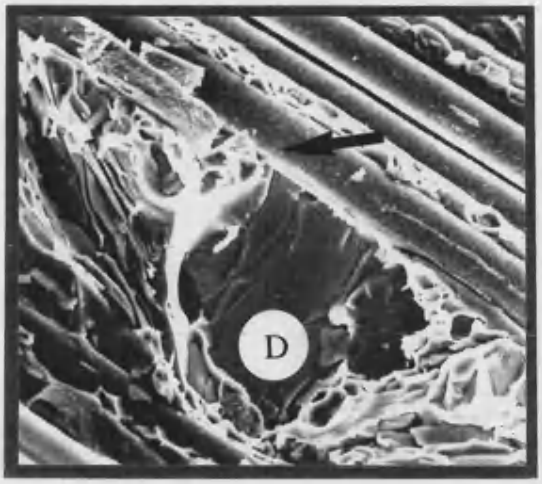

Figure 3.125 The fracture surface of the alumina region, with the fibres in the transverse orientation, the large intermetallic, D, in the centre is associated with perpendicular fibre failure marked with the arrow.

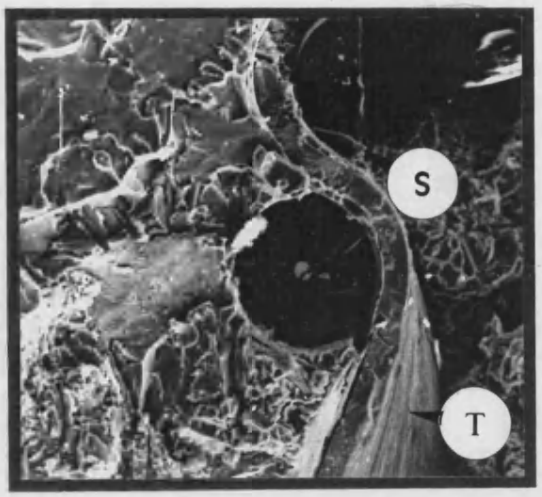

Figure 3.126 The fracture surface of the Borsic fibre region of the hybrid composite with the fibre splitting, S, and debonding at the titanium weft, T.

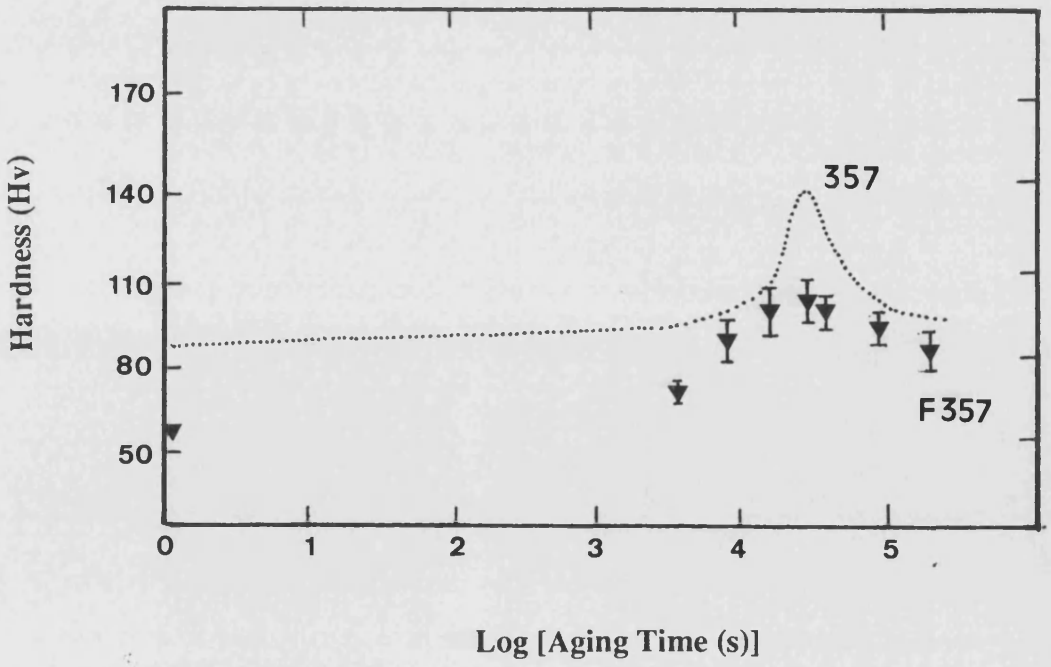

Figure 3.127 The hardness versus post solution treatment heat treatment time. Heat treatment carried out at 160°C.

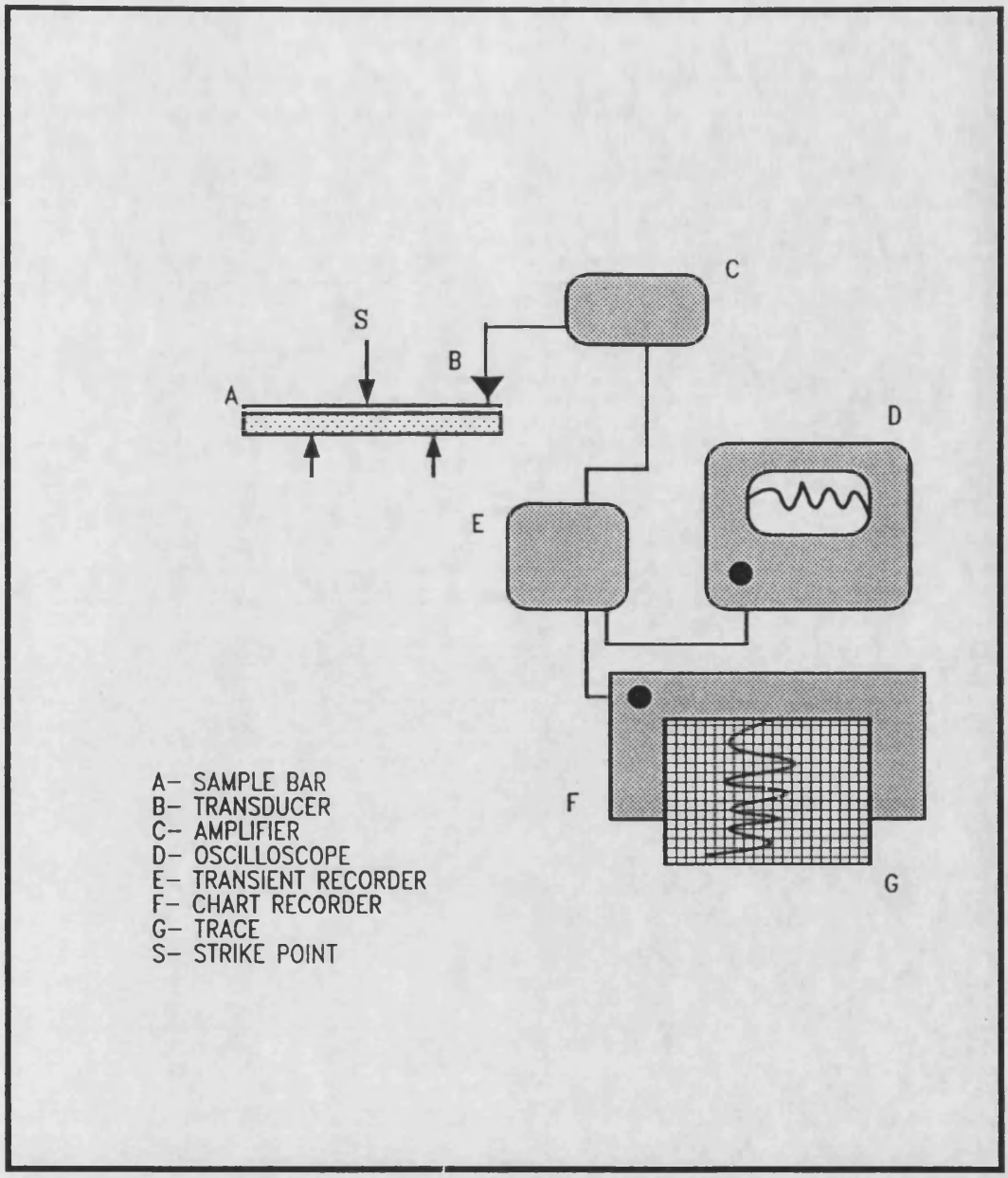

Figure 3.128 A schematic diagram of the arrangement used to measure the dynamic modulus.

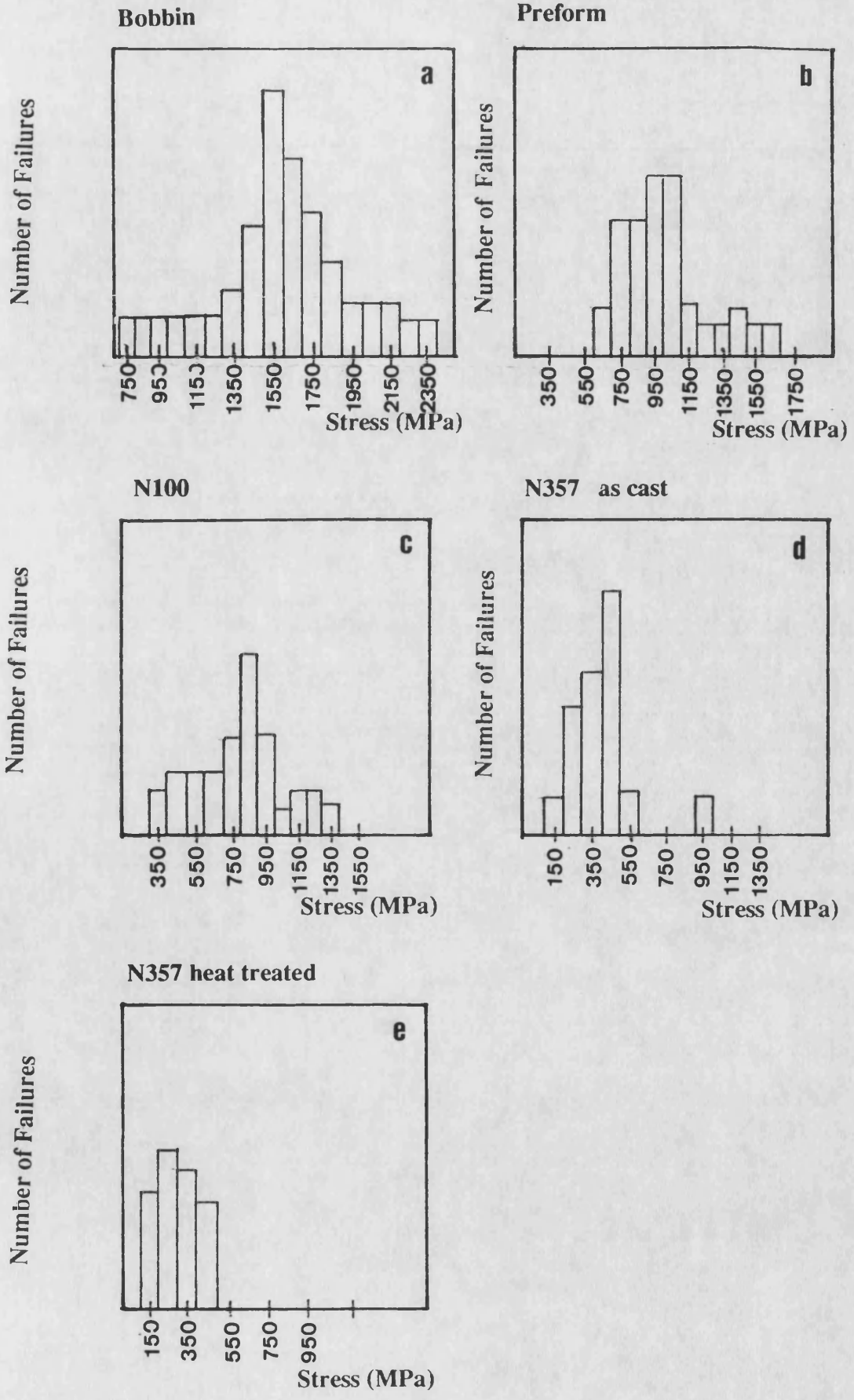

Figure 3.129 Measured strengths of fibres from each environment, a, as-received, b, preform, c pure aluminium composite, d, as cast alloy composite and e, heat treated composite.

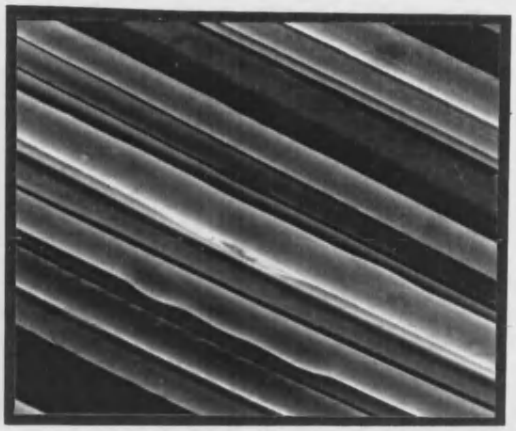

Figure 3.130 A SEM of the as received Nicalon fibres with the size on the surface.

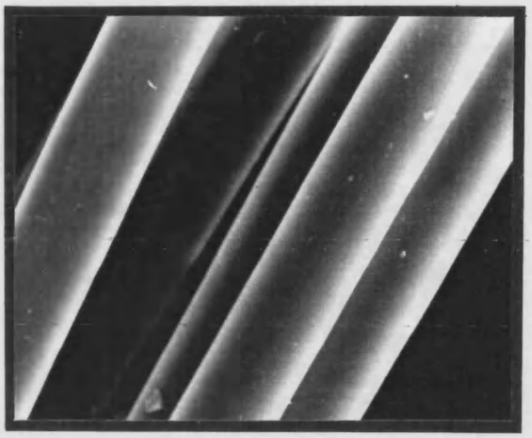

Figure 3.131 The Nicalon fibres after desizing.

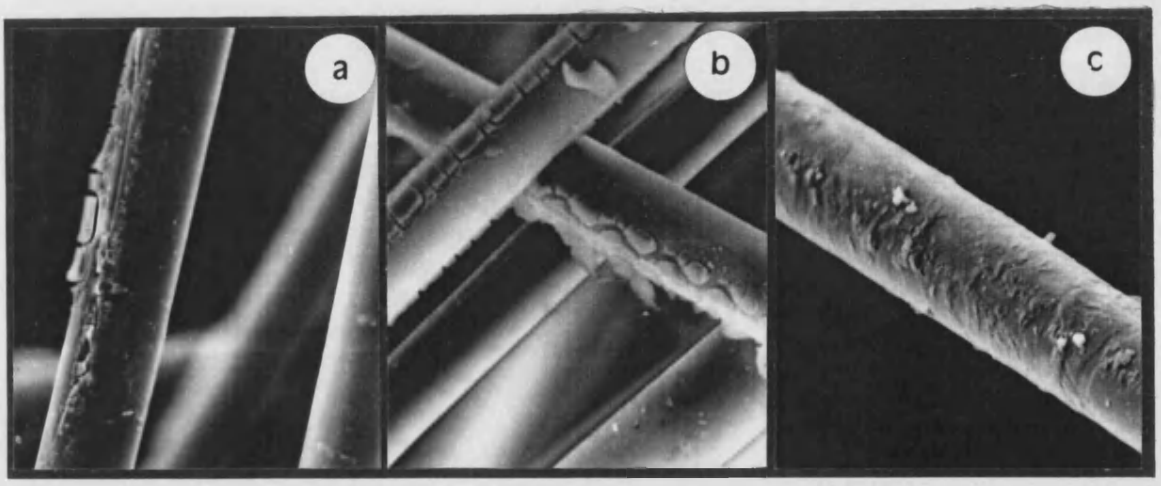

Figure 3.132 The Nicalon fibre as removed from the alloy based composite, showing silicon on the surface, a, extensive interphases, b, and reacted interface, c.

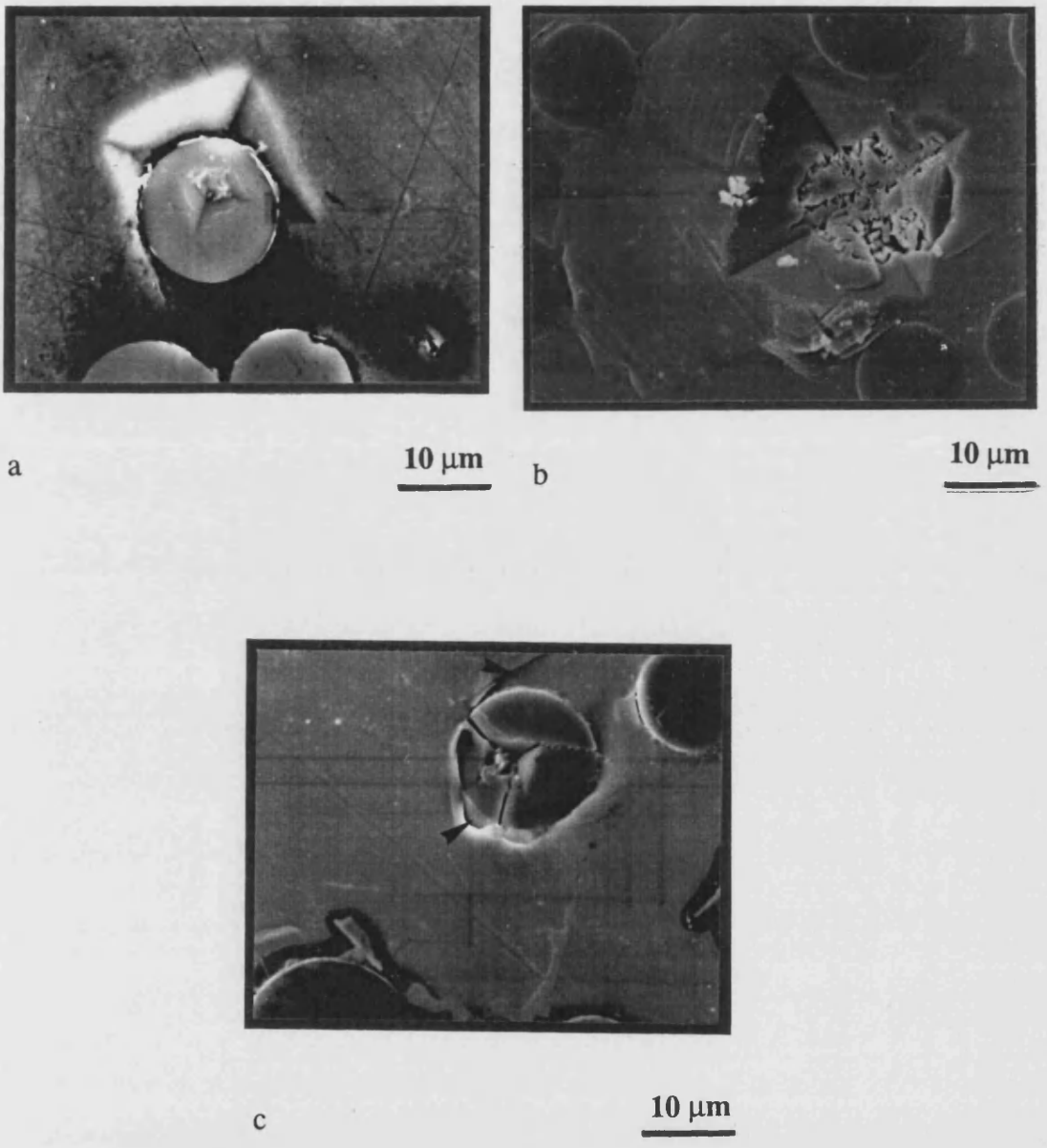

Figure 3.133 Typical indents produced in fibre/matrix interfacial shear tests with a, indent in fibre and matrix, b, a shattered fibre and deformed aluminum and c, matrix phases attached to a split and depressed fibre.

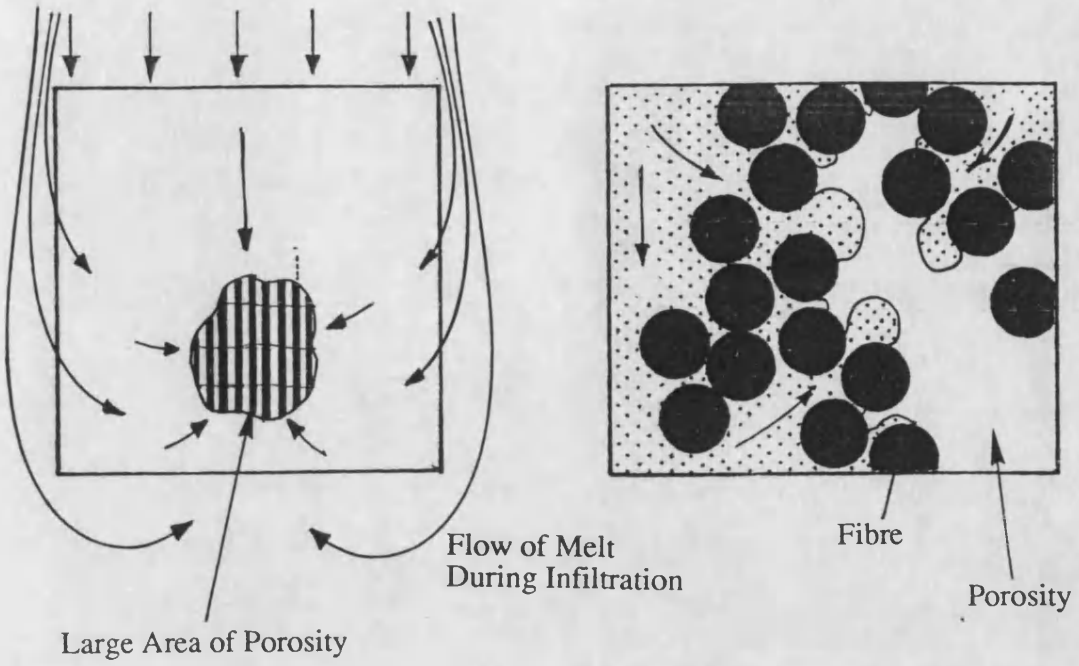

(a)

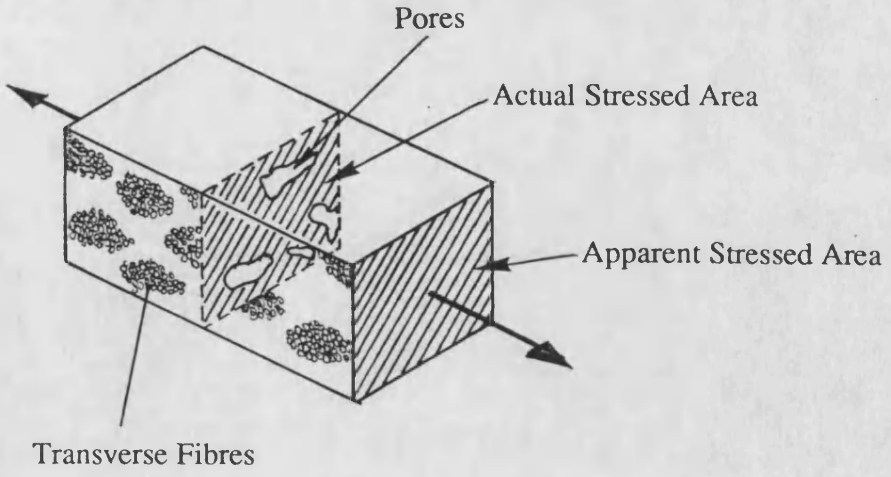

(b)

Figure 4.1 The formation of the porosity in the composite due to freeze off of the melt front, a, and the reduction of the loaded area due to porosity, b.

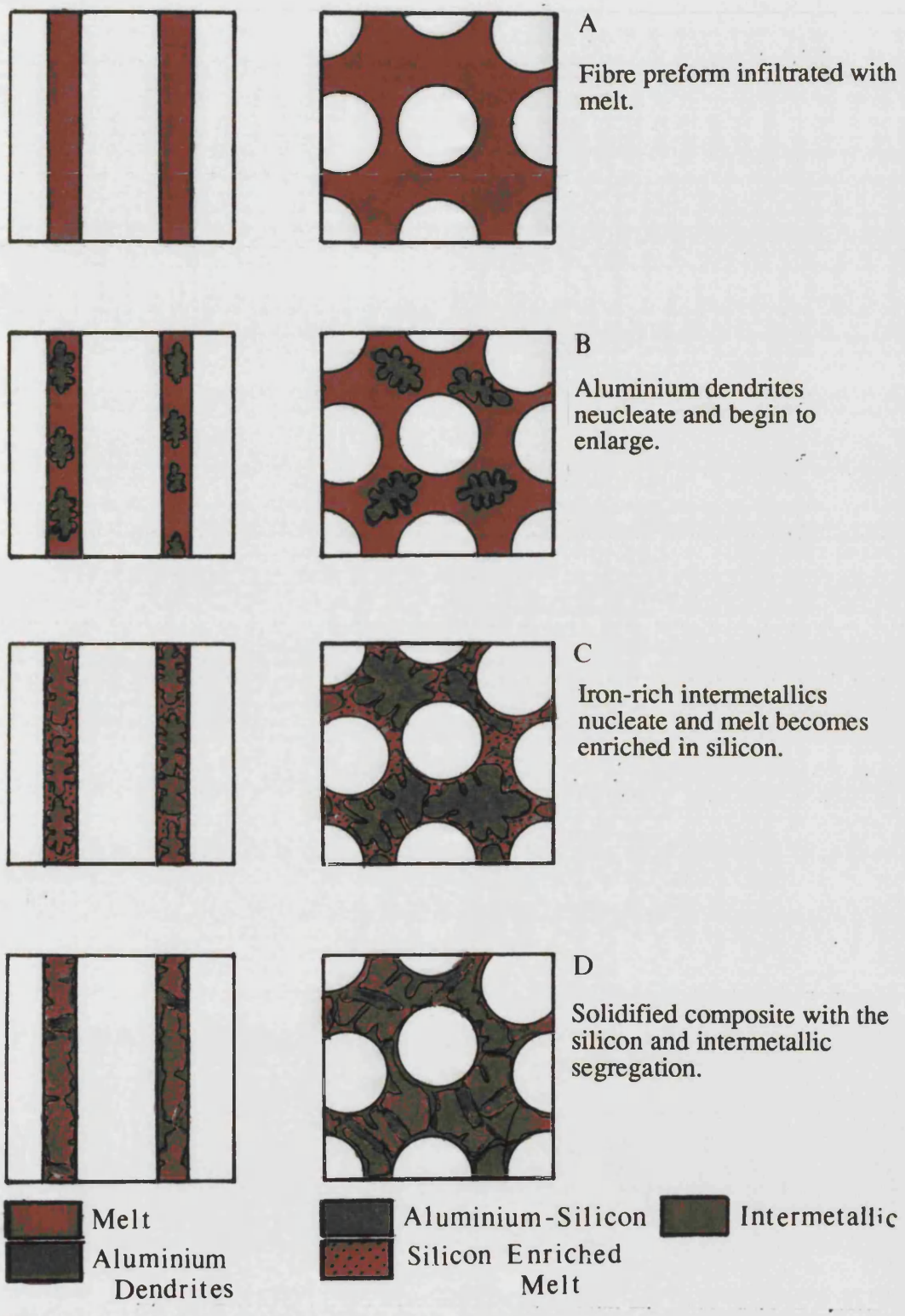

Figure 4.2 Schematic diagram representing the solidification of the Nicalon composite, in a, the matrix fully infiltrated into the fibre mass, the aluminium dendrites nucleate and start to extend, b, pushing the silicon and iron rich melt towards the fibres, the intermetallics nucleate and grow, c, finally the silicon eutectic remaining to solidify close to the fibres.

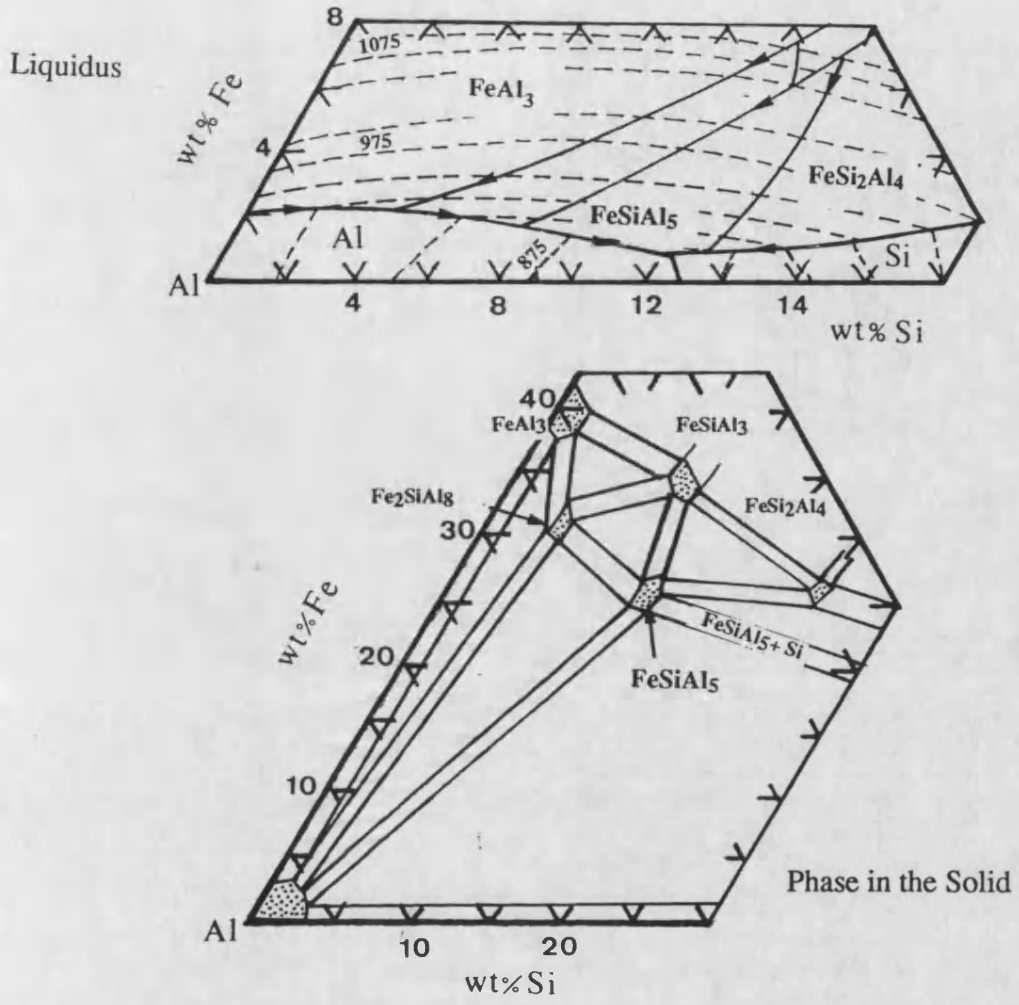

Figure 4.3 The aluminium corner of the aluminium-silicon-iron phase diagram, the liquidus and the phases in the solid.

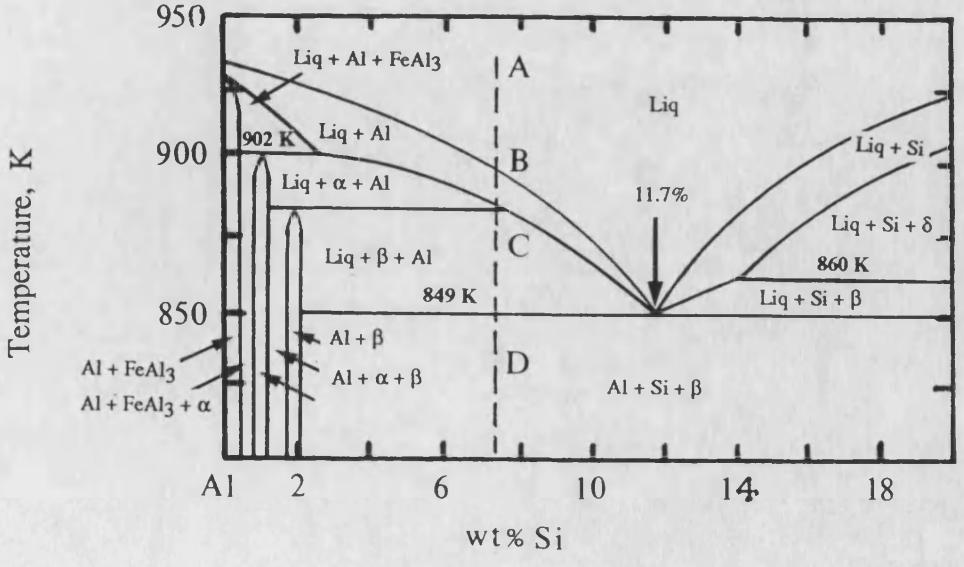

Figure 4.4 A pseudo binary phase diagram at 7.5 % iron, between aluminium and silicon.

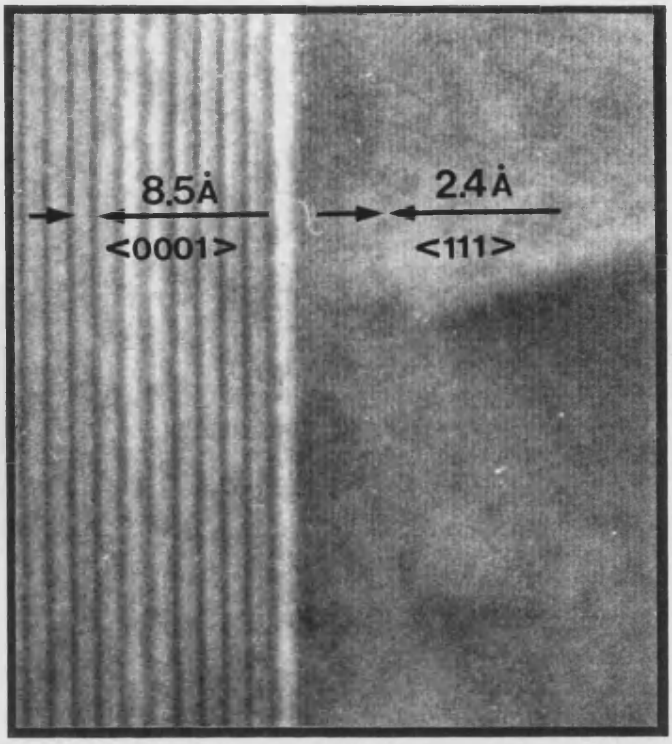

Figure 4.5 Partially transformed $FeSi_2Al_4$ intermetallic with orientation relationship to the stable $FeSiAl_5$ form, after Yang and Scott.

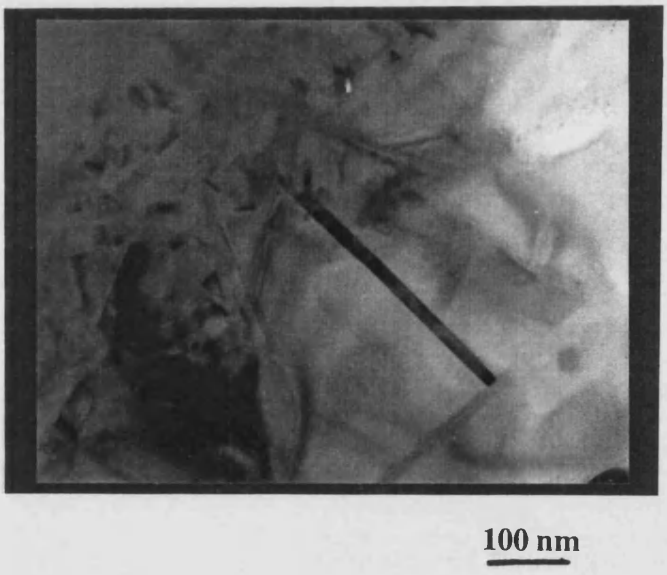

Figure 4.9 A TEM micrograph of the aluminium carbide formation at the interface of aluminium and carbon fibre, after Yang and Scott.

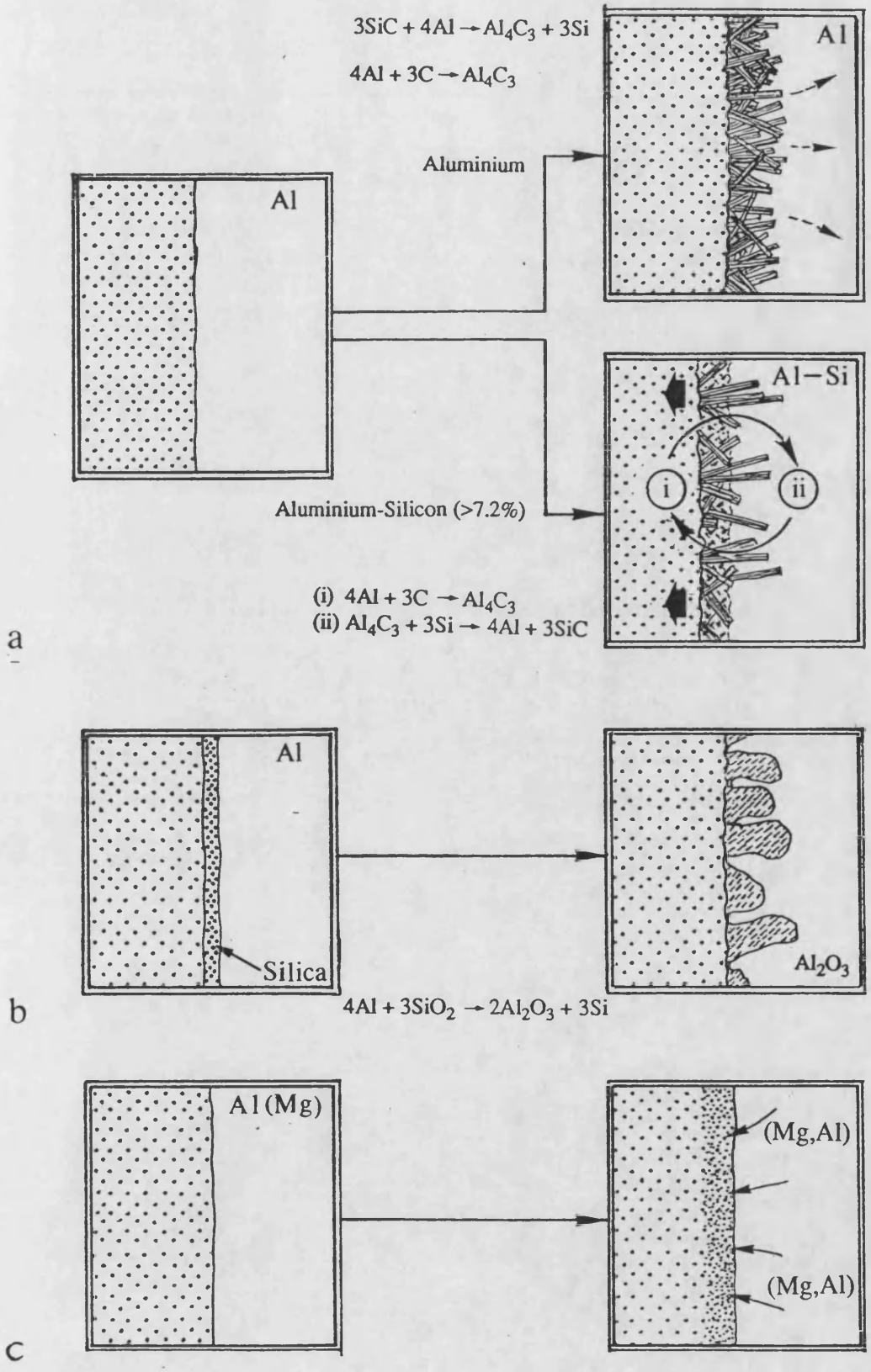

Figure 4.6 Schematic diagram of the interfacial reactions in the Nicalon composites. The interaction between aluminium and carbon containing phases to form aluminium carbide, a, the formation of alumina by reaction of aluminium and surface silica, b, and the diffusion/reaction of aluminium and silicon at the interface, c.

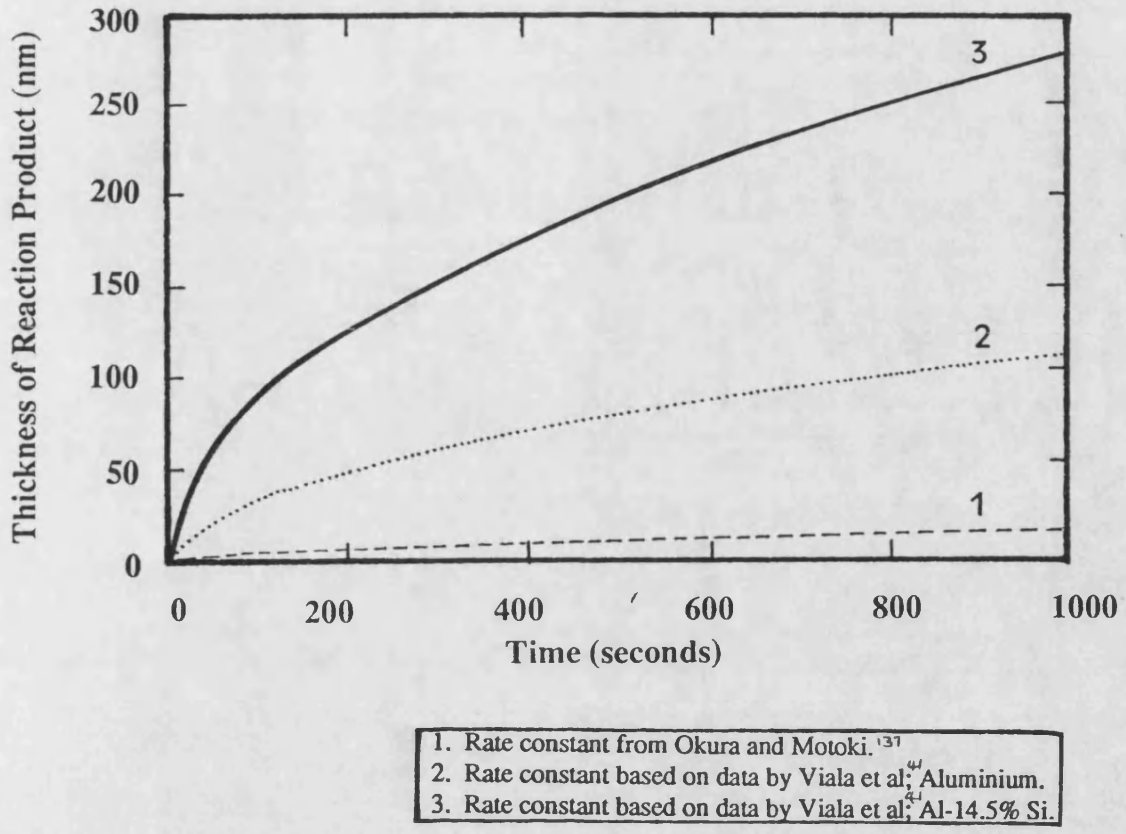

Figure 4.7 The reaction product thickness versus reaction time for the reaction between aluminium and carbon (Parabolic rate constant from Okur and Motoki[137]), aluminium and Nicalon (Parabolic rate constant calculated from Viala et al)[44] and aluminium-silicon alloy and Nicalon (rate constant calculated from Viala et al)[44] at 1000°C.

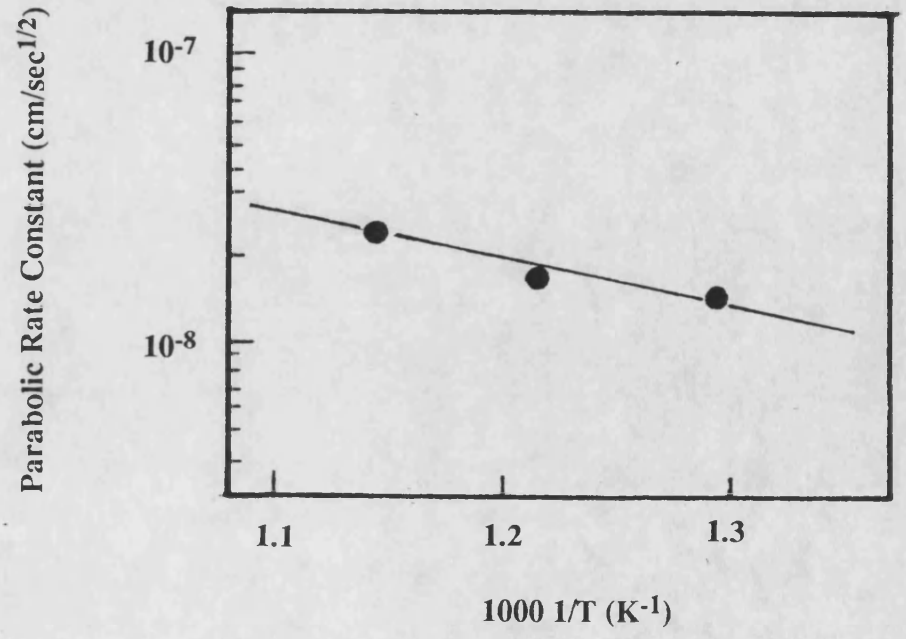

Figure 4.8 The variation of the rate constant with the reaction temperature

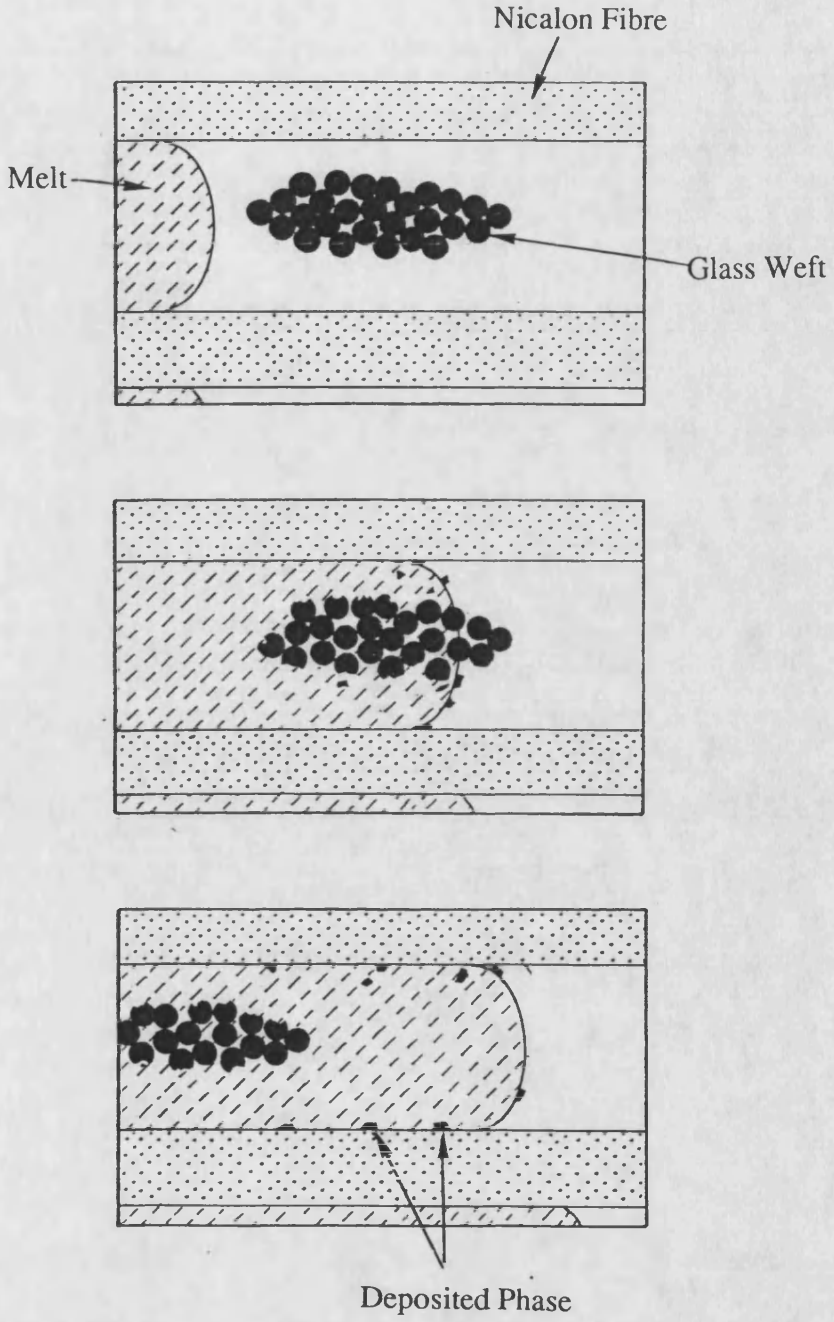

Figure 4.10 Schematic diagram of the deposition of phases at the fibre/matrix interface.

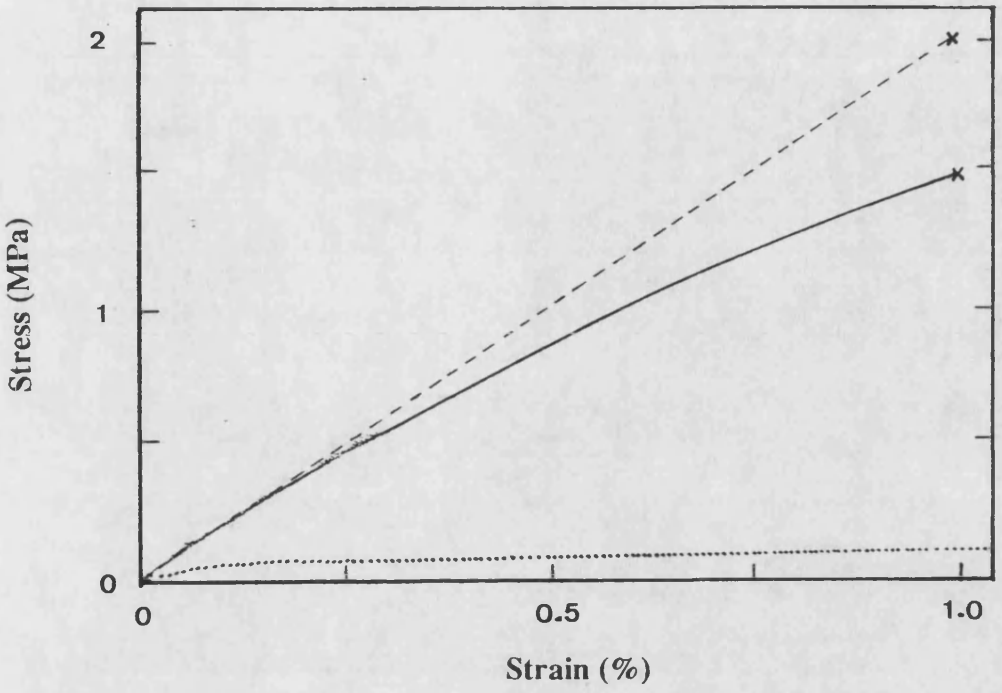

Figure 4.11 The predicted stress versus strain curve for the Nicalon-357 composite, based on the measured matrix properties and the fibre properties given by their manufacture.

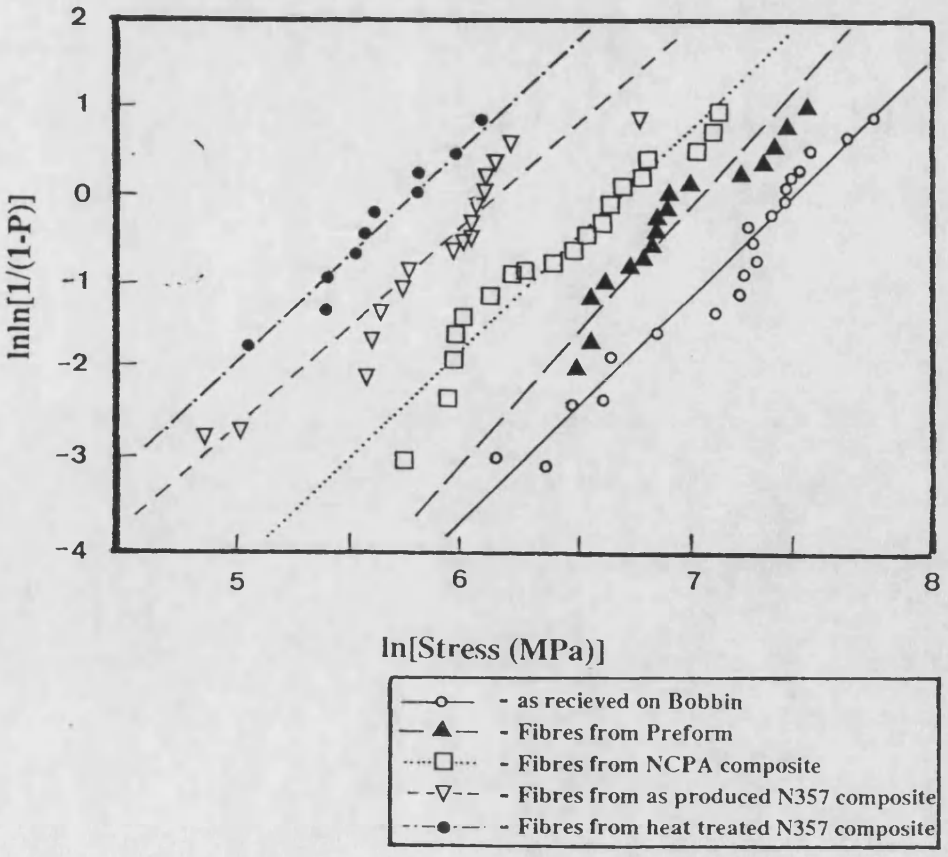

Figure 4.12 Weibull probability distribution plots for each fibre environment, from the single fibre tests.

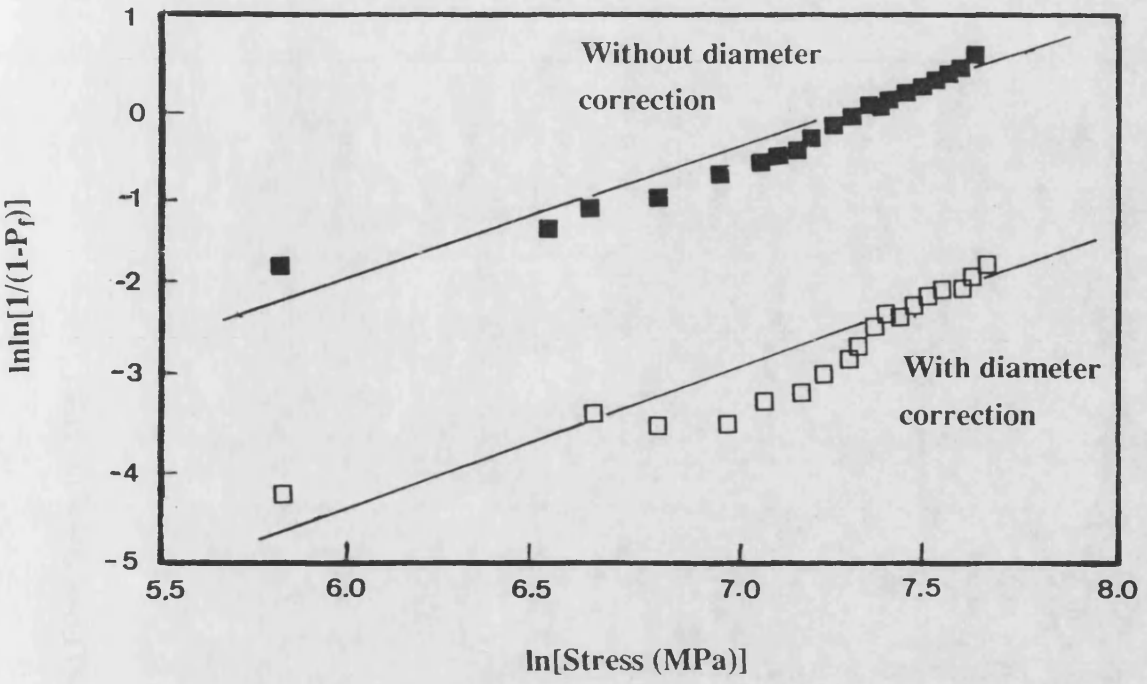

Figure 4.13 The Weibull probability distribution with and without a diameter correction.

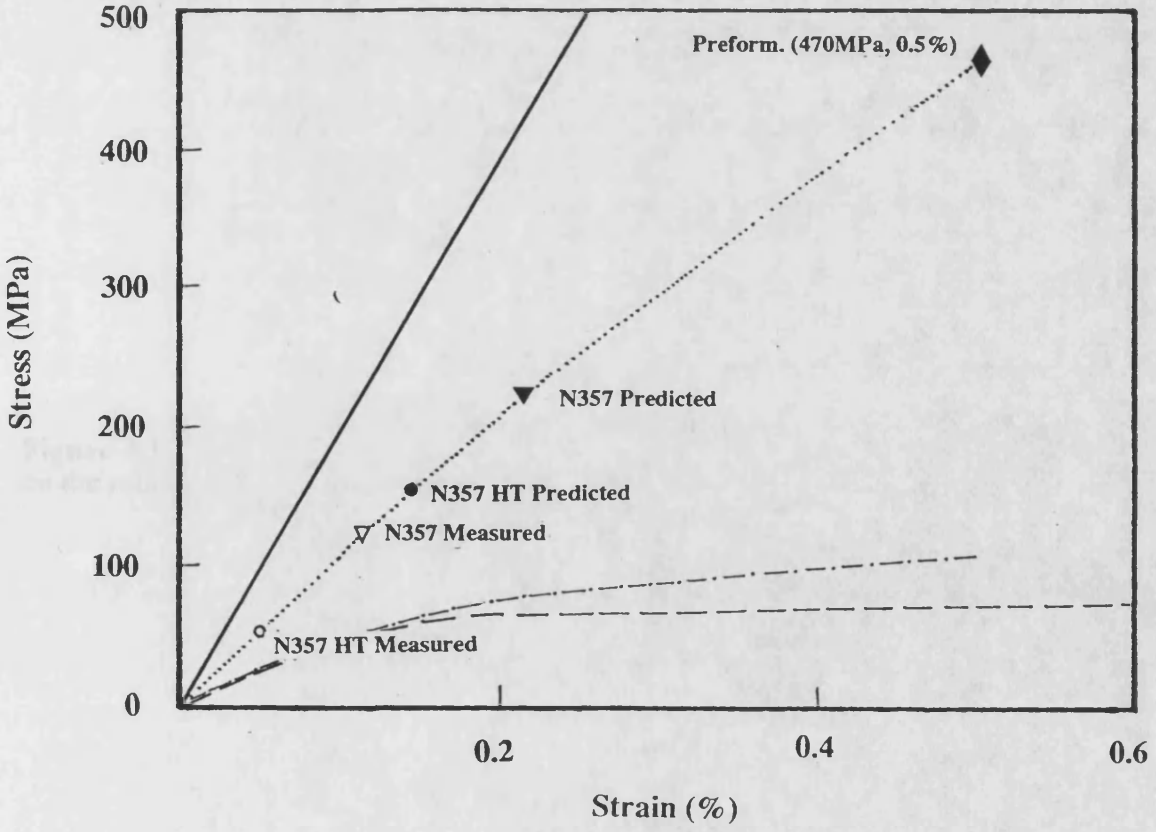

Figure 4.14 The stress versus strain curve for the Nicalon-357 composite with the failure points from the rule of mixtures using different fibre measured strengths.

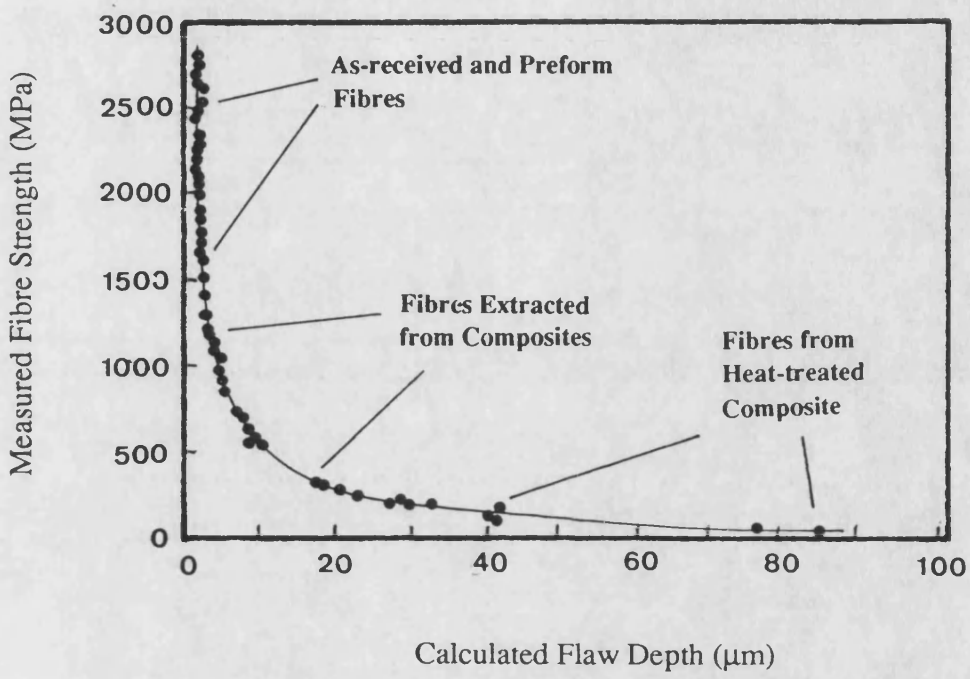

Figure 4.15 The calculated flaw size that would result in the fibre strength measured. Based on the relationship; $K_{IC}=Y.s.\sqrt{(p.a_f)}$, with the fracture toughness, $K_{IC}=3MN\ mm^{-3/2}$.

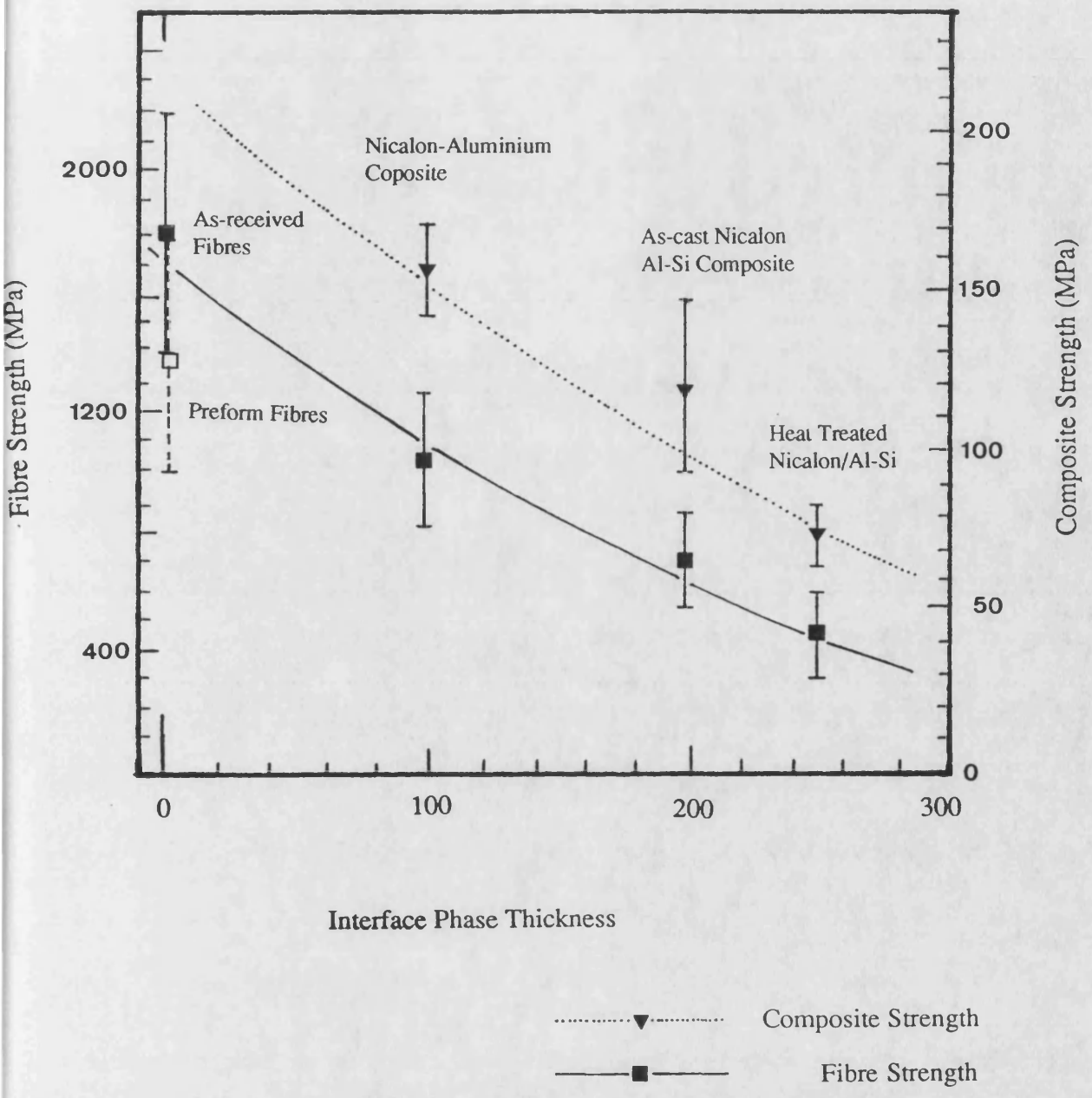

Figure 4.16 The measured strength of the fibre and composite versus the estimated interfacial reaction product thickness, the thickness was estimated from the TEM investigation.

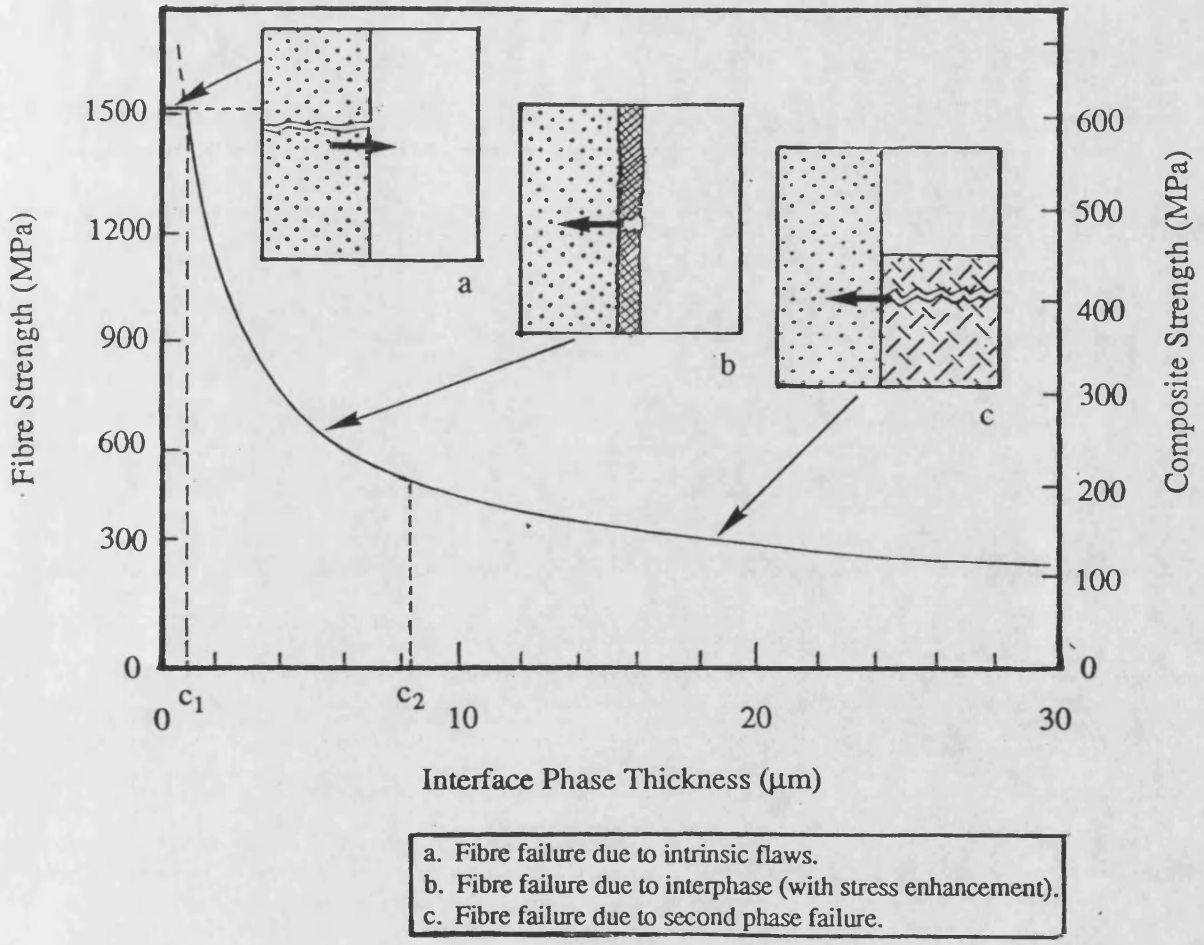

Figure 4.17 The theoretical strength dependence on the brittle interphase thickness for the Nicalon composite, with three zones. The first is failure due to fibre intrinsic flaws, secondly, the reaction phases at the interface and finally the fracture due to matrix phases.

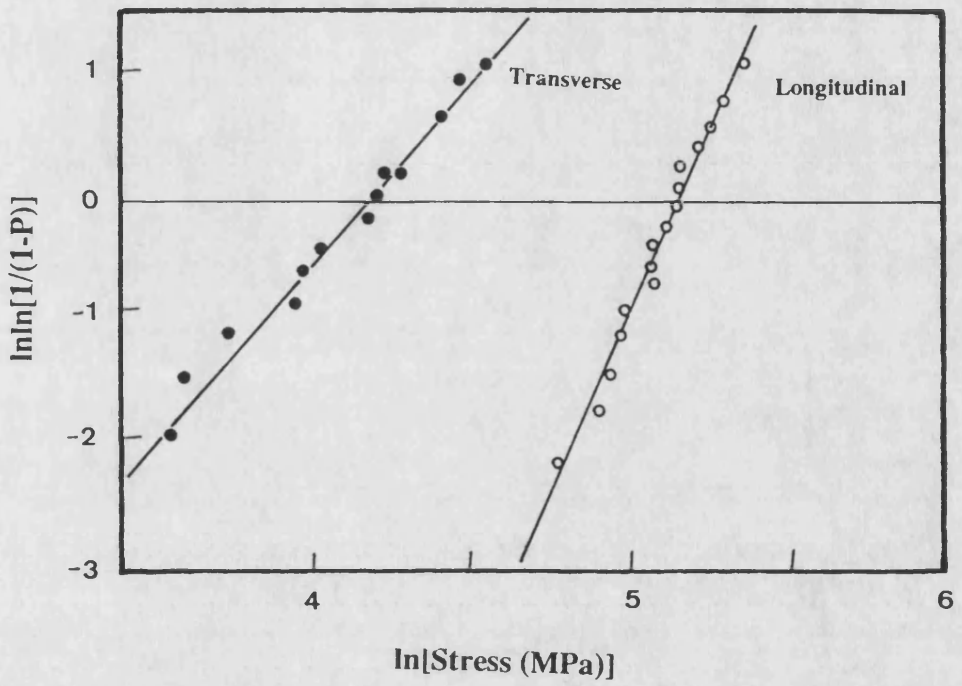

Figure 4.18 The Weibull probability distributions for the tensile tests on the Nicalon-357 composite, in longitudinal and transverse fibre orientations.

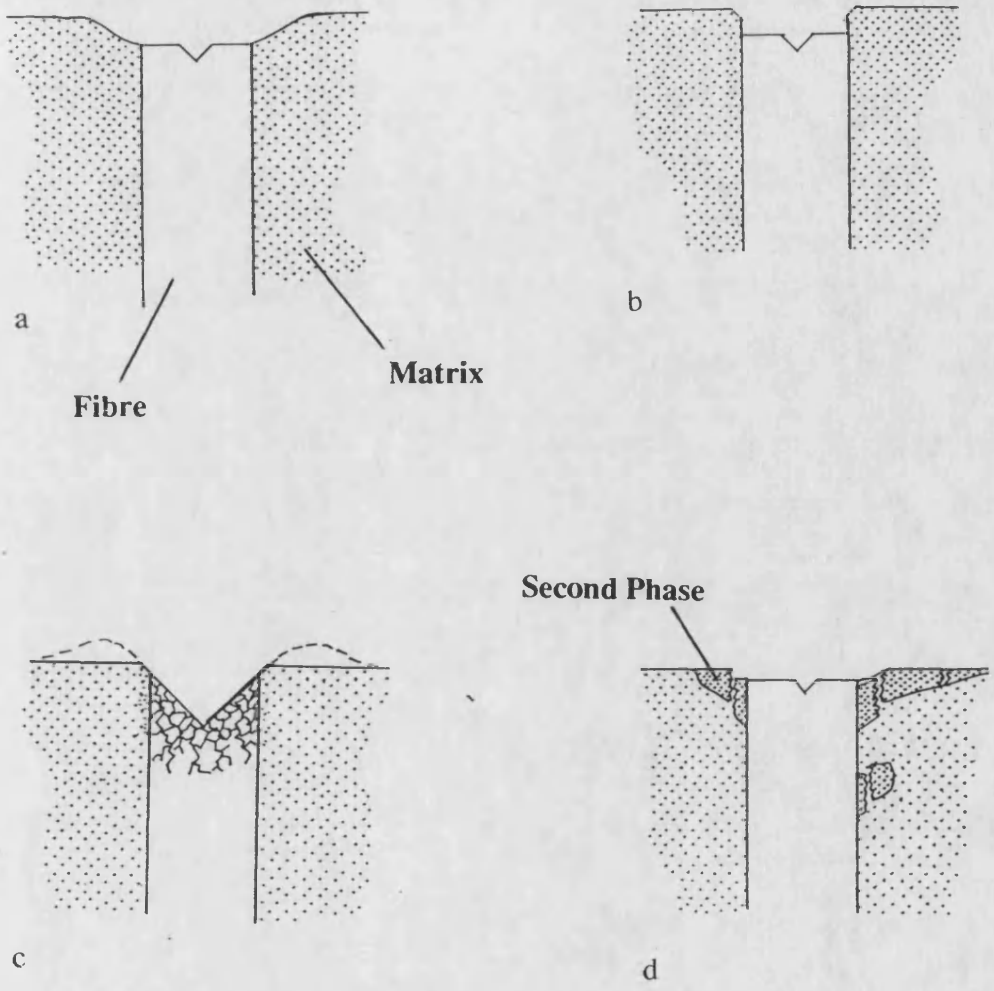

Figure 4.19 A schematic diagram of the possible contributions to the interfacial bond strength measured in fibre/matrix interfacial shear testing for metal matrix composites. These include the plastic deformation of the matrix, a, the fracture of the bond followed by sliding, b, fibre fracture with no fibre movement, c, and fibre and attached matrix phase failure, d.

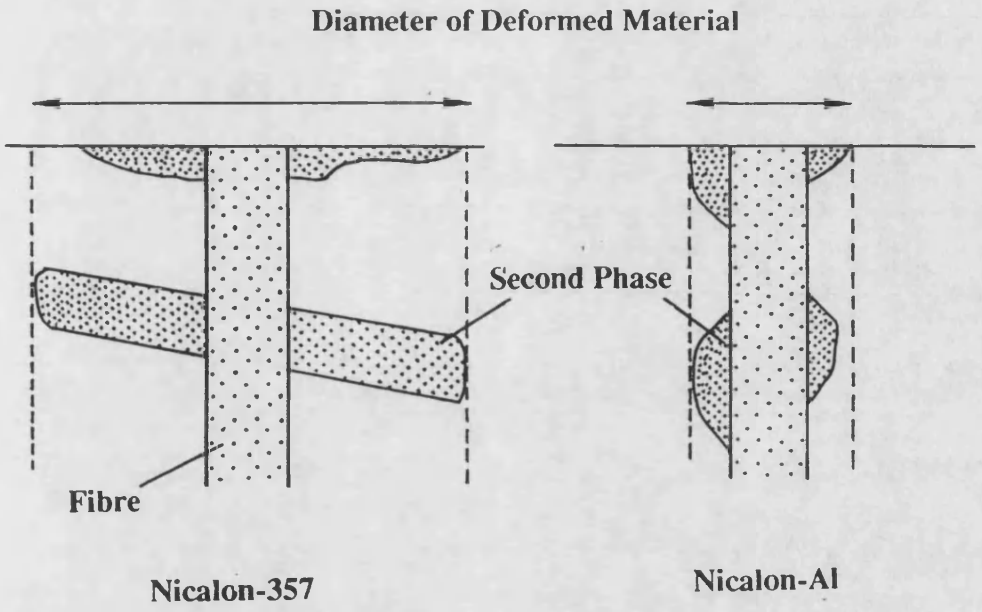

Figure 4.20 A schematic diagram of the volume of material associated with the interfacial fibre/matrix test, depending on the size of the attached matrix phase.

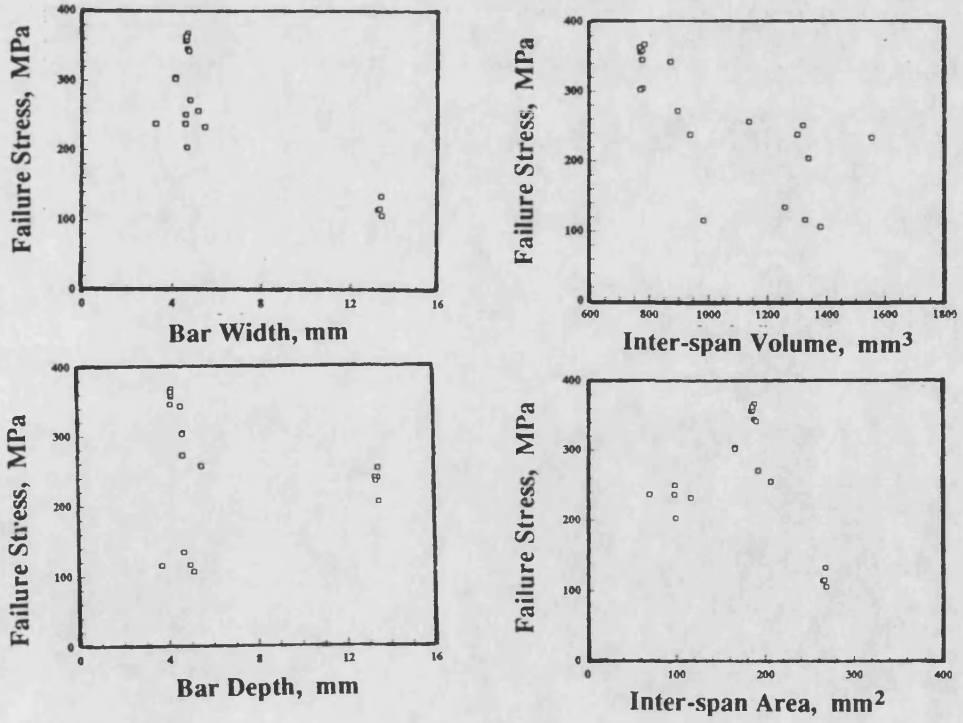

Figure 4.21 The flexural strength for longitudinal orientated specimens, versus geometrical variables for each set of bar geometry used.

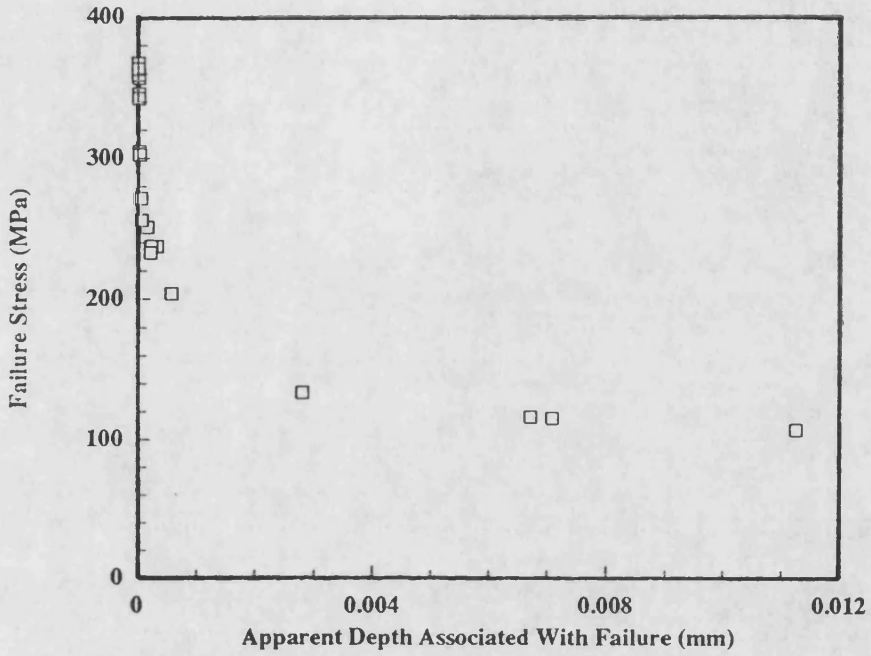

Figure 4.22 The measured composite strength in flexural test, versus a calculated apparent depth associated with fracture.

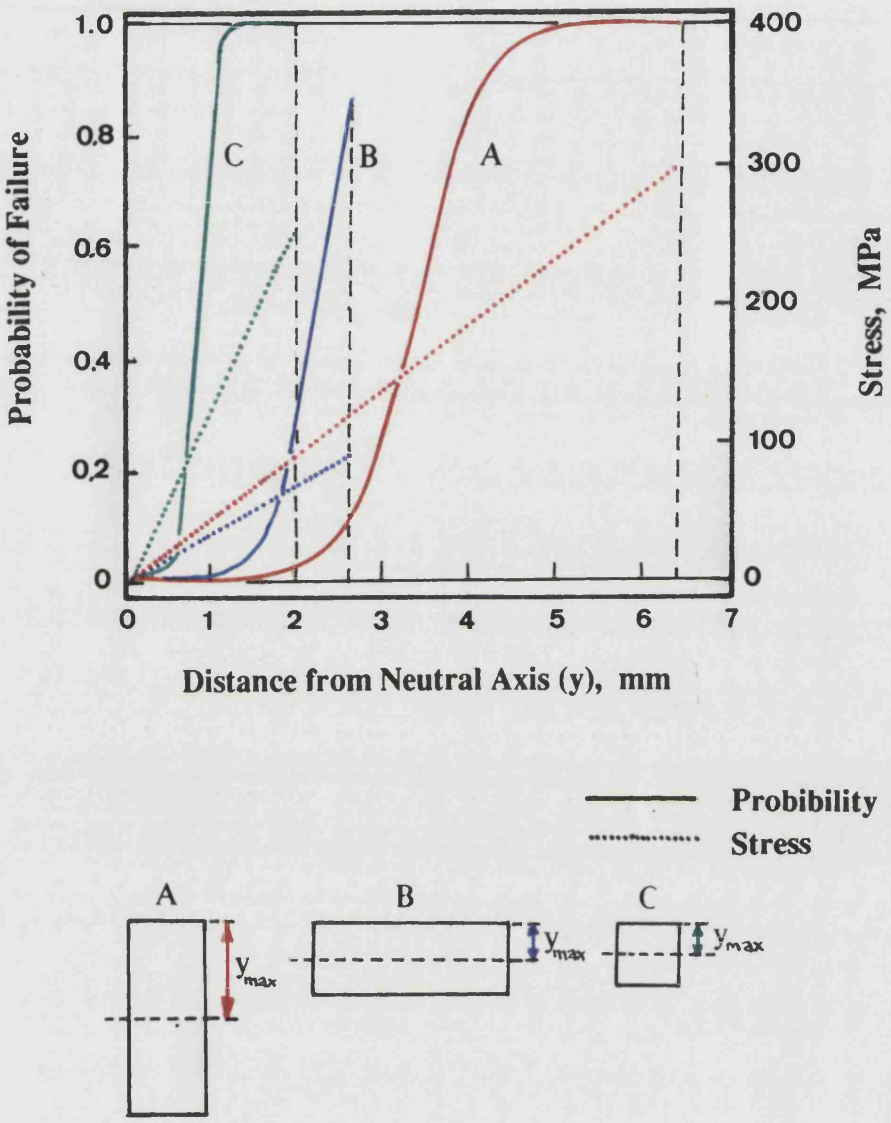

Figure 4.23 The theoretical variation of load and associated probability of composite failure with the distance from the neutral axis of flexural test bar, for each of the bar geometries used.